Mathematical modeling of compressible and incompressible multiphase flow based on mixture theory

by

Yangyang Qiao

Thesis submitted in fulfillment of
the requirements for degree of
PHILOSOPHIAE DOCTOR
(PhD)

University
of Stavanger

Faculty of Science and Technology
Department of Energy and Petroleum Engineering
2020

University of Stavanger
N-4036 Stavanger
NORWAY
www.uis.no

ISBN: 978-82-7644-904-4
ISSN: 1819-1387
PhD thesis UiS No. 501

Preface

This dissertation is submitted in partial fulfillment of the requirements for the degree of Philosophiae Doctor at the University of Stavanger, Norway. The doctoral research was funded by the Norwegian Ministry of Education and Research. The research lasted from October 2016 until October 2019 and was conducted at the Department of Energy and Petroleum Engineering at the University of Stavanger, excluding a summer internship at Equinor from June 2019 until August 2019. The main supervisor was Professor Steinar Evje and co-supervisors were Professor II Dag Chun Standnes and Associate Professor Pål Østebø Andersen.

Stavanger, November 2019
Yangyang Qiao

Acknowledgements

First, and most importantly, I want to express my sincere gratitude to my supervisor Steinar Evje for providing me such a great opportunity to study mathematical modeling, and I am very appreciative for his supportive mentorship. His profound knowledge and earnestness and persistence in research are really admirable.

I would like to acknowledge my co-supervisors, Dag Chun Standnes and Pål Østebø Andersen. They always responded quickly to my questions and provided constructive suggestions whenever I contacted them. Special thanks to Dag Chun Standnes for taking the initiative to care for me from time to time.

I also want to thank Professor Huanyao Wen for introducing me to the knowledge of mathematical analysis during my two visits at South China University of Technology, and many friends who took care of me there.

In addition, thanks to Norbert Puttkamer, Jahn Otto Waldeland, Payam Allahvirdizadeh and other colleagues who worked around me and created a very nice working environment in the department.

Last but not least, I am very grateful to my parents for being supportive of my life and my girlfriend for accompanying and encouraging me during my study.

Abstract

MIXTURE THEORY has been developed based on balance laws and conservation principles which is well known in continuum mechanics, and has been widely applied to systems which can be characterized as a mixture of interacting continua. In this thesis we present a general mathematical model for the compressible and incompressible multiphase flows based on the theory of mixtures and investigate the corresponding numerical schemes that are used to solve different kinds of flow phenomena. Mathematical analysis, which essentially boils down to deriving various estimates in appropriate functional spaces, is also used as a tool to gain insight into the models that have been explored.

The first part (Paper I and II) of this thesis implements a novel two-phase momentum-equation-approach to include the viscous coupling effect involved in counter-current and co-current flows during spontaneous imbibition process for oil recovery. The formulation can automatically capture the effective relative permeabilities of the flowing phases and offers improvements over conventional modelling. The model also accounts for the fact that oil must overcome the so-called capillary backpressure when it is produced counter-currently. It is shown that this parameter can influence the extent of counter-current production and hence viscous coupling.

The second part (i.e., Paper III-V) of this thesis focuses on the development of numerical schemes for solving the general multiphase flow model. We consider two-phase and three-phase flow in porous media for both incompressible and compressible cases. We also explore in Paper III and IV different estimates that can deepen the insight into the system which is studied as well as ensure existence of solutions subject to appropriate assumptions. Specifically, in Paper III, a general two-phase model without source terms is solved and the investigations indicate that interstitial velocity seems more natural to use in the viscous term than Darcy velocity for the momentum balance equation. In Paper IV, source terms are taken into account and different physical effects are highlighted such as compressibility and viscous coupling. Various a priori estimates are derived that give rise to an existence result for the general two-phase model with and without source terms. In addition, we also extended the two-phase model to the three-phase model in Paper V and illustrated the stability of the developed numerical schemes by investigating several numerical examples, both for the case with incompressible and compressible fluids.

In the last part of this thesis, represented by Paper VI, we explore a general cell-fluid Navier-Stokes model to mimic an evolution process of the bacterial plumes development. The generality of the mixture theory approach allows us to incorporate a new migration effect, so-called chemotaxis, in the momentum balance for the cell phase. Chemotaxis and gravity segregation are two main driving forces that result in a complex flow pattern formation of bacterial. The nonlinear dynamics is explored in a 2D setting by using an appropriate finite difference scheme. This model can be interpreted as a generalization of the well-known chemotaxis-Stokes model which has attracted much attention the last decade.

List of Papers

Paper I

Qiao, Yangyang, Andersen, Pål Østebø, Evje, Steinar and Standnes, Dag Chun. 'A mixture Theory Approach to Model Co- and Counter-current Two-phase Flow in Porous Media Accounting for Viscous Coupling'. In: *Advances in Water Resources,* **112** pp.170-188 (2018).

Paper II

Andersen, Pål Østebø, Qiao, Yangyang, Standnes, Dag Chun and Evje, Steinar. 'Cocurrent Spontaneous Imbibition in Porous Media with the Dynamics of Viscous Coupling and Capillary Backpressure'. In: *SPE Journal,* **24** pp.158-177 (2019).

Paper III

Qiao, Yangyang, Wen, Huanyao and Evje, Steinar. 'Compressible and Viscous Two-phase Flow in Porous Media Based on Mixture Theory Formulation'. In: *Networks and Heterogeneous Media,* **14 (3)** pp.489-536 (2019).

Paper IV

Qiao, Yangyang, Wen, Huanyao and Evje, Steinar. 'Viscous Two-phase Flow in Porous Media Driven by Source Terms: Analysis and Numerics'. In: *SIAM Journal on Mathematical Analysis,* **51 (6)** pp.5103-5140 (2019).

Paper V

Qiao, Yangyang and Evje, Steinar. 'A Compressible Viscous Three-phase Model for Porous Media Flow Based on the Theory of Mixtures'. Under review in: *Advances in Water Resources.*

Paper VI

Qiao, Yangyang and Evje, Steinar. 'A General Cell-fluid Navier-Stokes Model with Inclusion of Chemotaxis'. Accepted in: *Mathematical Models and Methods in Applied Sciences.*

Contents

Chapter 1

Introduction

> *"I do not feel obliged to believe that the same God who has endowed us with sense, reason, and intellect has intended us to forgo their use."*
>
> — Galileo Galilei (1564 - 1642)

1.1 A generalized multiphase flow model based on mixture theory

The importance of multiphase flow in porous media has long been recognized in many fields. Mathematical modelling of multiphase flow is essential in practical applications like enhanced oil recovery and geological CO_2 storage in depleted oil and gas reservoirs (Juanes 2008; Wu 2015) as well as biological and medical-related processes (Evje 2017; Evje et al. 2018; Lemon et al. 2006; Urdal et al. 2019; Waldeland et al. 2018).

Conventional modeling of two-phase flow in porous media is based on Darcy's extended law which was originally developed empirically for single-phase flow (Darcy 1856; Rose 2000) and extended to multiphase flow by incorporation of relative permeabilities (Muskat et al. 1937). The relative permeability is commonly assumed to be a function of saturation only, implying that the presence of another phase has a unique impact on the phase's flux, i.e., no coupling is accounted for through the velocity or pressure gradient of the other phase. Generally, the conventional model takes the form of

$$\begin{aligned} &(\phi s_i \rho_i)_t + \nabla \cdot (\rho_i \mathbf{U}_i) = Q_i, && (i = w, o) \\ &\mathbf{U}_i = -\frac{K \mathbf{k}_{ri}}{\mu_i} \nabla (P_i - \rho_i \mathbf{g}), && \mathbf{U}_i = \phi s_i \mathbf{u}_i \end{aligned} \tag{1.1}$$

where $\mathbf{U}_i, \mathbf{u}_i$ are Darcy and interstitial velocities respectively, Q_i represents source term, K is the absolute permeability, P_i is phase pressure, $\mathbf{k}_{ri}$ is the phase relative permeability, ϕ is the porosity of the medium, ρ_i represents density and s_i the volume fraction (saturation). The phase pressures are dependent due to the capillary pressure function $P_c(s_w) = P_o - P_w$.

Several experimental observations, however, indicate that the flow mode (co- or counter-current) can have a more or less strong impact on the phase mobilities. Previous studies of counter-current flow settings (see below for more details) support that relative permeability in a counter-current flow setting can be significantly lower than in co-current flow settings. In conventional simulation tools, the dependence of the saturation functions (i.e., relative permeability and capillary pressure) on the flow direction (co-current or counter-current) and phase velocities is commonly ignored. This indicates that the use of the extended Darcy's law may be questionable.

The starting point for developing our model that can account for more detailed physical mechanisms for water-oil flow in porous media than conventional modeling, is the theory of mixtures.

This is a theory based on balance laws and conservation principles which is well known in continuum mechanics (Ambrosi et al. 2002; Bowen 1980; Byrne et al. 2003; Preziosi et al. 2002; Rajagopal et al. 1995), and has been widely applied to systems which can be characterized as a mixture of interacting continua.

Development of models within the framework of mixture theory has found many applications within the study of multiphase flow in porous media relevant for life science (biomechanics), see for instance, (Ambrosi et al. 2002; Byrne et al. 2003; Preziosi et al. 2002).

An instructive overview is given in (Rajagopal 2007) of how generalizations of the standard Darcy's law for single phase flow can be derived within the context of mixture theory. Starting with more general momentum balance equations and using different sets of assumptions leads to a hierarchy of mathematical models.

In this work, we apply mixture theory to derive a model that is appropriate to a water-oil flow scenario in porous media and the formulation of the model takes the following form:

$$\begin{aligned}
(\phi n)_t + \nabla\cdot(\phi n \mathbf{u}_o) &= Q_o, \qquad n = s_o\rho_o \\
(\phi m)_t + \nabla\cdot(\phi m \mathbf{u}_w) &= Q_w, \qquad m = s_w\rho_w \\
s_o\nabla P_o - n\mathbf{g} &= -\hat{k}_o\mathbf{u}_o + \hat{k}_{ow}(\mathbf{u}_w - \mathbf{u}_o) + \varepsilon_o\nabla\cdot(n\nabla\mathbf{u}_o) \\
s_w\nabla P_w - m\mathbf{g} &= -\hat{k}_w\mathbf{u}_w - \hat{k}_{ow}(\mathbf{u}_w - \mathbf{u}_o) + \varepsilon_w\nabla\cdot(m\nabla\mathbf{u}_w) \\
P_c &= P_o - P_w = P_c(s_w).
\end{aligned} \tag{1.2}$$

Herein, $\hat{k}_w$, $\hat{k}_o$, and $\hat{k}_{ow}$ represent, respectively, the water-rock resistance force, the oil-rock resistance force and the water-oil drag force effect. Furthermore, $\varepsilon_w, \varepsilon_o$ (assumed to be constant) characterize the magnitude of the viscous terms. We explore (1.2) both for compressible flow and incompressible. For compressible fluids we use simplified pressure laws of the form

$$\rho_w - \tilde{\rho}_{w0} = \frac{P_w}{C_w}, \qquad \rho_o - \tilde{\rho}_{o0} = \frac{P_o}{C_o}, \qquad \left(\rho_g = \frac{P_g}{C_g}\right) \tag{1.3}$$

where C_w and C_o (C_g) essentially represent the inverse of the compressibility of water and oil (gas), respectively. This is often referred to as bulk modulus which is a constant that describes how resistant a substance is to compression. Hence, a weakly compressible fluid corresponds to a large C_i $(i = w, o, g)$ value.

A natural extension of (1.2) to a three-phase model is also investigated in this work (Paper V).

1.2 A general model for cell-fluid flow

In the real world, vast numbers of microorganisms are suspended in temperate aqueous environments. Oceans and rivers, puddles and droplets, the fluid interiors of animals, all host an array of splendidly varied creatures (Pedley et al. 1992). Although their presence is usually not obvious, they constitute the major part of the world's biomass. Microorganisms interact with each other and with the world, at length scales that vary upward from the size of an individual, say 10^{-4} cm, to the dimensions of the entire body of fluid in which they live. Various microorganisms respond to stimuli by swimming (in average) in particular directions. Such phenomena are called taxes. Common examples of taxes of importance are gravitaxis (or geotaxis), a response to gravity or acceleration; phototaxis, a response to light; and chemotaxis, a response to chemical gradients.

Bioconvection is the name given to the process of spontaneous pattern formation in suspensions of upswimming microorganisms. Typically, the cells are denser than the medium they swim in, nevertheless they tend to swim upwards, on average, in still water, and the patterns die away if the cells stop swimming. The cause of the upswimming orientation can be different (gravity-sensing, bottom-heaviness, chemotaxis, phototaxis), but the patterns show great similarities between different species and orientation mechanisms.

Complex bioconvection patterns form when a suspension of the bacterium Bacillus subtilis is placed in a chamber with its upper surface open to the air (Hillesdon et al. 1996; Hillesdon et al. 1995). These arise because the cells are heavier (approximately 10%) than water, yet, they are able to swim up an oxygen gradient and concentrate in a layer below the water surface, which will undergo Rayleigh-Taylor type instabilities for sufficiently high concentrations. The reason that the cells swim upwards is that they are aerotactic, i.e., they swim up gradients of oxygen, and they consume oxygen. When the vertical density gradient becomes large enough, an overturning instability occurs, analogous to Rayleigh-Bénard convection in a layer of fluid heated from below, which ultimately evolves into the observed patterns as illustrated in Fig. 1.1.

Several related coupled chemotaxis-fluid models have been proposed to describe the collective behaviour of a suspension of oxytactic bacteria in an incompressible fluid under the assumptions that the contribution of bacteria to the bacteria-fluid suspension is suffciently small and that more detailed cell-cell interactions (such as hydrodynamic interaction) are neglected (Chertock et al. 2012). The suspension is considered to be dilute, so that the volume fraction $vV_b \ll 1$ where v is the number density of cells (bacteria) and V_b is the average volume of the cell. Assuming fluid and bacteria are incompressible, the following model has been proposed (Tuval et al. 2005)

$$\begin{aligned} & v_t + \mathbf{u}\cdot\nabla v + \chi\nabla\cdot(vr(C)\nabla C) = D_v\Delta v \\ & \rho(\mathbf{u}_t + \mathbf{u}\cdot\nabla\mathbf{u}) + \nabla p = v\nabla\mathbf{\Phi} + \eta\Delta\mathbf{u}, \qquad \nabla\cdot\mathbf{u} = 0 \\ & C_t + \mathbf{u}\cdot\nabla C = D_C\Delta C - \kappa v r(C). \end{aligned} \tag{1.4}$$

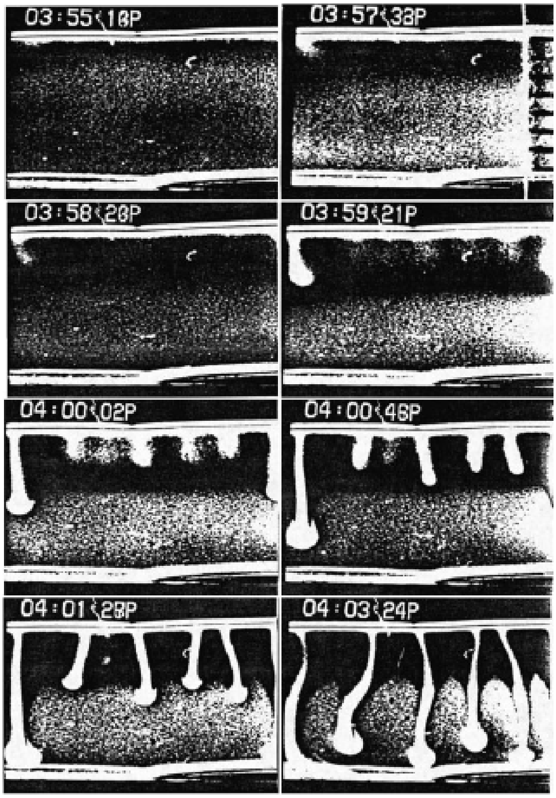

Figure 1.1: A time sequence of photographs of a deep champer ($h \approx 7 - 8mm$) containing a suspension of the aerobic bacteria Bacillus subtilis (Hillesdon et al. 1995).

The first equation of (1.4) describes the mass balance equation for the bacteria v subject to an internal interplay between a fluid-driven advection effect through $\mathbf{u} \cdot \nabla v$, chemotaxis toward higher concentration of oxygen C via $\nabla \cdot (nr(C)\nabla C)$, and diffusive spreading of bacteria in the fluid through $D_v \Delta v$. Herein, C is the concentration of oxygen, $\mathbf{u}$ is the velocity field of a fluid which is governed by the incompressible Navier-Stokes equations with density ρ, pressure p and viscosity η, as expressed by $(1.4)_2$. Moreover, in the fluid momentum balance equation of $(1.4)_2$, the term $\nabla \mathbf{\Phi} = V_b g(\rho_b - \rho)\mathbf{e}_y$ describes the gravitational force exerted by a bacterium onto the fluid along the downwards unit vector $\mathbf{e}_y$ proportional to the volume of the bacterium V_b with density ρ_b where ρ_b is slightly higher than the fluid density ρ. This formulation relies on the the Boussinesq approximation in which the density variations caused by bacteria appear only through the buoyant forcing $\nabla \mathbf{\Phi}$. A dimensionless cut-off function $r(C)$ models an inactivity threshold of the bacteria due to low oxygen supply. Experiments suggest that the cut-off function can be modelled by a step function

Variable	Description
α_c,α_w	volume fraction of cell, fluid
ρ_c,ρ_w	cell density, fluid density
$\mathbf{u}_c$,$\mathbf{u}_w$	cell velocity, fluid velocity
C	oxygen concentration
P_c, P_w	cell pressure, fluid pressure
ΔP, Λ	cell-cell stress, chemotactic stress
ε_c,ε_w	effective viscosity cell, fluid
$\hat{\zeta}$	cell-fluid interaction coefficient (drag force)
K	consumption rate (oxygen)
D_C	diffusion coefficient (oxygen)

Table 1.1: Nomenclature description for model (1.5)

$r(C) = H(C - C^*)$ (Tuval et al. 2005) where $H(\cdot)$ denotes the Heaviside function. The parameters χ and κ control the magnitude of chemotaxis and consumption of oxygen, respectively, whereas D_v and D_C are diffusion constants.

In Paper VI we develop a general cell-fluid model which naturally can represent the model (1.4) as a special case. Hence, we shall in the following describe such a model by relying on a mixture theory multiphase formulation. In the multiphase modeling framework, the cell-fluid environment is considered as a mixture of two interacting continua (Bowen 1976; Drew et al. 2006; Qiao et al. 2018; Rajagopal 2007; Rajagopal et al. 1995). The cellular phase comprises cells represented by a volume fraction α_c moving with a velocity $\mathbf{u}_c$ and the fluid phase represented by the volume fraction α_w moving with a velocity $\mathbf{u}_w$. The model takes the following form (see Table 1.1 for the different variables):

$$\begin{aligned}
n_t + \nabla\cdot(n\mathbf{u}_c) &= 0, \qquad\qquad n = \alpha_c\rho_c\\
m_t + \nabla\cdot(m\mathbf{u}_w) &= 0, \qquad\qquad m = \alpha_w\rho_w\\
(n\mathbf{u}_c)_t + \nabla\cdot(n\mathbf{u}_c\otimes\mathbf{u}_c) + \alpha_c\nabla P_c &= \hat{\zeta}(\mathbf{u}_w - \mathbf{u}_c) + n\mathbf{g} + \varepsilon_c\nabla\cdot(n(\nabla\mathbf{u}_c + \nabla\mathbf{u}_c^T))\\
(m\mathbf{u}_w)_t + \nabla\cdot(m\mathbf{u}_w\otimes\mathbf{u}_w) + \alpha_w\nabla P_w &= \hat{\zeta}(\mathbf{u}_c - \mathbf{u}_w) + m\mathbf{g} + \varepsilon_w\nabla\cdot(m(\nabla\mathbf{u}_w + \nabla\mathbf{u}_w^T))\\
C_t + \nabla\cdot(C\mathbf{u}_w) &= \nabla\cdot(D_C\nabla C) - K\alpha_c C.
\end{aligned} \tag{1.5}$$

The two first equations describe mass balance of the cell and fluid phase, respectively. The entire volume is occupied by the two phases, i.e., $\alpha_c + \alpha_w = 1$. The next two equations in (1.5) are the corresponding momentum balance equations. The cell momentum equation $(1.5)_3$ accounts for two migration mechanisms: (i) diffusive migration towards a lower volume fraction of cells α_c; (ii) chemotactic migration towards a region with higher concentration of oxygen C. This is achieved by letting the cell phase pressure P_c feel additional stress due to cell-cell interaction through a term $\Delta P(\alpha_c)$ as well as a chemotaxis-related stress $\Lambda(C)$ through the relation $P_c = P_w + \Delta P(\alpha_c) + \Lambda(C)$.

Chapter 2

Mathematical models and numerical schemes

> *"I seem to have been only like a boy playing on the seashore, and diverting myself in now and then finding a smoother pebble or a prettier shell than ordinary, whilst the great ocean of truth lay all undiscovered before me."*
>
> — Isaac Newton (1642 - 1727)

In this chapter, we summarize the generalized two-phase and three-phase models together with a general cell-fluid Navier-Stokes model. The numerical schemes are also presented based on a finite difference approach.

2.1 A two-phase model and its numerical scheme

The generalized 1-D two-phase model for porous media flow takes the following form with (n, m, u_w, u_o) as the main variables

$$\begin{aligned}
(n)_t + (nu_o)_x &= -nQ_p, \qquad\qquad n = s_o\rho_o \\
(m)_t + (mu_w)_x &= -mQ_p + \rho_w Q_I, \qquad m = s_w\rho_w \\
s_o(P_o)_x &= -\hat{k}_o u_o + \hat{k}(u_w - u_o) + ng + \varepsilon_o(nu_{ox})_x \\
s_w(P_w)_x &= -\hat{k}_w u_w - \hat{k}(u_w - u_o) + mg + \varepsilon_w(mu_{wx})_x \\
P_c = P_o - P_w &= P_c(s_w)
\end{aligned} \tag{2.1}$$

subject to the boundary condition

$$\begin{aligned}
&u_w(x=0,t) = u_o(x=0,t) = 0 \\
&u_w(x=1,t) = u_o(x=1,t) = 0, \qquad t > 0
\end{aligned} \tag{2.2}$$

and initial condition

$$n(x, t=0) = n_0(x), \qquad m(x, t=0) = m_0(x), \qquad x \in [0,1]. \tag{2.3}$$

Note that the gravity constant g can take both signs depending on the orientation of the x-coordinate axis. Above we assume that positive direction of x-axis points downward and $g > 0$. In addition, porosity ϕ is assumed to be 1 for simplicity. For compressible fluids we use simplified pressure laws of the form

$$\rho_w - \tilde{\rho}_{w0} = \frac{P_w}{C_w}, \qquad \rho_o - \tilde{\rho}_{o0} = \frac{P_o}{C_o}. \tag{2.4}$$

2.1.1 Compressible model

We consider discrete schemes for both the compressible and incompressible version of (2.1). For that purpose we introduce a reformulation that brings the compressible model closer to the incompressible model. In particular, we solve explicitly only for the mass transport of $m = s_w\rho_w$ whereas the mass n is computed implicitly. This will be in the spirit of the incompressible approach where we solve the mass balance equation for s_w and compute $s_o = 1-s_w$. Details are given below. The starting point is the model (2.1) with (n, m, u_w, u_o) as the main (unknown) variables. We rewrite the model in the following equivalent form with (m, P_w, u_w, u_o) as the main variables:

$$\begin{aligned}
(m)_t + (mu_w)_x &= -mQ_p + \rho_w Q_I \\
P_{wt} + \tilde{\eta}\rho_w(nu_o)_x + \tilde{\eta}\tilde{\rho}_o(mu_w)_x &= \tilde{\eta}\rho_w\rho_o(Q_I - Q_p) - \tilde{\eta}\frac{s_o P_c'}{C_o}(\rho_w Q_I - mQ_p) \\
s_w(P_w)_x &= -(\hat{k}_w + \hat{k})u_w + \hat{k}u_o + mg + \varepsilon_w(mu_{wx})_x \\
s_o(P_w + P_c)_x &= -(\hat{k}_o + \hat{k})u_o + \hat{k}u_w + ng + \varepsilon_o(nu_{ox})_x
\end{aligned} \tag{2.5}$$

with

$$\tilde{\eta} = \frac{C_w C_o}{s_o\rho_w C_w + s_w\tilde{\rho}_o C_o}, \qquad \tilde{\rho}_o = \rho_o - \frac{s_o P_c'}{C_o}. \tag{2.6}$$

We refer to Appendix C in Paper III which gives the pressure evolution equation $(2.5)_2$. Note that s_w, s_o, n, P_o are determined by

$$\begin{aligned}
s_w &= \frac{m}{\rho_w(P_w)}, \qquad s_o = 1 - s_w \\
n &= s_o\rho_o(P_o) = \Big(1 - \frac{m}{\rho_w(P_w)}\Big)\rho_o(P_o) = n(m, P_w) \\
P_o &= P_c(s_w) + P_w = P_o(m, P_w).
\end{aligned} \tag{2.7}$$

We solve (2.5) on our domain Ω with boundary conditions

$$u_w|_{\partial\Omega} = u_o|_{\partial\Omega} = 0 \tag{2.8}$$

and initial condition

$$m(x, t = 0) = m_0(x), \qquad P_w(x, t = 0) = P_w(m_0(x), n_0(x)). \tag{2.9}$$

System of ODEs

We consider the domain $\Omega = [0, 1]$ and introduce a grid of N_x cells with nodes x_j placed at the center of the cells

$$x_1 = \frac{1}{2}\Delta x, \quad x_2 = (1+\frac{1}{2})\Delta x, \quad \dots, \quad x_j = (j-\frac{1}{2})\Delta x, \quad \dots, \quad x_{N_x} = (N_x-\frac{1}{2})\Delta x$$

and cell interfaces $x_{j+1/2}$ at the cell interfaces

$$x_{1/2}=0, \quad x_{3/2}=\Delta x, \quad \dots, \quad x_{j+1/2}=j\Delta x, \quad \dots, \quad x_{N_x+1/2}=N_x\Delta x=1$$

where $\Delta x = 1/N_x$. We introduce the approximate mass and pressure $\{m_j(t)\}_{j=1}^{N_x}$ and $\{P_{w,j}(t)\}_{j=1}^{N_x}$ associated with the nodes $\{x_j\}_{j=1}^{N_x}$ whereas the approximate velocities $\{u_{w,j+1/2}\}_{j=0}^{N_x}$ and $\{u_{o,j+1/2}\}_{j=0}^{N_x}$ are associated with the cell interfaces $\{x_{j+1/2}\}_{j=0}^{N_x}$. In the following we describe a fully discrete version of (2.5).

A fully discrete scheme for the compressible model

We assume that we have given $(m_j^k, P_{w,j}^k, u_{w,j}^k, u_{o,j}^k)$. We then compute the approximate solution at time t^{k+1} expressed by $(m_j^{k+1}, P_{w,j}^{k+1}, u_{w,j}^{k+1}, u_{o,j}^{k+1})$ as follows:

Step 1: Mass transport

$$\frac{m_j^{k+1}-m_j^k}{\Delta t}+\frac{1}{\Delta x}([mu_w]_{j+1/2}^k-[mu_w]_{j-1/2}^k)=-m_j^kQ_{p,j}+\rho_{wj}^kQ_{I,j} \tag{2.10}$$

where

$$[mu_w]_{j+1/2}^k=\begin{cases} m_j^k u_{w,j+1/2}^k, & \text{if } u_{w,j+1/2}^k \ge 0; \\ m_{j+1}^k u_{w,j+1/2}^k, & \text{if } u_{w,j+1/2}^k < 0. \end{cases} \tag{2.11}$$

Having computed m_j^{k+1} we can compute an updated water saturation $s_{w,j}^{k+1/2}$ given by

$$s_{w,j}^{k+1/2}=\frac{m_j^{k+1}}{\rho_w(P_{w,j}^k)}. \tag{2.12}$$

Similarly, we compute updated mass $n_j^{k+1/2}=(1-s_{w,j}^{k+1/2})\rho_o(P_{o,j}^{k+1/2})$ and $P_{o,j}^{k+1/2}=P_{w,j}^k+P_c(s_{w,j}^{k+1/2})$, according to (2.7), which are needed to evaluate coefficients in the next step.

Step 2: Computation of velocities and pressure

Next, we solve simultaneously for $P_{w,j}^{k+1}$ and $u_{w,j+1/2}^{k+1}$ and $u_{o,j+1/2}^{k+1}$ by considering the following algebraic system

$$\begin{aligned} \frac{P_{wj}^{k+1}-P_{wj}^k}{\Delta t} &+[\tilde\eta\rho_w]_j^{k+1/2}\frac{1}{\Delta x}\Big([n^{k+1/2}u_o^{k+1}]_{j+1/2}-[n^{k+1/2}u_o^{k+1}]_{j-1/2}\Big) \\ &+[\tilde\eta\tilde\rho_o]_j^{k+1/2}\frac{1}{\Delta x}\Big([m^{k+1}u_w^{k+1}]_{j+1/2}-[m^{k+1}u_w^{k+1}]_{j-1/2}\Big) \\ &=[\tilde\eta\rho_w\rho_o]_j^{k+1/2}(Q_{I,j}-Q_{p,j})-\Big[\tilde\eta\frac{s_oP_c'}{C_o}\Big]_j^{k+1/2}(\rho_{wj}^kQ_{I,j}-m_j^{k+1}Q_{p,j}) \end{aligned} \tag{2.13}$$

which is combined with the momentum balance equations

$$\begin{aligned}
&s^{k+1/2}_{w,j+1/2}\frac{1}{\Delta x}(P^{k+1}_{w,j+1}-P^{k+1}_{w,j}) = \\
&\qquad -\hat{k}^{k+1/2}_{w,j+1/2}u^{k+1}_{w,j+1/2}-\hat{k}^{k+1/2}_{j+1/2}\Big(u^{k+1}_{w,j+1/2}-u^{k+1}_{o,j+1/2}\Big)+m^{k+1}_{j+1/2}g \\
&\quad +\varepsilon_w\frac{1}{\Delta x^2}\Big(m^{k+1}_{j+1}[u_{w,j+3/2}{}^{k+1}-u^{k+1}_{w,j+1/2}]-m^{k+1}_{j}[u^{k+1}_{w,j+1/2}-u^{k+1}_{w,j-1/2}]\Big), \\
&s^{k+1/2}_{o,j+1/2}\frac{1}{\Delta x}(P^{k+1}_{w,j+1}-P^{k+1}_{w,j}) = -s^{k+1/2}_{o,j+1/2}\frac{1}{\Delta x}(P^{k+1/2}_{c,j+1}-P^{k+1/2}_{c,j}) \\
&\qquad -\hat{k}^{k+1/2}_{o,j+1/2}u^{k+1}_{o,j+1/2}+\hat{k}^{k+1/2}_{j+1/2}\Big(u^{k+1}_{w,j+1/2}-u^{k+1}_{o,j+1/2}\Big)+n^{k+1/2}_{j+1/2}g \\
&\quad +\varepsilon_o\frac{1}{\Delta x^2}\Big(n^{k+1/2}_{j+1}[u_{o,j+3/2}{}^{k+1}-u^{k+1}_{o,j+1/2}]-n^{k+1/2}_{j}[u^{k+1}_{o,j+1/2}-u^{k+1}_{o,j-1/2}]\Big).
\end{aligned} \tag{2.14}$$

Equipped with $(P^{k+1}_{w,j}, u^{k+1}_{w,j+1/2}, u^{k+1}_{o,j+1/2})$ we can now update the saturation $s_{w,j}$ by

$$s^{k+1}_{w,j} = \frac{m^{k+1}_j}{\rho_w(P^{k+1}_{w,j})} \tag{2.15}$$

from which we also compute the updated oil mass n^{k+1}_j and pressure $P^{k+1}_{o,j}$ via (2.7). If necessary, we may repeat step 2 to improve the accuracy before we proceed to next time level.

Remark 2.1.1. The upwind discretization of $[n^{k+1/2}u^{k+1}_o]_{j+1/2}$ and $[m^{k+1}u^{k+1}_w]_{j+1/2}$ appearing in (2.13) are based on "old" velocities $u^k_{o,j+1/2}$ and $u^k_{w,j+1/2}$.

2.1.2 Incompressible model

When fluids are incompressible the model (2.1) takes the following form with unknown variables (s_w, P_w, u_w, u_o)

$$\begin{aligned}
(s_w)_t+(s_wu_w)_x &= -s_wQ_p+Q_I \\
(s_o)_t+(s_ou_o)_x &= -s_oQ_p \\
s_w(P_w)_x &= -\hat{k}_wu_w-\hat{k}(u_w-u_o)+s_w\rho_wg+\varepsilon_w\rho_w(s_wu_{wx})_x \\
s_o(P_w+P_c)_x &= -\hat{k}_ou_o+\hat{k}(u_w-u_o)+s_o\rho_og+\varepsilon_o\rho_o(s_ou_{ox})_x
\end{aligned} \tag{2.16}$$

subject to the boundary condition

$$u_w|_{\partial\Omega} = u_o|_{\partial\Omega} = 0 \tag{2.17}$$

and initial condition

$$s_w(x,t=0) = s_{w0}(x). \tag{2.18}$$

Note that we can only determine P_w up to a constant and a reference pressure P^* at some point in the domain may be specified. An equivalent formulation of

(2.16) is given by (after a summation of the two mass balance equation)

$$\begin{aligned}(s_w)_t + (s_w u_w)_x &= -s_w Q_p + Q_I \\ (s_w u_w + s_o u_o)_x &= -Q_p + Q_I \\ s_w (P_w)_x &= -\hat{k}_w u_w - \hat{k}(u_w - u_o) + s_w \rho_w g + \varepsilon_w \rho_w (s_w u_{wx})_x \\ s_o (P_w + P_c)_x &= -\hat{k}_o u_o + \hat{k}(u_w - u_o) + s_o \rho_o g + \varepsilon_o \rho_o (s_o u_{ox})_x.\end{aligned} \tag{2.19}$$

This formulation is consistent with and follows directly from (2.5) by letting $C_w, C_o \to \infty$ (i.e., the fluids become incompressible). This is a consequence of the fact that $\tilde{\eta} \to \infty$ and $\tilde{\rho}_o \to \rho_o$, see (2.6).

A fully discrete scheme for the incompressible model

We can now proceed with a description of a full discrete scheme for the incompressible case which bears clear similarity to the scheme for the compressible model.

Step 1: Mass transport

$$\frac{s_{w,j}^{k+1} - s_{w,j}^{k}}{\Delta t} + \frac{1}{\Delta x}([s_w u_w]_{j+1/2}^{k} - [s_w u_w]_{j-1/2}^{k}) = -s_{w,j}^{k} Q_{p,j} + Q_{I,j} \tag{2.20}$$

where

$$[s_w u_w]_{j+1/2}^{k} = \begin{cases} s_{w,j}^{k} u_{w,j+1/2}^{k}, & \text{if } u_{w,j+1/2}^{k} \geq 0; \\ s_{w,j+1}^{k} u_{w,j+1/2}^{k}, & \text{if } u_{w,j+1/2}^{k} < 0. \end{cases} \tag{2.21}$$

Having computed $s_{w,j}^{k+1}$ we can compute pressure and velocities simultaneously at time level $k+1$.

Step 2: Computation of velocities and pressure

We solve for $P_{w,j}^{k+1}$ and $u_{w,j+1/2}^{k+1}$ and $u_{o,j+1/2}^{k+1}$ by considering the following algebraic system

$$\begin{aligned}&\frac{1}{\Delta x}([s_w^{k+1} u_w^{k+1}]_{j+1/2} - [s_w^{k+1} u_w^{k+1}]_{j-1/2}) + \\ &\qquad \frac{1}{\Delta x}([s_o^{k+1} u_o^{k+1}]_{j+1/2} - [s_o^{k+1} u_o^{k+1}]_{j-1/2}) = Q_{I,j} - Q_{p,j}\end{aligned} \tag{2.22}$$

which is combined with the momentum balance equations

$$
\begin{aligned}
&s_{w,j+1/2}^{k+1}\frac{1}{\Delta x}(P_{w,j+1}^{k+1}-P_{w,j}^{k+1}) = \\
&\qquad -\hat{k}_{w,j+1/2}^{k+1}u_{w,j+1/2}^{k+1}-\hat{k}_{j+1/2}^{k+1}\Big(u_{w,j+1/2}^{k+1}-u_{o,j+1/2}^{k+1}\Big)+s_{w,j+1/2}^{k+1}\rho_w g \\
&\quad +\varepsilon_w\frac{\rho_w}{\Delta x^2}\Big(s_{w,j+1}^{k+1}[{u_{w,j+3/2}}^{k+1}-u_{w,j+1/2}^{k+1}]-s_{w,j}^{k+1}[u_{w,j+1/2}^{k+1}-u_{w,j-1/2}^{k+1}]\Big), \\
&s_{o,j+1/2}^{k+1}\frac{1}{\Delta x}(P_{w,j+1}^{k+1}-P_{w,j}^{k+1}) = -s_{o,j+1/2}^{k+1}\frac{1}{\Delta x}(P_{c,j+1}^{k+1}-P_{c,j}^{k+1}) \\
&\qquad -\hat{k}_{o,j+1/2}^{k+1}u_{o,j+1/2}^{k+1}+\hat{k}_{j+1/2}^{k+1}\Big(u_{w,j+1/2}^{k+1}-u_{o,j+1/2}^{k+1}\Big)+s_{o,j+1/2}^{k+1}\rho_o g \\
&\quad +\varepsilon_o\frac{\rho_o}{\Delta x^2}\Big(s_{o,j+1}^{k+1}[{u_{o,j+3/2}}^{k+1}-u_{o,j+1/2}^{k+1}]-s_{o,j}^{k+1}[u_{o,j+1/2}^{k+1}-u_{o,j-1/2}^{k+1}]\Big).
\end{aligned}
\tag{2.23}
$$

Remark 2.1.2. The upwind discretization of $[s_w^{k+1}u_w^{k+1}]_{j+1/2}$ and $[s_o^{k+1}u_o^{k+1}]_{j+1/2}$ appearing in (2.22) are based on "old" velocities $u_{w,j+1/2}^k$ and $u_{o,j+1/2}^k$.

2.2 A three-phase model and its numerical scheme

A generalized 1-D model is given for three immiscible fluids moving in a porous media where porosity ϕ is assumed to be 1 for simplicity. The model takes the form with (m, n, c, u_w, u_o, u_g) as the main variables

$$
\begin{aligned}
(n_w)_t+(n_w u_w)_x &= -n_w Q_p+\rho_w Q_{Iw}, \qquad n_w = s_w\rho_w \\
(n_o)_t+(n_o u_o)_x &= -n_o Q_p, \qquad\qquad\quad\; n_o = s_o\rho_o \\
(n_g)_t+(n_g u_g)_x &= -n_g Q_p+\rho_g Q_{Ig}, \qquad n_g = s_g\rho_g \\
s_w(P_w)_x &= -\hat{k}_w u_w-\hat{k}_{wo}(u_w-u_o)-\hat{k}_{wg}(u_w-u_g)+n_w g+\varepsilon_w(n_w u_{wx})_x \\
s_o(P_o)_x &= -\hat{k}_o u_o-\hat{k}_{wo}(u_o-u_w)-\hat{k}_{og}(u_o-u_g)+n_o g+\varepsilon_o(n_o u_{ox})_x \\
s_g(P_g)_x &= -\hat{k}_g u_g-\hat{k}_{wg}(u_g-u_w)-\hat{k}_{og}(u_g-u_o)+n_g g+\varepsilon_g(n_g u_{gx})_x \\
\Delta P_{ow}(s_w) &= P_o-P_w, \qquad \Delta P_{go}(s_g) = P_g-P_o.
\end{aligned}
\tag{2.24}
$$

We may solve (2.24) on our domain Ω with boundary conditions

$$
u_w|_{\partial\Omega} = u_o|_{\partial\Omega} = u_g|_{\partial\Omega} = 0 \tag{2.25}
$$

and initial condition

$$
n_w(x,t=0) = n_{w0}(x), \qquad n_o(x,t=0) = n_{o0}(x), \qquad n_g(x,t=0) = n_{g0}(x). \tag{2.26}
$$

For compressible fluids, it must be combined with appropriate closure relations for $\rho_i = \rho_i(P_i)$. Here we represent the three phases by linear pressure-density relations of the form

$$
\rho_w-\tilde{\rho}_{w0} = \frac{P_w}{C_w}, \qquad \rho_o-\tilde{\rho}_{o0} = \frac{P_o}{C_o}, \qquad \rho_g = \frac{P_g}{C_g}. \tag{2.27}
$$

2.2.1 Compressible model

We consider a slight reformulation of the model (2.24) where we shall make use of the pressure evolution equation (refer to Appendix A in Paper V). Then we may rewrite the model in the following equivalent form with $(n_w, n_o, P_w, u_w, u_o, u_g)$ as the main variables

$$\begin{aligned}
(n_w)_t + (n_w u_w)_x &= -n_w Q_p + \rho_w Q_{Iw} \\
(n_o)_t + (n_o u_o)_x &= -n_o Q_p \\
P_{wt} + \tilde{\eta}_1 (n_w u_w)_x + \tilde{\eta}_2 (n_o u_o)_x + \tilde{\eta}_3 (n_g u_g)_x &= \tilde{\eta}_4 Q_p + \tilde{\eta}_5 Q_{Iw} + \tilde{\eta}_6 Q_{Ig} \\
s_w (P_w)_x &= -\hat{k}_w u_w - \hat{k}_{wo}(u_w - u_o) - \hat{k}_{wg}(u_w - u_g) - n_w g + \varepsilon_w (n_w u_{wx})_x \\
s_o (P_w + \Delta P_{ow})_x &= -\hat{k}_o u_o - \hat{k}_{wo}(u_o - u_w) - \hat{k}_{og}(u_o - u_g) - n_o g + \varepsilon_o (n_o u_{ox})_x \\
s_g (P_w + \Delta P_{ow} + \Delta P_{go})_x &= -\hat{k}_g u_g - \hat{k}_{wg}(u_g - u_w) - \hat{k}_{og}(u_g - u_o) - n_g g + \varepsilon_g (n_g u_{gx})_x \\
\Delta P_{ow}(s_w) = P_o - P_w \qquad & \qquad \Delta P_{go}(s_g) = P_g - P_o.
\end{aligned} \tag{2.28}$$

Here n_g is determined by

$$\begin{aligned}
n_g = s_g \rho_g(P_g) &= (1 - s_w - s_o)\rho_g(P_g) \\
&= \Big(1 - \frac{n_w}{\rho_w(P_w)} - \frac{n_o}{\rho_o(P_o)}\Big)\rho_g(P_g) = n_g(n_w, n_o, P_w)
\end{aligned} \tag{2.29}$$

where $P_o = P_o(s_w, P_w) = P_o(n_w, P_w)$ and $P_g = P_g(s_w, s_o, P_w) = P_g(n_w, n_o, P_w)$.

System of ODEs

We consider the domain $\Omega = [0, 1]$ and introduce a grid of N_x cells with nodes x_j placed at the center of the cells

$$x_1 = \frac{1}{2}\Delta x, \quad x_2 = (1+\frac{1}{2})\Delta x, \quad \dots, \quad x_j = (j-\frac{1}{2})\Delta x, \quad \dots, \quad x_{N_x} = (N_x - \frac{1}{2})\Delta x$$

and cell interfaces $x_{j+1/2}$ at the cell interfaces

$$x_{1/2} = 0, \quad x_{3/2} = \Delta x, \quad \dots, \quad x_{j+1/2} = j\Delta x, \quad \dots, \quad x_{N_x+1/2} = N_x \Delta x = 1$$

where $\Delta x = 1/N_x$. We introduce the approximate masses $\{n_{wj}(t)\}_{j=1}^{N_x}$, $\{n_{oj}(t)\}_{j=1}^{N_x}$, and $\{n_{g_j}(t)\}_{j=1}^{N_x}$ associated with the nodes $\{x_j\}_{j=1}^{N_x}$ whereas the approximate velocities $\{u_{w,j+1/2}\}_{j=0}^{N_x}$, $\{u_{o,j+1/2}\}_{j=0}^{N_x}$, and $\{u_{g,j+1/2}\}_{j=0}^{N_x}$ are associated with the cell interfaces $\{x_{j+1/2}\}_{j=0}^{N_x}$.

We refer to Appendix B in Paper V for the discretization of the three-phase compressible model since it is similar to the numerical scheme for the two-phase compressible model in Section 2.1.1.

2.2.2 Incompressible model

When fluids are incompressible the model (2.24) takes the form

$$\begin{aligned}
(s_w)_t + (s_w u_w)_x &= -s_w Q_p + Q_{Iw} \\
(s_o)_t + (s_o u_o)_x &= -s_o Q_p \\
(s_w u_w + s_o u_o + s_g u_g)_x &= -Q_p + Q_{Iw} + Q_{Ig} \\
s_w (P_w)_x &= -\hat{k}_w u_w - \hat{k}_{wo}(u_w - u_o) - \hat{k}_{wg}(u_w - u_g) + n_w g + \varepsilon_w \rho_w (s_w u_{wx})_x \\
s_o (P_o)_x &= -\hat{k}_o u_o - \hat{k}_{wo}(u_o - u_w) - \hat{k}_{og}(u_o - u_g) + n_o g + \varepsilon_o \rho_o (s_o u_{ox})_x \\
s_g (P_g)_x &= -\hat{k}_g u_g - \hat{k}_{wg}(u_g - u_w) - \hat{k}_{og}(u_g - u_o) + n_g g + \varepsilon_g \rho_g (s_g u_{gx})_x \\
\Delta P_{ow}(s_w) = P_o - P_w, &\qquad \Delta P_{go}(s_g) = P_g - P_o.
\end{aligned} \tag{2.30}$$

The discrete scheme for the three-phase incompressible model (refer to Appendix C in Paper V) is omitted here since it follows by analogy from what is done for the two-phase incompressible model in Section 2.1.2.

2.3 A general cell-fluid Navier-Stokes model and its numerical approximation

We write the general cell-fluid model (1.5) in component form for a 2D domain with $\mathbf{x} = (x, y) \in \Omega$ where y is the downward unit vector in vertical direction and with velocity fields $\mathbf{u}_c = (u_c^x, u_c^y)$ and $\mathbf{u}_w = (u_w^x, u_w^y)$. In the following we focus on the incompressible version.

$$\begin{aligned}
&(\alpha_c)_t + (\alpha_c u_c^x)_x + (\alpha_c u_c^y)_y = 0 \\
&C_t + (C u_w^x)_x + (C u_w^y)_y = (D_C C_x^x)_x + (D_C C_x^y)_y - K \alpha_c C \\
&(\alpha_c u_c^x)_x + (\alpha_c u_c^y)_y + (\alpha_w u_w^x)_x + (\alpha_w u_w^y)_y = 0 \\
&(m u_w^x)_t + (m u_w^x u_w^x)_x + (m u_w^x u_w^y)_y + \alpha_w P_{wx} \\
&\qquad\qquad = -\hat{\zeta}(u_w^x - u_c^x) + m g^x + 2\varepsilon_w (m u_{wx}^x)_x + \varepsilon_w (m u_{wx}^y)_y + \varepsilon_w (m u_{wy}^x)_y \\
&(n u_c^x)_t + (n u_c^x u_c^x)_x + (n u_c^x u_c^y)_y + \alpha_c P_{cx} \\
&\qquad\qquad = +\hat{\zeta}(u_w^x - u_c^x) + n g^x + 2\varepsilon_c (n u_{cx}^x)_x + \varepsilon_c (n u_{cx}^y)_y + \varepsilon_c (n u_{cy}^x)_y \\
&(m u_w^y)_t + (m u_w^y u_w^y)_y + (m u_w^x u_w^y)_x + \alpha_w P_{wy} \\
&\qquad\qquad = -\hat{\zeta}(u_w^y - u_c^y) + m g^y + 2\varepsilon_w (m u_{wy}^y)_y + \varepsilon_w (m u_{wy}^x)_x + \varepsilon_w (m u_{wx}^y)_x \\
&(n u_c^y)_t + (n u_c^y u_c^y)_y + (n u_c^x u_c^y)_x + \alpha_c P_{cy} \\
&\qquad\qquad = +\hat{\zeta}(u_w^y - u_c^y) + n g^y + 2\varepsilon_c (n u_{cy}^y)_y + \varepsilon_c (n u_{cy}^x)_x + \varepsilon_c (n u_{cx}^y)_x
\end{aligned} \tag{2.31}$$

with phase pressure relation

$$P_c = P_w + \Delta P(\alpha_c) + \Lambda(C). \tag{2.32}$$

The model may be combined with the boundary conditions

$$\mathbf{u}_c|_{\partial\Omega} = 0, \qquad \mathbf{u}_w|_{\partial\Omega} = 0, \qquad \frac{\partial}{\partial\nu} C|_{\partial\Omega} = 0, \qquad t > 0 \tag{2.33}$$

where ν is the outward normal on $\partial\nu$. Corresponding initial data are

$$\alpha_c(\mathbf{x}, t = 0) = \alpha_{c0}(\mathbf{x}), \qquad C(\mathbf{x}, t = 0) = C_0(\mathbf{x}). \tag{2.34}$$

We refer to Appendix A in Paper VI for the discretization of (2.31). The main principles are similar to the techniques used for the two-phase incompressible model in Section 2.1.2.

Chapter 3

Paper contributions

> *"Nothing in life is to be feared, it is only to be understood. Now is the time to understand more, so that we may fear less."*
>
> — Marie Curie (1867 - 1934)

The main contribution of this work is six articles where five of them have been published or is in the process of being published in peer-reviewed journals whereas one of them is currently under review. In this chapter, a brief summary of each paper is given.

Paper I - A mixture theory approach to model co- and counter-current two-phase flow in porous media accounting for viscous coupling.

This paper presents a model where momentum equations based on a general mixture theory replace Darcy's law in order to account for viscous coupling between the fluid phases and between fluid and rock. We carry out a systematic comparison of the generalized model and the conventional model (Darcy-based approach) for a specific flow case relevant for naturally fractured reservoirs. The inclusion of the fluid-fluid interaction term implies that this term contains a modification that automatically accounts for counter-current effects not captured by the conventional model. Fig. 3.1 illustrates the geometry of the flow system we study and Fig. 3.2 demonstrates the difference between the generalized and conventional models with inclusion of both gravity and capillary terms, which will give rise to mixed co-current and counter-current driven flow.

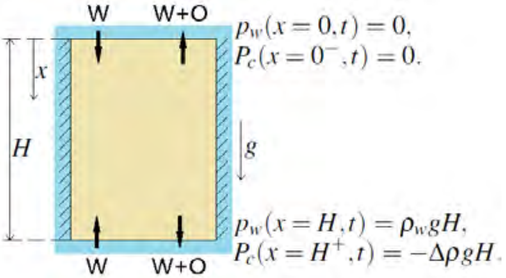

Figure 3.1: Geometry of the system. A water-wet matrix block of height H is exposed to water both at the top ($x=0$) and bottom ($x=H$). Spontaneous imbibition and gravity drainage mechanisms displace the oil by water in 1-D flow.

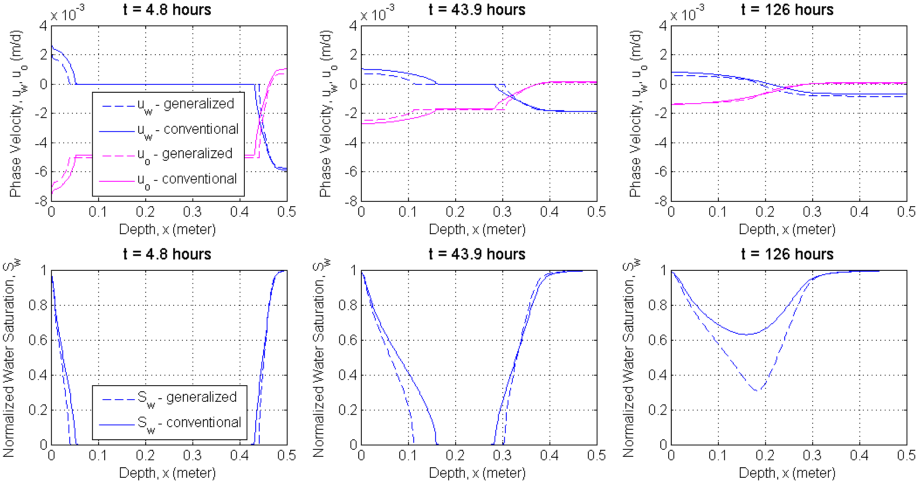

Figure 3.2: Comparison between the generalized and conventional models for the case with two open-boundaries. Profiles of $u_w(x), u_o(x)$ (top) and normalized water saturation $S_w(x)$ (bottom) are shown after 4.8, 43.9 and 126 hours. Counter-current flow is present mainly in the upper and lower parts of the block, while co-current flow dominates the central part.

Paper II - Co-current spontaneous imbibition in porous media with the dynamics of viscous coupling and capillary back pressure.

In this paper we consider a water-wet matrix block in one dimension that is exposed to oil on one side and water on the other side. This setup favors co-current spontaneous imbibition. We also account for the fact that oil produced counter-currently into water must overcome the so-called capillary back pressure, which represents a resistance for oil to be produced as droplets. This parameter can thus influence the extent of counter-current production and hence, viscous coupling. Fig. 3.3 shows the geometry of the flow system we study and in Fig. 3.4 it is seen that due to viscous coupling, the saturation front is steeper in the generalized model compared to the conventional and the distributions are strongly affected by the introduction of the capillary back pressure.

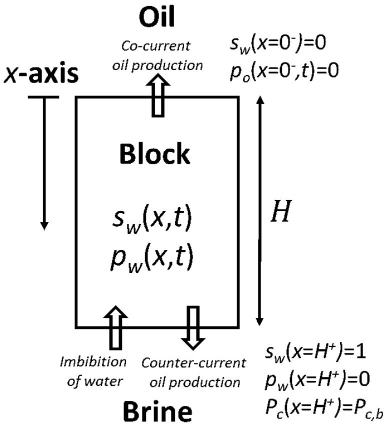

Figure 3.3: Geometry of the system. A water-wet matrix block of height H is exposed to water at the bottom ($x = H$) and oil at the top ($x = 0$). Co- and counter-current spontaneous imbibition displaces oil by water in 1-D flow.

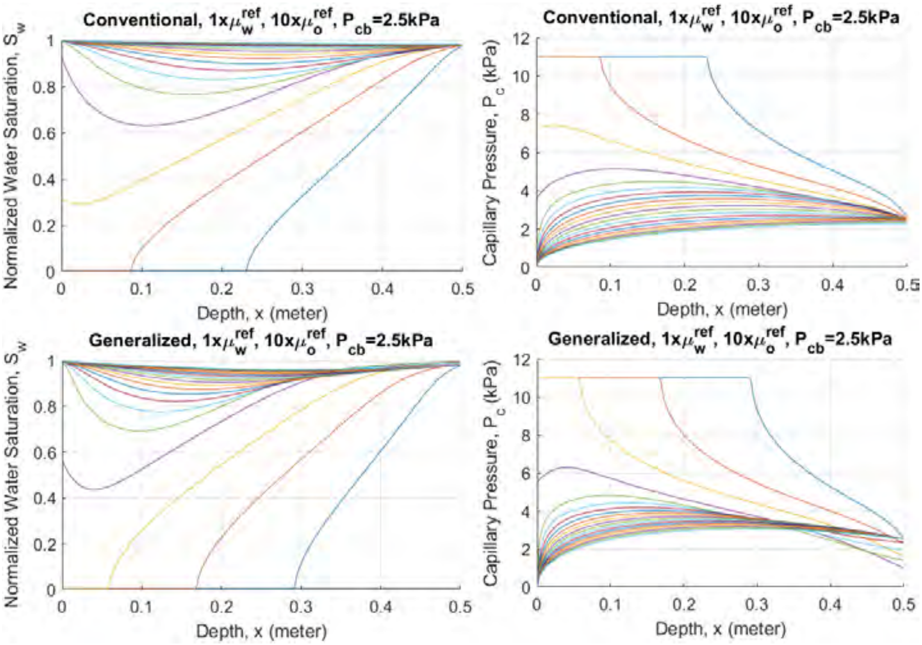

Figure 3.4: Distribution of saturation and capillary pressure along the core at 20 equal time intervals with total time 500 hours. The first row and second row represent, respectively, conventional model and generalized model. μ_o=10μ_o^{ref} corresponds to mobility ratio M=1 and capillary back pressure P_{cb}=2.5 kPa.

Paper III - Compressible and viscous two-phase flow in porous media based on mixture theory formulation.

This paper investigates a generalized two-phase model for porous media flow. The momentum balance equations account for fluid-rock resistance forces as well as fluid-fluid drag force effects, in addition to internal viscosity through a Brinkmann type viscous term. We rely on the energy method and use compressibility in combination with the structure of the viscous term to obtain H^1-estimates as well upper and lower uniform bounds of mass variables. These a priori estimates imply existence of solutions in a suitable functional space for a global time $T > 0$. Discrete schemes are also derived both for the incompressible and compressible case to explore the role of the viscosity term (Brinkmann type) as well as the incompressible versus the compressible case. We demonstrate similarities and differences between a formulation that is based, respectively, on interstitial velocity and Darcy velocity in the viscous term. The numerical test is a 10-day flooding process in a horizontal reservoir layer with a constant interstitial water injection rate and a constrained water saturation (0.8) at left boundary. It is observed in Fig. 3.5 that there is a delay in the solution of the compressible model compared with the incompressible model and the numerical scheme tends to give more oscillatory behavior by using Darcy velocity in the viscous term.

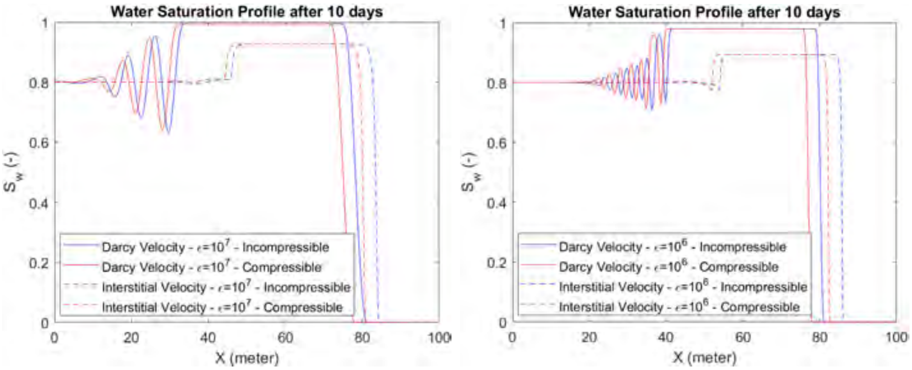

Figure 3.5: Comparison between the compressible model and the incompressible model for water-oil flow with $\varepsilon_w = \varepsilon_o = 10^7, 10^6$. After the same period of 10 days, water flow in the compressible model is delayed compared with water profiles in the incompressible model, for both situations with interstitial velocity and Darcy velocity in viscous terms.

Paper IV - Viscous two-phase flow in porous media driven by source terms: analysis and numerics.

This paper explores a one-dimensional version of a generalized compressible model where we account for two-phase dynamics driven by injection and production of fluids through realistic source terms and where physically relevant capillary pressure is accounted for. Firstly, various a priori estimates are derived that give rise to an existence result subject to a constraint on the magnitude of the viscous terms and the strength of the injection and production rate. Secondly, a numerical finite difference scheme, designed for dealing effectively with the strong nonlinear coupling between the mass and momentum equations, is then used to demonstrate a variety of two-phase injection-production scenarios for a realistic reservoir setting. Different physical effects are highlighted such as the difference between compressible and incompressible flow, balance between gravity and pressure-driven flow, and effect of viscous coupling. Fig. 3.6 shows a 1D reservoir layer with one injection well at the center of the layer and two production wells at the left and right side. A comparison between the compressible and incompressible vertical ($\theta = 90^0$) water-gas models is illustrated in Fig. 3.7.

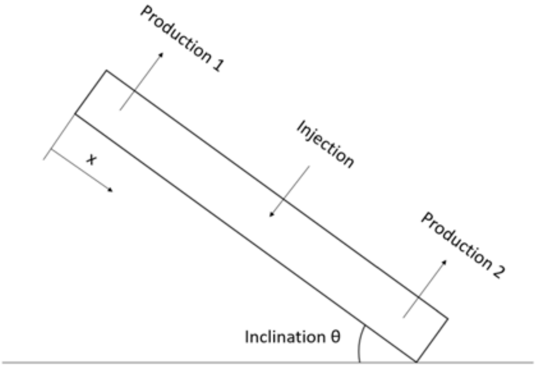

Figure 3.6: 1D inclined reservoir. Water is pumped into the injection well to displace reservoir fluids (90% gas and 10% water, initially) and its injection rate is double times of the production rate at two sides of the reservoir layer.

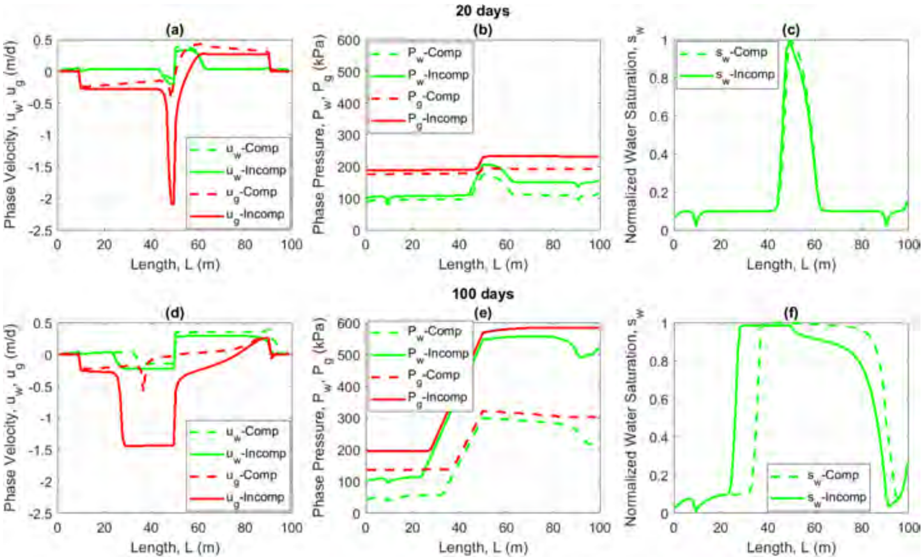

Figure 3.7: Comparison between the compressible and incompressible vertical water-gas models at 20 and 100 days. (a,d) Interstitial velocity u_w, u_g. (b,e) Phase pressure P_w, P_g. (c,f) Water saturation s_w. After a time $T = 100$ days we see that there is a steady flow of gas from the lower region to the upper for the incompressible model (panel d). In particular, water will not block this migration (panel f). For the compressible model, on the other hand, water will block for this upward migration of gas (compare gas velocities in panel d).

Paper V - A compressible viscous three-phase model for porous media flow based on the theory of mixtures.

A main objective of this paper is to explore a three-phase model, which appears to be more realistic than standard formulation, in the context of petroleum related applications. We first provide development of stable numerical schemes in a one-dimensional setting which can be used to explore the generalized water-oil-gas model, both for the compressible and incompressible case. Then, several numerical examples with water flooding in a gas reservoir and water alternating gas (WAG) experiments in an oil reservoir are investigated. Fig. 3.8 demonstrates the case for water flooding in a 1D inclined ($\theta = 90^0$) gas-oil reservoir as shown in Fig. 3.6 with the initial condition: 90% gas and 10% oil.

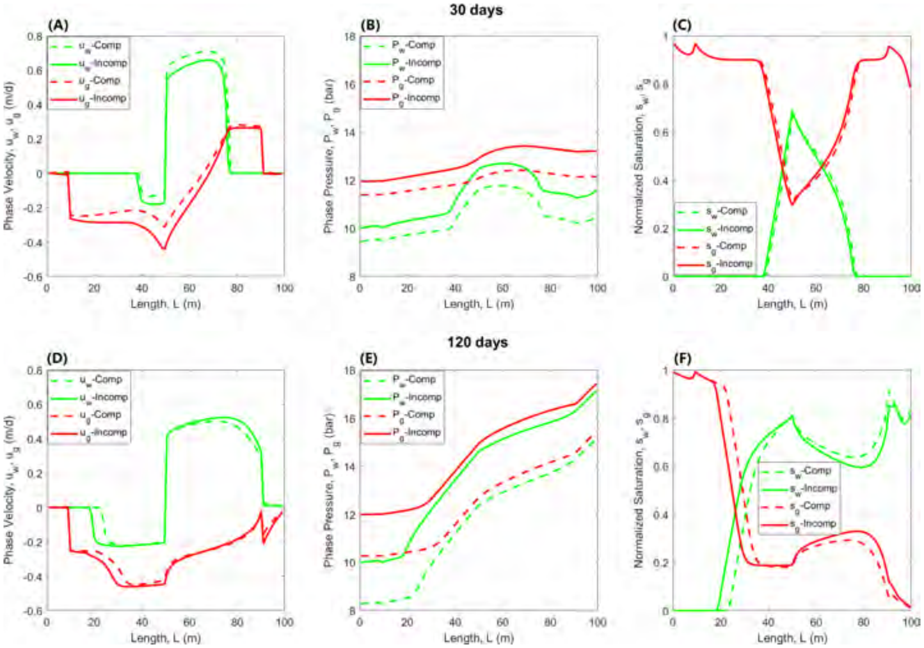

Figure 3.8: Comparison between the compressible and incompressible model with vertical three-phase flow. (A,D) Phase velocity u_w and u_g for water and gas, respectively. (B,E) Pressure P_w and P_g for water and gas, respectively. Almost incompressible water is injected whereas the compressible model senses that compressed gas is removed through the producers. This gives rise to a lower pressure level for the compressible model as compared to the incompressible. (C,F) Saturation s_w and s_g for water and gas, respectively.

Paper VI - A general cell-fluid Navier-Stokes model with inclusion of chemotaxis.

The main purpose of this work is to explore a general cell-fluid model which is based on a mixture theory formulation that accounts for the interplay between oxytactically (chemotaxis toward gradient in oxygen) moving bacteria cells in water and the bouyance forces caused by the difference in density between cells and fluid. The model involves two mass balance and two general momentum balance equations, respectively, for the cell and fluid phase, combined with a convection-diffusion-reaction equation for oxygen. In particular, the momentum balance equations include interaction terms which describe the cell-fluid drag force effect. Hence, the model is an extension of the classical Navier-Stokes equation. The model can be understood as a natural generalization of the much studied chemotaxis-Stokes model explored by Tuval et al. (2005). Assuming that cells and water are incompressible, we explore the nonlinear dynamics inherent in the model in a 2D setting by using an appropriate finite difference scheme. The general cell-fluid model provides new insight into the role played by the cell-fluid interaction term. Formation of falling plumes requires a sufficiently strong cell-fluid interaction such that the difference between cell and water velocity becomes small. Fig. 3.9 describes the investigated system with high concentration cells in the upper part, initially. The formation of falling plumes is illustrated in Fig. 3.10.

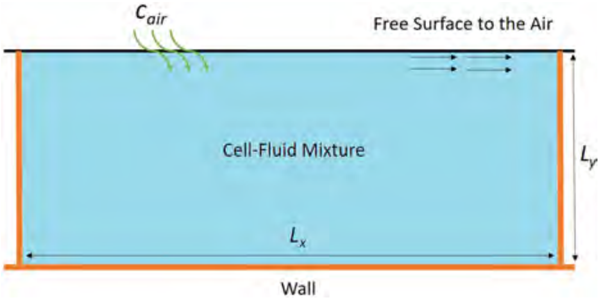

Figure 3.9: Boundary conditions for the system. The air–water interface, where the oxygen concentration is equal to that of air, is not crossed by bacteria; the fluid and cell vertical velocity components equal zero and the fluid and cells are assumed to be free of tangential stress. The container walls are impermeable to bacteria and oxygen.

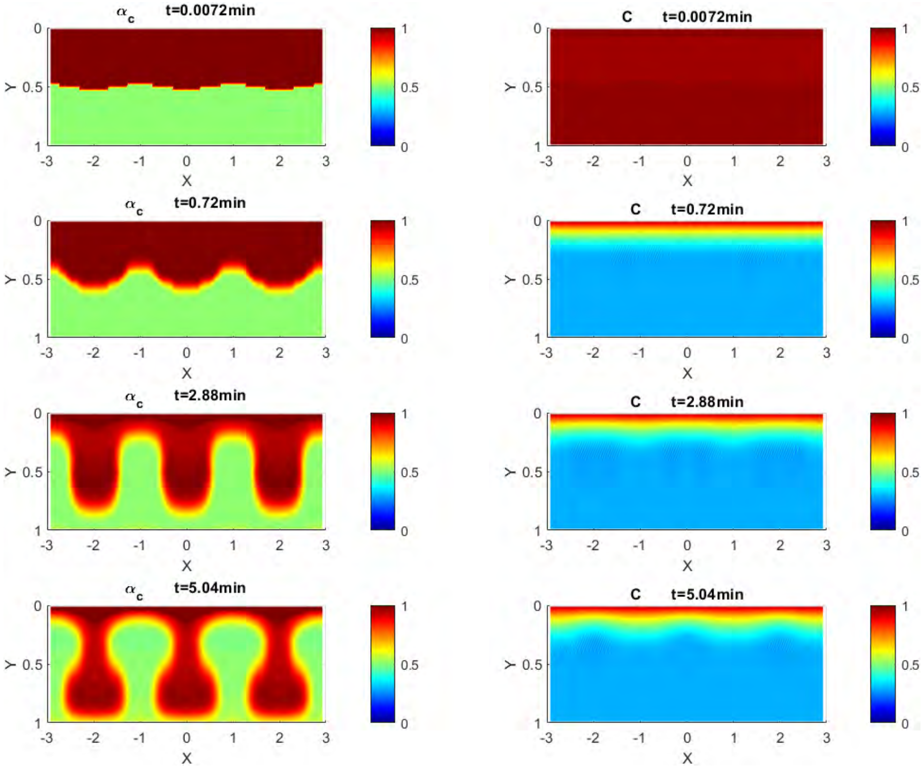

Figure 3.10: Initially, a high cell volume fraction region dominates in the upper part of the domain (left column, top). We see that oxygen is consumed faster at the beginning in this region (right column, top). Since the whole system is open to the air at top side oxygen can constantly diffuse into the box whereas in the lower part oxygen is consumed by the cells such that the oxygen concentration reaches the lower limit $C = C^* = 0.3$. Beyond this limit the chemotaxis effect vanishes and gravity becomes the dominating force and the plumes will develop as cells sink towards the bottom. Clearly, cells are kept coherent in the upper region of the domain reflecting that the gravity and chemotaxis driven transport work together such that the developing plumes are maintained.

Chapter 4

Conclusions and further works

> *"The most beautiful experience we can have is the mysterious. It is the fundamental emotion that stands at the cradle of true art and true science."*
>
> — Albert Einstein (1879 - 1955)

The generalized two-phase model apparently can automatically capture fluid-fluid interaction effects and better represent mobility functions for mixed flow regimes in the context of multiphase flow in porous media relevant for reservoir simulation. Directly implementing co-currently measured relative permeability curves, as is standard, into reservoir simulation, may yield too optimistic results since viscous coupling can be enhanced at more general flow regimes (Paper I). The simulations indicate that the viscous coupling effects could become more significant with time in the case where both gravity and capillary pressure forces are present as counter-current flow dominates a larger portion of the core at late times.

The role of viscous coupling in the context of co-current spontaneous imbibition of water that displaces oil in porous media was discussed (Paper II). The model predicts that when oil or water viscosity is increased, viscous coupling effects increase. At low water/oil-mobility ratios, the spontaneous imbibition process is dominated by co-current production with sharp saturation fronts. The role of viscous coupling then does not have much impact. At high water/oil-mobility ratios, countercurrent production becomes more dominant and the saturation profile becomes smoother along the core, rather than acting as a shock. Because of viscous coupling, the generalized model displays more resistance to countercurrent flow and thus results in less countercurrent production than the conventional model. In addition, the capillary backpressure can reduce the countercurrent production by lowering the capillary pressure gradient at the water side.

An existence result for the generalized two-phase model was obtained where the source terms were set to zero by exploiting the fact that the viscous term depends on the interstitial fluid flow velocity (Paper III). The finite difference schemes we formulated allow us to systematically gain some insight into the effect of compressibility as well as the effect from the viscous terms that account for the frictional resistance within the fluid. It is also observed that by using Darcy velocity in the viscous term, the resulting scheme tends to give more oscillatory behavior.

We have derived estimates and obtained an existence result where the role of source terms related to injection and production wells are accounted for (Paper

IV). We have found that a consequence of having the source terms as a driver for the dynamics is that the energy can no longer be controlled without taking into account higher order regularity terms. The developed numerical scheme works well for the simulations with source terms as well. The simulation results demonstrate that differences between the compressible and incompressible models can be significant for the case involved gas.

The generalized two-phase flow model was also extended to the three-phase version based on the theory of mixtures (Paper V). It was demonstrated that the corresponding developed numerical scheme is also stable for both incompressible and compressible models which involve a combination of co-current and counter-current flow.

Finally, a general full two-phase cell-fluid Navier-Stokes model was explored and linked to the widely studied model (Paper VI). Our general model provides new insight into the role played by the cell-fluid interaction term. Formation of falling plumes requires a sufficiently strong cell-fluid interaction such that the difference between cell and water velocity becomes small. A weakening of this term typically implies that the falling plumes will detach from the upper layer. Hence, this term controls the competition between gravity segregation and chemotaxis effect on the formation of cell plumes.

The generalized model seems to offer a nice framework for various new and interesting further investigations like:

a) Consider complex systems that involve a combination of porous media based flow and Navier-Stokes based flow. The general model formulation naturally contains both of them.

b) Consider porous media multiphase flow where the effects of chemical components are included. For example, the effect of "smart water" in IOR or CO_2 storage related problems. The mixture model formulation opens for a more precise description of how chemical effects will affect the creeping flow.

c) Explore the generalized models in the context of aggressive tumor cell behavior. This can be done by an appropriate extension/modification of the cell-fluid model presented in this thesis combined with recent approaches as studied in (Urdal et al. 2019; Waldeland et al. 2018).

d) Explore various improved versions of the numerical schemes presented in this work. Explore finite volume or finite element based methods, various techniques for improved accuracy, and techniques for more efficient solvers of the implicit part of the numerical approach.

e) Explore the model in the context of wellbore-reservoir flow scenarios.

Bibliography

Ambrosi, D. and Preziosi, L. (2002). “On the closure of mass balance models for tumor growth”. In: *Mathematical Models and Methods in Applied Sciences* 12.05, pp. 737–754.

Bowen, R. M. (1980). “Incompressible porous media models by use of the theory of mixtures”. In: *International Journal of Engineering Science* 18.9, pp. 1129–1148.

Bowen, R. (1976). “Theory of mixtures in continuum physics”. In: *Mixtures and Electromagnetic Field Theories* 3.

Byrne, H. and Preziosi, L. (2003). “Modelling solid tumour growth using the theory of mixtures”. In: *Mathematical Medicine and Biology: A Journal of the IMA* 20.4, pp. 341–366.

Chertock, A., Fellner, K., Kurganov, A., Lorz, A., and Markowich, P. (2012). “Sinking, merging and stationary plumes in a coupled chemotaxis-fluid model: a high-resolution numerical approach”. In: *Journal of Fluid Mechanics* 694, pp. 155–190.

Darcy, H. (1856). “Les fontaines publiques de la ville de Dijon, Dalmont”. In: *Paris: Dalmont.*

Drew, D. A. and Passman, S. L. (2006). *Theory of multicomponent fluids.* Vol. 135. Springer Science & Business Media.

Evje, S. (2017). “An integrative multiphase model for cancer cell migration under influence of physical cues from the microenvironment”. In: *Chemical Engineering Science* 165, pp. 240–259.

Evje, S. and Wen, H. (2018). “A Stokes two-fluid model for cell migration that can account for physical cues in the microenvironment”. In: *SIAM Journal on Mathematical Analysis* 50.1, pp. 86–118.

Hillesdon, A. and Pedley, T. (1996). “Bioconvection in suspensions of oxytactic bacteria: linear theory”. In: *Journal of Fluid Mechanics* 324, pp. 223–259.

Hillesdon, A., Pedley, T., and Kessler, J. (1995). “The development of concentration gradients in a suspension of chemotactic bacteria”. In: *Bulletin of Mathematical Biology* 57.2, pp. 299–344.

Juanes, R. (2008). “Nonequilibrium effects in models of three-phase flow in porous media”. In: *Advances in Water Resources* 31.4, pp. 661–673.

Lemon, G., King, J. R., Byrne, H. M., Jensen, O. E., and Shakesheff, K. M. (2006). “Mathematical modelling of engineered tissue growth using a multiphase porous flow mixture theory”. In: *Journal of Mathematical Biology* 52.5, pp. 571–594.

Muskat, M., Wyckoff, R., Botset, H., and Meres, M. (1937). “Flow of gas-liquid mixtures through sands”. In: *Transactions of the AIME* 123.01, pp. 69–96.

Pedley, T. and Kessler, J. (1992). “Hydrodynamic phenomena in suspensions of swimming microorganisms”. In: *Annual Review of Fluid Mechanics* 24.1, pp. 313–358.

Preziosi, L. and Farina, A. (2002). “On Darcy’s law for growing porous media”. In: *International Journal of Non-Linear Mechanics* 37.3, pp. 485–491.

Qiao, Y., Andersen, P., Evje, S., and Standnes, D. (2018). “A mixture theory approach to model co-and counter-current two-phase flow in porous media accounting for viscous coupling”. In: *Advances in Water Resources* 112, pp. 170–188.

Rajagopal, K. (2007). “On a hierarchy of approximate models for flows of incompressible fluids through porous solids”. In: *Mathematical Models and Methods in Applied Sciences* 17.02, pp. 215–252.

Rajagopal, K. and Tao, L. (1995). “Mechanics of mixtures, Series on Advances in Mathematics for Applied Sciences. Vol. 35, World Scientiffic Publishiing Co”. In: *Inc, River Edge, NJ*.

Rose, W. (2000). “Myths about later-day extensions of Darcy’s law”. In: *Journal of Petroleum Science and Engineering* 26.1-4, pp. 187–198.

Tuval, I., Cisneros, L., Dombrowski, C., Wolgemuth, C. W., Kessler, J. O., and Goldstein, R. E. (2005). “Bacterial swimming and oxygen transport near contact lines”. In: *Proceedings of the National Academy of Sciences* 102.7, pp. 2277–2282.

Urdal, J., Waldeland, J. O., and Evje, S. (2019). “Enhanced cancer cell invasion caused by fibroblasts when fluid flow is present”. In: *Biomechanics and Modeling in Mechanobiology* 18.4, pp. 1047–1078.

Waldeland, J. O. and Evje, S. (2018). “A multiphase model for exploring tumor cell migration driven by autologous chemotaxis”. In: *Chemical Engineering Science* 191, pp. 268–287.

Wu, Y. (2015). *Multiphase fluid flow in porous and fractured reservoirs*. Gulf Professional Publishing.

Papers

Paper I

A Mixture Theory Approach to Model Co- and Counter-current Two-phase Flow in Porous Media Accounting for Viscous Coupling

By:
Qiao, Yangyang
Andersen, Pål Østebø
Evje, Steinar
Standnes, Dag Chun

Printed in:
Advances in Water Resources, 112: 170-188 (2018).

Advances in Water Resources 112 (2018) 170–188

Contents lists available at ScienceDirect

Advances in Water Resources

journal homepage: www.elsevier.com/locate/advwatres

A mixture theory approach to model co- and counter-current two-phase flow in porous media accounting for viscous coupling

Y. Qiao[a], P.Ø. Andersen*,[a,b], S. Evje[a,b], D.C. Standnes[a]

[a] *Department of Petroleum Technology, University of Stavanger 4036, Norway*
[b] *The National IOR Centre of Norway, Norway*

ARTICLE INFO

Keywords:
Multiphase flow in porous media
Viscous coupling
Mixture theory
Dynamic relative permeability
Mathematical modeling
Co- and counter-current flow

ABSTRACT

It is well known that relative permeabilities can depend on the flow configuration and they are commonly lower during counter-current flow as compared to co-current flow. Conventional models must deal with this by manually changing the relative permeability curves depending on the observed flow regime. In this paper we use a novel two-phase momentum-equation-approach based on general mixture theory to generate effective relative permeabilities where this dependence (and others) is automatically captured. In particular, this formulation includes two viscous coupling effects: (i) Viscous drag between the flowing phases and the stagnant porous rock; (ii) viscous drag caused by momentum transfer between the flowing phases. The resulting generalized model will predict that during co-current flow the faster moving fluid accelerates the slow fluid, but is itself decelerated, while for counter-current flow they are both decelerated. The implications of these mechanisms are demonstrated by investigating recovery of oil from a matrix block surrounded by water due to a combination of gravity drainage and spontaneous imbibition, a situation highly relevant for naturally fractured reservoirs. We implement relative permeability data obtained experimentally through co-current flooding experiments and then explore the model behavior for different flow cases ranging from counter-current dominated to co-current dominated. In particular, it is demonstrated how the proposed model seems to offer some possible interesting improvements over conventional modeling by providing generalized mobility functions that automatically are able to capture more correctly different flow regimes for one and the same parameter set.

1. Introduction

Conventional modeling of two-phase flow in porous media is based on Darcy's extended law which was originally developed empirically for single-phase flow (Darcy, 1856; Rose, 2000) and extended to multiphase flow by incorporation of relative permeabilities (Muskat et al., 2013). The relative permeability is commonly assumed to be a function of saturation only, implying that the presence of another phase has a unique impact on the phase's flux, i.e. no coupling is accounted for through the velocity or pressure gradient of the other phase. Several experimental observations, however, indicate that the flow mode (co- or counter-current) can have a more or less strong impact on the phase mobilities. Previous studies of counter-current flow settings (see below for more details) support that relative permeability in a counter-current flow setting can be significantly lower than in co-current flow settings. In conventional simulation tools, the dependence of the saturation functions (i.e., relative permeability and capillary pressure) on the flow direction (co-current or counter-current) and phase velocities is commonly ignored. This indicates that the use of the extended Darcy's law may be questionable.

1.1. *Previous works on coupled multiphase flow*

Fluid-fluid interactions, referred to herein as *viscous coupling*, can play a significant role related to two-phase flow in porous media. Yuster (1951) was the first to mention such phenomena by theoretical analysis of two-phase flow in capillary tubes where he derived that relative permeability should not only be a function of saturation, but also of viscosity ratio. Researchers have proposed that relative permeabilities depend on saturations, capillary number and viscosity ratio between two fluids (Avraam and Payatakes, 1995a; Ehrlich, 1993) and on how the fluids flow relative to each other (Bentsen and Manai, 1992; Bourbiaux and Kalaydjian, 1990). Momentum transfer due to differences in interstitial velocities induces acceleration of the slower and deceleration of the faster moving fluid if the fluids are moving co-currently. Deceleration of both fluid velocities will occur if they are moving counter-currently (Ayodele, 2006; Babchin et al., 2006; Bentsen and Manai, 1993; Dullien and Dong, 1996; Li et al., 2004). Hence, the extent of fluid-fluid interaction and the flow mode is significantly impacting fluid mobilities and relative permeabilities. There are several

---

* Corresponding author at: Department of Pet. Tech., University of Stavanger, The National IOR Center of Norway, Stavanger 4036, Norway.
E-mail address: pal.andersen@uis.no (P.Ø. Andersen).

https://doi.org/10.1016/j.advwatres.2017.12.016
Received 6 July 2017; Received in revised form 15 December 2017; Accepted 16 December 2017

List of symbols

Roman

a_1, a_2, k_1, k_2, c:	dimensionless capillary pressure correlation parameters, -
$\mathbf{b}$	external force term in Brinkman's equation, m/s^2
f_{ij}	interphase force on phase i exerted by phase j, Pa/m
f_w	water fractional flow function, –
g	acceleration of gravity, 9.8 m/s^2
$\mathbf{g}_i$	external body force of phase i, Pa/m
H	height of block, m
I_w	water-solid interaction coefficient, –
I_o	oil-solid interaction coefficient, –
I	water-oil interaction coefficient, (Pa · s)$^{-1}$
$\mathbf{I}$	identity tensor, –
J	scaled capillary pressure function, –
K	absolute permeability, mD
k_{ro}, k_{rw}	relative permeability of oil/water, –
$k_{ro}^{\max}$, $k_{rw}^{\max}$	end point relative permeability values of oil/water, –
n_o, n_w	Corey exponents for oil and water, –
P_c	capillary pressure, Pa
p_o, p_w	oil/water phase pressure, Pa
R_o	oil-solid interaction term, Pa · s/m^2
R_w	water-solid interaction term, Pa · s/m^2
R	oil-water interaction term, Pa · s/m^2
RF	recovery factor of mobile oil, –
s	front speed determined by Rankine–Hugoniot criterion, m/d
s_o, s_w	oil/water saturation, –
S_o, S_w	normalized oil/water saturation, –
s_{or}, s_{wr}	residual oil/water saturation, –
S_w^e	effective saturation in Barenblatt non-equilibrium model, –
t	time, hour
u_T	total Darcy velocity, m/d
u_T^0	initial total Darcy velocity, m/d
u_o, u_w	oil/water phase Darcy velocity, m/d
v_o, v_w	interstitial oil/water average velocity over a representative elementary volume, m/s
$\hat{\mathbf{v}}_o$, $\hat{\mathbf{v}}_w$	intrinsic velocity on microscopic scale, m/s
W	generalized mobility term for capillary diffusion, m^2/(Pa · s)
x	block depth, m

Greek

α_0	drag force coefficient in Brinkman's equation, Pa · s/m^2
α	exponent for water phase, –
β	exponent for oil phase, –
β_{12}, β_{21}	mixture interaction coefficients, Pa · s/m^2
$\Delta\rho$	density difference, g/cm^3
θ_i	volume fraction of phase i, –
κ_i	bulk viscosity i, Pa · s
$\hat{\lambda}_{oo}$, $\hat{\lambda}_{ww}$	generalized diagonal mobilities, m^2/(Pa · s)
$\hat{\lambda}_{ow}$, $\hat{\lambda}_{wo}$	generalized cross term mobilities, m^2/(Pa · s)
λ_o, λ_w	phase mobilities, m^2/(Pa · s)
$\hat{\lambda}_o$, $\hat{\lambda}_w$	generalized phase mobilities, m^2/(Pa · s)
μ_o, μ_w	oil/water viscosity, cP
σ	oil-water interfacial tension, mN/m
ρ_o, ρ_w	density of oil/water, g/cm^3
ϕ	porosity, –
ϕ_e	effective porosity, –
Ψ_i	macroscopic stress tensor of phase i, Pa

theoretical approaches aiming at developing generalized models that account for viscous coupling effects. An effort to extend the single-phase Darcy's law to multiphase flow was made by de la Cruz and Spanos (1983) who derived theoretically Darcy's empirical extended law by applying the method of volume averaging to Stokes equation. Kalaydjian (1987, 1990) developed flow equations using the concepts of irreversible thermodynamics from a macroscopic understanding of two-phase flow in porous media. Moreover, a number of researchers tried to gain insight into how two immiscible phases flow through a porous medium by using simple analogous models such as tubular flow (Bacri et al., 1990; Yuster, 1951). Common for such generalized models, the flux of each phase is a function of both phases' pressure gradients and it therefore contains four generalized coefficients (diagonal and cross-term mobilities) which are referred to as generalized mobilities. Avraam and Payatakes (1995b) measured such cross-terms experimentally in 2-D micro models vs. wetting phase saturation in steady-state co-current flow of water and oil. They concluded that coupling is important over broad ranges of wetting phase saturation, capillary number and viscosity ratio. Dullien and Dong (1996) likewise measured cross-terms in two-phase flow in sand packs using a fluid system with viscosity ratio of unity. The value of the cross terms ranged from 10 to 35 % of the value of the effective permeability to water and from 5 to 15 % of the effective permeability to oil, respectively. Langaas and Papatzacos (2001) used the Lattice Boltzmann (LB) approach to investigate viscous coupling and concluded that co-current relative permeabilities always are larger than the corresponding counter-current curves caused partly by viscous coupling and different levels of capillary forces. Li et al. (2005) also used LB to investigate viscous coupling and they concluded that their model was able to capture main experimental effects normally interpreted as caused by this effect. They also concluded that the interfacial area between the fluids is a key variable for understanding of multiphase flow and hence relative permeability functions when two immiscible fluids are flowing through porous media.

1.2. Objectives of this work

The main objective of this work is to explore how to develop a model that naturally can account for viscous coupling effects (i.e., fluid-fluid interaction) by applying the theory of mixtures (Lemon et al., 2006; Rajagopal, 2007; Rajagopal and Tao, 1995; Schuff et al., 2013). In this formulation each phase momentum balance equation is a function of both fluid velocities. More precisely, based on a two-fluid Stokes type of formulation for creeping flow we derive generalized mobility functions that are sensitive to both solid-fluid interaction as well as fluid-fluid interaction. In other words, the obtained mobility functions automatically include terms that sense contributions from the counter-current flow and other terms that sense contributions from the co-current flow. In particular, the mobility functions ensure that for co-current flow the fluid with highest speed decelerates whereas the slower fluid is accelerated. For counter-current flow both fluids will experience a reduced velocity depending on the strength of the fluid-fluid interaction. A first presentation of this idea was given in Standnes et al. (2017). The model studied in that work was simplified in the sense that no impact of gravity forces and capillary pressure was accounted for in the final expressions. It was also used for steady state investigations only.

The potential usefulness of the proposed generalized model is illustrated by studying a specific example with an oil-saturated matrix block submerged in water where the resulting flow involves a rather delicate balance between counter-current and co-current flow depending on the relative strength of capillary pressure driven flow (spontaneous imbibition) and gravity driven. Spontaneous imbibition is regarded as a key driving mechanism for oil production in naturally fractured water-wet reservoirs (Andersen et al., 2014; Mason and Morrow, 2013). This process is featured by water imbibing spontaneously into the matrix blocks by capillary forces simultaneously expelling oil to the surrounding fracture system, either counter-currently if the matrix blocks are totally submerged in water, or in a co-current flow mode if parts of the blocks are covered by oil (Andersen et al., 2017a). Hence, the rate of imbibition is determined by the capillary forces and the corresponding fluid mobilities which are strong functions of the flow mode (co- versus counter-current flow).

An important aspect of the imbibition process is the fact that capillary forces decrease rapidly when the water saturation increases, implying that gravity forces under such conditions no longer can be ignored and will have significant impact on fluid saturation distribution and flow of oil and water. Viscous coupling effects can thus potentially have important implications and modeling advantages for the understanding of two-phase flow in this context, both since (i) relative permeabilities are always measured co-currently in the laboratory and counter-current flow can thus behave differently than predicted from those measurements, and (ii) since a dynamic variation can occur regarding the magnitude of co- versus counter-current flow. In a conventional model this case would be challenging to deal with because regions with different flow behavior (co-current and counter-current) must be identified and then corresponding relative permeability functions assigned manually. As an example of such implementation, an interesting recent study of viscous coupling effects in a three-phase setting is found in Sherafati and Jessen (2017). The authors investigated the impact of mobility changes due to flow reversals from co-current to counter-current flow on the displacement performance of water alternating gas (WAG) injection processes. Their method consists of switching between using co-current relative permeability functions and counter-current depending on a criterion that classifies flow either as co- or counter-current. With the proposed generalized model of this paper, one set of parameters could potentially describe all such flow combinations dynamically. The presented generalized model further has the advantage of accounting for the effect of fluid viscosities on relative permeabilites and imbibition rates (Standnes and Andersen, 2017; Standnes et al., 2017).

It seems appropriate to mention here another related direction where researchers have proposed alternatives to Darcy-type formulations in order to remedy some of the shortcomings of classical multiphase extension of Darcy's law. The Hassanizadeh–Gray model (Hassanizadeh and Gray, 1993) and the Barenblatt model (Barenblatt and Vinnichenko, 1980) both suggest to include non-equilibrium effects in capillary pressure and/or relative permeability functions. We refer to (Juanes, 2008; Silin and Patzek, 2004) for a comprehensive overview of different works where these ideas have been implemented and tested. There is a similarity between the Barenblatt approach and the use of the more general momentum balance equations we suggest in the sense that experimentally obtained flow functions (like relative permeability) are *process-dependent*. In order to account for this non-equilibrium effect, the Barenblatt approach consists of introducing an additional variable S_w^e (effective water saturation) and an additional equation which describes the difference between the actual water saturation S_w and the effective S_w^e in terms of a time-dependent, but non-specific process. Capillary pressure and relative permeability curves are then expressed in terms of the effective saturation S_w^e. The current manuscript focuses more on one specific effect that will make relative permeability functions process-dependent, namely the fluid-fluid interaction effect (drag-force effect) between the flowing phases.

For a proper demonstration of properties of the generalized model proposed in this manuscript, the behavior of the model is compared against results obtained from a conventional two-phase modeling which relies on standard Darcy's extended law. The model is parameterized using experimental results from the literature where viscous coupling could be quantified. In particular, co-currently measured relative permeability curves from the literature are implemented and experimental data of counter-current spontaneous imbibition from the same rock-fluid system is history matched. We demonstrate the model for three different cases: (1) A co-current dominated flow mode where oil is mainly displaced upwards by water in the water-surrounded system, due to dominant gravity forces, i.e. buoyancy; (2) a counter-current dominated flow mode where dominant capillary forces induce counter-current spontaneous imbibition symmetrically from all sides (which are open to water phase); and (3) a case where gravity and capillary forces have similar magnitude.

The paper is organized in the following way: In Section 2 we derive the relevant mathematical models used to represent the gravity drainage/spontaneous imbibition controlled flow system we are interested in: (i) First using the conventional Darcy law approach; (ii) then, with momentum balance equations that account for viscous coupling. In Section 3 we give a compact summary of these two models for the readers convenience together with a brief description of the solution algorithm. In Section 4, using representative input data, we carefully consider the model behavior at different degrees of capillary- and gravity-dominated flow regimes. The two modeling approaches are compared and discussed. Conclusions are given in Section 5.

2. Theory

2.1. Geometry

The system we consider is a matrix block surrounded by water (Fig. 1), representative of the state below the water level in a naturally fractured reservoir during water injection, or an Amott test in the laboratory. For simplicity, only 1-D flow is considered along the vertical axis. The mechanisms at work are spontaneous imbibition and gravity drainage. No forced displacement is considered.

2.2. Conventional 1-D model based on Darcy's law

Transport equations for incompressible and immiscible phases oil (o) and water (w) in a 1-D porous media are given by:

$$\partial_t(\phi s_i) = -\partial_x u_i, \qquad (i = w, o), \tag{1}$$

where ϕ is porosity, s_i is phase saturation, and u_i is the flux (Darcy velocity) of each phase $i = o, w$. A 1-D system is considered along the vertical axis (denoted x, positive direction downwards). Darcy's law in such a 1-D vertical system is given by:

$$u_i = -\frac{Kk_{ri}}{\mu_i}(\partial_x p_i - \rho_i g), \qquad (i = w, o), \tag{2}$$

where K is the absolute permeability, p_i is phase pressure, $g = 9.8$ m/s^2 is the acceleration of gravity and k_{ri}, ρ_i and μ_i are phase relative permeability, density and viscosity, respectively. The phase pressures are dependent due to the capillary pressure function $p_o - p_w = P_c$. Also, we introduce the total Darcy velocity u_T as follows:

$$u_T = u_w + u_o = -\lambda_o \partial_x P_c - \lambda_T \partial_x p_w + (\lambda_o \rho_o + \lambda_w \rho_w)g, \tag{3}$$

where the mobilities λ_i, λ_T are defined as:

$$\lambda_i := K\frac{k_{ri}}{\mu_i}, \qquad (i = w, o), \qquad \lambda_T = \lambda_w + \lambda_o. \tag{4}$$

It follows from adding the conservation laws (1) that:

$$\partial_x u_T = 0. \tag{5}$$

Solving (3) with respect to $\partial_x p_w$ and inserting this into (2), the water velocity can be expressed in the following form:

$$u_w = f_w u_T + f_w \lambda_o \Delta\rho g - f_w \lambda_o \partial_x P_c. \tag{6}$$

Therefore, the water transport equation becomes:

$$\partial_t(\phi s_w) = -\partial_x(f_w u_T + f_w \lambda_o \Delta\rho g) - \partial_x(f_w \lambda_o \partial_x P_c), \qquad x \in [0, H], \tag{7}$$

where $f_w = \frac{\lambda_w}{\lambda_T}$ is the water fractional flow function and $\Delta\rho = \rho_w - \rho_o$. Note that the RHS of (7) is expressed in terms of an advective/gravitational term and a capillary diffusion term, respectively.

Remark 2.1. Note that u_T represents co-current flow through the system. Its numerical value depends on an interplay of pressure gradients, gravity and boundary conditions, see (3). In this work u_T results from buoyancy (i.e. gravity effects) as no applied pressure driving force is considered. If different phases are simultaneously present at the matrix boundaries, u_T can also result from spontaneous imbibition (Andersen et al., 2017a). u_T is one of the unknowns in the system but is found from (3) after applying ∂_x and combining with (5). This gives an elliptic equation for p_w which can be solved when combined with the boundary conditions. The resulting water pressure p_w and available water saturation s_w can be inserted in (3) to compute u_T. We refer to Section 3 for details.

2.3. *A generalized multiphase flow model based on mixture theory*

The starting point for developing our model that can account for more detailed physical mechanisms for water-oil flow in porous media than conventional modeling, is the theory of mixtures. This is a theory based on balance laws and conservation principles which is well known in continuum mechanics (Ambrosi and Preziosi, 2002; Bowen, 1976; 1980; Byrne and Preziosi, 2003; Preziosi and Farina, 2002; Rajagopal and Tao, 1995), and has been widely applied to systems which can be characterized as a mixture of interacting continua. A theoretical outline of the general components of mixture theory is presented in Appendix A together with a description of various applications. In the following Section 2.3.1 we apply this theory to derive a model that is appropriate to a water-oil flow scenario in porous media. The presentation, of the general theory in Appendix A and of the adapted model in this section, closely follows the description in Lemon et al. (2006); Rajagopal (2007); Schuff et al. (2013) which in turn builds on Bowen (1980); Drew and Passman (1999).

Compared to the general theory, we make some minor modifications to ensure that the formulation is consistent with conventional two-phase modeling based on Darcy's law, as described in Section 2.2. We will here deal with three phases: Solid matrix, water, and oil. Since matrix does not move or change, mass and momentum balance equations are only formulated for water and oil. However, the momentum balance equations for the fluids will, motivated by the general mixture theory approach, account for frictional resistance both at the porous boundaries of the solid as well as at the moving water-oil boundaries. Moreover, we will follow the conventional assumption that these resistance forces are far greater than internal frictional resistance due to viscosity and therefore ignore viscous stress tensor terms (see details in Section A.3). Finally, the model must account for the fact that a limited range of volume fractions are available for flow as denoted by residual saturations, and that the flow takes place inside the porous space of the rock as defined by introducing the rock porosity. In Section 2.3.2 we formulate a 1-D version of the generalized multiphase model that is comparable to the conventional model described in Section 2.2.

2.3.1. *Formulation in 3-D*

Hence, mass balance equations without any source terms are in the case of incompressible water-oil transport given by:

$$\partial_t(\phi s_i) + \nabla\cdot(\mathbf{u}_i) = 0, \tag{8}$$

$$\mathbf{u}_i = \phi(s_i - s_{ir})\mathbf{v}_i, \qquad (i = w, o), \tag{9}$$

where the second equation expresses the relation between the Darcy velocity $\mathbf{u}_i$ and the interstitial velocity $\mathbf{v}_i$ of phase i in the *mobile* domain. We also introduce normalized saturations S_i for the further derivations such that:

$$S_w = \frac{s_w - s_{wr}}{1 - s_{wr} - s_{or}}, \qquad S_o = 1 - S_w. \tag{10}$$

s_{ir} $(i = w, o)$ denote residual saturations. Moreover, introducing an effective porosity ϕ_e:

$$\phi_e = \phi(1 - s_{or} - s_{wr}), \tag{11}$$

allows us to write:

$$\mathbf{u}_i = \phi_e S_i \mathbf{v}_i, \qquad (i = w, o). \tag{12}$$

Neglecting inertial effects (acceleration effects), as is usual when dealing with creeping flow in porous materials, the mechanical stress balance is given by (Ambrosi and Preziosi, 2002):

$$0 = \nabla\cdot(S_i \mathbf{\Psi}_i) + \mathbf{m}_i + \mathbf{g}_i, \qquad (i = w, o), \tag{13}$$

where $\mathbf{\Psi}_i$ refers to the Cauchy stress tensor, $\mathbf{m}_i$ represents the interaction forces exerted on the constituents by other constituents of the mixture, and $\mathbf{g}_i = S_i \rho_i \mathbf{g}$ is the external body force due to gravity. Following the conventional approximation that the viscous stress tensor can be ignored and the dominating effects is due to the fluid-matrix and fluid-fluid interaction forces we have

$$\mathbf{\Psi}_i = -p_i \mathbf{I}, \qquad (i = w, o). \tag{14}$$

The difference in water pressure p_w and oil pressure p_o is expressed by the capillary pressure $P_c = p_o - p_w$. According to general principles of the theory of mixtures, the interaction forces $\mathbf{m}_i$ between the constituents appearing in (13) may be described as (Ambrosi and Preziosi, 2002; Preziosi and Farina, 2002):

$$\begin{aligned} \mathbf{m}_o &= p_o \nabla S_o + \mathbf{F}_{ow} + \mathbf{M}_{om}, \\ \mathbf{m}_w &= p_w \nabla S_w - \mathbf{F}_{ow} + \mathbf{M}_{wm}, \end{aligned} \tag{15}$$

where $\mathbf{F}_{ow}$ denotes the force (drag) that the water phase exerts on the oil. The oil exerts an equal and opposite force $-\mathbf{F}_{ow}$. Similarly, $\mathbf{M}_{om}$ and $\mathbf{M}_{wm}$ represent interaction forces (drag forces) between fluid and pore walls (solid matrix), respectively, for oil and water. The terms $p_o\nabla S_o$ and $p_w\nabla S_w$ are interfacial forces that arise from an averaging process. To close the system we must specify the drag force term $\mathbf{F}_{ow}$ and interaction force terms $\mathbf{M}_{im}$ between fluid $(i = w, o)$ and matrix. Drag force represents the interaction between the oil and water phase and is modeled as (Ambrosi and Preziosi, 2002; Preziosi and Farina, 2002; Rajagopal, 2007):

$$\mathbf{F}_{ow} = R(\mathbf{v}_w - \mathbf{v}_o), \tag{16}$$

where R (dimension $\mathrm{Pa\cdot s/m^2}$) remains to be determined. Typically, $R \sim S_o S_w$ to reflect that this force term will vanish when one of the phases vanishes. Similarly, the interaction force between fluid and pore wall (matrix, which is stagnant) is naturally expressed then as (Ambrosi and Preziosi, 2002; Preziosi and Farina, 2002; Rajagopal, 2007; Rajagopal and Tao, 1995)

$$\mathbf{M}_{im} = -R_i \mathbf{v}_i, \qquad (i = w, o). \tag{17}$$

The coefficients R and R_i (dimension $\mathrm{Pa\cdot s/m^2}$), that characterize the magnitude of interaction terms, can be chosen such that the model recovers the classical porous media model based on Darcy's law. At the same time the approach used here will open for development of reservoir models where more detailed physics can be taken into account.

2.3.2. *Formulation in 1-D*

Assuming a 1-D domain (along the downward vertical axis, x) the combination of (13)–(17) gives us:

$$\begin{aligned} S_w \partial_x p_w &= -R_w v_w + R(v_o - v_w) + S_w \rho_w g, \\ S_o \partial_x p_o &= -R_o v_o - R(v_o - v_w) + S_o \rho_o g, \end{aligned} \tag{18}$$

where the terms on the right hand side represent, respectively, rock-fluid interaction, fluid-fluid interaction and gravity. $R_i \geq 0$ and $R \geq 0$ are solid-fluid interaction and fluid-fluid interaction terms, respectively. Solving (18) with respect to interstitial velocities v_i and inserting into (12) results in:

$$\begin{aligned} u_w &= \phi_e S_w v_w = -\hat{\lambda}_{ww}(\partial_x p_w - \rho_w g) - \hat{\lambda}_{wo}(\partial_x p_o - \rho_o g), \\ u_o &= \phi_e S_o v_o = -\hat{\lambda}_{ow}(\partial_x p_w - \rho_w g) - \hat{\lambda}_{oo}(\partial_x p_o - \rho_o g), \end{aligned} \tag{19}$$

or equivalently (using $P_c = p_o - p_w$):

$$\begin{aligned} u_w &= -(\hat{\lambda}_{ww} + \hat{\lambda}_{wo})\partial_x p_w - \hat{\lambda}_{wo}\partial_x P_c + (\hat{\lambda}_{ww}\rho_w + \hat{\lambda}_{wo}\rho_o)g, \\ u_o &= -(\hat{\lambda}_{ow} + \hat{\lambda}_{oo})\partial_x p_w - \hat{\lambda}_{oo}\partial_x P_c + (\hat{\lambda}_{ow}\rho_w + \hat{\lambda}_{oo}\rho_o)g, \end{aligned} \tag{20}$$

with the following defined generalized diagonal mobilities $\hat{\lambda}_{ii}$ and crossterm mobilities $\hat{\lambda}_{ij}$:

$$\begin{aligned} \hat{\lambda}_{ww} &:= \frac{S_w^2(R_o + R)}{R_o R_w + R(R_o + R_w)}\phi_e, \qquad \hat{\lambda}_{oo} := \frac{S_o^2(R_w + R)}{R_o R_w + R(R_o + R_w)}\phi_e, \\ \hat{\lambda}_{wo} &:= \hat{\lambda}_{ow} = \frac{R S_w S_o}{R_o R_w + R(R_o + R_w)}\phi_e. \end{aligned} \tag{21}$$

Further, we define the following notation for generalized phase mobilities $\widehat{\lambda_i}$ and total mobility $\widehat{\lambda_T}$:

$$\begin{aligned} \hat{\lambda}_w &:= \hat{\lambda}_{ww} + \hat{\lambda}_{wo} = \frac{S_w^2 R_o + S_w R}{R_o R_w + R(R_o + R_w)}\phi_e, \\ \hat{\lambda}_o &:= \hat{\lambda}_{ow} + \hat{\lambda}_{oo} = \frac{S_o^2 R_w + S_o R}{R_o R_w + R(R_o + R_w)}\phi_e, \\ \hat{\lambda}_T &:= \hat{\lambda}_o + \hat{\lambda}_w = \frac{S_w^2 R_o + S_o^2 R_w + R}{R_o R_w + R(R_o + R_w)}\phi_e. \end{aligned} \tag{22}$$

By summing u_w and u_o in (20) and using the notation introduced in (22), it follows that the total Darcy velocity can be expressed as:

$$u_T = u_w + u_o = -\hat{\lambda}_T \partial_x p_w - \hat{\lambda}_o \partial_x P_c + g(\hat{\lambda}_w \rho_w + \hat{\lambda}_o \rho_o). \tag{23}$$

The water pressure gradient $\partial_x p_w$ can, as seen from (23), be expressed as:

$$\partial_x p_w = -\frac{1}{\hat{\lambda}_T}u_T - (1 - \hat{f}_w)\partial_x P_c + g(\hat{f}_w \rho_w + (1 - \hat{f}_w)\rho_o), \tag{24}$$

with generalized water fractional flow function $\hat{f}_w = \hat{\lambda}_w / \hat{\lambda}_T$. Inserting (24) into (20) (and using the notation introduced in (22)) we get:

$$\begin{aligned} u_w &= u_T \hat{f}_w + W\Delta\rho g + W\partial_x P_c, \\ u_o &= u_T \hat{f}_o - W\Delta\rho g - W\partial_x P_c, \end{aligned} \tag{25}$$

with $\Delta\rho = \rho_w - \rho_o$ where we have defined:

$$\begin{aligned} \hat{f}_w(s_w) &:= \frac{\hat{\lambda}_w}{\hat{\lambda}_T} = \frac{\hat{\lambda}_w}{\hat{\lambda}_w + \hat{\lambda}_o} = \frac{S_w^2 R_o + S_w R}{S_w^2 R_o + (1 - S_w)^2 R_w + R} \\ W(s_w) &:= \hat{f}_w \hat{\lambda}_o - \frac{S_o S_w R \phi_e}{R_o R_w + R(R_o + R_w)} = \frac{S_w^2(1 - S_w)^2 \phi_e}{S_w^2 R_o + (1 - S_w)^2 R_w + R}. \end{aligned} \tag{26}$$

Inserting the water flux (25) into the 1-D version of the water conservation Eq. (8) we obtain:

$$\partial_t(\phi s_w) = -\partial_x(u_T \hat{f}_w + W\Delta\rho g) - \partial_x(W\partial_x P_c), \qquad (0 < x < H). \tag{27}$$

The generalized model (27) can be solved once we have computed u_T. As mentioned before, we can apply ∂_x to (23) and make use of

$$\partial_x u_T = 0, \tag{28}$$

to obtain a second order elliptic equation for p_w. This is combined with appropriate boundary conditions and the available saturation s_w. Having computed p_w we can obtain u_T which is defined by (23). We refer to Section 3 for details. Note that (27) takes the same form as the conventional model (7), except that the term W has an additional term compared to the product $\hat{\lambda}_o \hat{f}_w$, as in the conventional model, see (26).

Remark 2.2. A closer inspection of the momentum force balance Eqs. (18) shows that we can extract information about the role played by the fluid-fluid interaction term $\pm R(v_o - w_w)$ for the two different flow regimes of co-current and counter-current flow.

(a) For **co-current** flow it follows that v_w and v_o have the same sign. Let us assume that $v_w, v_o > 0$. If $v_w > v_o$, then $R(v_o - v_w) < 0$. Consequently, it follows from $(18)_1$ (holding $S_w \partial_x p_w$ and $S_w \rho_w g$ fixed) that there is a reduction in the magnitude of v_w compared to the case with $R = 0$. On the other hand, since $-R(v_o - v_w) > 0$ it is clear from $(18)_2$ that v_o must increase in order to maintain the force balance. Consequently, the influence from the fluid-fluid interaction term is that is generates a deceleration of the fluid with highest velocity (v_w) and an acceleration of the slowest fluid (v_o).

(b) For **counter-current** flow it follows that v_w and v_o have the opposite sign. Let us assume that $v_w < 0$ and $v_o > 0$. Then $R(v_o - v_w) > 0$, and in view of the balance law $(18)_1$, it is clear that this must generate a reduced v_w compared to the case with $R = 0$. Similarly, $(18)_2$ combined with the fact that $-R(v_o - v_w) < 0$ allows us to conclude that v_o must also decrease. Consequently, the influence from the fluid-fluid interaction term is that is generates a deceleration of both fluids.

Remark 2.3. Co-current flow is accounted for by the $u_T \hat{f}_i$ term in (25) whereas counter-current flow is represented by the capillary pressure and gravity related terms with coefficient W. The precise role of the fluid-rock interaction force term and the fluid-fluid interaction term is expressed by R_i and R, respectively, in the expression for $\hat{f}_w$ and W in (26). The occurrence of the fluid-fluid interaction coefficient R in the co-current term $\hat{f}_i$ as well as the counter-current term W, expresses exactly the behavior more loosely observed in Remark 2.2. For example, for counter-current flow it follows from the expression for W that $R > 0$ will give rise to a deceleration effect for both fluids. For co-current flow a decrease in u_w due to a decrease in $\hat{f}_w$ (caused by the presence of R) corresponds to an increase in u_o since $\hat{f}_o = 1 - \hat{f}_w$. This is in accordance with several experimental observations as mentioned in the introduction, see for example, Bentsen and Manai (1992, 1993); Bourbiaux and Kalaydjian (1990); Sherafati and Jessen (2017) and references therein.

Remark 2.4. The essential difference between the conventional model and the generalized comes to the surface in the expression for the counter-current related coefficient W in $(26)_2$. Conventional modeling amounts to using $\hat{f}_w \hat{\lambda}_o$ whereas the generalized model includes a correction term that depends on the strength R of the fluid-fluid interaction.

Hence, it is clear that the generalized mobility functions (22) have a built-in capacity to compensate for a change in flow regime (counter-current versus co-current or a mixture of these two). In Section 4 we will test how the generalized model can account for both flow regimes (co- and counter-current flow) in a relevant manner with one and the same set of parameters in contrast to a conventional model that must use different mobility functions depending on the flow regime under consideration. Before we are ready for that, we will need to specify expressions for the interactions coefficients R_i $(i = w, o)$ and R.

2.3.3. *Interaction terms*

The frictional interaction terms must be specified for computing $\hat{f}_w$ and W in (27). It is clear that the solid-fluid interaction terms $R_i (i = w, o)$ should obey the relationship $R_i \propto \mu_i / K$ in order to be consistent with standard porous media flow formulation based on Darcy's law (2). The following interaction terms were suggested to be included in the generalized model (21) in order to capture the interaction effects between two movable fluids when they are flowing simultaneously through a porous medium (Standnes et al., 2017):

$$R_w:=I_w S_w^{\alpha}\frac{\mu_w}{K}\phi_e,\qquad R_o:=I_o S_o^{\beta}\frac{\mu_o}{K}\phi_e,\qquad R:=IS_wS_o\frac{\mu_w\mu_o}{K}\phi_e. \tag{29}$$

All the interaction terms have dimension $\mathrm{Pa\cdot s/m^2}$, α and β are dimensionless exponents, I_w and I_o are dimensionless friction coefficients characterizing the strength of fluid-solid interaction and I is a coefficient characterizing the strength of the fluid-fluid drag force with dimension $(\mathrm{Pa\cdot s})^{-1}$. Using (29) in combination with (26) we obtain full expressions for the generalized fraction flow functions $\hat{f}_w$ and W given by:

$$\begin{aligned}\hat{f}_w(s_w) &= \frac{S_w(1-S_w)^{\beta-1}\mu_o I_o + S_w\mu_w\mu_o I}{S_w(1-S_w)^{\beta-1}\mu_o I_o + (1-S_w)S_w^{\alpha-1}\mu_w I_w + \mu_w\mu_o I},\\ W(s_w) &= \frac{S_w(1-S_w)K}{S_w(1-S_w)^{\beta-1}\mu_o I_o + (1-S_w)S_w^{\alpha-1}\mu_w I_w + \mu_w\mu_o I}.\end{aligned} \tag{30}$$

2.3.4. Generalized relative permeabilities

We see from (25) that the terms responsible for co-current flow are represented by $\hat{f}_w$ and $\hat{f}_o$. The corresponding generalized mobility functions are given by $\hat{\lambda}_w$ and $\hat{\lambda}_o$ as expressed in (22). This gives rise to generalized relative permeabilities $\hat{k}_{ri}$ for $(i = w, o)$ defined as:

$$\begin{aligned}\hat{k}_{rw} &= \frac{\mu_w}{K}\hat{\lambda}_w = \frac{I_oS_wS_o^{\beta-1} + I\mu_wS_w}{I_wI_oS_w^{\alpha-1}S_o^{\beta-1} + I(I_wS_w^{\alpha}\mu_w + I_oS_o^{\beta}\mu_o)},\\ \hat{k}_{ro} &= \frac{\mu_o}{K}\hat{\lambda}_o = \frac{I_wS_oS_w^{\alpha-1} + I\mu_oS_o}{I_wI_oS_w^{\alpha-1}S_o^{\beta-1} + I(I_wS_w^{\alpha}\mu_w + I_oS_o^{\beta}\mu_o)}.\end{aligned} \tag{31}$$

It can be seen that the generalized relative permeabilities are viscosity-dependent if $I \neq 0$. Viscosity dependent relative permeabilities has been suggested by several authors (Odeh, 2013; du Prey, 1973; Yuster, 1951). If the interaction coefficient I is 0 the corresponding expressions for generalized relative permeability reduce to traditional Corey-type expressions:

$$\hat{k}_{ro}:=\frac{S_o^{2-\beta}}{I_o},\qquad \hat{k}_{rw}:=\frac{S_w^{2-\alpha}}{I_w}, \tag{32}$$

where Corey exponents n_w and n_o are related to the exponents α and β by:

$$\alpha = 2-n_w,\qquad \beta = 2-n_o, \tag{33}$$

under the condition of no viscous coupling between water and oil $(I = 0)$.

Remark 2.5. We may refer to (31) as **co-current** generalized relative permeability curves $\hat{k}_{rw}^{coc}$ and $\hat{k}_{ro}^{coc}$ as we see that, by applying the co-current related assumption $\partial_x p_w = \partial_x p_o$, it follows from (19) that the generalized mobilities $\hat{\lambda}_w:=\hat{\lambda}_{ww}+\hat{\lambda}_{wo}$, $\hat{\lambda}_o:=\hat{\lambda}_{ow}+\hat{\lambda}_{oo}$ given in (22) represent mobility in the "conventional" sense. That is, in the sense of Darcy's law (2) with $\lambda_i = \frac{Kk_{ri}}{\mu_i}$. Later, in Section 4 when we explore properties of the generalized model (27), we apply (31) to identify the parameters I_w, I_o, I, α and β such that a good fit is obtained when compared with relative permeability curves obtained from co-current type of flow experiments.

2.4. Capillary pressure

In the examples it will be assumed that the capillary pressure follows Leverett J-function scaling (Bear, 1988):

$$P_c = \sigma\sqrt{\frac{\phi}{K}}J(S_w), \tag{34}$$

where σ is oil-water interfacial tension and the dimensionless capillary pressure function $J(S_w)$ takes the form (Andersen et al., 2014):

$$J(S_w) = \frac{a_1}{1+k_1S_w} - \frac{a_2}{1+k_2(1-S_w)} + c. \tag{35}$$

$a_1, a_2, k_1, k_2 > 0$ and c are curve fitting parameters.

2.5. Initial and boundary conditions

We assume the matrix block initially is filled with oil at irreducible water saturation s_{wr}:

$$s_w(x, t=0) = s_{wr}. \tag{36}$$

The water pressure p_w is defined to be zero at the top (T) located at position $x = 0$ and increases hydrostatically outside the block to its maximum value at bottom (B) located at position $x = H$ (see Fig. 1):

$$p_{w,T} = p_w(x=0, t) = 0,\qquad p_{w,B} = p_w(x=H, t) = \rho_w gH. \tag{37}$$

The oil pressure p_o is taken equal to the water pressure at the top and also increases hydrostatically outside the block, resulting in a net phase pressure difference:

$$P_{c,T} = P_c(x=0^-, t) = 0,\qquad P_{c,B} = P_c(x=H^+, t) = -\Delta\rho gH. \tag{38}$$

2.6. Equilibrium

At equilibrium, when no phases are flowing in the system $u_i = 0$, we can set $\partial_t s_w = 0$ and $u_T = 0$ in (7) for the conventional model and in (27) for the generalized model. The water flux being zero allows us to express the following relation for the capillary pressure gradient in both models:

$$\partial_x P_c(S_{w,\infty}) = -\Delta\rho g, \tag{39}$$

where $S_{w,\infty}(x)$ represents the equilibrium water saturation. Combined with (38) it follows that $P_c(S_{w,\infty}(x))$ is distributed linearly from 0 at the top to $-\Delta\rho gH$ at the bottom. Hence, the equilibrium water saturation distribution $S_{w,\infty}(x)$ can be calculated from the given $P_c(S_w)$ correlation.

2.7. Oil recovery factor

Oil recovery factor $RF(t)$ is calculated as the fraction of produced oil divided by mobile oil initially in place (and not total oil initially in place):

$$RF(t) = \frac{\int_0^H (s_w(x,t) - s_{wr})dx}{H(1-s_{wr}-s_{or})} = \overline{S}_w(t), \tag{40}$$

which is equivalent to the average normalized saturation $\overline{S}_w(t)$. If all mobile oil is displaced we obtain $RF = 1$, while initially $RF = 0$.

3. Summary of the mathematical models

The conventional model (7) and generalized model (26) take the same form of mathematical description for the problem shown in Fig. 1:

$$\begin{aligned}\partial_t(\phi s_w) &= -\partial_x(u_T\hat{f}_w + V\Delta\rho g) - \partial_x(V\partial_x P_c),\\ u_T &= -\hat{\lambda}_T\partial_x p_w - \hat{\lambda}_o\partial_x P_c + g(\hat{\lambda}_w\rho_w + \hat{\lambda}_o\rho_o),\qquad \partial_x u_T = 0,\\ u_w &= u_T\hat{f}_w + V\Delta\rho g + V\partial_x P_c,\qquad u_o = u_T - u_w,\\ \text{with}\quad P_c &= \sigma\sqrt{\frac{\phi}{K}}J(S_w),\qquad S_w = \frac{s_w - s_{wr}}{1-s_{wr}-s_{or}},\end{aligned} \tag{41}$$

where $V = f_w\lambda_o$ and $\hat{f}_w, \hat{\lambda}_i$ are replaced by f_w, λ_i as described in Section 2.2 for the conventional model, whereas $V = W$ for the generalized model. The initial condition is a uniform distribution of irreducible water saturation

$$s_w(x, t=0) = s_{wr}, \tag{42}$$

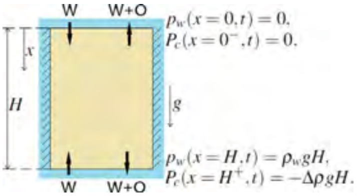

Fig. 1. Geometry of the system. A water-wet matrix block of height H is exposed to water both at the top ($x = 0$) and bottom ($x = H$). Spontaneous imbibition and gravity drainage mechanisms displace the oil by water in 1-D flow.

and boundary conditions are given by

$$\begin{aligned} p_w(x = 0, t) &= 0, \qquad p_w(x = H, t) = \rho_w gH, \\ P_c(x = 0^-, t) &= 0, \qquad P_c(x = H^+, t) = -\Delta\rho gH. \end{aligned} \tag{43}$$

The reader interesting in the relevant discretized scheme of this model is referred to Appendix B. Here we just note that, after writing the model on dimensionless form, the main steps are:

1) At a given time, use $(41)_2$ together with boundary conditions (43) to calculate the pressure distribution $p_w(x)$ and the constant (in space) total velocity u_T.
2) Calculate $s_w(x, t)$ a local time step forward (assuming u_T is held fixed) using the transport Eq. $(41)_1$.
3) Iterate until full simulation time has been obtained.

Based on the variables p_w, u_T, s_w, output variables such as P_c, u_o, u_w and oil recovery can be calculated. The model was discretized into 300 cells in the x-direction with sufficiently small time steps to achieve acceptable resolution and convergence.

3.1. Buoyancy

For a simple interpretation of u_T a special case can be considered: At initial state we have a uniform saturation profile with thus a fixed capillary pressure in the block, which yields from $(41)_2$:

$$u_T^0 = -\hat{\lambda}_T^0 \partial_x p_w^0 + g(\hat{\lambda}_w^0 \rho_w + \hat{\lambda}_o^0 \rho_o), \tag{44}$$

where u_T^0 is the initial total Darcy velocity and all mobilities are evaluated at s_{wr} as denoted by the index ^{0}. Since the water pressure is continuous with the hydrostatic pressure at both boundaries we can set $\partial_x p_w^0 = \rho_w g$ to obtain:

$$u_T^0 = -\hat{\lambda}_o^0 \Delta\rho g, \tag{45}$$

demonstrating that gravity, controlled by the density difference of water and oil and by the mobility of oil in particular, initiate a co-current flow of the phases in upwards direction (negative u_T). As seen from the general Eq. $(41)_2$, further changes in u_T depend on the distribution of pressure and saturations along the block.

4. Results and discussion

A possible challenge for reservoir simulation is that conventional mobility functions based on relative permeability functions obtained through co-current flow experiments, do not represent well other flow regimes where strong counter-current effects are involved (Bentsen and Manai, 1992; 1993; Bourbiaux and Kalaydjian, 1990; Sherafati and Jessen, 2017). The root of this problem is the ignorance of fluid-fluid interaction in conventional modeling (based on Darcy's law). Consequently, the drag force effect between two moving fluids for which co-current flow leads to a deceleration effect for the fluid with highest speed and an acceleration effect for the slower moving fluid and for counter-current flow leads to a deceleration of both fluids, is ignored. We refer to Remarks 2.2 and 2.3 for details. Normally this problem is fixed by manually reducing the mobility functions (relative permeability functions) when used for flow scenarios that involve counter-current flow. However, realistic flow systems will often involve a more or less complicated mixture of these two flow regimes.

The main purpose of this section is to explore how the generalized model seems to offer some improvements (compared to conventional modeling) by providing generalized mobility functions that automatically are able to capture several flow regimes for one and the same parameter set. Careful investigations are carried out for the flow system in Fig. 1 where we compare the behavior predicted by the conventional model and the generalized. See Remark 2.4 for a precise description of the difference between the generalized and conventional model.

First, motivated by experimental data from Bourbiaux and Kalaydjian (1990) where co-currently measured relative permeability curves were obtained, and counter-current spontaneous imbibition for the same rock-fluid system was measured, we provide a set of parameters (in Section 4.1) needed in the generalized model that lead to a good match, see also Remark 2.5. These data are then used in all further simulations to define $\hat{f}_w$ and W in (26). For reference, it is demonstrated that the conventional and generalized models produce equivalent results in strictly co-current flow in Section 4.2.1. The ability of the model to capture reduced mobility effects seen in experimental data during counter-current flow is demonstrated in Section 4.2.2. Next in Section 4.3, we carefully test the two models (generalized and conventional) for our flow system. We discuss three cases: (i) A gravity dominated case (with well defined co-current vertical flow); (ii) a capillary pressure flow dominated case (i.e., counter-current dominated when all open phases are exposed to water); (iii) a combination where gravity and capillary pressure forces have similar strength (mixed flow regimes). This allows us to obtain precise insight into differences and similarities between the conventional and the generalized model. The numerical scheme was validated by comparison of the conventional model simulations of these cases with results obtained from the commercial simulator Eclipse 100. We refer to Appendix C for this demonstration.

4.1. Input data

The input parameters (Table 1) used in the simulations are mainly collected from Bourbiaux and Kalaydjian (1990). To put more emphasis on gravity we use a block of 0.5 m height which is 70% higher than in their experiments. Their measured relative permeability data from co-current flow were matched as described in the following. The end-points are related by:

$$I_w = 1/k_{rw}^{max}, \qquad I_o = 1/k_{ro}^{max}, \tag{46}$$

as found by setting $S_o = 1$ or $S_w = 1$ in (31). The expression (31) was further matched to the shape of the data by varying the parameters I, α and β. We recall that the interaction term I reflects the strength of the fluid-fluid interaction term R, see (29). By assigning a certain value $I > 0$ to this term, it follows that we account for viscous coupling information that will be important when we consider other flow regimes that involve counter-current type of flow due to gravity and/or capillary pressure. In particular, the magnitude of I is also quality checked by assessing the simulated rate of counter-current spontaneous imbibition against experimental measurements performed by Bourbiaux and Kalaydjian (1990) on the same rock-fluid system (as where co-current relative permeabilities were measured). This role played by I is explicitly reflected by the expression for W, see $(26)_2$ or $(30)_2$, and contains effects not accounted for in the conventional

Table 1
Reference input parameters in the simulations. ^{1}Data from (Bourbiaux and Kalaydjian, 1990); ^{2}Input to both the interaction terms (29) and co-current relative permeabilities (31) as matched to data from (Bourbiaux and Kalaydjian, 1990); ^{3}Input to the capillary pressure correlation (35) as matched to data from (Bourbiaux and Kalaydjian, 1990).

Parameter	Dimensional Value	Parameter	Dimensional Value
H	0.5 m	^2I_w	23.26
$^1\phi$	0.233	^2I_o	2.15
$^1\rho_w$	1.09 g/cm^3	^2I	3500 $(\text{Pa}\cdot\text{s})^{-1}$
$^1\rho_o$	0.76 g/cm^3	$^2\alpha$	− 0.2
$^1s_{wr}$	0.4	$^2\beta$	1.5
$^1s_{or}$	0.425	$^1\sigma$	15.8 mN/m
$^1\mu_o$	1.5 cP	$^3a_1$	0.6
$^1\mu_w$	1.2 cP	$^3a_2$	8
^1K	118 mD	$^3k_1$	1.3
$^1k_{rw}^{\max}$	0.043	$^3k_2$	5000
$^1k_{ro}^{\max}$	0.465	^3c	− 0.1

modeling which amounts to using the coefficient $\hat{f}_w\hat{\lambda}_o$. In Fig. 3 we show a plot of W and the conventional part $\hat{f}_w\hat{\lambda}_o$ which illustrates the effect from fluid-fluid interaction term R.

The co-current relative permeability curves shown in Fig. 2 and represented by (31) are given as direct input in the conventional model. The viscous coupling effects which occur during co-current flow is thus integrated in these curves, but are (implicitly) assumed not to change in the conventional model when we consider other flow scenarios involving counter-current effects due to gravity and/or capillary pressure. By using the generalized model, this assumption (of fixed curves) is put to a test since generalized mobilities are related to both phase pressure gradients, see (19) and (21). Hence, this representation of the relative permeabilities is more general and it is expected that it is capable of capturing effects due to flow direction and/or interaction between the fluids and solids. We refer to Section 4.2.2 for an example that illustrates this clearly. Note that the same parameterization, given in Table 1, is applied to both models in the following.

Remark 4.1. Note that we have two equivalent formulations of fluid velocity, for instance u_w, in the generalized model: (i) The use of two mobility functions $\hat{\lambda}_{ww}$ and $\hat{\lambda}_{wo}$, one associated with $\partial_x p_w$, the other with $\partial_x p_o$ as in (19); (ii) the use of phase mobility functions $\hat{\lambda}_w = \hat{\lambda}_{ww} + \hat{\lambda}_{wo}$ and $\hat{\lambda}_o = \hat{\lambda}_{ow} + \hat{\lambda}_{oo}$ associated with pure co-current flow, see (25)$_1$ and (26)$_1$, combined with inclusion of capillary pressure driven counter-current flow with a non-conventional coefficient W given by (26)$_2$.

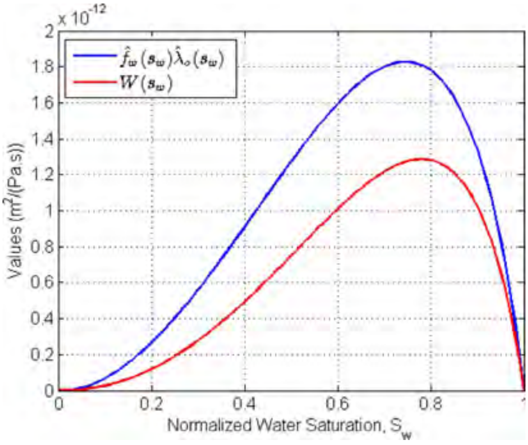

Fig. 3. Comparison of the generalized counter-current coefficient W and the "conventional part" $\hat{f}_w\hat{\lambda}_o$ appearing in (26)$_2$ for the data set given in Table 1. The difference between these two curves reflects the difference between the conventional and the generalized model.

4.2. Basic validation

4.2.1. Model comparison during co-current flow

In this example the generalized and conventional models are, for validation purposes, compared under conditions that should yield identical results. A pure co-current flow test was considered. This was realized by assuming $P_c(s_w) = 0$ and that the phase outside the block at the top was oil instead of water, as assumed in Fig. 1. Then a stable gravity displacement of the low density oil in the block by high density water is achieved in co-current fashion due to buoyancy. All counter-current terms are negligible in this situation. The comparison of the conventional and generalized model revealed a perfect match, as shown in Fig. 4. This may be explained as follows: As mentioned, the difference between the two models lies in the coefficient in front of the gravity term appearing in (41)$_1$: One uses $\hat{\lambda}_o\hat{f}_w$ (conventional), the other uses W (generalized). In Fig. 5 we include plots of the corresponding total advective / gravitational fluxes, $F_{con}(s_w) = u_T\hat{f}_w + \hat{\lambda}_o\hat{f}_w\Delta\rho g$ and $F_{gen}(s_w) = u_T\hat{f}_w + W\Delta\rho g$, (see (41)) for a fixed time t where $u_T = u_T^0/10$,

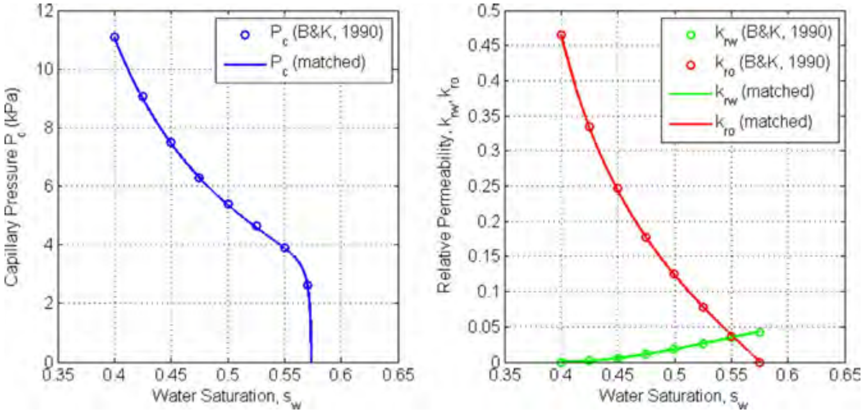

Fig. 2. Left: Input capillary pressure from (Bourbiaux and Kalaydjian, 1990) matched to the correlation (35). The capillary pressure goes to large negative values when water saturation is close to $1 - s_{or}$. Right: Generalized co-current relative permeabilities $\hat{k}_{rw}^{coc}$ and $\hat{k}_{ro}^{coc}$, see (31), parameterized to match measurements from (Bourbiaux and Kalaydjian, 1990). These relative permeabilities are directly applied in the conventional model, but for the generalized model these curves are only representative in strictly co-current flow regimes.

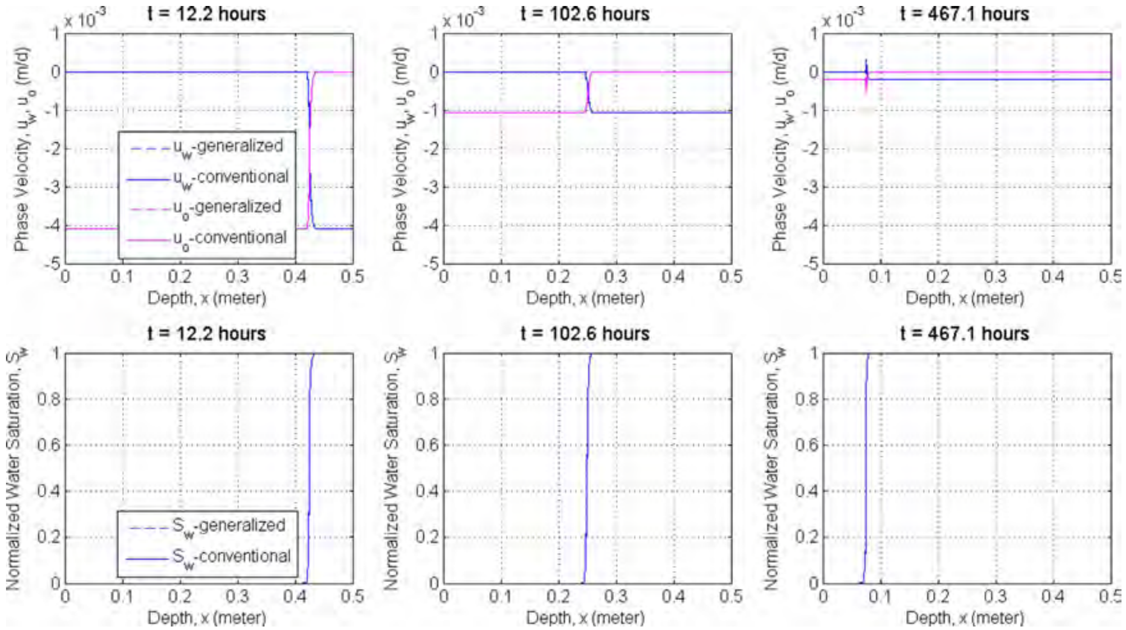

Fig. 4. Comparison between the generalized and conventional models for the pure co-current flow case. Profiles of $u_w(x)$, $u_o(x)$ (top) and normalized water saturation $S_w(x)$ (bottom) are shown after 12.2, 102.6 and 467.1 (hours). The comparison of the two models reveals a perfect match.

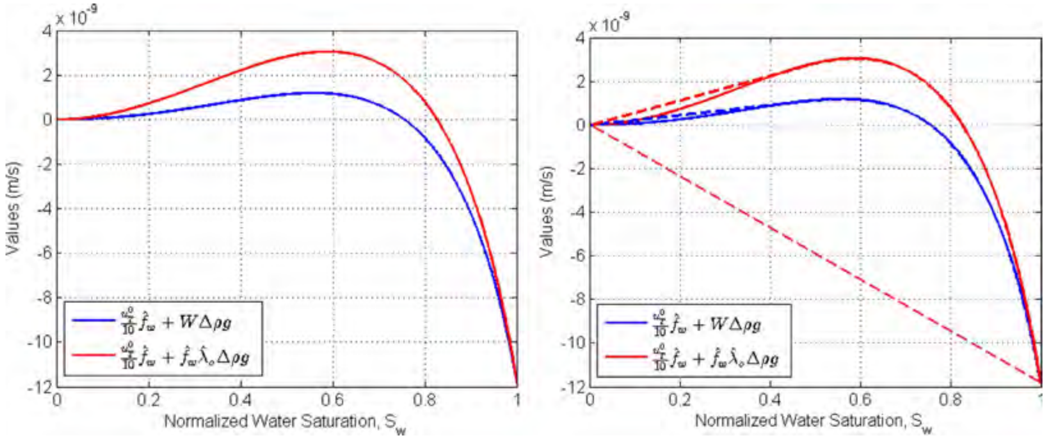

Fig. 5. Left: Plot of the total advective/gravitational flux $F_{con}(s_w) = u_T\hat{f}_w + \hat{\lambda}_o\hat{f}_w\Delta\rho g$ and $F_{gen}(s_w) = u_T\hat{f}_w + W\Delta\rho g$ for a fixed time t where $u_T = u_T^0/10$. Right: Same as left, where the lower convex hull and upper convex hull of the flux functions are indicated by dashed lines. Note that the lower convex hull is the same for F_{con} and F_{gen} (indicating that the upward moving front from $S_w = 0$ to 1 is identical for both models, see examples in Sections 4.2.1 and 4.3.2), but their upper convex hull are not (and the downward moving fronts are thus different both in front height and front speed, see example in Section 4.3.2).

where u_T^0 is the initial total Darcy velocity of the system. For this flow case an upward moving front (increasing jump in scaled saturation from 0 to 1) is formed at the bottom. According to the theory of solutions of Riemann problems for scalar nonlinear conservation laws (see Chapter 16 in Le Veque (2002)) the entropy satisfying solution is given in terms of a shock solution that moves with the speed s determined by the Rankine–Hugoniot condition $s = \frac{F_i(1) - F_i(0)}{1}$ for ($i = con, gen$). Consequently, it is only the endpoints of the two functions F_i that matter. More precisely, the construction of the solution depends on the *lower convex hull* of $F_i(s_w)$ in the interval [0, 1] and this is the same for both $i = con$ and $i = gen$. See Fig. 5 (right) where the lower convex hull is indicated for this example and more explanation. Hence, there is not room for any effects from the fluid-fluid interaction term, which makes good sense due to the fact that $R \sim S_w S_o$, see (29), such that the difference between W and $\hat{f}_w\hat{\lambda}_o$ does not affect end points (see also Fig. 3). Some rapid variations in the phase velocity curves is observed around $x = 0.075$ m after 467.1 hours when u_T is low. This is related to the slope change of the advection / gravitational flux.

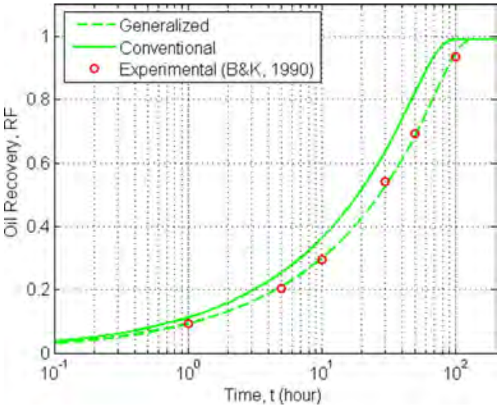

Fig. 6. Results comparison of the generalized and conventional models with the experimental work (Bourbiaux and Kalaydjian, 1990) for the pure counter-current spontaneous imbibition test.

4.2.2. Comparison against experimental counter-current data

Secondly, the generalized and conventional models were used to simulate a strictly counter-current spontaneous imbibition test where the bottom boundary is closed in Fig. 1 and both capillary and gravity effects are considered. This case was conducted experimentally in Bourbiaux and Kalaydjian (1990) using the indicated data shown in Table 1 except for a core of length 0.29 m, thus also implemented in the simulations here. The results in terms of oil recovery are shown in Fig. 6. We observe that the generalized model produces an oil recovery curve that largely matches the experimental results. This nice prediction also justifies the value of the interaction coefficient *I* resulting from matching the relative permeability curves. The conventional model, which directly implements the co-currently measured relative permeabilities, yields higher recovery rates than the experimental data and generalized model. In particular, the mobility associated with the counter-current flow effect is too strong, which is expected since the relative permeability curves used are based on co-current flow regime. Motivated by these results, we now turn our attention to the flow system depicted in Fig. 1 and represented by the model (41), (42) and (43).

4.3. Investigation of flow regimes

4.3.1. Case I: Capillary-dominated system

For the capillary-dominated case we reduce all terms related to gravity to negligible magnitude, both in the transport Eqs. (7) and (27) and the velocity Eqs. (3) and (23). Also, the capillary pressure at $x = H$ goes to 0, see (38). The system can thus be regarded as a purely counter-current spontaneous imbibition process. Fig. 7 shows the profiles of water and oil Darcy velocities $u_w(x)$, $u_o(x)$ and normalized water saturation $S_w(x)$ at three given times: 1.5, 15.5 and 46.6 h (corresponding to RF = 15, 50 and 85% in the conventional model, respectively). The duration of the test is 150 hours. Due to the counter-current dominated process and equal boundary conditions the profiles are symmetric. During counter-current flow both phases decelerate, as is seen from the form of the coefficient *W* in $(26)_2$, which reflects the additional viscous coupling effects through the *R*-dependent term. As a consequence, the inflowing water fronts move slower compared to the conventional model where the co-current relative permeabilities are applied, which amounts to using $\hat{f}_w\hat{\lambda}_o$ as the capillary pressure coefficient. The saturation profiles predicted by the generalized model are delayed and the imbibition process is generally slower.

The saturation fronts almost converge after 15.5 h and the center saturation is at 75% after 46.6 h in the conventional model, while in the generalized model all saturations have travelled significantly shorter distance from the boundaries. It is also observed that the discrepancy

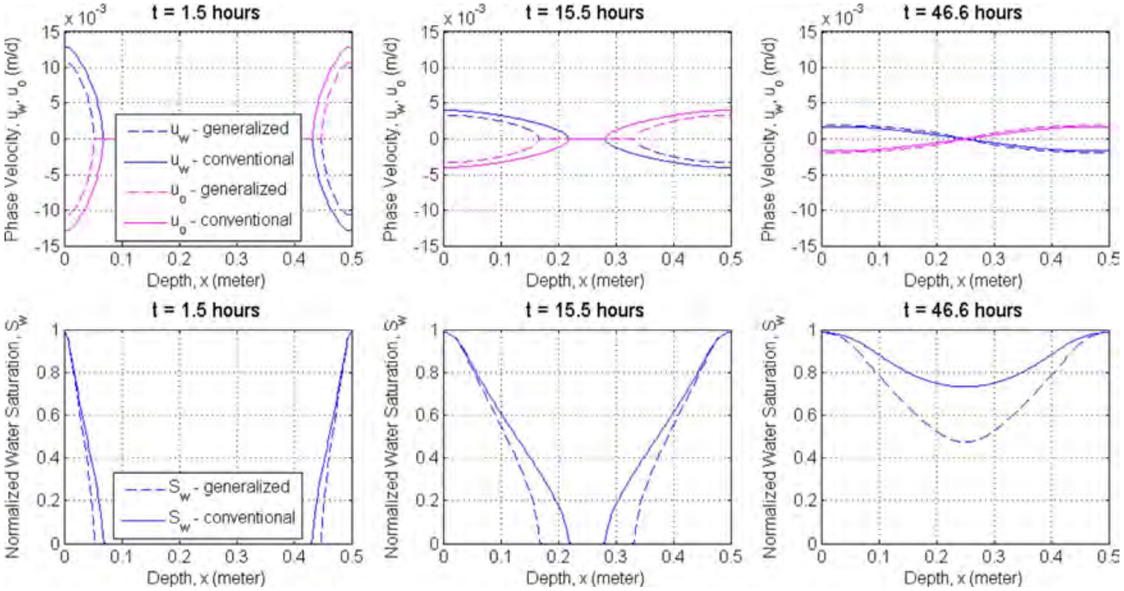

Fig. 7. Comparison between the generalized and conventional models for the capillary-dominated case I. Profiles of $u_w(x)$, $u_o(x)$ (top) and normalized water saturation $S_w(x)$ (bottom) are shown after 1.5, 15.5 and 46.6 h. The profiles are symmetric since there is no gravitational effect. In the generalized model: At 1.5 h and 15.5 h, the phase velocities are lower due to viscous coupling, also reflected by delayed saturation fronts; at 46.6 hours phase velocities are higher but saturation front is still delayed. This is because viscous coupling delays the imbibition process as accounted for by the *R*-dependent term in *W*, see $(26)_2$.

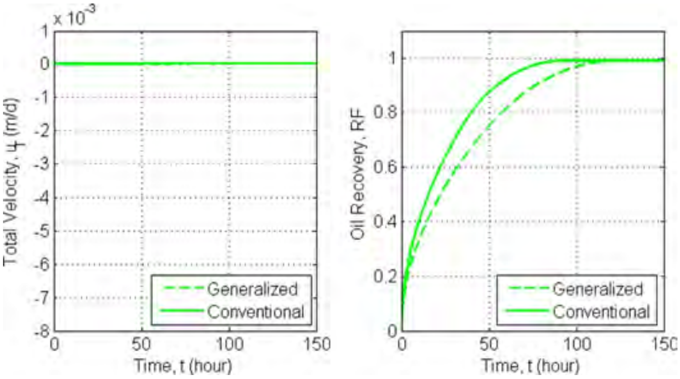

Fig. 8. Comparison between the generalized and conventional model in terms of total velocity $u_T(t)$ (left) and oil recovery $RF(t)$ (right) plotted against time for the capillary-dominated case I. u_T is constant 0 since the process is purely counter-current. Oil recovery is delayed in the generalized model due to increased viscous fluid-fluid interaction.

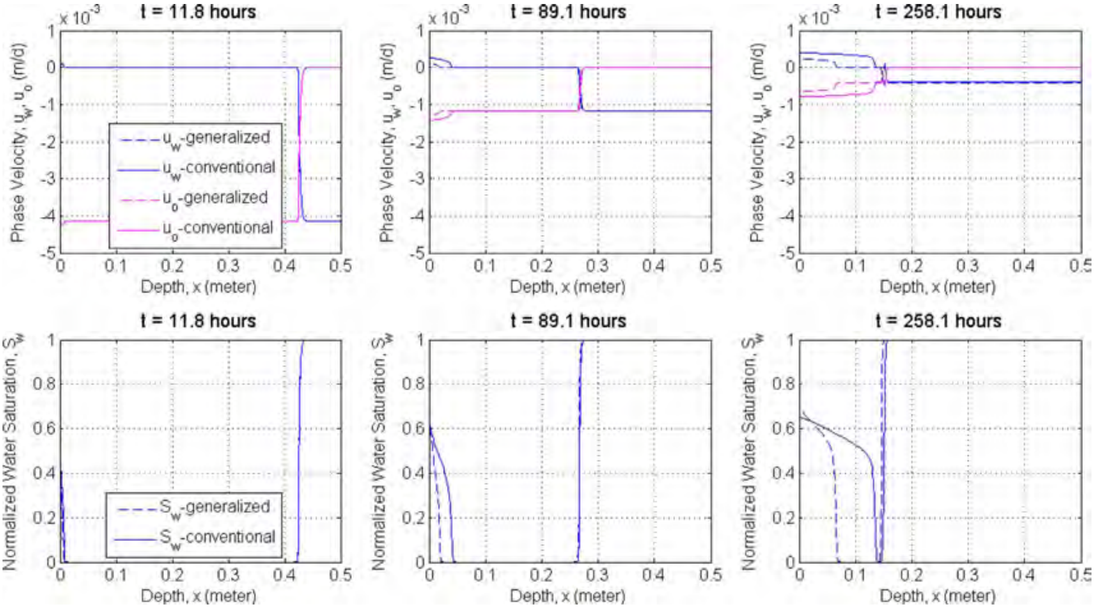

Fig. 9. Comparison between the generalized and conventional models for the gravity-dominated case II. Profiles of $u_w(x)$, $u_o(x)$ (top) and normalized water saturation $S_w(x)$ (bottom) are shown after 11.8, 89.1 and 258.1 h). Co-current flow upwards dominates the early phase, 89.1 h. Counter-current in the upper part of the block shows stronger effect in the later stage, 258.1 h.

between the two model saturation profiles increases as time elapses.

Fig. 8 shows the total Darcy velocity u_T from (3) and (23) and oil recovery from (40) plotted vs. time. The total velocity is zero throughout the process, indicative of counter-current flow. Recovery by spontaneous imbibition from a linear system follows a square root of time profile until significant boundary effects are encountered (Andersen et al., 2014). The generalized model displays a slower imbibition process than the conventional model with lower recovery than the conventional model at all times: At 90% recovery there is around 23 h delay in time between the models (55 vs 78 h) which means the time scale has increased by roughly 42%. The conventional model represents the ideal (but unrealistic) behavior of the reservoir in the sense that the co-current relative permeabilities do not account for the change in viscous coupling that reduce the phase velocities. Both models do however produce the same end recovery, which is given by the saturation where the capillary forces vanish, $P_c = 0$, corresponding to $S_w \approx 1$ as seen in Fig. 2 and $RF \approx 1$.

4.3.2. *Case II: Gravity-dominated system*

In this case we assume that capillary effects are ignored in the system and $P_c(s_w)$ is equal to 0 everywhere (including the boundary conditions). Thus, all terms related to capillary pressure are neglected both in the transport Eqs. (7) and (27) and the velocity Eqs. (3) and (23). This case is similar to the one studied in Section 4.2.2 except that water is now available to enter the block also at the top. This will give rise to interesting new behavior as water entering at the top will form a downward going water front. Striking differences will be seen between the upward going water front and the downward moving front that elucidate the role of viscous coupling effects.

Fig. 9 shows the profiles of water and oil Darcy velocities $u_w(x)$,

47

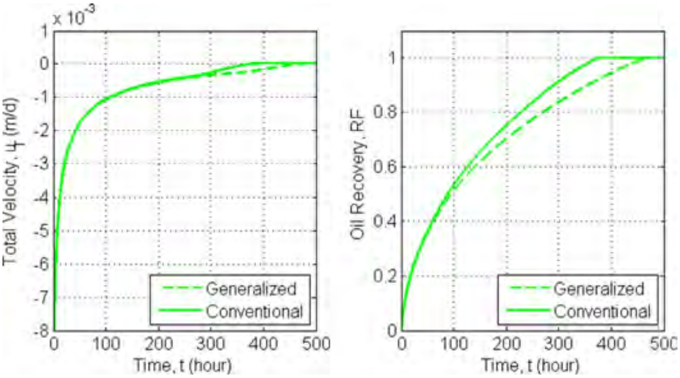

Fig. 10. Comparison between the generalized and conventional models in terms of total velocity $u_T(t)$ (left) and oil recovery factor RF (t) (right) plotted against time for the gravity-dominated case II. There is little difference between the models in terms of total velocity until after 260 h, while RF differs already after 60 h.

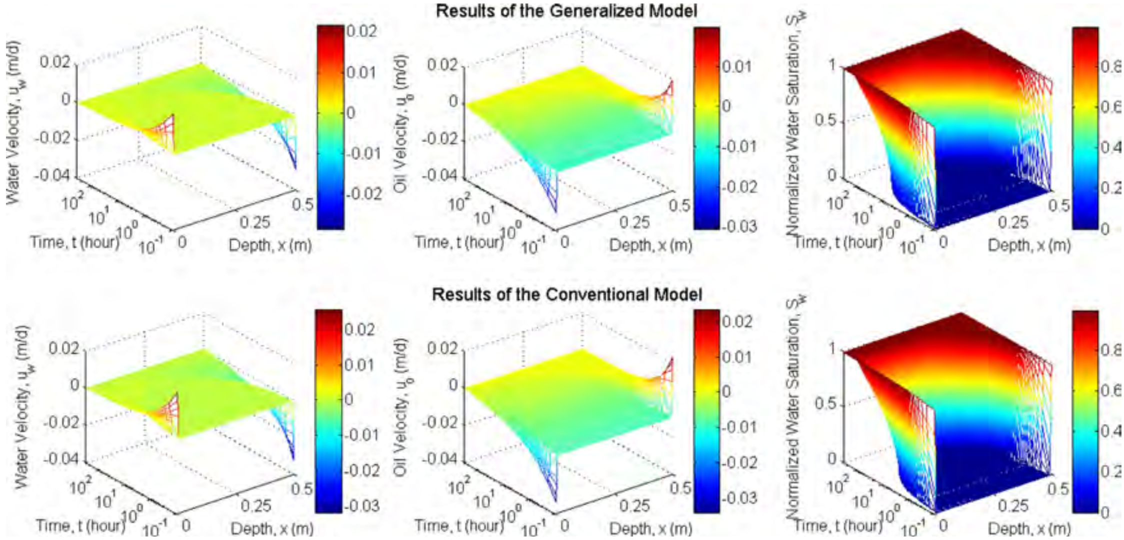

Fig. 11. Time and space plot of u_w, u_o and S_w for the generalized (top) and conventional (bottom) models in the combined case III. The phase velocities are not symmetric but stronger in the lower part of the block. Water imbibes more efficiently near the bottom. The difference between the generalized and the conventional model is not easily seen from these plot. We refer to Figs. 12 and 13 for plots that show this in more details.

$u_o(x)$ and normalized water saturation $S_w(x)$ at three given times: 11.8, 89.1 and 258.1 h (corresponding to 15%, 50% and 85% oil recovery in the conventional model). The system is no longer symmetric, rather one can see that the system is predominantly co-current: At 11.8 h we see that near the bottom, water has a large negative velocity (moves upwards) while oil has been displaced and has negligible flux there. In the upper part of the system mainly oil flows upwards, while water has a negligible flux. Dense water, slowly migrating from the top converges with the co-current water front travelling from the bottom of the block at 258.1 h, resulting in a more complex flow pattern. At this time the uppermost region ($0 < x < 0.15$ m in the conventional model and $0 < x < 0.07$ m in the generalized model) displays significant velocities for both phases in opposite directions, i.e. this region displays counter-current flow.

This advanced flow pattern is a combination of co- and counter-current flow initially dominated by co-current. It is thus seen that the conventional and generalized models produce almost equivalent profiles in the lower part of the block even after 258.1 h (85% recovery), while the counter-current wave travelling from the top results in significantly different behavior between the two models due to viscous coupling effects.

What is the precise explanation of the difference seen in the behavior at the top? This can be explained as follows: As noted for the case in Section 4.2.1, the behavior in the conventional model and the generalized is completely determined by the flux functions F_i for $i = con, gen$ (and their lower convex hull), as described and shown in Fig. 5. This explains the alikeness in the behavior at the bottom, see Section 4.2.2. However, at the top there is a decreasing jump formed. The Riemann problem for a decreasing jump is dictated by the *upper convex hull* of F_i which will be different for $F_{con}(s_w)$ and $F_{gen}(s_w)$. We refer to Fig 5 for illustrations. In particular, we see from the upper convex hull of $F_{gen}(s_w)$ that for the generalized model, a slowly moving front will be formed that jumps from $s_w = 0$ to approximately $s_w = 0.45$, followed by a rarefaction wave. The conventional model however will produce, according to the upper convex hull of $F_{con}(s_w)$, a fast moving front that jumps from $s_w = 0$ to approximately $s_w = 0.5$ followed by a

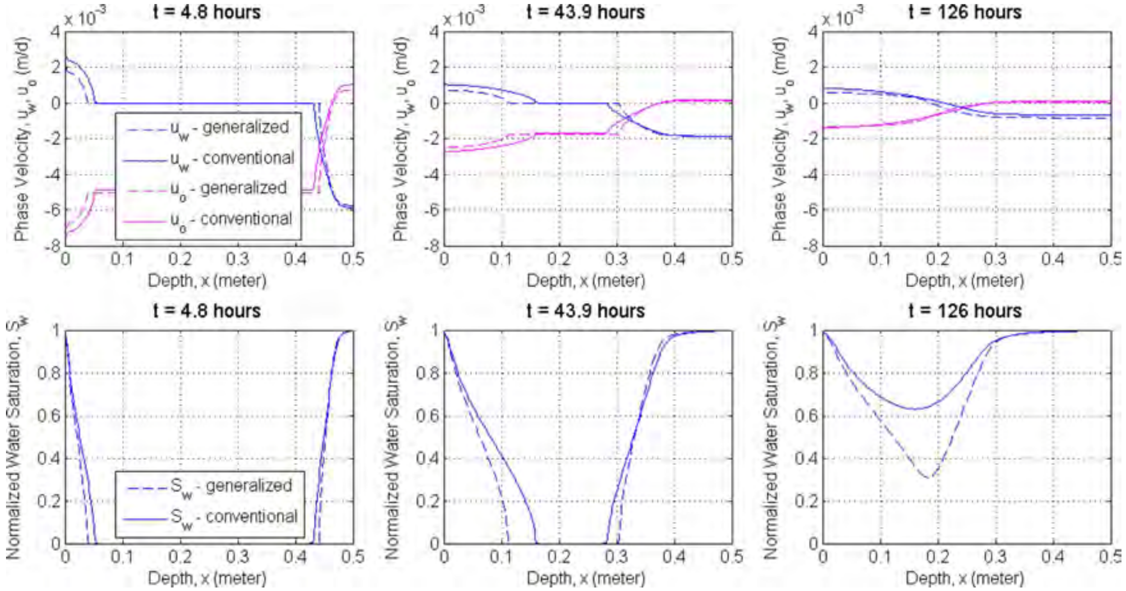

Fig. 12. Comparison between the generalized and conventional models for the combined case III. Profiles of $u_w(x)$, $u_o(x)$ (top) and normalized water saturation $S_w(x)$ (bottom) are shown after 4.8, 43.9 and 126 h. Counter-current flow is present mainly in the upper and lower parts of the block, while co-current flow dominates the central part.

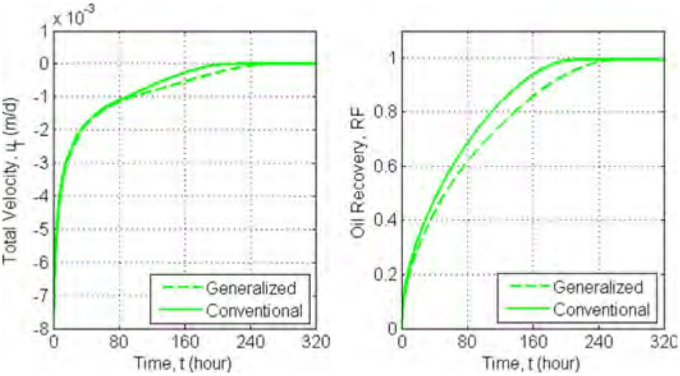

Fig. 13. Comparison between the generalized and conventional models in terms of total velocity $u_T(t)$ (left) and oil recovery $RF(t)$ (right) plotted against time for the combined case III. The models start to differ from the beginning. The differences increase with time which can be related to counter-current flow dominating a larger part of the system.

rarefaction wave.

Fig. 10 illustrates the total Darcy velocity, (3) and (23), and oil recovery (40) vs. time. All the mobile oil is recovered during the gravity drainage process such that $RF = 1$ in the end. The delay in oil recovery between the two models is significantly reduced compared to the previous example (Fig. 8). There is around 24.3% time delay when comparing the end states of the oil recovery processes (370 h for the conventional model and 460 h for the generalized model). Since the flow is mainly co-current, using the co-current relative permeabilities in the conventional model gives a better description of the system in this case with less deviation from the generalized model, compared to the counter-current case.

It is further worth noticing that the rate u_T displayed in Fig. 10 (left) does not show distinct model behavior until after 260 h, corresponding to the time when the co-current and counter-current waves in the conventional model meet, see Fig. 9. The recovery factor seen in Fig. 10 (right), on the other hand, differs visible already after 60 h which is due to the importance of counter-currently produced oil at this time.

4.3.3. Case III: Combined flow regimes

In this case we consider the situation with inclusion of both gravity and capillary terms, which will give rise to mixed co-current and counter-current driven flow, both in the conventional and generalized model. In order to clearly see this mixed effect we reduce the interfacial tension σ by five times since the magnitude of capillary pressure shown in Fig. 2 is much higher than the gravity force. Variations of water and oil Darcy velocities u_w, u_o, and normalized water saturation S_w in space and time (logarithmic) are shown in Fig. 11. The highest Darcy velocities are seen at the top and bottom faces of the block and the magnitudes are similar at the top and bottom although there are some differences. This can be explained by capillary forces being strong compared to gravity.

Fig. 12 shows the profiles of water and oil Darcy velocities $u_w(x)$, $u_o(x)$ and normalized water saturation $S_w(x)$ at the given times 4.8, 43.9 and 126 h (corresponding to RF = 15, 50 and 85% in the conventional model). Fig. 12 shows that there are strong phase velocities near the bottom and top of the block, decreasing towards the center. However, there is also a net co-current flow upwards due to gravity that also mobilizes the central oil (even before the imbibition front reaches the center) as seen in the central region.

The velocity profiles in Fig. 12 are not symmetric at 4.8 h and 43.9 h, but shifted towards more negative values (due to co-current flow upwards). It is thus seen that more water has entered the block from the bottom, although a significant imbibition front has also entered from the top. The generalized model velocities are lower in the outer regions where counter-current flow dominates. At 126 h the two models produce more asymmetric behavior at the upper part of the core and the two phases travel in opposite directions over a larger part of the core ($0 < x < 0.2$ m and $0.3 < x < 0.5$ m). Only the central region displays co-current flow (both u_w and u_o are negative, both phases travel upwards). At earlier times larger fractions of the block display co-current flow. In other words, it appears that counter-current flow becomes more dominant with time.

Comparing the saturation profiles in Fig. 12, especially after 43.9 h, it is seen that the water fronts travelling from the top behave more different between the conventional and generalized model compared to the front travelling from the bottom of the block. This can be attributed to the observation that gravity enhances counter-current flow at the top, while it counter-acts capillary diffusion and works to keep the phases separate at the bottom. For this reason the generalized model exhibits more delay compared to the conventional model at the top than it does at the bottom.

In similarity with the gravity-dominated case it appears thus that also here the main delay in recovery occurs at late times, see Fig. 13 (right). The overall delay is situated in magnitude between the two previously shown cases I and II.

5. Conclusions

This paper presents a model where momentum equations based on a general mixture theory replace Darcy's law in order to account for viscous coupling between the fluid phases and between fluid and rock. We carry out a systematic comparison of the generalized model and the conventional model (Darcy-based approach) for a specific flow case relevant for naturally fractured reservoirs. To parameterize the model realistically we match experimental data from Bourbiaux and Kalaydjian (1990) where co-current and counter-current data were able to distinguish such effects quantitatively. In the conventional model we directly apply co-current relative permeability curves, while in the generalized model relative permeability curves are a result of using more general momentum balance equations. The exact difference between the two models is manifested in the counter-current coefficient W expressed in $(26)_2$. The inclusion of the fluid-fluid interaction term R implies that the term W contains a modification that automatically accounts for counter-current effects not captured by the conventional model.

As a demonstration of the model, we consider gravity-aided spontaneous imbibition into a matrix block fully surrounded by water on all sides, representative of the conditions in a naturally fractured reservoir. The geometry was 1-D with flow along the vertical axis only. It should be noted that both initial state, boundary conditions and Bond number contribute to the flow regimes for different situations. The choice of having all open sides exposed to water allowed flow conditions where co- and counter-current flow regimes were naturally involved. Based on a systematic study of the model behavior we reach the following conclusions:

- Directly implementing co-currently measured relative permeability curves, as is standard, into reservoir simulation, may yield too optimistic results since viscous coupling can be enhanced at more general flow regimes.
- In the capillary-dominated case (all open faces exposed to water) the flow is mainly counter-current. This results in significant viscous coupling and increases the time scale of recovery.
- In the gravity-dominated case the flow is mainly co-current upwards (buoyancy) although some counter-current flow at the top (dense water sinking opposite way of light oil) produces viscous interaction also in this case. Directly applying co-currently measured relative permeabilities from the lab is a better assumption under such conditions (than for strongly counter-current flow), and the conventional and generalized models produced very similar behavior.
- Increasing the magnitude of capillary forces results in more counter-current flow and thus more viscous coupling. Larger differences were observed between the conventional and generalized models.
- Interestingly, the simulations indicate that the viscous coupling effects could become more significant with time in combined cases (where both gravity and capillary pressure forces are present) as counter-current flow dominates a larger portion of the core at late times.
- The generalized model apparently can automatically capture fluid-fluid interaction effects and better represent mobility functions for mixed flow regimes.

The usefulness and validity of the proposed model has been demonstrated in this work by matching experimental data with evident features of viscous coupling and by demonstrating the listed trends in fluid transport with flow regime. Previous works have demonstrated the model's ability to capture experimental non-standard trends in relative permeability functions with variations in viscosity ratio and flow direction (Standnes et al., 2017) and also the ability to improve scaling of counter-current spontaneous imbibition at conditions where viscous coupling should be more pronounced (Standnes and Andersen, 2017). The proposed model, equipped with generalized mobility functions, should however be further tested regarding its ability to capture different flow behavior (using one and the same parameter set) for more general cases and flow regimes. An interesting direction to explore could be to combine or compare the proposed generalized model with approaches like the Barenblatt model (where the saturation functions only gradually approach unique relations with saturation). Two natural questions in that context are:

- Which experimental features could be captured both by the Barenblatt model and our generalized model and what would be distinct? Obviously, both models would predict reduced mobility during spontaneous imbibition (a transient process) as compared to steady state measured relative permeability curves. The mechanisms are different though, as the Barenblatt model would display visible distinctions only during transient flow, while the generalized model is sensitive also to variations in steady state flow regimes (Standnes et al., 2017).
- What would be the effect of introducing the non-equilibrium effect of the Barenblatt approach in our generalized model? And how could this be distinguished from current mechanisms? One such feature could lie in the transient nature, more apparent in the Barenblatt model, while flow regime, and perhaps not so much time changes affects the generalized model.

Further, tortuosity (Cai et al., 2014) could be a relevant parameter to incorporate, as the actual travel length of the fluids should be more closely related to the overall momentum transfer and pressure drop for a given core sample, than the straight line path.

These questions and others, considered to be beyond the scope of the current manuscript, will be addressed in future work.

Acknowledgements

The 1st author thanks the Research Council of Norway for funding his PhD position at the University of Stavanger. The 2nd author acknowledges the Research Council of Norway and the industry partners;

ConocoPhillips Skandinavia AS, Aker BP, Eni Norge AS, Maersk Oil Norway AS, DONG Energy A/S, Denmark, Statoil Petroleum AS, ENGIE E&P NORGE AS, Lundin Norway AS, Halliburton AS, Schlumberger Norge AS, Wintershall Norge AS of The National IOR Centre of Norway for support. The 4th author thanks Statoil ASA for supporting the adjunct professor position at the University of Stavanger.

Appendix A. Mixture theory

In this section we give a general outline of mixture theory.

A.1. Continuity and momentum equations

For simplicity reason we consider a mixture of two phases $i = 1, 2$ and let θ_i, $\mathbf{v}_i$, and ρ_i denote volume fraction, velocity (intrinsic), and density of phase i. We assume incompressible fluids and that there is no source terms.

$$\partial_t \theta_i + \nabla\cdot(\theta_i \mathbf{v}_i) = 0, \qquad (i = 1, 2). \tag{47}$$

The intrinsic velocity, $\mathbf{v}_i$, is related to the superficial velocity (Darcy velocity), $\mathbf{u}_i$, by $\mathbf{u}_i = \theta_i \mathbf{v}_i$. The no-voids constraint implies that the volume fractions must sum to unity:

$$\theta_1 + \theta_2 = 1. \tag{48}$$

The dynamics of the phases at any point will be described using a flow model whereby the motion of each phase is in response to the stress within that phase and the pressures exerted by the other component phases. Neglecting inertial effects, including the momentum change caused by interchange of mass between the phases, the momentum balance equation for phase i is

$$\begin{aligned} \nabla\cdot(\theta_1 \boldsymbol{\Psi}_1) + \mathbf{f}_{12} + \mathbf{g}_1 &= 0, \\ \nabla\cdot(\theta_2 \boldsymbol{\Psi}_2) + \mathbf{f}_{21} + \mathbf{g}_2 &= 0, \end{aligned} \tag{49}$$

where $\boldsymbol{\Psi}_i$ refers to the macroscopic (averaged) stress tensor associated with phase i whereas the quantity $\mathbf{f}_{ij}$ denotes the interphase force which is exerted by the jth phase on the ith phase. Clearly, $\mathbf{f}_{ij} = -\mathbf{f}_{ji}$ by Newton's third law. Finally, $\mathbf{g}_i = \theta_i \rho_i \mathbf{g}$ refers to the external body force on phase i due to gravity and $\mathbf{g}$ refers to the gravity vector with the direction of gravitational pull and magnitude $g = 9.8$.

A.2. Interphase forces $\mathbf{f}_{ij}$

The interphase forces $\mathbf{f}_{ij}$ represent the forces acting at the interfaces between pairs of phases. Many works assume that a simplified approach can be used whereby these forces are expressed in terms of interphase pressure and drag force components. The following expression is postulated:

$$\begin{aligned} \mathbf{f}_{12} &= p_{12}\theta_2\nabla\theta_1 - p_{21}\theta_1\nabla\theta_2 + \beta_{12}\theta_1\theta_2(\mathbf{v}_2 - \mathbf{v}_1), \\ \mathbf{f}_{21} &= p_{21}\theta_1\nabla\theta_2 - p_{12}\theta_2\nabla\theta_1 + \beta_{21}\theta_1\theta_2(\mathbf{v}_1 - \mathbf{v}_2). \end{aligned} \tag{50}$$

We refer to Lemon et al. (2006) for more details regarding the interpretation of the different terms. Here we simply note that different relations have been proposed by various authors motivated by the special flow system under consideration. We see that if $\beta_{12} = \beta_{21}$ and $p_{12} = p_{21}$, then (50) simplifies to:

$$\begin{aligned} \mathbf{f}_{12} &= p_{12}\nabla\theta_1 + \beta_{12}\theta_1\theta_2(\mathbf{v}_2 - \mathbf{v}_1), \\ \mathbf{f}_{21} &= p_{21}\nabla\theta_2 + \beta_{21}\theta_1\theta_2(\mathbf{v}_1 - \mathbf{v}_2), \end{aligned} \tag{51}$$

in view of (48), and it follows that $\mathbf{f}_{12} = -\mathbf{f}_{21}$. Note that solid components like structural proteins that comprise the matrix in connective tissue in the context of tissue engineering or rock in the context of multiphase flow in a reservoir, can also naturally be included within this modeling framework. In this case the momentum balance (49) is not relevant since the velocity associated with this phase is zero if deformation of the matrix is ignored. However, the volume fraction of this solid phase must of course be taken into account as well as interaction force terms (the last term on the right-hand-side of (51)).

A.3. Constitutive relations

As described in Lemon et al. (2006), the partial stress tensor $\boldsymbol{\Psi}_i$ is decomposed into the following form:

$$\boldsymbol{\Psi}_i = -p_i\mathbf{I} + \boldsymbol{\Psi}_{i,d}, \qquad (i = 1, 2), \tag{52}$$

where p_i refers to the locally averaged (intraphase) pressure for phase i and $\boldsymbol{\Psi}_{i,\,d}$ is the deviatoric part of the partial stress tensor and $\mathbf{I}$ is the identity tensor. At the microscopic scale $\boldsymbol{\Psi}_{i,\,d}$ is related to the intrinsic velocity on a local scale; $\hat{\mathbf{v}}_i$. For viscous fluids:

$$\boldsymbol{\Psi}_{i,d} = \mu_i(\nabla\hat{\mathbf{v}}_i + \nabla\hat{\mathbf{v}}_i^T) + \kappa_i(\nabla\cdot\hat{\mathbf{v}}_i)\mathbf{I}, \qquad (i = 1, 2), \tag{53}$$

which includes both the effect of shear viscosity μ_i and bulk viscosity κ_i. On a macroscopic scale where velocities are averaged over a representative elementary volume (REV), i.e. giving the intrinsic average velocities $\mathbf{v}_i$, the form of the stress term must be more carefully evaluated. Several works account for the viscous stress term $\boldsymbol{\Psi}_{i,\,d}$ by directly implementing the average interstitial velocities $\mathbf{v}_i$ into (53), see Lemon et al. (2006); Schuff et al. (2013); Wu et al. (2017). On the other hand, when defining the partial stress of a fluid constituent, the viscous forces are also often neglected such that $\boldsymbol{\Psi}_{i,d} = 0$ in (52), see e.g. Ambrosi and Preziosi (2002); Lemon et al. (2006). For a porous media in which the fluid drag on the porous matrix dominates this may be a valid assumption. As mentioned in Rajagopal (2007) the underlying assumptions imply that the viscosity of the fluid and the roughness of the solid surface lead to far greater frictional resistance (and hence dissipation) at the porous boundaries of the solid in comparison to the frictional resistance (and hence the dissipation) in the fluid.

Note that the above modeling framework is general enough to also account for elastic deformation of, for example, the solid matrix components in a reservoir. Modeling of deformation of solid components like matrix constituents in a reservoir or tissue growth involving elastic constituents is significantly more complicated and implies that we cannot assume that $\mathbf{\Psi}_{i,d} = 0$ (Schuff et al., 2013). An interesting example of this can be found in Ambrosi and Preziosi (2009) which focuses on flow systems composed of cells (viscous fluid), extracellular matrix (solid constituent), and water (inviscid fluid) where also elastic deformation is taken into consideration. In the mathematical formulation this gives rise to a stress tensor $\mathbf{\Psi}_{i,\ d}$ where the extracellular matrix is treated as a compressible elastic body.

Remark A.1. An instructive overview is given in (Rajagopal, 2007) of how generalizations of the standard Darcy's law for single phase flow can be derived within the context of mixture theory. Starting with more general momentum balance equations and using different sets of assumptions leads to a hierarchy of mathematical models. In particular, it can be shown that popular models due to Brinkman, Biot and many others can be obtained via various approximations. For example, Brinkman's equation (see (54)) accounts for frictional effects in the fluid by using a partial stress tensor (53) where the first term is included. This may be relevant for porous media having large permeability and/or being dominated by a network of fractures. The resulting momentum balance equation then takes the following form for a fluid-matrix system:

$$\nabla p = -\alpha_0 \mathbf{v} + \rho \mathbf{b} + \mu \nabla \cdot \nabla \mathbf{v}, \tag{54}$$

where the quantities refer to the fluid phase, i.e. p is fluid pressure and $\mathbf{v}$ is pore velocity, ρ phase density and μ phase viscosity. $\mathbf{b}$ denotes external body forces (e.g. for gravity $\mathbf{b} = \mathbf{g}$), and α_0 the magnitude of the fluid-matrix drag force. The final term, involving second order derivatives of velocity, marks a clear distinction from Darcy's law for single phase flow.

Further extension of the viscous stress tensor is necessary in order to account for non-Newtonian fluid properties corresponding to shear-thickening or shear-thinning behavior (Rajagopal, 2007). We refer to the same work for more discussions related to weakly compressible fluids and small deformations and appropriate extensions of Darcy's equation.

Remark A.2. Water weakening effects and deformation of solid matrix constituents are currently subject to extensive experimental investigations Andersen et al. (2017b). Various creep tests are carried out to detect detailed mechanisms related to deformation of matrix in chalk reservoirs. However, this behavior cannot be separated from the flow of liquid phases which carry various chemicals that may react with the solid components and thereby have an impact of the deformation behavior. At the same time these fluids and their chemical components may also have an impact on the solid-fluid interaction terms as well as fluid-fluid interaction terms. The mixture theory formulation seems to offer a framework that is broad enough to allow for mathematical models that can bring together systematic studies of all these different aspects of multiphase flow in a reservoir.

Remark A.3. Development of models within the framework of mixture theory has found many applications within the study of multiphase flow in porous media relevant for life science (biomechanics), see for instance, (Ambrosi and Preziosi, 2002; Byrne and Preziosi, 2003; Preziosi and Farina, 2002). See also Evje (2017) for a recent work where a general compressible cell-fluid model, with interaction terms similar to (16) and (17), is proposed to explore cancer cell migration dynamics. For mathematical results related to compressible versions of two-fluid models that involve gravity driven segregation, see (Evje and Wen, 2015) and for models that discuss the role of capillary pressure and its stabilizing effect, we refer the interesting reader to (Evje et al., 2016; Evje and Wen, 2016) and references therein.

Appendix B. Discretization of the generalized model

Two dimensionless variables t_D and x_D are introduced in addition to the normalized saturation S_w (see (10)).

$$x_D = x/H, \qquad t_D = |u_T^0| t/(\phi H), \tag{55}$$

where u_T^0 is a reference velocity (taken as the initial total Darcy velocity). Skipping the notations 'w' for S_w and 'D' for x_D and t_D, the dimensionless form of (41), (42) and (43) becomes:

$$\begin{aligned}
\partial_t S &= -\partial_x\left(\frac{u_T f_w + W\Delta\rho g}{|u_T^0|(1 - s_{or} - s_{wr})}\right) - \partial_x\left(\frac{W}{|u_T^0| H(1 - s_{or} - s_{wr})}\partial_x P_c\right),\\
u_T &= -\frac{\hat{\lambda}_T}{H}\partial_x p_w - \frac{\hat{\lambda}_o}{H}\partial_x P_c + g(\hat{\lambda}_w \rho_w + \hat{\lambda}_o \rho_o),\\
u_w &= u_T f_w + W\Delta\rho g + \frac{W}{H}\partial_x P_c,\\
P_c &= \sigma\sqrt{\frac{\phi}{K}} J(S),
\end{aligned} \tag{56}$$

with conditions of

$$\begin{aligned}
S(x, t = 0) &= 0, &&\\
p_w(x = 0, t) &= 0, &\quad p_w(x = 1, t) &= \rho_w g H,\\
P_c(x = 0^-, t) &= 0, &\quad P_c(x = 1^+, t) &= -\Delta\rho g H.
\end{aligned} \tag{57}$$

Consider a discretization of spatial domain [0,1] into M cells and one more extra cell is added to the top and the bottom cells outside the block. This gives rise to grid points $\{x_j\}_{j=0}^{M+1}$ where x_j is located in the center of the cell $I_j = [x_{j-1/2}, x_{j+1/2}]$. The length of each cell is $\Delta x = x_{j+1/2} - x_{j-1/2}$. All cells are of equal length. We also consider a discretization of the time interval [0,T] into N steps (of the same length) represented by times $\{t^n\}_{n=1}^N$ where the length of each time step is $\Delta t = t^{n+1} - t^n$. In addition, the boundary conditions of capillary pressure are defined at the center of the boundary extra cells 0 and $M + 1$, which means that, $P_{c,\ T}$, S_T at x_0 and $P_{c,\ B}$, S_B at x_{M+1} are referred as the boundary conditions of capillary pressures and saturations at top and bottom of the block.

$$\begin{aligned}
P_{c,0} &= P_{c,T}, &\quad P_{c,M+1} &= P_{c,B},\\
S_0 &= S_T, &\quad S_{M+1} &= S_B.
\end{aligned} \tag{58}$$

Certainly, the boundary saturations should depend on the boundary capillary pressures:

$$S_T = P_c^{-1}(P_{c,T}), \qquad S_B = P_c^{-1}(P_{c,B}). \tag{59}$$

However, the boundary conditions of water pressure are set with the top water pressure $p_{w,\,T}$ at $x_{1/2}$ and the bottom water pressure $p_{w,\,B}$ at $x_{M+1/2}$.

$$p_{w,1/2} = p_{w,T}, \qquad p_{w,M+1/2} = p_{w,B}. \tag{60}$$

1) Calculate total velocity and pressure distributions of water/oil at current time step (t^n) with a discretization of Eq. $(56)_2$. There are M equations and M unknowns including u_T^n and $(p_w)_{j+1/2}^n$ ($j = 1,\ ...,M-1$), and a matrix solver can be used to solve these unknowns simultaneously (see below).

For $j = 1,\ ...,M$,

$$Hu_T^n + \widehat{\lambda}_T\frac{(p_w)_{j+1/2}^n - (p_w)_{j-1/2}^n}{\Delta x} = H[\widehat{\lambda}_o(S_j^n)\rho_o + \widehat{\lambda}_w(S_j^n)\rho_w]g - \widehat{\lambda}_o(S_j^n)\frac{(P_c)_{j+1/2}^n - (P_c)_{j-1/2}^n}{\Delta x} \tag{61}$$

where P_c can be further approximated by $(P_c)_{j+1/2}^n = \frac{P_c\left(S_j^n\right) + P_c\left(S_{j+1}^n\right)}{2}$ for $j = 1,\ ...,M-1$.

Importantly, one should notice the evaluation of the boundary conditions here, that is:

$$\begin{aligned}(p_w)_{1/2}^n &= p_w(x=0,\,t^n) = p_{w,T}, \quad (p_w)_{M+1/2}^n = p_w(x=1,\,t^n) = p_{w,B},\\ (P_c)_{1/2}^n &= P_c(x=0^+,\,t^n) = P_c(S_1^n), \quad (P_c)_{M+1/2}^n = P_c(x=1^-,\,t^n) = P_c(S_M^n).\end{aligned} \tag{62}$$

After solving p_w at the interface of neighbouring cells, water pressure at the center of each cell is approximated with:

$$(p_w)_j^n = \frac{(p_w)_{j-1/2}^n + (p_w)_{j+1/2}^n}{2}, \qquad (j = 1,...,M). \tag{63}$$

Then $(p_o)_j^n$ can be easily solved by $(p_o)_j^n = P_c(S_j^n) + (p_w)_j^n$.

2) The velocity of water is calculated by using Eq. $(56)_3$ where $\widehat{f}_w$ is approximated by using the upstream value based on the direction of total velocity u_T and the gravity segregation coefficient W needs to be evaluated locally.

$$(u_w)_j^n = u_T^n\widehat{f}_w(S_{j+1}^n) + W(S_j^n)\Delta\rho g + W(S_j^n)\cdot\frac{P_c(S_{j+1}^n) - P_c(S_{j-1}^n)}{2H\Delta x}, \qquad (j = 1,...,M). \tag{64}$$

The corresponding oil velocity is:

$$(u_o)_j^n = u_T^n - (u_w)_j^n, \qquad (j = 1,...,M). \tag{65}$$

3) Update the saturations at new time step. Simplify Eq. $(56)_1$ with the following form:

$$\partial_t(S) = -\partial_x\widehat{F} + \partial_x\widehat{D}, \tag{66}$$

with the advection term $\widehat{F}$ and the diffusion term $\widehat{D}$: $\widehat{F} = \frac{u_T f_w + W\Delta\rho g}{|u_T^0|\,(1 - s_{or} - s_{wr})}$, and $\widehat{D} = -\frac{W}{|u_T^0|H(1 - s_{or} - s_{wr})}\partial_x P_c$.

A discrete version of (66) with an explicit discretization in time then takes the form of:

$$\frac{S_j^{n+1} - S_j^n}{\Delta t} = -\frac{1}{\Delta x}(\widehat{F}_{j+1/2}^n - \widehat{F}_{j-1/2}^n) + \frac{1}{\Delta x}(\widehat{D}_{j+1/2}^n - \widehat{D}_{j-1/2}^n), \qquad (j = 1,...,M). \tag{67}$$

Since the derivative of $\widehat{F}^n$ can take both positive and negative values due to the gravity effect, the local Lax–Friedrichs scheme can be implemented to express the advection flux term, i.e. $\widehat{F}_{j+1/2}^n$:

$$\widehat{F}_{j+1/2}^n = \frac{1}{2}[\widehat{F}_j^n + \widehat{F}_{j+1}^n] - \frac{a_{j+1/2}^n}{2}[S_{j+1}^n - S_j^n], \qquad (j = 1,...,M-1). \tag{68}$$

where $\widehat{F}_j^n$ follows the same type of approximation as the one for updating water velocity, therefore

$$\widehat{F}_j^n = \frac{u_T^n\widehat{f}_w(S_{j+1}^n) + W(S_j^n)\Delta\rho g}{|u_T^0|(1 - s_{or} - s_{wr})}, \qquad (j = 1,...,M), \tag{69}$$

and the local parameter $a_{j+1/2}^n \geq 0$ is chosen such that

$$a_{j+1/2}^n = \frac{|\widehat{F}'(S_{j+1}^n)| + |\widehat{F}'(S_j^n)|}{2}. \tag{70}$$

For the boundary advection term, the physical flux is used as follows:

$$\widehat{F}_{1/2}^n = \frac{u_T^n\widehat{f}_w(S_1^n) + W\left(\frac{S_T + S_1^n}{2}\right)\Delta\rho g}{|u_T^0|(1 - s_{or} - s_{wr})}, \qquad \widehat{F}_{M+1/2}^n = \frac{u_T^n\widehat{f}_w(S_B) + W\left(\frac{S_M^n + S_B}{2}\right)\Delta\rho g}{|u_T^0|(1 - s_{or} - s_{wr})}. \tag{71}$$

In addition, stability condition for the advection term $\widehat{F}$ must also be satisfied:

$$a_{max}^n\frac{(\Delta t)^n}{\Delta x} \leq 1, \tag{72}$$

where

$$\max_S|(\widehat{F}^n(S))'| \leq a_{max}^n, \qquad S \in [0,\,1]. \tag{73}$$

Denote variable $d(S) = -\frac{W(S)}{|u_T^0|H(1 - s_{or} - s_{wr})}$ and the diffusion term $\widehat{D}$ can be expressed as follows:

$$\widehat{D}^n_{j+1/2} = d^n_{j+1/2}(\partial_x P_c)^n_{j+1/2} = \frac{d(S^n_{j+1}) + d(S^n_j)}{2}\cdot\frac{P_c(S^n_{j+1}) - P_c(S^n_j)}{\Delta x}, \qquad (j = 1, \dots, M-1). \tag{74}$$

Corresponding to the advection term, physical approximation of the diffusion coefficient $d(S)$ is implemented for the boundary diffusion terms:

$$\widehat{D}^n_{1/2} = d\left(\frac{S_T + S_1^n}{2}\right)\cdot\frac{P_c(S_1^n) - P_{c,T}}{\Delta x}, \qquad \widehat{D}^n_{M+1/2} = d\left(\frac{S_M^n + S_B}{2}\right)\cdot\frac{P_{c,B} - P_c(S_M^n)}{\Delta x}. \tag{75}$$

The stability condition for the diffusion term $\widehat{D}$ should also meet the requirement:

$$b\frac{\Delta t}{(\Delta x)^2} \le \frac{1}{2} \quad \text{and} \quad b = \max_S[d(S)P_c'(S)], \qquad S \in [0, 1]. \tag{76}$$

With the upper two stability conditions, a requirement of the time length Δt should satisfy that:

$$(\Delta t)^n \le \min\left\{\frac{\Delta x}{a^n_{max}}, \frac{(\Delta x)^2}{2b}\right\} \tag{77}$$

at the time step t^n.

4) Repeat step 1, 2 and 3 for the new time step t^{n+1}.

Appendix C. Numerical validation

Eclipse 100 was used to examine the validity of the numerical method. Direct comparison between Eclipse simulations and modeling results from the conventional model and the generalized model is shown in Fig. 14 in terms of recovery factor vs time. The Eclipse results are in excellent agreement with the conventional model (i.e. where co-current relative permeabilities are implemented to model flow regimes with varying extent of counter-current flows), while naturally there is significant difference with the results from the generalized model.

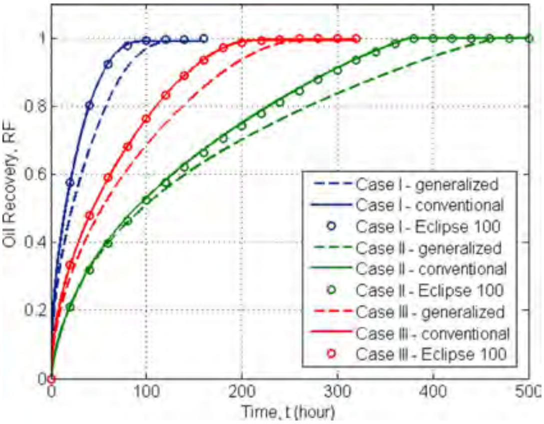

Fig. 14. Comparison between Eclipse 100, conventional and generalized models for Case I, II and III in terms of recovery factor vs time.

References

Ambrosi, D., Preziosi, L., 2002. On the closure of mass balance models for tumor growth. Math. Models Methods Appl. Sci. 12 (5), 737–754. http://dx.doi.org/10.1142/S0218202502001878.

Ambrosi, D., Preziosi, L., 2009. Cell adhesion mechanisms and stress relaxation in the mechanics of tumours. Biomech. Model Mechanobiol. 8, 397–413.

Andersen, P.Ø., Evje, S., Hiorth, A., 2017. Modeling of spontaneous-imbibition experiments with porous disk - on the validity of exponential prediction. SPE J. 22 (5), 1326–1337. http://dx.doi.org/10.2118/186094-PA, SPE-186094-PA.

Andersen, P.Ø., Evje, S., Kleppe, H., 2014. A model for spontaneous imbibition as a mechanism for oil recovery in fractured reservoirs. Transp. Porous Media 101 (2), 299–331. http://dx.doi.org/10.1007/s11242-013-0246-7.

Andersen, P.Ø., Wang, W., Madland, M.V., Zimmermann, U., Korsnes, R.I., Bertolino, S.R.A., Minde, M., Schulz, B., Gilbricht, S., 2017. Comparative study of five outcrop chalks flooded at reservoir conditions: chemo-mechanical behaviour and profiles of compositional alteration. Transp. Porous Media, In press. http://dx.doi.org/10.1007/s11242-017-0953-6.

Avraam, D.G., Payatakes, A.C., 1995. Flow regimes and relative permeabilities during steady-state two-phase flow in porous media. J. Fluid Mech. 293, 207–236.

Avraam, D.G., Payatakes, A.C., 1995. Generalized relative permeability coefficients during steady-state two-phase flow in porous media, and correlation with the flow mechanisms. Transp. Porous Media 20 (1–2), 135–168.

Ayodele, O.R., 2006. Theoretical analysis of viscous coupling in two-phase flow through porous media. Transp. Porous Media 64 (2), 171–184. http://dx.doi.org/10.1007/s11242-005-2809-8.

Babchin, A., Yuan, J., Nasr, T., 2006. Generalized phase mobilities in gravity drainage processes. In: 49th Annual Technical Meeting of the Petroleum Society of Canada, Calgary, Alberta, Canada, June 8–10. http://dx.doi.org/10.2118/98-09, PETSOC-98-09.

Bacri, J.C., Chaouche, M., Salin, D., 1990. Modele simple de permeabilities croisees. C.R. Acad. Sci. 311, 591–596. Series II.

Barenblatt, G.I., Vinnichenko, A.P., 1980. Non-equilibrium seepage of immiscible fluids. Adv. Mech. 3, 35–50.

Bear, J., 1988. Dynamics of Fluids in Porous Media. Dover Books on Physics and Chemistry, New York, USA.

Bentsen, R.G., Manai, A.A., 1992. Measurement of concurrent and countercurrent relative permeability curves using the steady-state method. AOSTRA J. Res. 7, 169–181.

Bentsen, R.G., Manai, A.A., 1993. On the use of conventional cocurrent and counter-current effective permeabilities to estimate the four generalized permeability coefficients which arise in coupled, two-phase flow. Transp. Porous Media 11, 243–262.

Bourbiaux, B.J., Kalaydjian, F.J., 1990. Experimental study of cocurrent and counter-current flows in natural porous media. SPE Reservoir Eng. 5 (3), 361–368. http://dx.doi.org/10.2118/18283-PA.

Bowen, R.M., 1976. Theory of Mixtures. In: Eringen, A.C. (Ed.), Continuum Physics.

Academic, New York.

Bowen, R.M., 1980. Incompressible porous media model by use of the theory of mixtures. Int. J. Eng. Sci. 18 (9), 1129–1148.

Byrne, H.M., Preziosi, L., 2003. Modelling solid tumour growth using the theory of mixtures. Math. Med. Biol. 20 (4), 341–366.

Cai, J., Perfect, E., Cheng, C., Hu, X., 2014. Generalized modeling of spontaneous imbibition based on hagen-poiseuille flow in tortuous capillaries with variably shaped apertures. Langmuir 30, 5142–5151.

de la Cruz, V., Spanos, T.J.T., 1983. Mobilization of oil ganglia. AIChE J. 29 (5), 854–858.

Darcy, H., 1856. Les Fontaines Publiques de La Ville de Dijon, Dalmont, paris.

Drew, D.A., Passman, S.L., 1999. Theory of Multicomponent Fluids. Springer.

Dullien, F.A.L., Dong, M., 1996. Experimental determination of the flow transport coefficients in the coupled equations of two-phase flow in porous media. Transp. Porous Media 25, 97–120.

Ehrlich, R., 1993. Viscous coupling in two-phase flow in porous media and its effect on relative permeabilities. Transp. Porous Media 11 (3), 201–218.

Evje, S., 2017. An integrative multiphase model for cancer cell migration under influence of physical cues from the microenvironment. Chem. Eng. Sci. 165, 240–259.

Evje, S., Wang, W., Wen, H.Y., 2016. Global well-posedness and decay rates of strong solutions to a non-conservative compressible two-fluid model. Arch. Ration. Mech. Anal. 221 (3), 1285–1316.

Evje, S., Wen, H.Y., 2015. Analysis of a compressible two-fluid stokes system with constant viscosity. J. Math. Fluid Mech. 17 (3), 423–436.

Evje, S., Wen, H.Y., 2016. Stability of a compressible two-fluid hyperbolic-elliptic system arising in fluid mechanics. Nonlinear Anal. Real World Appl. 31, 610–629.

Hassanizadeh, S.M., Gray, W.G., 1993. Toward an improved description of the physics of two-phase flow. Adv. Water. Resour. 16, 53–67.

Juanes, R., 2008. Nonequilibrium effects in models of three-phase flow in porous media. Adv. Wat. Res. 31, 661–673.

Kalaydjian, F., 1987. A macroscopic description of multiphase flow in porous media involving spacetime evolution of fluid/fluid interface. Transp. Porous Media 2, 537–552.

Kalaydjian, F., 1990. Origin and quantification of coupling between relative permeabilities for two-phase flows in porous media. Transp. Porous Media 5 (3), 215–229.

Langaas, K., Papatzacos, P., 2001. Numerical investigations of the steady state relative permeability of a simplified porous medium. Transp. Porous Media 45, 241–266.

Le Veque, R., 2002. Finite Volume Methods for Hyperbolic Problems. In: Cambridge Texts in Applied Mathematics. Cambridge University Press.

Lemon, G., King, J.R., Byrne, H.M., Jensen, O.E., Shakesheff, K.M., 2006. Mathematical modelling of engineered tissue growth using a multiphase porous flow mixture theory. J. Math. Biol. 52, 571–594.

Li, H., Pan, C., Miller, C.T., 2004. Viscous coupling effects for two-phase flow in porous media. Dev. Water Sci. 55 (Part 1), 247–256.

Li, H., Pan, C., Miller, C.T., 2005. Pore-scale investigation of viscous coupling effects for two-phase flow in porous media. Phys. Rev. E, 72.

Mason, G., Morrow, N.R., 2013. Developments in spontaneous imbibition and possibilities for future work. J. Petrol. Sci. Eng. 110, 268–293. http://dx.doi.org/10.1016/j.petrol.2013.08.018.

Muskat, M., Wyckoff, R.D., Botset, H.G., Meres, M.M., 2013. Flow of gas-liquid mixtures through sands. SPE Trans. AIME 123 (1), 69–96. http://dx.doi.org/10.2118/937069-G.

Odeh, A.S., 2013. Effect of viscosity ratio on relative permeability. J. Petrol. Technol. 11, 346–354.

du Prey, L., 1973. Factors affecting liquid-liquid relative permeabilities of a consolidated porous medium. SPE J. 13 (1), 39–47.

Preziosi, L., Farina, A., 2002. On darcy's law for growing porous media. Int. J. Non Linear Mech. 37, 485–491.

Rajagopal, K.R., 2007. On a hierarchy of approximate models for flows of incompressible fluids through porous solids. Math. Mod. Met. Appl. Sci. 17, 215–252.

Rajagopal, K.R., Tao, L., 1995. Mechanics of Mixtures. In: Series on Advances in Mathematics for Applied Sciences. 35 World Scientific. 1995

Rose, W., 2000. Myths about later-day extensions of darcy's law. J. Petrol. Sci. Eng. 26, 187–198.

Schuff, M.M., Gore, J.P., Nauman, E.A., 2013. A mixture theory model of fluid and solute transport in the microvasculature of normal and malignant tissues. i. theory. J. Math. Biol. 66, 1179–1207.

Sherafati, M., Jessen, K., 2017. Dynamic relative permeability and simulation of WAG injection processes. Transp. Porous Media 117, 125–147. http://dx.doi.org/10.1007/s11242-017-0825-0.

Silin, D., Patzek, T., 2004. On barenblatts model of spontaneous countercurrent imbibition. Transp. Porous Media 54, 297–322.

Standnes, D.C., Andersen, P.O., 2017. Analysis of the impact of fluid viscosities on the rate of countercurrent spontaneous imbibition. Energy Fuels 31 (7), 6928–6940. http://dx.doi.org/10.1021/acs.energyfuels.7b00863.

Standnes, D.C., Evje, S., Andersen, P.O., 2017. A novel relative permeability model based on mixture theory approach accounting for solid-fluid and fluid-fluid interactions. Transp. Porous Media 119, 707–738. http://dx.doi.org/10.1007/s11242-017-0907-z.

Wu, W., Aubry, N., Antaki, J.F., Massoudi, M., 2017. Flow of a fluid-solid mixture: normal stress differences and slip boundary condition. Int. J. Non Linear Mech. 90, 39–49. http://dx.doi.org/10.1016/j.ijnonlinmec.2017.01.004.

Yuster, S.T., 1951. Theoretical considerations of multiphase flow in idealized capillary systems. World Petroleum Cong. Proc., Section II, The Hague. pp. 437–445.

Paper II

Cocurrent Spontaneous Imbibition in Porous Media with the Dynamics of Viscous Coupling and Capillary Backpressure

By:
Andersen, Pål Østebø
Qiao, Yangyang
Standnes, Dag Chun
Evje, Steinar

Printed in:
SPE Journal, 24: 158-177 (2019).

Paper III

Compressible and Viscous Two-phase Flow in Porous Media Based on Mixture Theory Formulation

By:
Qiao, Yangyang
Wen, Huanyao
Evje, Steinar

Printed in:
Networks and Heterogeneous Media, 14 (3): 489-536 (2019).

NETWORKS AND HETEROGENEOUS MEDIA
©American Institute of Mathematical Sciences
Volume **14**, Number **3**, September **2019**
doi:10.3934/nhm.2019020
pp. **489–536**

COMPRESSIBLE AND VISCOUS TWO-PHASE FLOW IN POROUS MEDIA BASED ON MIXTURE THEORY FORMULATION

Yangyang Qiao
Department of Energy and Petroleum Engineering, University of Stavanger
Stavanger, NO-4068, Norway

Huanyao Wen
School of Mathematics, South China University of Technology
Guangzhou, 510641, China

Steinar Evje*
Department of Energy and Petroleum Engineering, University of Stavanger
Stavanger, NO-4068, Norway

(Communicated by Paola Goatin)

Abstract. The purpose of this work is to carry out investigations of a generalized two-phase model for porous media flow. The momentum balance equations account for fluid-rock resistance forces as well as fluid-fluid drag force effects, in addition, to internal viscosity through a Brinkmann type viscous term. We carry out detailed investigations of a one-dimensional version of the general model. Various a priori estimates are derived that give rise to an existence result. More precisely, we rely on the energy method and use compressibility in combination with the structure of the viscous term to obtain H^1-estimates as well upper and lower uniform bounds of mass variables. These a priori estimates imply existence of solutions in a suitable functional space for a global time $T > 0$. We also derive discrete schemes both for the incompressible and compressible case to explore the role of the viscosity term (Brinkmann type) as well as the incompressible versus the compressible case. We demonstrate similarities and differences between a formulation that is based, respectively, on interstitial velocity and Darcy velocity in the viscous term. The investigations may suggest that interstitial velocity seems more natural to use in the formulation of momentum balance than Darcy velocity.

1. **Introduction.** The importance of multiphase flow in porous media has long been recognized in many fields. Mathematical modelling of multiphase flow is essential in practical applications like enhanced oil recovery and geological CO_2 storage in depleted oil and gas reservoirs [25, 42] as well as biological processes [29, 14, 18, 39, 40, 37]. Traditional formulations of multiphase flow describe macroscopic fluid fluxes with a straightforward extension, first proposed by Muskat [30, 3],

---

2010 *Mathematics Subject Classification.* 65M06, 76T10, 76N10.

Key words and phrases. Darcy's equation, mixture theory, two-phase flow, Brinkman's equation, viscous coupling, compressible flow, incompressible flow, Navier-Stokes.

Wen was supported by the National Natural Science Foundation of China (Grant No. 11671150, 11722104) and by GDUPS (2016).

* Corresponding author: Steinar Evje.

of Darcy's equation for single-phase flow. Unlike in the single-phase case, this extension cannot be rigorously obtained from first principles [22, 23]. The multiphase extension of Darcy's equation may be described as a quasi-linear relation, because the fluid flux depends linearly on the "driving force", which includes viscous, capillary, and gravity forces, and all the nonlinearity is agglutinated in the relative permeability and capillary pressure functions [25]. An instructive overview is given in [32] of how generalizations of the standard Darcy's law for single phase flow can be derived within the context of mixture theory. Starting with more general momentum balance equations and using different sets of assumptions leads to a hierarchy of mathematical models. In particular, it can be shown that popular models due to Brinkman, Biot and many others can be obtained via various approximations. Interesting extensions of the classical multiphase formulation are also discussed by Wu [42].

1.1. A compressible and viscous two-fluid model for porous media flow.

The model we are interested in describes flow of two compressible immiscible fluids, e.g., water (w), oil (o), or gas (g), moving in a porous media and takes the following form (we use "w" and "o" in the following as index):

$$\begin{aligned}
(\phi n)_t + \nabla\cdot(\phi n\mathbf{u}_o) &= Q_o, \qquad n = s_o\rho_o\\
(\phi m)_t + \nabla\cdot(\phi m\mathbf{u}_w) &= Q_w, \qquad m = s_w\rho_w\\
s_o\nabla P_o + n\mathbf{g} &= -\hat{k}_o\mathbf{u}_o + \hat{k}_{ow}(\mathbf{u}_w-\mathbf{u}_o) + \varepsilon_o\nabla\cdot(n\nabla\mathbf{u}_o)\\
s_w\nabla P_w + m\mathbf{g} &= -\hat{k}_w\mathbf{u}_w - \hat{k}_{ow}(\mathbf{u}_w-\mathbf{u}_o) + \varepsilon_w\nabla\cdot(m\nabla\mathbf{u}_w)
\end{aligned} \tag{1.1}$$

with capillary pressure P_c defined as the difference between the non-wetting fluid (oil) pressure P_o and wetting fluid (water) pressure P_w

$$P_c = P_o - P_w = P_c(s_w), \qquad P_c'(s_w) < 0. \tag{1.2}$$

Herein, ϕ is the porosity of the medium, ρ_i represents density and s_i the volume fraction (saturation) where $i = w, o$. In addition, we have the fundamental relation that expresses that the water and oil occupy the pore space

$$s_o + s_w = 1. \tag{1.3}$$

Furthermore, $\varepsilon_w, \varepsilon_o$ (assumed to be constant) characterize the magnitude of the viscous terms. The model can be derived (or at least motivated) from general mixture theory [11, 32] where we study a continuum composed of matrix occupying a volume fraction $(1-\phi)$ and a pore space of volume ϕ that is filled with a mixture of water and oil represented, respectively, by ϕs_w and ϕs_o such that $(1-\phi)+\phi s_w+\phi s_o = 1$. The matrix is stagnant whereas the two fluids move with (locally) averaged interstitial velocities $\mathbf{u}_w$ and $\mathbf{u}_o$. We refer to the recent work [31] for more details leading to (1.1). See also [1, 29, 34] and references therein for interesting examples of similar models developed in the mixture theory framework.

Note that the viscous terms $\varepsilon_o\nabla\cdot(n\nabla\mathbf{u}_o)$ and $\varepsilon_w\nabla\cdot(m\nabla\mathbf{u}_w)$ (Brinkman type of term) included in $(1.1)_{3,4}$ involve a mass dependent coefficient whose magnitude is governed by the parameter ε_i. This reflects that we have introduced kinematic viscosity ε that is related to dynamic viscosity μ by $\varepsilon\rho = \mu$ for single-phase flow of a fluid with density ρ [28]. Combined with the two-phase momentum balance for water and oil this gives rise to mass dependent viscosity coefficients of the form $\varepsilon_o n$ and $\varepsilon_w m$. We refer to [14] (and references) therein for more details. More generally, we may think of $\varepsilon_o n$ and $\varepsilon_w m$ as "effective" viscosities since the model (1.1) must be understood as the result of a volume averaging process where variables have been obtained through averaging over a small representative volume element, implying that detailed information about complex interfaces between the two phases have been lost and are represented only in an averaged sense [11, 32]. Some authors also denote this viscosity as the "Brinkman viscosity" whereas the viscosity associated with the rock-fluid friction term $\hat{k}_i$ $(i = o, w)$ is denoted the "Darcy viscosity" [27]. This issue is also discussed in [38] where it is observed by means of an up-scaling procedure based on volume averaging methods, that the use of a slip boundary condition gives rise to an effective viscosity different from the one corresponding to the fluid phase.

In the following we will focus on nonlinear coupling mechanisms and we therefore assume physical parameters like porosity ϕ, absolute permeability K, Darcy viscosity μ_i (will be introduced later), and Brinkman viscosity ε_i to be constant. Generally, $\hat{k}_o$, $\hat{k}_w$, and $\hat{k}_{ow}$ depend on the fluid composition through s_i and ρ_i.

1.1.1. *Closure relations.* The above model must be endowed with appropriate closure relations for densities $\rho_i = \rho_i(P_i)$. The two phases will be treated as weakly compressible fluids. More precisely, we represent the water and the oil by linear pressure-density relations of the form

$$\rho_w - \tilde{\rho}_{w0} = \frac{P_w}{C_w}, \qquad \rho_o - \tilde{\rho}_{o0} = \frac{P_o}{C_o}, \tag{1.4}$$

where C_w and C_o reflect the compressibility of water and oil, respectively. An essential role is played by the interaction coefficients $\hat{k}_{ow}$, $\hat{k}_w$, and $\hat{k}_o$. We will come back with more details about the choice of these. In addition, a functional form of the capillary pressure $P_c(s_w)$ must also be specified. Combining (1.2), (1.3), and (1.4) it follows that $\rho_w = \rho_w(m, n)$ and $\rho_o = \rho(m, n)$ are well-defined as functions of m and n for $m, n \geq 0$, from which we also can compute $s_w = s_w(m, n)$ and $s_o = s_o(m, n)$, see (2.17)-(2.21) for details.

1.1.2. *Initial and boundary conditions.* Boundary conditions are prescribed as no-flux conditions:

$$\mathbf{u}_i \cdot \nu = 0, \qquad x \in \partial\Omega, \quad t > 0, \qquad i = w, o \tag{1.5}$$

where ν is the outward normal on $\partial\Omega$. The corresponding initial data is

$$n(x, t = 0) = n_0(x), \qquad m(x, t = 0) = m_0(x), \qquad x \in \Omega. \tag{1.6}$$

1.2. **The model (1.1) as a generalization of Darcy's equation based formulation.** We may ignore the effects from the viscous terms in $(1.1)_{3,4}$ by setting $\varepsilon_o = \varepsilon_w = 0$. In addition, we neglect the fluid-fluid interaction effect by setting $\hat{k}_{ow} = 0$, combined with the assumption that fluid-pore resistance force coefficient $\hat{k}_i$ takes the form

$$\hat{k}_i \overset{\text{def}}{:=} s_i^2 \phi \frac{\mu_i}{K k_{ri}}, \qquad i = w, o \tag{1.7}$$

where K is the absolute permeability (assumed here to be a scalar, i.e., we assume a homogeneous media), k_{ri} is relative permeability, and μ_i viscosity. This gives from $(1.1)_{3,4}$ the following reduced momentum equations

$$\mathbf{U}_i \overset{\text{def}}{:=} \phi s_i \mathbf{u}_i = -K\frac{k_{ri}}{\mu_i}(\nabla P_i + \rho_i \mathbf{g}) = -\lambda_i(\nabla P_i + \rho_i \mathbf{g}), \qquad \lambda_i := K\frac{k_{ri}}{\mu_i}, \tag{1.8}$$

for $i = w, o$ which is nothing but the classical Darcy law where $\mathbf{U}_i$ is the Darcy velocity. When combined with $(1.1)_{1,2}$ we arrive at the classical two-phase formulation [42]. The model (1.1) involves two main extensions from classical formulation based on two-phase Darcy's equation, as elaborated upon in the following:

- The interaction forces on the RHS of $(1.1)_{3,4}$ involve a fluid-fluid drag force effect $\hat{k}_{ow}(\mathbf{u}_w - \mathbf{u}_o)$ in addition to fluid-rock drag force $-\hat{k}_o\mathbf{u}_o$ and $-\hat{k}_w\mathbf{u}_w$. The only interaction force in Darcy's equation is the latter one representing friction between fluid and boundaries of the pores [32]. Moreover, while the drag force depends on the velocity, it is by no means necessary that it in general depends linearly on the relative velocity. See for example [42] for extensions that include nonlinear dependence on fluid velocity (Forchheimer). Moreover, it has been observed that inclusion of the fluid-fluid interaction term $\hat{k}_{ow}(\mathbf{u}_w - \mathbf{u}_o)$ can give improvements over standard Darcy's equation based formulation for water-oil flow in porous media. We refer to [35, 31] for a first discussion of this in the context of core scale modelling and generalized permeability functions and [36] for a discussion of this generalized two-phase flow in the context of imbibition (i.e., capillary pressure driven counter-current flow).
- The viscous terms $\varepsilon_o\nabla\cdot(n\nabla\mathbf{u}_o)$ and $\varepsilon_w\nabla\cdot(m\nabla\mathbf{u}_w)$ in $(1.1)_{3,4}$ can account for frictional forces within the fluid due to its viscosity. Ignoring these terms essentially imply that the viscosity of the fluid and the roughness of the solid surface lead to far greater frictional resistance (and hence dissipation) at the porous boundaries of the solid in comparison to the frictional resistance in the fluid [32]. Note that $(1.1)_{3,4}$ can naturally be interpreted as a two-phase version of Brinkman's equation. Brinkman's equation amounts to using a momentum balance equation that takes the following form for a fluid-matrix system [32]:
$$\nabla p + \rho\mathbf{g} = -\alpha_0\mathbf{u} + \mu\nabla\cdot(\nabla\mathbf{u}), \tag{1.9}$$
where the quantities refer to the fluid phase, i.e., p is fluid pressure and $\mathbf{u}$ is pore velocity, ρ phase density and μ phase viscosity. $\mathbf{g}$ denotes the external gravity force and α_0 the magnitude of the fluid-matrix drag force. The final term, involving second order derivatives of velocity, marks a clear distinction from Darcy's law for single phase flow. This may be relevant for porous media having large permeability and/or being dominated by a network of fractures [27].

Some more precise remarks seem useful in order to set the model (1.1) into a broader context.

Remark 1.1. We may replace the viscous term in $(1.1)_{3,4}$ that accounts for the fluid viscous shear effects that oppose the flow through the porous structure by a more general term
$$\nabla\cdot(\varepsilon_{i,\text{eff}}\nabla\mathbf{u}_i),$$
where the effective viscosity coefficient $\varepsilon_{i,\text{eff}}$ depends on other variables than the mass. We refer to [38] for a discussion of this, both from theoretical and numerical investigations. For example, from physical considerations and experimental investigations it seems clear that it could depend on pressure [32]. It is concluded that it might be reasonable to include dependence on pressure both in modelling of fluid-pore friction force as well as frictional effects within the fluid itself [32]. More generally, one should also account for the possibility that the flow may not be

steady implying that one should add a term $\rho \mathbf{u}_t$ to (1.9) in the single-phase case or $(\phi s_i \rho_i \mathbf{u}_i)_t$ in the more general two-phase model (1.1). Moreover, nonlinear inertial effects in the fluid cannot be ignored if the flow is not sufficiently slow.

Remark 1.2. An interesting study of a two-phase Brinkman type of model is found in [9]. A two-phase formulation based on Darcy's equations of the following form is studied with $s = s_w$

$$\begin{aligned} s_t + \nabla \cdot (\mathbf{U}_w) = 0, \qquad & \mathbf{U}_w = f(s)\mathbf{U}_T = -\lambda_w(s)\nabla P \\ \nabla \cdot \mathbf{U}_T = 0 & \\ \mathbf{U}_T = -\lambda_T(s)\nabla P, & \end{aligned} \tag{1.10}$$

where $\phi \equiv 1$, $P_w = P_o = P$ (zero capillary pressure), $\lambda_T(s) = \lambda_w(s) + \lambda_o(s)$ is total mobility and $f(s) = \lambda_w(s)/\lambda_T(s)$ is the fractional flow function for water phase. $\mathbf{U}_T$ is the total Darcy velocity $\mathbf{U}_T = \mathbf{U}_w + \mathbf{U}_o$. The following two-phase version of Brinkman's equation based on Darcy's velocity $\mathbf{U}_i$ is proposed as a generalization of Darcy's equation:

$$-\mu \Delta \mathbf{U}_i + \mathbf{U}_i = -\lambda_i \nabla P, \qquad i = w, o. \tag{1.11}$$

Summing the two momentum equations in (1.11) gives rise to a Brinkman type of momentum equation for the mixture of the two phases expressed in terms of the total Darcy velocity $\mathbf{U}_T = \mathbf{U}_w + \mathbf{U}_o$:

$$-\mu \Delta \mathbf{U}_T + \mathbf{U}_T = -\lambda_T(s)\nabla P. \tag{1.12}$$

Taking the divergence of (1.12) gives in light of the total mass balance equation $(1.10)_2$ the following Brinkman based approximation of (1.10)

$$\begin{aligned} s_t + \nabla \cdot (\mathbf{U}_w) = 0, \qquad & \mathbf{U}_w = f(s)\mathbf{U}_T \\ -\nabla \cdot (\lambda_T(s)\nabla P) = 0 & \\ -\mu \Delta \mathbf{U}_w + \mathbf{U}_w = -\lambda_w(s)\nabla P, \qquad & \lambda_w(s) = f(s)\lambda_T(s). \end{aligned} \tag{1.13}$$

In [9] a notion of weak solutions to the Brinkman model (1.13) is introduced and convergence of an iterative approximation as well as full numerical scheme is demonstrated. Numerical experiments show that the numerical approximation is quite sensitive to the choice of μ and creates oscillatory behavior. Interestingly, numerical experiments also indicate that this solution may not converge to the solution of the model (1.10) corresponding to $\mu = 0$.

Remark 1.3. In the literature there seems to be an ongoing interesting discussion of various formulations of two-phase versions of porous media flow based on Brinkman's equation. See for example the work [41] for a discussion of this. Traditionally, the superficial phase velocity (Darcy velocity) $\mathbf{U}_i$ has been used in two-phase versions of Brinkman's equation similar to (1.11). In [41] it is argued that the most natural choice, at least for the flow system they consider with creeping flow inside moving permeable particles, is to use interstitial (intrinsic) phase velocity $\mathbf{u}_i$ in the macroscopic equations. Their conclusion is based on numerical computations and comparison of the model based on, respectively, phase velocity $\mathbf{U}_i = s_i \mathbf{u}_i$ and interstitial phase velocity $\mathbf{u}_i$.

1.3. **Purpose of this work and brief review of related works.** The aim of this paper is three-fold: (i) Present an example of stability analysis motivated by the study of compressible Navier-Stokes equation (and different from traditional two-phase porous media stability analysis) which exploits the structure of the viscous term in the momentum balance and accounts for compressibility; (ii) Present an example of a numerical scheme both for the compressible and incompressible version of (1.1) in a one-dimensional setting and demonstrate similarities and differences through some specific simulations; (iii) Gain some insight into the impact the viscosity terms have on the solution.

We end this section by giving a brief review of other works on the two-phase porous media model based on Darcy's law. Most works focus on the incompressible, immiscible two-phase flow case. For example, [2] studied the existence of weak solutions for the incompressible two-phase model in fractured porous media based on a dual-porosity formulation. Regularity and stability results were obtained in [8] when analysing a coupled system involving a saturation and a global pressure. In [6, 5] the authors showed existence of a solution for an incompressible two-phase flow within a heterogeneous porous medium made of two rock types. Considering dynamic capillary pressure [24] for the incompressible two-phase flow in porous media, [7] proved the existence of a weak solution to a degenerate elliptic parabolic system whereas in [13, 12] existence conditions for the traveling wave solution were derived. In particular, non-monotone weak solutions for the Buckley-Leverett equation were obtained. Interesting contributions have also been made concerning the compressible immiscible two-phase flow in porous media where phase densities are assumed to depend on their own pressure. Without using the feature of global pressure, Khalil and Saad [26] established an existence result for a three-dimensional model. In addition, the implicit finite volume scheme was studied in [33] to obtain convergence to a weak solution.

2. **Stability analysis and existence of solution in the one-dimensional setting.** The purpose of this section is to derive a priori estimates of the solution of (1.1). The approach is quite different from the approach used for the incompressible model and formulation based on Darcy velocity $\mathbf{U}_i$ where the first step is to derive estimate for pressure [9]. It is also different from mathematical analysis of compressible two-phase models that are based on global pressure [19, 20, 21]. We rely on the energy method where we first derive an energy-type of estimate. In addition, the special structure of the viscous terms allows one to obtain estimate of m, n in H^1 along the lines of the Bresch-Desjardin method [4] for a two-phase Navier-Stokes model. For analysis of related models we refer the interesting reader to [15, 16, 17, 18], and references therein. In the following we consider the 1D version of (1.1) where source terms have been set such that water is injected and possibly produced whereas oil is produced only, i.e., $Q_o = -nQ_p$ whereas $Q_w = -mQ_p + \rho_w Q_I$ for constant Q_p, Q_I. The model takes the following form with (n, m, u_w, u_o) as the main variables

$$\begin{aligned}
(n)_t + (nu_o)_x &= -nQ_p, \qquad\qquad n = s_o\rho_o\\
(m)_t + (mu_w)_x &= -mQ_p + \rho_w Q_I, \qquad m = s_w\rho_w\\
s_o(P_o)_x &= -\hat{k}_o u_o + \hat{k}(u_w - u_o) + ng + \varepsilon_o(nu_{ox})_x,\\
s_w(P_w)_x &= -\hat{k}_w u_w - \hat{k}(u_w - u_o) + mg + \varepsilon_w(mu_{wx})_x,\\
P_c &= P_o - P_w = P_c(s_w),
\end{aligned} \tag{2.14}$$

subject to the boundary condition

$$u_w(x = 0, t) = u_o(x = 0, t) = 0$$

$$u_w(x=1,t) = u_o(x=1,t) = 0, \qquad t>0 \tag{2.15}$$

and initial condition

$$n(x,t=0) = n_0(x), \qquad m(x,t=0) = m_0(x), \qquad x \in [0,1]. \tag{2.16}$$

Note that the gravity constant g can take both signs depending on the orientation of the x-coordinate axis. Above we assume that positive direction of x-axis points downward and $g>0$. We also use the notation $\hat{k} = \hat{k}_{ow}$ in (2.14), for simplicity reason only.

Definition of $(\rho_o, \rho_w, s_o, s_w)$. Let us first see how we can obtain ρ_w and ρ_o as a function of masses m and n. We focus on the situation where $m, n > 0$. The cases where $m=0$ or $n=0$ are treated separately. We rewrite $s_o + s_w = 1$ as

$$m\rho_o + n\rho_w = \rho_w \rho_o \qquad (\text{i.e. } \rho_o = \frac{n\rho_w}{\rho_w - m}). \tag{2.17}$$

On the other hand, from (1.2) we have

$$P_c(s_w) = P_o - P_w = C_o\rho_o - C_w\rho_w + C_w\tilde{\rho}_{w0} - C_o\tilde{\rho}_{o0}. \tag{2.18}$$

Combining (2.18) with (2.17), we get

$$P_o - P_w - P_c(s_w) = C_o(\frac{n\rho_w}{\rho_w - m}) - C_w\rho_w + C_w\tilde{\rho}_{w0} - C_o\tilde{\rho}_{o0} - P_c(\frac{m}{\rho_w}) \overset{\text{def}}{:=} F(\rho_w; m, n), \tag{2.19}$$

where we have introduced the function $F(\rho_w; m, n)$ where m, n are thought of as parameters. Clearly, for any choice of $m, n > 0$, we want to verify that $F(u; m, n)$ (where we use u as the main variable) has a unique zero point which we denote as $\rho_w(m, n)$. Let us check some basic properties of $F(u; m, n)$ as a function of u.

By the definition of m, it is natural to look for ρ_w which belongs to $(m, +\infty)$. Moreover, from (2.19) we observe that (i) $F(u \to m^+; m, n) = +\infty$; (ii) $F(u \to +\infty; m, n) = -\infty$. Next, we check monotonicity properties of $F(u; m, n)$ as a function of u.

$$F'_u(u; m, n) = C_o \frac{-mn}{(u-m)^2} - C_w + P'_c(\frac{m}{u})(\frac{m}{u^2}). \tag{2.20}$$

Since $F'_u(u, m, n) < 0$ in $(m, +\infty)$ for any given $m, n > 0$, and $F : (m, +\infty) \mapsto (-\infty, +\infty)$ as observed above, it follows (from the intermediate value theorem) that there is a unique $\rho_w = \rho_w(m, n) \in (m, +\infty)$ such that $F(\rho_w; m, n) = 0$. In addition, since $F'_u(\rho_w; m, n) \neq 0$, it concludes that the function ρ_w is differentiable with respect to m or n (from the implicit function theorem). Furthermore, ρ_o, s_o, and s_w are then obtained as follows:

$$\rho_o(m,n) = \frac{n\rho_w}{\rho_w - m}, \qquad s_w = \frac{m}{\rho_w}, \qquad s_o = 1 - \frac{m}{\rho_w} = \frac{n}{\rho_o}. \tag{2.21}$$

For the limit case when $m = 0$, there are two options: (i) $s_w = 0$, which implies that $\rho_o = n$ and ρ_w is found from (2.18); (ii) $s_w > 0$, which implies that $\rho_w = 0$ and where ρ_o is found from (2.18). Similarly, we can compute ρ_w and ρ_o for the case $n = 0$.

Notation. We first give some notation.

- $L^p = L^p([0,1])$ for $p \in [1, \infty]$
- We define

$$\tilde{m}(t) = \int_0^1 m(x,t)\,dx; \qquad \tilde{n}(t) = \int_0^1 n(x,t)\,dx. \tag{2.22}$$

Assumptions. The following assumptions are made:

- Capillary pressure $P_c(s_w)$:
  We assume that for $\Phi(s_w)$ such that $\Phi'(s_w) = P_c(s_w)$, the following property holds:
  $$\Phi(s_w) \leq P_c(\tilde{s}_w)s_w, \qquad 0 \leq s_w \leq 1 \tag{2.23}$$
  where $\tilde{s}_w = s_w(\tilde{m}, \tilde{n})$ and $\tilde{m}$ and $\tilde{n}$ refer to the total masses given by (2.22), which are constant due to Remark 2.1. Moreover, we assume that
  $$\sup_{s_w\in(0,1)} |P_c(s_w)| < \infty, \qquad \inf_{s_w\in(0,1)} [-P_c'(s_w)] \geq 0 \tag{2.24}$$
  and that
  $$C_w\tilde{\rho}_{w0} - C_o\tilde{\rho}_{o0} - \sup_{s_w\in(0,1)} P_c(s_w) \geq 0. \tag{2.25}$$
  Note that these constraints on the capillary pressure $P_c(s_w)$ are all mild and physical reasonable conditions.
- Source terms in $(2.14)_{1,2}$ are ignored by setting $Q_p = 0 = Q_I$.
- Interaction term $\hat{k}_w$, $\hat{k}_o$, and $\hat{k}$ are set as follows:
  $$\hat{k}_w = I_w\frac{m^2}{m+n}, \qquad \hat{k}_o = I_o\frac{n^2}{m+n}, \qquad \hat{k} = I_{wo}\frac{mn}{m+n}. \tag{2.26}$$

Remark 2.1. Clearly, in view of $(2.14)_{1,2}$, the condition (2.15), and assumption $Q_p = Q_I = 0$, it follows from (2.22) that

$$\tilde{m}(t) = \int_0^1 m_0(x)\,dx = \tilde{m}_0, \qquad \tilde{n}(t) = \int_0^1 n_0(x)\,dx = \tilde{n}_0 \tag{2.27}$$

where $\tilde{m}_0, \tilde{n}_0$ are constant.

Remark 2.2. As far as the condition on capillary pressure $P_c(s_w)$ as given by (2.23) is concerned, we may observe that this appears to be a weak structural constraint. Consider for example a capillary pressure curve of the form $P_c(s_w) = -P_c^* \ln(\delta + \frac{s_w}{a})$, for some $\delta, a > 0$ as a typical example of a physical relevant function. Clearly, from the relation $\Phi'(s_w) = P_c(s_w)$ we can introduce two positive constants C_1 and C_2 to be determined such that

$$\begin{aligned}\Phi(s_w) &= -P_c^* \int_0^{s_w} \ln(\frac{x}{a} + \delta)dx - C_1 - C_2\\ &= -P_c^* a \int_\delta^{s_w/a+\delta} \ln(u)du - C_1 - C_2 = P_c^* a(u - u\ln(u))\Big|_\delta^{s_w/a+\delta} - C_1 - C_2\\ &= P_c^* s_w + P_c^* a\Big[\delta\ln(\delta) - (s_w/a+\delta)\ln(s_w/a+\delta)\Big] - C_1 - C_2.\end{aligned} \tag{2.28}$$

Since $x\ln(x)$ is an increasing function for $x \geq e^{-1}$ whereas for $x \in [0, e^{-1})$ decreases from zero for $x = 0$ and takes a minimum $-e^{-1}$, it is clear that we can secure that

$$P_c^* a\Big[\delta\ln(\delta) - (s_w/a+\delta)\ln(s_w/a+\delta)\Big] - C_1 \leq 0, \qquad s_w \in [0,1]$$

for an appropriate choice of C_1 such that we conclude from (2.28) that

$$\Phi(s_w) \leq P_c^* s_w - C_2.$$

What remains to show then is that

$$P_c^* s_w - C_2 \leq P_c(\tilde{s}_w)s_w, \qquad 0 \leq s_w \leq 1.$$

Clearly, $(P_c^* - P_c(\tilde{s}_w))s_w \leq C_2$ for an appropriate choice of the constant $C_2 = C_2(P_c^*, \tilde{s}_w)$ since $s_w \in [0,1]$.

2.1. **Main results.** First, we present a local (in time) existence result whose proof is presented in Appendix A. Then, we state an (almost) global in time existence result which relies on the local existence result combined with certain a priori estimates, see (2.29). Section 2.2 is devoted to these estimates.

Theorem 2.1. *(Local existence) Assume that* $m_0 \in H^1$*,* $n_0 \in H^1$ *and* $\inf\limits_{x\in[0,1]} n_0 > 0$*,* $\inf\limits_{x\in[0,1]} m_0 > 0$*, and that*

$$\begin{cases} \frac{I_{wo}k_1}{\varepsilon_w k_0} + \frac{I_{wo}k_1}{\varepsilon_o k_0} \leq \frac{1}{4}, \\ \max\left\{\frac{I_{wo}k_1}{k_0\varepsilon_o} + E_{\varepsilon_o,1}, \frac{I_{wo}k_1}{k_0\varepsilon_w} + E_{\varepsilon_w,1}\right\} \leq \frac{1}{2}, \end{cases}$$

where I_{wo} *refers to the coefficient in* (2.26)*,* $k_0 = \min\left\{\frac{\inf n_0}{e}, \frac{\inf m_0}{e}\right\}$ *and* $k_1 = \max\left\{e\sup m_0, e\sup n_0\right\}$*, and*

$$\begin{cases} E_{\varepsilon_w,1} = \frac{1}{\varepsilon_w}\left[\frac{10C}{(k_0)^2}(1+\frac{10C}{k_0})\frac{I_{wo}k_1}{2k_0} + \frac{10I_wI_{wo}k_1}{\varepsilon_w k_0} + \frac{20I_wI_{wo}k_1}{\varepsilon_w k_0} + \frac{20I_wI_{wo}k_1}{\varepsilon_w k_0}\right], \\ E_{\varepsilon_o,1} = \frac{1}{\varepsilon_o}\left[\frac{10C}{(k_0)^2}(1+\frac{10C}{k_0})\frac{I_{wo}k_1}{2k_0} + \frac{20(I_{wo})^2k_1}{\varepsilon_o k_0} + \frac{10I_oI_{wo}k_1}{\varepsilon_o k_0} + \frac{20(I_{wo})^2k_1}{\varepsilon_o k_0}\right], \end{cases}$$

where I_w, I_o *are coefficients given by* (2.26) *and* C *is a positive constant depending on* k_0*,*k_1 *and some other known data but independent of* ε_o *and* ε_w *(see Step 2 in Appendix A for more details). Then there exists a positive constant* T_0*, such that the system (2.14) with initial-boundary conditions (2.15) and (2.16) has a unique solution* (m,n,u_w,u_o) *on* $[0,1]\times[0,T_0]$ *in the sense that*

$$\begin{aligned} &(m,n) \in C([0,T_0];H^1)\cap C^1([0,T_0];L^2), \ (u_w,u_o) \in C([0,T_0];H^2\cap H_0^1), \\ &\inf m > 0, \inf n > 0. \end{aligned}$$

Now we are in the position to state our second result on the almost global existence.

Theorem 2.2. *(Almost global existence) In addition to the assumptions of Theorem 2.1, for any given* $T > 0$*, if* $K_1 < \min\left\{\varepsilon_w\tilde{m}, \varepsilon_o\tilde{n}\right\}$*, then the system (2.14) with initial-boundary conditions (2.15) and (2.16) has a unique solution* (m,n,u_w,u_o) *on* $[0,1]\times[0,T]$ *in the sense that*

$$(m,n) \in C([0,T];H^1)\cap C^1([0,T];L^2), \ (u_w,u_o) \in C([0,T];H^2\cap H_0^1),$$

where K_1 *is given by (2.45).*

Moreover, we have the following estimates:

$$\int_0^1 \left[(s_w)_x^2 + (s_o)_x^2 + (\rho_w)_x^2 + (\rho_o)_x^2\right] dx \leq C(T),$$

$$\int_0^1 \left[(s_w)_t^2 + (s_o)_t^2 + (\rho_w)_t^2 + (\rho_o)_t^2\right] dx \leq C(T),$$

for any $t \in [0,T]$.

Remark 2.3. The constraint $K_1 < \min\Big\{\varepsilon_w\tilde m, \varepsilon_o\tilde n\Big\}$ where K_1 is given by (2.45), implies smallness of initial data combined with assumption about sufficiently large viscosity ε_w and ε_o. More precisely, from the definition of K_1 for a fixed $T > 0$ we may choose m_0 and n_0 such that $K_1 \le 2[g^2(\tilde m + \tilde n)T + K_0]\exp(T)$ where $\varepsilon_w, \varepsilon_o$ are chosen sufficiently large to ensure that
(i) $\bar a \max\{\frac{1}{\varepsilon_w}, \frac{1}{\varepsilon_o}\} \le 1$; (ii) $2[g^2(\tilde m + \tilde n)T + K_0]\exp(T) < \min\Big\{\varepsilon_w\tilde m, \varepsilon_o\tilde n\Big\}$. Note that this constraint is only used to get the positive lower bound of m and n. See Corollary 2.3 for more details. Hence, the obtained estimates cannot be used to investigate the limit when $\varepsilon_w, \varepsilon_o \to 0$.

2.2. **Proof of Theorem 2.2.** Equipped with Theorem 2.1, we are going to prove Theorem 2.2. More precisely, let T^* denote the maximum time for the existence of solutions as in Theorem 2.1[1]. Then Theorem 2.1 implies that $T^* > 0$. To prove the almost global existence, it suffices to show that T^* is larger than the given T which can be taken as large as possible. For otherwise, i.e., $T^* \le T$, it will lead to a contradiction based on the following estimates uniformly for t, i.e.,

$$\begin{cases} \|(m, n, s_w, s_o, \rho_w, \rho_o)(t)\|_{H^1} + \|(u_w, u_o)(t)\|_{H^2} \le C(T), \\ \big\|\big(m_t, n_t, (s_w)_t, (s_o)_t, (\rho_w)_t, (\rho_o)_t\big)(t)\big\|_{L^2} \le C(T), \\ \inf\limits_{(x,t)\in Q_{T^*}} m(x,t) > 0, \quad \inf\limits_{(x,t)\in Q_{T^*}} n(x,t) > 0, \end{cases} \tag{2.29}$$

for any $t \in [0, T^*)$, where $Q_{T^*} = [0,1] \times [0, T^*)$. In fact, (2.29) implies that T^* is not the maximum time for the existence which is the desired contradiction.

To get (2.29), we need the following lemmas. To simplify the proof, we let $C(T)$ denote a generic positive constant depending on the initial data and T. Moreover, for any given $T > 0$, $C(T) < \infty$. We let $t < T^* \le T$ throughout the rest of this section, i.e., in Lemma 2.2–Corollary 2.5. Note that $C(T) \ge C(T^*)$ and $K_1 = K_1(T) \ge K_1(T^*)$ in Lemma 2.2.

(a) Energy estimate.

Lemma 2.1. *For any $t \in [0, T^*)$, it holds that*

$$\begin{aligned} E(t) &+ \int_0^t\int_0^1 (\varepsilon_w m u_{wx}^2 + \varepsilon_o n u_{ox}^2)\,dxdt \\ &+ \int_0^t\int_0^1 \hat k(u_w - u_o)^2\,dxdt + \int_0^t\int_0^1 \hat k_w u_w^2\,dxdt + \int_0^t\int_0^1 \hat k_o u_o^2\,dxdt = E(0), \end{aligned} \tag{2.30}$$

where $E(t)$ is given by

$$\begin{aligned} E(t) =& C_w\int_0^1 m\int_{\tilde\rho_w}^{\rho_w}\frac{s - \tilde\rho_w}{s^2}\,ds\,dx + C_o\int_0^1 n\int_{\tilde\rho_o}^{\rho_o}\frac{s - \tilde\rho_o}{s^2}\,ds\,dx \\ &+ \int_0^1\Big[P_c(\tilde s_w)s_w - \Phi(s_w)\Big]\,dx + \int_0^1\int_0^x g(n+m)\,dy\,dx, \end{aligned} \tag{2.31}$$

where $\tilde\rho_w = \rho_w(\tilde m, \tilde n), \tilde\rho_o = \rho_o(\tilde m, \tilde n)$, and $\tilde s_w = s_w(\tilde m, \tilde n)$.

---

[1] It means that the solution exists on $[0, T^*)$ but not on $[0, T^*]$.

Proof. From the two momentum equations of (2.14)$_{3,4}$ we get after a multiplication, respectively, by u_o and u_w, followed by integration over $[0,1]$, integration by parts and use of (2.15)

$$\begin{aligned}\int_0^1 (\varepsilon_w m u_{wx}^2 + \varepsilon_o n u_{ox}^2)\,dx + \int_0^1 \hat{k}(u_w - u_o)^2\,dx + \int_0^1 \hat{k}_w u_w^2\,dx + \int_0^1 \hat{k}_o u_o^2\,dx \\ = (\int_0^1 n g u_o\,dx + \int_0^1 m g u_w\,dx) - \int_0^1 (s_o P_{ox} u_o + s_w P_{wx} u_w)\,dx := I_0 + I_1.\end{aligned} \tag{2.32}$$

For I_0, integrating the two mass equations (2.14)$_{1,2}$ on $(0,x)$ for any given $x \in (0,1)$, and using the boundary condition, we have

$$\begin{cases} \dfrac{d}{dt}\displaystyle\int_0^x n(y,t)\,dy = -n u_o(x,t), \\ \dfrac{d}{dt}\displaystyle\int_0^x m(y,t)\,dy = -m u_w(x,t). \end{cases}$$

Thus we have

$$I_0 = -\frac{d}{dt}\int_0^1 \int_0^x g(n+m)\,dy\,dx. \tag{2.33}$$

As to I_1, we observe that by using (1.4) and (2.14)$_{1,2}$ we can compute as follows

$$\begin{aligned}\int_0^1 s_o u_o P_{ox}\,dx &= C_o \int_0^1 s_o u_o (\rho_o)_x\,dx = C_o \int_0^1 n u_o (\ln(\rho_o))_x\,dx \\ &= -C_o \int_0^1 (n u_o)_x \ln(\rho_o)\,dx = C_o \int_0^1 n_t \ln(\rho_o)\,dx \\ &= C_o \frac{d}{dt}\int_0^1 n \ln(\rho_o)\,dx - C_o \int_0^1 s_o (\rho_o)_t\,dx \\ &= C_o \frac{d}{dt}\int_0^1 n \ln(\rho_o)\,dx - C_o \frac{d}{dt}\int_0^1 n\,dx + C_o \int_0^1 (s_o)_t \rho_o\,dx \\ &= C_o \frac{d}{dt}\int_0^1 n \ln(\rho_o)\,dx + \int_0^1 (s_o)_t P_o\,dx + C_o \tilde{\rho}_{o0} \int_0^1 (s_o)_t\,dx,\end{aligned} \tag{2.34}$$

and, by similar calculations

$$\begin{aligned}\int_0^1 s_w u_w P_{wx}\,dx &= C_w \int_0^1 s_w u_w (\rho_w)_x\,dx = C_w \int_0^1 m u_w (\ln(\rho_w))_x\,dx \\ &= -C_w \int_0^1 (m u_w)_x \ln(\rho_w)\,dx = C_w \int_0^1 m_t \ln(\rho_w)\,dx \\ &= C_w \frac{d}{dt}\int_0^1 m \ln(\rho_w)\,dx - C_w \int_0^1 s_w (\rho_w)_t\,dx \\ &= C_w \frac{d}{dt}\int_0^1 m \ln(\rho_w)\,dx - C_w \frac{d}{dt}\int_0^1 m\,dx + C_w \int_0^1 (s_w)_t \rho_w\,dx \\ &= C_w \frac{d}{dt}\int_0^1 m \ln(\rho_w)\,dx + \int_0^1 (s_w)_t P_w\,dx + C_w \tilde{\rho}_{w0} \int_0^1 (s_w)_t\,dx.\end{aligned} \tag{2.35}$$

Note that here we have also used (2.27). Consequently, using that $P_w = P_o - P_c$ and (1.3), we find from summing (2.34) and (2.35)

$$\begin{aligned} -I_1 = C_o \frac{d}{dt}\int_0^1 n\ln(\rho_o)\,dx + C_w \frac{d}{dt}\int_0^1 m\ln(\rho_w)\,dx - \int_0^1 s_{wt}P_c(s_w)\,dx \\ + C_o\tilde{\rho}_{o0}\frac{d}{dt}\int_0^1 s_o\,dx + C_w\tilde{\rho}_{w0}\frac{d}{dt}\int_0^1 s_w\,dx. \end{aligned}$$

That is,

$$\begin{aligned} -I_1 = C_o \frac{d}{dt}\int_0^1 n\ln(\rho_o)\,dx + C_w \frac{d}{dt}\int_0^1 m\ln(\rho_w)\,dx - \int_0^1 \Phi(s_w)_t\,dx \\ + C_o\tilde{\rho}_{o0}\frac{d}{dt}\int_0^1 s_o\,dx + C_w\tilde{\rho}_{w0}\frac{d}{dt}\int_0^1 s_w\,dx, \qquad \Phi'(s_w) = P_c(s_w). \end{aligned}$$

Moreover, we see that

$$\begin{aligned} \int_0^1 m\int_{\tilde{\rho}_w}^{\rho_w} \frac{s-\tilde{\rho}_w}{s^2}\,ds\,dx &= \int_0^1 m\Big[\ln(s) + \frac{\tilde{\rho}_w}{s}\Big]\Big|_{\tilde{\rho}_w}^{\rho_w}\,dx \\ &= \int_0^1 m\Big[\ln(\rho_w) - \ln(\tilde{\rho}_w) + \frac{\tilde{\rho}_w}{\rho_w} - \frac{\tilde{\rho}_w}{\tilde{\rho}_w}\Big]\,dx \\ &= \int_0^1 m\ln(\rho_w)\,dx - \ln(\tilde{\rho}_w)\int_0^1 m\,dx + \tilde{\rho}_w\int_0^1 s_w\,dx - \int_0^1 m\,dx, \end{aligned} \tag{2.36}$$

for some reference density $\tilde{\rho}_w > 0$. Hence, again by using (2.27)

$$C_w\frac{d}{dt}\int_0^1 m\ln(\rho_w)\,dx = C_w\frac{d}{dt}\int_0^1 m\int_{\tilde{\rho}_w}^{\rho_w}\frac{s-\tilde{\rho}_w}{s^2}\,ds\,dx - C_w\tilde{\rho}_w\frac{d}{dt}\int_0^1 s_w\,dx \tag{2.37}$$

and

$$C_o\frac{d}{dt}\int_0^1 n\ln(\rho_o)\,dx = C_o\frac{d}{dt}\int_0^1 n\int_{\tilde{\rho}_o}^{\rho_o}\frac{s-\tilde{\rho}_o}{s^2}\,ds\,dx - C_o\tilde{\rho}_o\frac{d}{dt}\int_0^1 s_o\,dx. \tag{2.38}$$

Thus, it follows that

$$\begin{aligned} &-I_1 + \frac{d}{dt}\int_0^1 \Phi(s_w)\,dx \\ &= C_o\frac{d}{dt}\int_0^1 n\ln(\rho_o)\,dx + C_w\frac{d}{dt}\int_0^1 m\ln(\rho_w)\,dx \\ &\qquad + C_o\tilde{\rho}_{o0}\frac{d}{dt}\int_0^1 s_o\,dx + C_w\tilde{\rho}_{w0}\frac{d}{dt}\int_0^1 s_w\,dx \\ &= C_w\frac{d}{dt}\int_0^1 m\int_{\tilde{\rho}_w}^{\rho_w}\frac{s-\tilde{\rho}_w}{s^2}\,ds\,dx + C_o\frac{d}{dt}\int_0^1 n\int_{\tilde{\rho}_o}^{\rho_o}\frac{s-\tilde{\rho}_o}{s^2}\,ds\,dx \\ &\qquad + C_o[\tilde{\rho}_{o0} - \tilde{\rho}_o]\frac{d}{dt}\int_0^1 s_o\,dx + C_w[\tilde{\rho}_{w0} - \tilde{\rho}_w]\frac{d}{dt}\int_0^1 s_w\,dx. \end{aligned} \tag{2.39}$$

Note that in view of (1.4), the last line of (2.39) gives us

$$\begin{aligned} &C_o[\tilde{\rho}_{o0} - \tilde{\rho}_o]\frac{d}{dt}\int_0^1 s_o\,dx + C_w[\tilde{\rho}_{w0} - \tilde{\rho}_w]\frac{d}{dt}\int_0^1 s_w\,dx \\ &= -P_o(\tilde{\rho}_o)\frac{d}{dt}\int_0^1 s_o\,dx - P_w(\tilde{\rho}_w)\frac{d}{dt}\int_0^1 s_w\,dx \end{aligned}$$

$$
\begin{aligned}
&= -P_o(\tilde{\rho}_o)\frac{d}{dt}\int_0^1 s_o\,dx - P_o(\tilde{\rho}_o)\frac{d}{dt}\int_0^1 s_w\,dx + P_c(\tilde{s}_w)\frac{d}{dt}\int_0^1 s_w\,dx\\
&= P_c(\tilde{s}_w)\frac{d}{dt}\int_0^1 s_w\,dx,
\end{aligned}
$$

where $\tilde{\rho}_o$, $\tilde{\rho}_w$, and $\tilde{s}_w$ are related to each other by common masses $\tilde{m}, \tilde{n}$, i.e., we have that
(i) $\tilde{\rho}_o = \rho_o(\tilde{m},\tilde{n})$, $\tilde{\rho}_w = \rho_w(\tilde{m},\tilde{n})$, and $\tilde{s}_w = s_w(\tilde{m},\tilde{n})$;
(ii) $P_o(\tilde{\rho}_o) = P_w(\tilde{\rho}_w) + P_c(\tilde{s}_w)$.
Hence, it follows from (2.39) that

$$
\begin{aligned}
-I_1 = {} & C_w\frac{d}{dt}\int_0^1 m\int_{\tilde{\rho}_w}^{\rho_w}\frac{s-\tilde{\rho}_w}{s^2}\,ds\,dx + C_o\frac{d}{dt}\int_0^1 n\int_{\tilde{\rho}_o}^{\rho_o}\frac{s-\tilde{\rho}_o}{s^2}\,ds\,dx\\
&+\frac{d}{dt}\int_0^1 [P_c(\tilde{s}_w)s_w - \Phi(s_w)]\,dx.
\end{aligned}
\tag{2.40}
$$

Inserting (2.40) and (2.33) in (2.32) we get

$$
\begin{aligned}
& C_w\frac{d}{dt}\int_0^1 m\int_{\tilde{\rho}_w}^{\rho_w}\frac{s-\tilde{\rho}_w}{s^2}\,ds\,dx + C_o\frac{d}{dt}\int_0^1 n\int_{\tilde{\rho}_o}^{\rho_o}\frac{s-\tilde{\rho}_o}{s^2}\,ds\,dx\\
& + \frac{d}{dt}\int_0^1 [P_c(\tilde{s}_w)s_w - \Phi(s_w)]\,dx + \frac{d}{dt}\int_0^1\int_0^x g(n+m)\,dy\,dx\\
& + \int_0^1 (\varepsilon_w m u_{wx}^2 + \varepsilon_o n u_{ox}^2)\,dx + \int_0^1 \hat{k}(u_w-u_o)^2\,dx + \int_0^1 \hat{k}_w u_w^2\,dx + \int_0^1 \hat{k}_o u_o^2\,dx\\
& = 0.
\end{aligned}
\tag{2.41}
$$

We can rewrite (2.41) to be

$$
\begin{aligned}
\frac{d}{dt}E(t) + \int_0^1 (\varepsilon_w m u_{wx}^2 + \varepsilon_o n u_{ox}^2)\,dx + \int_0^1 \hat{k}(u_w-u_o)^2\,dx&\\
+\int_0^1 \hat{k}_w u_w^2\,dx + \int_0^1 \hat{k}_o u_o^2\,dx = 0&
\end{aligned}
\tag{2.42}
$$

with $E(t)$ as given by (2.31). Hence, we conclude that (2.30) holds and where it is also clear from (2.23) that $\int_0^1 [P_c(\tilde{s}_w)s_w - \Phi(s_w)]\,dx \geq 0$. ☐

Lemma 2.1 implies the following corollary.

Corollary 2.1. *For any* $t \in [0,T^*)$, *it holds that*

$$
\int_0^t\int_0^1 (\varepsilon_w m u_{wx}^2 + \varepsilon_o n u_{ox}^2)\,dx\,ds + \int_0^t\int_0^1 \left[\hat{k}(u_w-u_o)^2 + \hat{k}_w u_w^2 + \hat{k}_o u_o^2\right]dx\,ds \leq K_0
$$

where

$$
\begin{aligned}
K_0 = {} & g(\tilde{n}_0+\tilde{m}_0) + C_w\int_0^1 m_0\int_{\tilde{\rho}_w}^{\rho_{w0}}\frac{s-\tilde{\rho}_w}{s^2}\,ds\,dx + C_o\int_0^1 n_0\int_{\tilde{\rho}_o}^{\rho_{o0}}\frac{s-\tilde{\rho}_o}{s^2}\,ds\,dx\\
& + \int_0^1 \Big[P_c(\tilde{s}_w)s_{w0} - \Phi(s_{w0})\Big]\,dx,
\end{aligned}
$$

where ρ_{i0} *and* s_{i0} *refer to initial states.*

Remark 2.4. The energy equality as expressed by (2.30) contains several dissipation terms on its left-hand-side. The three last terms reflect that there is a loss of energy (i.e., an energy transformation) through the three different friction terms, respectively, with coefficients $\hat{k}$, $\hat{k}_w$, and $\hat{k}_o$ and is a consequence of the viscous property of the involved fluids leading to drag force effects. Similarly, the internal viscosity of each fluid also creates resistance to move and is reflected by the two viscous terms, respectively, with coefficients ε_w and ε_o.

Remark 2.5. The energy $E(t)$ defined in (2.31) contains different terms each having a specific physical meaning. The use of compressible fluids implies that energy can be stored and released in the fluid due to pressure variations. An intuitive example of this is when there is influx of gas (oil) in a low reservoir layer where pressure is high. As this gas migrates towards a higher zone where pressure is lower, the gas (oil) will expand. That is, ρ_o decreases according to (1.4) and s_o increases since mass m_o is conserved and $m_o = s_o\rho_o$ and therfore typically will displace the surrounding water phase represented by s_w. This energy exchange is accounted for through the two first terms of $E(t)$. Capillary pressure $P_c = P_o - P_w$, accounts for the difference between the water and oil pressure P_w and P_o, and also acts as a driver (an additional pressure effect) for fluid motion. It naturally occurs in the energy functional $E(t)$ similar to the gravitational energy, see the last line of (2.31).

(b) More regularity estimates.

Lemma 2.2. *For any* $t \in [0, T^*)$, *it holds that*

$$\int_0^1 [\varepsilon_w \frac{m_x^2}{m} + \varepsilon_o \frac{n_x^2}{n}]\, dx \le K_1, \tag{2.43}$$

and

$$\begin{aligned}\int_0^t \int_0^1 s_o[(\rho_o^{1/2})_x]^2\, dx\, ds + \int_0^t \int_0^1 s_w[(\rho_w^{1/2})_x]^2\, dx\, ds \\ - \int_0^t \int_0^1 P_c'(s_w) s_{wx}^2\, dx\, ds \le C(T),\end{aligned} \tag{2.44}$$

where

$$K_1 = \Big[\int_0^1 [\varepsilon_w \frac{(m_0)_x^2}{m_0} + \varepsilon_o \frac{(n_0)_x^2}{n_0}]\, dx + g^2(\tilde{m} + \tilde{n})T + K_0\Big] \exp\Big\{\bar{a} \max\{\frac{1}{\varepsilon_w}, \frac{1}{\varepsilon_o}\} T\Big\}, \tag{2.45}$$

and $\bar{a} = \max\{1 + I_{wo} + I_w, 1 + I_{wo} + I_o\}$.

Proof. Note that from $(2.14)_2$ we get the following reformulated equation after expanding the advective term and taking a derivative in space:

$$(m_x)_t + (m_x u_w)_x = -(m u_{wx})_x. \tag{2.46}$$

Note the appearance of the viscosity term on the RHS of (2.46). Combining (2.46) with $(2.14)_4$ we arrive at

$$(\varepsilon_w m_x)_t + (\varepsilon_w m_x u_w)_x = -\varepsilon_w (m u_{wx})_x = -s_w P_{wx} - \hat{k}_w u_w - \hat{k}(u_w - u_c) + mg.$$

This is the same as

$$\Big[m(\varepsilon_w \frac{m_x}{m})\Big]_t + \Big[m(\varepsilon_w \frac{m_x}{m}) u_w\Big]_x = -s_w P_{wx} - \hat{k}_w u_w - \hat{k}(u_w - u_c) + mg$$

or

$$[\varepsilon_w m w]_t + [\varepsilon_w m w u_w]_x = -s_w P_{wx} - \hat{k}_w u_w - \hat{k}(u_w - u_c) + mg$$

for

$$w = \frac{m_x}{m}$$

which clearly, by using (2.14)$_2$, is the same as

$$\varepsilon_w m w_t + \varepsilon_w m u_w w_x = -s_w P_{wx} - \hat{k}_w u_w - \hat{k}(u_w - u_c) + mg. \tag{2.47}$$

Now, we test (2.47) with w and combine it with (2.14)$_2$ and (2.15) which leads us to

$$\begin{aligned} \frac{\varepsilon_w}{2}\frac{d}{dt}\int_0^1 m w^2\,dx = &-\int_0^1 s_w P_{wx} w\,dx - \int_0^1 \hat{k}_w u_w w\,dx \\ &-\int_0^1 \hat{k}(u_w - u_c) w\,dx + \int_0^1 m g w\,dx \end{aligned} \tag{2.48}$$

Similarly, for the oil phase we obtain

$$\begin{aligned} \frac{\varepsilon_o}{2}\frac{d}{dt}\int_0^1 n v^2\,dx = &-\int_0^1 s_o P_{ox} v\,dx - \int_0^1 \hat{k}_o u_o v\,dx \\ &+\int_0^1 \hat{k}(u_w - u_o) v\,dx + \int_0^1 n g v\,dx \end{aligned} \tag{2.49}$$

with

$$v = \frac{n_x}{n}.$$

Next, we focus on the terms appearing on the RHS of (2.48):

$$-\int_0^1 s_w P_{wx} w\,dx = -\int_0^1 s_w P_{wx}\Big(\frac{m_x}{m}\Big)\,dx := J_{w,1}.$$

We note that

$$\begin{aligned} J_{w,1} &= -\int_0^1 s_w P_{wx}\frac{m_x}{m}\,dx = -\int_0^1 s_{wx} P_{wx}\,dx - \int_0^1 s_w P_{wx}\frac{s_w \rho_{wx}}{m}\,dx \\ &= -\int_0^1 s_{wx} P_{wx}\,dx - 4C_w\int_0^1 s_w[(\rho_w^{1/2})_x]^2\,dx. \end{aligned} \tag{2.50}$$

Similarly, for $J_{o,1}$ associated with (2.49)

$$\begin{aligned} J_{o,1} &= -\int_0^1 s_o P_{ox}\frac{n_x}{n}\,dx = -\int_0^1 s_{ox} P_{ox}\,dx - \int_0^1 s_o P_{ox}\frac{\alpha_o \rho_{ox}}{n}\,dx \\ &= -\int_0^1 s_{ox} P_{ox}\,dx - 4C_o\int_0^1 s_o[(\rho_o^{1/2})_x]^2\,dx. \end{aligned} \tag{2.51}$$

To conclude, we see that by summing (2.48) and (2.49), using (2.50), and (2.51), we get

$$\begin{aligned} &\frac{1}{2}\frac{d}{dt}\int_0^1 [\varepsilon_w m w^2 + \varepsilon_o n v^2]\,dx + 4C_o\int_0^1 s_o[(\rho_o^{1/2})_x]^2\,dx + 4C_w\int_0^1 s_w[(\rho_w^{1/2})_x]^2\,dx \\ &= -\int_0^1 s_{wx} P_{wx}\,dx - \int_0^1 s_{ox} P_{ox}\,dx + \int_0^1 m g w\,dx + \int_0^1 n g v\,dx \end{aligned}$$

$$
\begin{aligned}
&-\int_0^1 \hat{k}(u_w-u_o)w\,dx+\int_0^1 \hat{k}(u_w-u_o)v\,dx-\int_0^1 \hat{k}_w u_w w\,dx-\int_0^1 \hat{k}_o u_o v\,dx\\
&=\int_0^1 s_{wx}^2 P_c'(s_w)\,dx+\int_0^1 mgw\,dx+\int_0^1 ngv\,dx\\
&-\int_0^1 \hat{k}(u_w-u_o)w\,dx+\int_0^1 \hat{k}(u_w-u_o)v\,dx-\int_0^1 \hat{k}_w u_w w\,dx-\int_0^1 \hat{k}_o u_o v\,dx
\end{aligned}
\tag{2.52}
$$

where we again have used $P_c(s_w)=P_o-P_w$ and $s_w+s_o=1$. That is,

$$
\begin{aligned}
&\frac{1}{2}\frac{d}{dt}\int_0^1 [\varepsilon_w m w^2+\varepsilon_o n v^2]\,dx\\
&\qquad+4C_o\int_0^1 s_o[(\rho_o^{1/2})_x]^2\,dx+4C_w\int_0^1 s_w[(\rho_w^{1/2})_x]^2\,dx-\int_0^1 s_{wx}^2 P_c'(s_w)\,dx\\
&=\int_0^1 g(m_x+n_x)\,dx-\int_0^1 \hat{k}(u_w-u_o)(\frac{m_x}{m})\,dx+\int_0^1 \hat{k}(u_w-u_o)(\frac{n_x}{n})\,dx\\
&\quad-\int_0^1 \hat{k}_w u_w(\frac{m_x}{m})\,dx-\int_0^1 \hat{k}_o u_o(\frac{n_x}{n})\,dx\\
&:=K_{ow0}+K_{w1}+K_{o1}+K_{w2}+K_{o2}.
\end{aligned}
\tag{2.53}
$$

For K_{ow0}, we use Cauchy inequality and the mass equations and have

$$
\begin{aligned}
K_{ow0}&=g\int_0^1 \frac{m_x}{\sqrt{m}}\sqrt{m}dx+g\int_0^1 \frac{n_x}{\sqrt{n}}\sqrt{n}dx\\
&\le\int_0^1 (\frac{m_x^2}{m}+\frac{n_x^2}{n})dx+\frac{1}{4}g^2\int_0^1 (m+n)dx=\int_0^1 (mw^2+nv^2)dx+\frac{1}{4}g^2(\tilde{m}+\tilde{n}).
\end{aligned}
\tag{2.54}
$$

In the following we make use of the functional form of the interaction coefficients $\hat{k}_w$, $\hat{k}_o$, and $\hat{k}$ as expressed in (2.26).

$$
\begin{aligned}
K_{w1}&=-\int_0^1 \hat{k}(u_w-u_o)(\frac{m_x}{m})dx\\
&\le\frac{1}{4}\int_0^1 \hat{k}(u_w-u_o)^2dx+\int_0^1 \hat{k}\frac{m_x^2}{m^2}dx\\
&\le\frac{1}{4}\int_0^1 \hat{k}(u_w-u_o)^2dx+I_{wo}\int_0^1 \frac{m_x^2}{m}dx=\frac{1}{4}\int_0^1 \hat{k}(u_w-u_o)^2dx+I_{wo}\int_0^1 mw^2dx
\end{aligned}
\tag{2.55}
$$

and

$$
\begin{aligned}
K_{o1}&=\int_0^1 \hat{k}(u_w-u_o)(\frac{n_x}{n})dx\\
&\le\frac{1}{4}\int_0^1 \hat{k}(u_w-u_o)^2dx+\int_0^1 \hat{k}\frac{n_x^2}{n^2}dx\\
&\le\frac{1}{4}\int_0^1 \hat{k}(u_w-u_o)^2dx+I_{wo}\int_0^1 \frac{n_x^2}{n}dx=\frac{1}{4}\int_0^1 \hat{k}(u_w-u_o)^2dx+I_{wo}\int_0^1 nv^2dx.
\end{aligned}
\tag{2.56}
$$

Furthermore,

$$\begin{aligned}
K_{w2} &= -\int_0^1 \hat{k}_w u_w (\frac{m_x}{m}) dx \\
&\leq \frac{1}{4}\int_0^1 \hat{k}_w u_w^2 dx + \int_0^1 \hat{k}_w \frac{m_x^2}{m^2} dx \\
&= \frac{1}{4}\int_0^1 \hat{k}_w u_w^2 dx + I_w \int_0^1 \frac{m_x^2}{m} dx = \frac{1}{4}\int_0^1 \hat{k}_w u_w^2 dx + I_w \int_0^1 m w^2 dx
\end{aligned} \tag{2.57}$$

and

$$\begin{aligned}
K_{o2} &= -\int_0^1 \hat{k}_o u_o (\frac{n_x}{n}) dx \\
&\leq \frac{1}{4}\int_0^1 \hat{k}_o u_o^2 dx + \int_0^1 \hat{k}_o \frac{n_x^2}{n^2} dx \\
&= \frac{1}{4}\int_0^1 \hat{k}_o u_o^2 dx + I_o \int_0^1 \frac{n_x^2}{n} dx = \frac{1}{4}\int_0^1 \hat{k}_o u_o^2 dx + I_o \int_0^1 n v^2 dx.
\end{aligned} \tag{2.58}$$

Putting the estimates (2.54)–(2.58) into (2.53), integrating the result over $(0,t)$, and using Corollary 2.1, we have

$$\begin{aligned}
&\int_0^1 [\varepsilon_w m w^2 + \varepsilon_o n v^2]\, dx + 4C_o \int_0^t \int_0^1 s_o [(\rho_o^{1/2})_x]^2 \, dx\, ds \\
&+ 4C_w \int_0^t \int_0^1 s_w [(\rho_w^{1/2})_x]^2 \, dx\, ds - \int_0^t \int_0^1 P_c'(s_w) s_{wx}^2 \, dx\, ds \\
&\leq \int_0^1 [\varepsilon_w m_0 w_0^2 + \varepsilon_o n_0 v_0^2]\, dx + \overline{a} \int_0^t \int_0^1 (m w^2 + n v^2) dx\, ds + \frac{1}{4} g^2 (\tilde{m} + \tilde{n}) t \\
&+ \frac{1}{2}\int_0^t \int_0^1 \hat{k}(u_w - u_o)^2 dx\, ds + \frac{1}{4}\int_0^t \int_0^1 \hat{k}_w u_w^2 dx\, ds + \frac{1}{4}\int_0^t \int_0^1 \hat{k}_o u_o^2 dx\, ds \\
&\leq \int_0^1 [\varepsilon_w m_0 w_0^2 + \varepsilon_o n_0 v_0^2]\, dx + \overline{a} \max\{\frac{1}{\varepsilon_w}, \frac{1}{\varepsilon_o}\} \int_0^t \int_0^1 (\varepsilon_w m w^2 + \varepsilon_o n v^2) dx\, ds \\
&+ g^2 (\tilde{m} + \tilde{n}) T + K_0,
\end{aligned} \tag{2.59}$$

where $\overline{a} = \max\{1 + I_{wo} + I_w, 1 + I_{wo} + I_o\}$.

Using Gronwall's inequality and (2.59), we get (2.43). (2.44) is given by (2.43) and (2.59). ☐

In view of Lemma 2.2 it follows that $\sqrt{m}, \sqrt{n} \in H^1(0,1)$. Combined with the Sobolev inequality $H^1(0,1) \hookrightarrow C([0,1])$ we have the following corollary.

Corollary 2.2. *It holds that*

$$\begin{cases} m(x,t) + n(x,t) \leq C(T), \\ \displaystyle\int_0^1 (m_x^2 + n_x^2)\, dx \leq C(T), \end{cases} \tag{2.60}$$

for any $(x,t) \in [0,1] \times [0,T^*)$.

(c) Upper and lower bounds of density and related quantities.

Lemma 2.3. *It holds that*

$$\begin{cases} n \le \rho_o \le C(T), \\ m \le \rho_w \le C(T), \end{cases} \tag{2.61}$$

for any $(x,t) \in [0,1] \times [0,T^*)$.

Proof. Since

$$\rho_o = \frac{C_w}{C_o}\rho_w - \frac{C_w}{C_o}\tilde{\rho}_{w0} + \tilde{\rho}_{o0} + \frac{1}{C_o}P_c(s_w), \tag{2.62}$$

we have

$$\rho_o = (s_o + s_w)\rho_o = n + s_w\Big[\frac{C_w}{C_o}\rho_w - \frac{C_w}{C_o}\tilde{\rho}_{w0} + \tilde{\rho}_{o0} + \frac{1}{C_o}P_c(s_w)\Big], \tag{2.63}$$

$$\rho_w = (s_w + s_o)\rho_w = m + s_o\Big[\frac{C_o}{C_w}\rho_o + \tilde{\rho}_{w0} - \frac{C_o}{C_w}\tilde{\rho}_{o0} - \frac{1}{C_w}P_c(s_w)\Big]. \tag{2.64}$$

Armed with the upper bounds of m and n from Corollary 2.2, we get the upper bounds of ρ_o and ρ_w from (2.63) and (2.64). Note that the term ρ_i appearing on the right-hand-side is grouped with the corresponding s_i which gives either m or n. In addition, we make use of the uniform bound on $P_c(s_w)$ given by (2.24). The lower bounds can be derived from the definitions $n = s_o\rho_o$ and $m = s_w\rho_w$ combined with (1.3). □

Corollary 2.3. *The following uniform lower bound holds*

$$m, n \ge \frac{1}{C}, \qquad \textit{for any } (x,t) \in [0,1] \times [0,T^*), \tag{2.65}$$

subject to the constraint that $K_1 < \min\{\varepsilon_w\tilde{m}, \varepsilon_o\tilde{n}\}$ *where* K_1 *is given by* (2.45).

Proof.

$$\begin{aligned} |m(x,t) - \tilde{m}| &= |\int_0^1 [m(x,t) - m(y,t)]\,dy| = |\int_0^1 \int_y^x m_\xi(\xi,t)\,d\xi\,dy| \\ &\le \int_0^1 |m_x(x,t)|\,dx = \int_0^1 \sqrt{m(x,t)}|\frac{m_x(x,t)}{\sqrt{m(x,t)}}|\,dx \\ &\le \Big(\int_0^1 m(x,t)\,dx\Big)^{\frac{1}{2}} \Big(\int_0^1 \frac{|m_x(x,t)|^2}{m}\,dx\Big)^{\frac{1}{2}} \le \Big(\frac{\tilde{m}K_1}{\varepsilon_w}\Big)^{\frac{1}{2}}. \end{aligned}$$

Letting $\left(\frac{\tilde{m}K_1}{\varepsilon_w}\right)^{\frac{1}{2}} < \tilde{m}$, i.e., $K_1 < \varepsilon_w\tilde{m}$, we have

$$m \ge \frac{1}{C}$$

on $[0,1] \times [0,T^*)$ for some positive constant C. Similarly, letting $\left(\frac{\tilde{n}K_1}{\varepsilon_o}\right)^{\frac{1}{2}} < \tilde{n}$, i.e., $K_1 < \varepsilon_o\tilde{n}$, we get the positive lower bound of n. □

(d) Higher-order estimates.

Lemma 2.4. *The following estimate holds*

$$\int_0^1 \left[(s_w)_x^2 + (s_o)_x^2 + (\rho_w)_x^2 + (\rho_o)_x^2\right] dx \le C(T) \tag{2.66}$$

for any $t \in [0, T^*)$.

Proof. Differentiating (2.64) with respect to x, we have

$$\begin{aligned}(\rho_w)_x =& m_x + \frac{C_o}{C_w}(s_o\rho_o)_x + \tilde{\rho}_{w0}(s_o)_x - \frac{C_o}{C_w}\tilde{\rho}_{o0}(s_o)_x \\ &- \frac{1}{C_w}(s_o)_x P_c(s_w) - \frac{1}{C_w}s_o P_c'(s_w)(s_w)_x \\ =& m_x + \frac{C_o}{C_w}n_x - (\tilde{\rho}_{w0} - \frac{C_o}{C_w}\tilde{\rho}_{o0})(s_w)_x \\ &+ [\frac{1}{C_w}P_c(s_w) - \frac{1}{C_w}s_o P_c'(s_w)](s_w)_x,\end{aligned} \tag{2.67}$$

where we have used $s_o + s_w = 1$ such that $(s_o)_x = -(s_w)_x$.

With (2.67), we proceed to estimate $(s_w)_x$.

$$\begin{aligned}(s_w)_x =& (\frac{m}{\rho_w})_x = \frac{m_x}{\rho_w} - \frac{s_w(\rho_w)_x}{\rho_w} \\ =& \frac{m_x}{\rho_w} - \frac{s_w}{\rho_w}[m_x + \frac{C_o}{C_w}n_x] + \frac{s_w}{\rho_w}(\tilde{\rho}_{w0} - \frac{C_o}{C_w}\tilde{\rho}_{o0})(s_w)_x \\ &- \frac{s_w}{\rho_w}[\frac{1}{C_w}P_c(s_w) - \frac{1}{C_w}s_o P_c'(s_w)](s_w)_x,\end{aligned}$$

which implies that

$$\begin{aligned}&(s_w)_x\Big[\rho_w - s_w(\tilde{\rho}_{w0} - \frac{C_o}{C_w}\tilde{\rho}_{o0}) + s_w[\frac{1}{C_w}P_c(s_w) - \frac{1}{C_w}s_o P_c'(s_w)]\Big] \\ =& m_x - s_w(m_x + \frac{C_o}{C_w}n_x).\end{aligned} \tag{2.68}$$

By (2.62), we have

$$\rho_w = \frac{C_o}{C_w}\rho_o + \tilde{\rho}_{w0} - \frac{C_o}{C_w}\tilde{\rho}_{o0} - \frac{1}{C_w}P_c(s_w).$$

Substituting this identity and that $1 - s_w = s_o$ into (2.68), we have

$$\begin{aligned}(s_w)_x =& (s_o m_x - s_w\frac{C_o}{C_w}n_x)\Big[\rho_w - s_w(\tilde{\rho}_{w0} - \frac{C_o}{C_w}\tilde{\rho}_{o0}) \\ &+ s_w[\frac{1}{C_w}P_c(s_w) - \frac{1}{C_w}s_o P_c'(s_w)]\Big]^{-1}.\end{aligned} \tag{2.69}$$

Since

$$\rho_w = \frac{C_o}{C_w}\rho_o + \tilde{\rho}_{w0} - \frac{C_o}{C_w}\tilde{\rho}_{o0} - \frac{1}{C_w}P_c(s_w), \tag{2.70}$$

we have

$$\begin{aligned}&\rho_w - s_w(\tilde{\rho}_{w0} - \frac{C_o}{C_w}\tilde{\rho}_{o0}) + s_w[\frac{1}{C_w}P_c(s_w) - \frac{1}{C_w}s_o P_c'(s_w)] \\ =& \frac{C_o}{C_w}\rho_o + s_o\Big[\tilde{\rho}_{w0} - \frac{C_o}{C_w}\tilde{\rho}_{o0} - \frac{1}{C_w}P_c(s_w)\Big] - \frac{1}{C_w}s_w s_o P_c'(s_w).\end{aligned} \tag{2.71}$$

Combining (2.71) with (2.69), (2.61), (2.65), and the assumptions (2.24) and (2.25), allow us to conclude that

$$\begin{aligned}\int_0^1 (s_w)_x^2\,dx \le& C\int_0^1 \frac{1}{\rho_o^2}(m_x^2+n_x^2)\,dx\\ \le& C\int_0^1 \frac{s_o^2}{n^2}(m_x^2+n_x^2)\,dx \le C(T).\end{aligned}\tag{2.72}$$

This combined with (2.67) and (2.60) gives

$$\int_0^1 (\rho_w)_x^2\,dx \le C(T).\tag{2.73}$$

By virtue of (2.70), the fact that $(s_w)_x = -(s_o)_x$, (2.72), and (2.73), we get the estimates of $(s_o)_x$ and $(\rho_o)_x$. □

Lemma 2.5. *For any* $t\in[0,T^*)$*, it holds that*

$$\int_0^1 \left[(u_w)_x^2+(u_o)_x^2\right]dx \le C(T).\tag{2.74}$$

Proof. By virtue of (2.32), we have

$$\begin{aligned}&\int_0^1 (\varepsilon_w m u_{wx}^2+\varepsilon_o n u_{ox}^2)\,dx + \int_0^1 \left[\hat{k}(u_w-u_o)^2+\hat{k}_w u_w^2+\hat{k}_o u_o^2\right]dx\\ =&-(\int_0^1 n g u_o\,dx+\int_0^1 m g u_w\,dx)-\int_0^1 (s_o P_{ox} u_o + s_w P_{wx} u_w)\,dx\\ \le& C(\|u_o\|_{L^\infty}+\|u_w\|_{L^\infty})+C\|(\rho_o)_x\|_{L^2}\|u_o\|_{L^2}+C\|(\rho_w)_x\|_{L^2}\|u_w\|_{L^2}\\ \le& C(T)\big(\|(u_o)_x\|_{L^2}+\|(u_w)_x\|_{L^2}\big)\le C(T)\big(\|\sqrt{n}(u_o)_x\|_{L^2}+\|\sqrt{m}(u_w)_x\|_{L^2}\big)\\ \le&\frac{1}{2}\int_0^1 (\varepsilon_w m u_{wx}^2+\varepsilon_o n u_{ox}^2)\,dx + C(T),\end{aligned}\tag{2.75}$$

where we use $\int_0^1 m\,dx=\tilde{m}$, $\int_0^1 n\,dx=\tilde{n}$ and Hölder inequality in the first inequality, and use the inequality $\|u_i\|_\infty\le C\|u_{ix}\|_{L^2}$, (2.66), (2.65), and Cauchy inequality in the rest.

Using (2.65) again, and (2.75), we get

$$\int_0^1 (u_{wx}^2+u_{ox}^2)\,dx \le C(T).\tag{2.76}$$

□

Corollary 2.4. *For any* $t\in[0,T^*)$*, it holds that*

$$\int_0^1 \left[(u_w)_{xx}^2+(u_o)_{xx}^2\right]dx \le C(T).\tag{2.77}$$

Proof. From the equation of u_w, we have

$$\varepsilon_w m(u_w)_{xx} = -\varepsilon_w m_x u_{wx} + s_w P_{wx} + \hat{k}_w u_w + \hat{k}(u_w-u_o)+mg,$$

which together with (2.65), (2.60), (2.66), and (2.74) gives

$$\begin{aligned}\int_0^1 (u_w)_{xx}^2\,dx \le & C(T)\int_0^1 m_x^2 u_{wx}^2\,dx + C(T)\\ \le & C(T)\|u_{wx}^2\|_{L^\infty}\int_0^1 m_x^2\,dx + C(T)\\ \le & C(T)\Big(\|(u_w)_x\|_{L^2}^2 + \int_0^1 |(u_w)_x(u_w)_{xx}|\,dx\Big) + C(T)\\ \le & \frac{1}{2}\int_0^1 (u_w)_{xx}^2\,dx + C(T),\end{aligned}$$

where we use $W^{1,1}(0,1) \hookrightarrow L^\infty(0,1)$ in the third inequality, and use $\int ab\,dx \le C\int a^2\,dx + \varepsilon\int b^2\,dx$ with appropriate choice of ε in the last one. This implies

$$\int_0^1 (u_w)_{xx}^2\,dx \le C(T).$$

Similarly, we get the estimate of $(u_o)_{xx}$. □

Corollary 2.5. *For any $t \in [0, T^*)$, it holds that*

$$\int_0^1 \Big[m_t^2 + n_t^2 + (s_w)_t^2 + (s_o)_t^2 + (\rho_w)_t^2 + (\rho_o)_t^2\Big]\,dx \le C(T). \tag{2.78}$$

Proof. By using the equation of m, Cauchy inequality, (2.60), and (2.74), we have

$$\begin{aligned}\int_0^1 m_t^2\,dx \le & 2\int_0^1 \Big[m^2(u_w)_x^2 + m_x^2 u_w^2\Big]\,dx\\ \le & 2\|m\|_{L^\infty}^2\int_0^1 (u_w)_x^2\,dx + 2\|u_w\|_{L^\infty}^2\int_0^1 m_x^2\,dx\\ \le & C(T).\end{aligned} \tag{2.79}$$

Similarly we get

$$\int_0^1 n_t^2\,dx \le C(T). \tag{2.80}$$

We consider (2.69) with ∂_x replaced by ∂_t, and use similar analysis as (2.72). Then

$$\begin{aligned}\int_0^1 (s_w)_t^2\,dx \le & C\int_0^1 \frac{1}{\rho_o^2}(m_t^2 + n_t^2)\,dx\\ \le & C\int_0^1 \frac{s_o^2}{n^2}(m_t^2 + n_t^2)\,dx \le C(T),\end{aligned} \tag{2.81}$$

where we use (2.65), (2.79), and (2.80). Since $(s_o)_t = -(s_w)_t$, we get

$$\int_0^1 (s_o)_t^2\,dx \le C(T).$$

By virtue of (2.67) where ∂_x is replaced by ∂_t, (2.79), (2.80), and (2.81), we have

$$\int_0^1 (\rho_w)_t^2\,dx \le C(T).$$

This combined with (2.70) and (2.81) gives

$$\int_0^1 (\rho_o)_t^2\, dx \le C(T).$$

□

With the above estimates, we get (2.29). Thus the proof of Theorem 2.2 is complete.

3. **Numerical results.** The main objective of this section is to carry out some testing of the numerical schemes presented in Appendix D, respectively, for the compressible and incompressible version of (1.1). First, we want to test general stability properties. Second, we seek some insight into the role played by using Darcy velocity $U_i = s_i u_i$ versus interstitial fluid velocity u_i $(i = w, o)$ in the viscous terms. In other words, we modify $(4.145)_{3,4}$ and use the following momentum equations for the compressible case

$$\begin{aligned} s_o(P_w + P_c)_x &= -(\hat{k}_o + \hat{k})u_o + \hat{k}u_w + ng + \varepsilon_o(\rho_o U_{ox})_x \\ s_w(P_w)_x &= -(\hat{k}_w + \hat{k})u_w + \hat{k}u_o + mg + \varepsilon_w(\rho_w U_{wx})_x, \end{aligned} \tag{3.82}$$

and modify $(4.165)_{3,4}$ as follows for the incompressible case

$$\begin{aligned} s_o(P_w + P_c)_x &= -(\hat{k}_o + \hat{k})u_o + \hat{k}u_w + ng + (\varepsilon_o\rho_o)U_{oxx} \\ s_w(P_w)_x &= -(\hat{k}_w + \hat{k})u_w + \hat{k}u_o + mg + (\varepsilon_w\rho_w)U_{wxx}. \end{aligned} \tag{3.83}$$

Third, we also test the behavior of the scheme as the coefficients $\varepsilon_w, \varepsilon_o$ are varied to see what kind of impact this term will have on the solution. This also allows us to get some understanding of whether the viscous model seems to converge to the inviscid version obtained by letting $\varepsilon_w, \varepsilon_o \to 0$. We conduct numerical tests similar to those reported in [9]. We refer to Remark 1.2 for more details regarding the model they solve. Most importantly, the viscous term in their model depends on the Darcy velocity U_w, U_o. We apply the scheme for the incompressible model for these investigations, see Section 3.1. However, in Section 3.2 we also include examples where we use the scheme derived for the compressible model (see Appendix D) and do some comparison with the results from the incompressible model. The following input data are chosen for the numerical examples.

We choose parameters as specified in Table 1. In particular, when combined with the relations (4.132) it gives rise to a fractional flow function given by

$$f_w = \frac{k_w/\mu_w}{k_w/\mu_w + k_o/\mu_o} = \frac{s_w^2}{s_w^2 + (1 - s_w)^2} = f_w(s_w).$$

The function is illustrated in Fig. 1 (left figure). The initial data of water saturation is set to be as in [9]:

$$s_w(x, t = 0) = \begin{cases} 0.8 & 0 \le x \le 2, \\ 0.8\exp(-150(x - 2)^2) & 2 < x \le 100. \end{cases} \tag{3.84}$$

A horizontal reservoir layer is considered in this case and porosity is also assumed to be 1. The whole test is a 10-day flooding process with a constant interstitial water injection rate at left boundary, $Q = 8.004m^3/d$. The relevant boundary values are: $s_w(x = 0, t) = 0.8$ and $u_w(x = 0, t) = 8.004m/d$. In addition, 2001 grids are used to simulate this displacement. Water and oil have the same properties such as density and viscosity. Fluid-fluid interaction effect is ignored here by setting $I = 0$ in the

Parameter	Dimensional Value	Parameter	Dimensional Value
L	100 m	I_w	1.5
ϕ	1	I_o	1.5
A	1 m^2	I	0 $(\mathrm{Pa{\cdot}s})^{-1}$
$\tilde{\rho}_{w0}$	1 $\mathrm{g/cm}^3$	α	0
$\tilde{\rho}_{o0}$	1 $\mathrm{g/cm}^3$	β	0
C_w	10^6 $\mathrm{m}^2/\mathrm{s}^2$	ε_w	$10^7, 10^6, 10^5, 10^4, 10^3, 10^2$ cP
C_o	$5 \cdot 10^5$ $\mathrm{m}^2/\mathrm{s}^2$	ε_o	$10^7, 10^6, 10^5, 10^4, 10^3, 10^2$ cP
μ_w	1 cP	K	1000 mD
μ_o	1 cP	$k_{rw}^{max} = 1/I_w$	0.667
Q	8.004 $\mathrm{m}^3/\mathrm{day}$	$k_{ro}^{max} = 1/I_o$	0.667
P_{wL}	10^6 Pa	T	10 days
N_x	2001	$\triangle t$	8640 s

TABLE 1. Input parameters of reservoir and fluid properties used for for the below simulations. Note that P_{wL} is the boundary pressure at left for the incompressible model whereas for the compressible model it represents the initial pressure distribution.

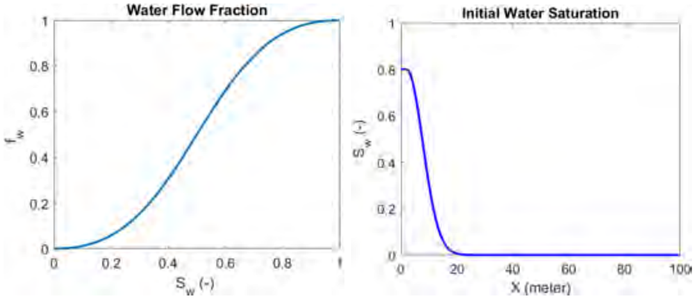

FIGURE 1. Water fractional flow function $\hat{f}_w(s_w)$ as given by (4.127) for the incompressible model obtained by using the parameters specified in Table 1 (left figure) and initial water saturation (3.84) profile (right), both similar to that used in [9].

correlations (4.132). The corresponding initial water saturation profile is shown in Fig. 1 (right figure).

3.1. The incompressible model.

Case 1. First, we want to compare the numerical results obtained by using the scheme from Appendix D (incompressible variant) and compare with similar results presented in [9], which are based on the model (1.13). We also mimic their scheme by slightly modifying the scheme prescribed in Appendix D (incompressible variant) where $s_i u_{ix}$ is replaced by U_{ix} in the viscous term, as described by (3.83). Results are illustrated in Fig. 2. We show water saturation profiles after 10 days flooding with, respectively, $\varepsilon_w = \varepsilon_o = 10^7$ and $\varepsilon_w = \varepsilon_o = 10^6$ (upper row) and compare with the corresponding results from Coclite et al. [9] (lower row). Main observations are:

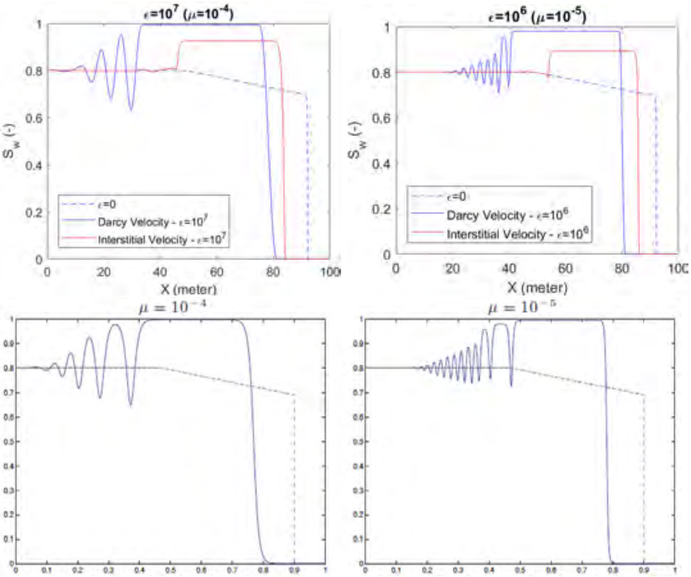

FIGURE 2. **Upper row**: Results produced by the discrete scheme described in Appendix D (incompressible model). Three kinds of curves are plotted including the case without viscous effect, i.e., $\varepsilon_w = \varepsilon_o = 0$, the one based on using Darcy velocity U_i $(i = w, o)$ in the viscous term, and the one with interstitial velocity u_i $(i = w, o)$ in the viscous term. The left figure shows results with $\varepsilon = \varepsilon_w = \varepsilon_o = 10^7$ whereas the right figure shows results with $\varepsilon = \varepsilon_w = \varepsilon_o = 10^6$. **Lower row**: The results of two corresponding cases with $\varepsilon_w = \varepsilon_o = 10^7$ and $\varepsilon_w = \varepsilon_o = 10^6$ after a dimensionless time, 0.65, produced by the numerical scheme described in [9] to solve the model (1.13). From these computations we see that the solution is sensitive to whether the interstitial velocity u_i or the Darcy velocity U_i appear in the viscous term. In particular, the use of Darcy velocity seems to generate considerably more oscillatory behavior behind the "water bank" formed at the front.

(i) A new "water bank" is formed behind the front of the water as a result of the viscous terms. This is a local effect restricted to the region right behind the water front where large gradients in velocity are present;
(ii) Internal viscous forces slow down the transport effect, especially at the saturation front where velocity involves dramatic changes. Right behind the water bank, the model with Darcy velocity involved in the viscous term tends to develop oscillatory behavior;
(iii) The solution shows a clear sensitivity to the magnitude of $\varepsilon_o, \varepsilon_w$ (i.e., 10^7 versus 10^6) for the scheme based on Darcy velocity U_i in the viscous terms. The

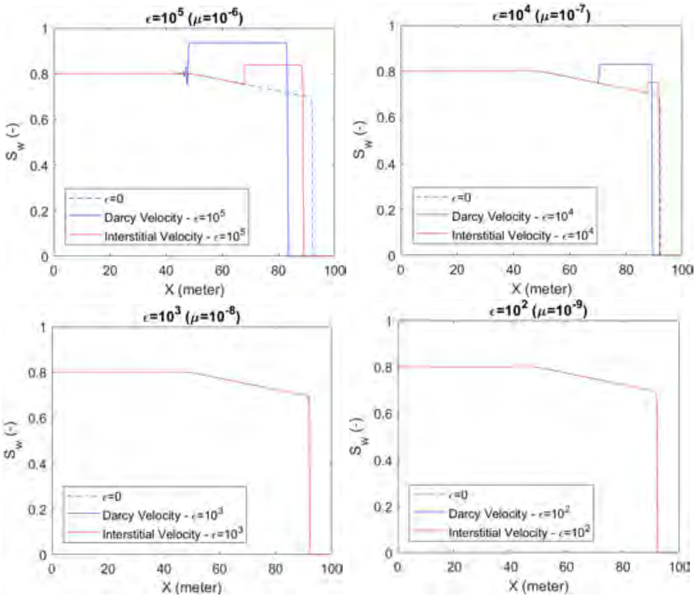

FIGURE 3. Simulation results with smaller viscous parameters after 10 days of water flooding. Three kinds of curves are compared: zero viscous effect, Darcy velocity U_i in viscous term and interstitial velocity u_i in viscous term. It shows that the viscous constant water level gradually vanishes when ε is as low as 10^3 and 10^2.

scheme with viscous term based on interstitial velocity u_i shows less sensitivity to this change in $\varepsilon_o, \varepsilon_w$.

The classical Buckley-Leverett model solution (i.e., $\varepsilon_w = \varepsilon_o = 0$) is composed of a sharp water front followed by a rare-faction wave which is due to a viscous effect associated with resistance forces between fluid (water and oil) and walls of the pore space. The new water bank is a consequence of internal viscosity within the fluid felt at the region behind the water front. The difference between solution when viscous term is based on Darcy velocity U_i versus solution when viscous term is based on interstitial velocity u_i, can be naturally understood in light of the expansion

$$\partial_x(\partial_x(s_i u_i)) = \partial_x(s_i \partial_x(u_i)) + \partial_x(u_i \partial_x(s_i)).$$

Clearly, the viscous term based on $U_i = s_i u_i$ gives rise to an additional term that naturally can be linked to the observed difference between the two schemes used to produce solutions in Fig. 2. It should be noted that Brinkman equation was developed empirically for single phase flow and afterwards has been extended to the multiphase setting in a heuristic manner. As noted in Remark 1.3 there seems to be an ongoing discussion in the literature whether to base the viscous term on Darcy velocity or interstitial velocity. Finally, in Fig. 3 is shown the result for the two schemes as $\varepsilon_w, \varepsilon_o$ get smaller. Both schemes seem to reflect convergence toward

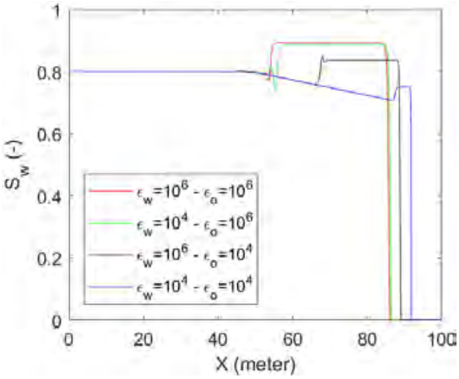

FIGURE 4. The results after 10 days with initial data are shown in Fig. 1 with interstitial velocity in viscous term. Four curves are compared: the one with large values of ε_w and ε_o, 10^6; the second one with large ε_o, 10^6 and small ε_w, 10^4; the third one with large ε_w, 10^6 and small ε_o, 10^4 and the last one with small values of ε_w and ε_o, 10^4. It shows that the displaced oil influences significantly on the constant level of water which displaces oil.

the solution of the inviscid model (i.e., $\varepsilon_w = \varepsilon_o = 0$) with a considerably faster convergence produced by the scheme with viscous term based on interstitial fluid u_i.

Case 2. In Fig. 4 we show simulation results when we vary the internal relation between ε_w and ε_o. It is intuitively understandable that oil viscous effects can have a strong impact on the constant water level right behind the water front. Apparently, the same change of magnitude of water viscous parameter ε_w from 10^4 to 10^6 with a constant ε_o has a dramatic effect when ε_o is small (i.e., 10^4) whereas the effect is rather small when ε_o is large (i.e., 10^6). We refer to Fig. 4 for simulation results.

Case 3. Now, we move to another case which has a different initial condition but still with the same injection rate of water, $8.004m^3/d$, as interstitial velocity at left boundary. The initial water saturation is illustrated in Fig. 5. Numerical results are shown in Fig. 6 where we compare the scheme based on interstitial viscosity (right figure) with the simulation result reported in [9] (left figure). In particular, it seems that the numerical solution based on using Darcy velocity produces an unphysical water saturation value near the left boundary. The numerical solution illustrated in Fig. 6 (right) does not contain this "defect". In addition, apparently the solution converges to the classical Buckley-Leverett type result with a small ε such as 10^3. This behavior seems different from the conclusion in [9].

3.2. **The compressible model.** Next, we use the numerical scheme described in Appendix D (compressible variant) to compute and illustrate the numerical behavior for the compressible model. Comparison is made with the cases shown in Fig. 2 for the incompressible model. The compressible fluids are assumed to be given by

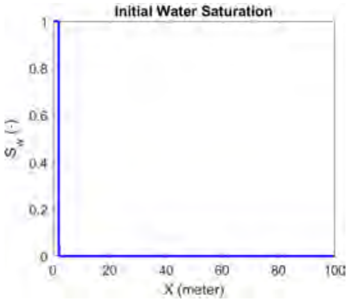

FIGURE 5. Initial water saturation profile from Coclite et al. [9].

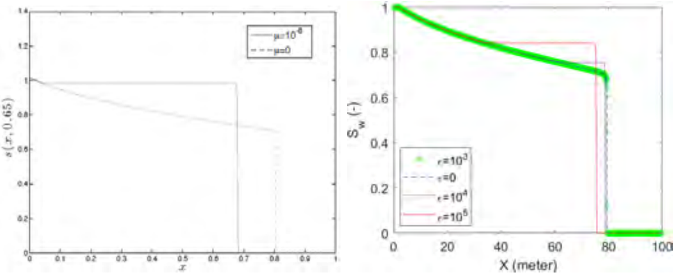

FIGURE 6. Left: The results from Coclite et al. [9] based on Darcy velocity in viscous term. Right: Numerical scheme (after 8 days) which uses interstitial velocity in viscous term with different viscous values $\varepsilon = 0, 10^3, 10^4, 10^5$ and $\varepsilon_w = \varepsilon_o = \varepsilon$.

the pressure-density relation (1.4). The initial water saturation is also the same as shown in Fig. 1. The water saturation s_w at left boundary is constrained with 0.8 and the initial water pressure at left boundary is 10^6 Pa. The numerical behavior is shown in Fig. 7. The essential difference is a delay in the solution of the compressible model.

In order to shed light on the difference observed in Fig. 7, we explore the pressure profiles at various times (shown in Fig. 8). It is clear from these plots that water pressure keeps increasing, especially for the water displacing part. Water can be compressed in the compressible model therefore the water density will also increase, which leads to a larger viscous effect since density is included in the coefficient of the viscous term. Water will feel more resistance forces and it is more difficult to displace oil resulting in a delay effect.

Injection of water versus gas. Finally, a numerical example is shown with gas injection to displace oil in the compressible model instead of water. The parameters of gas are the same as for water, as described in Table 1, except using the pressure-density relation: $\rho_g = P_g/C_g$ where $C_g = 10^5$. The left figure of Fig. 9 compares the results of gas injection and water injection. As expected, it is a much slower

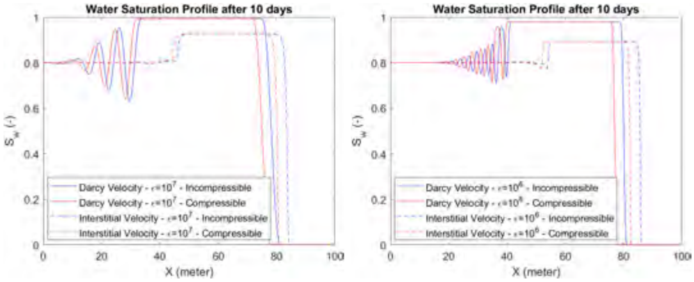

FIGURE 7. Comparison between the compressible model and the incompressible model for water-oil flow with $\varepsilon_w = \varepsilon_o = \varepsilon = 10^7, 10^6$. After the same period of 10 days, water flow in the compressible model is delayed compared with water profiles in the incompressible model, for both situations with interstitial velocity and Darcy velocity in viscous terms.

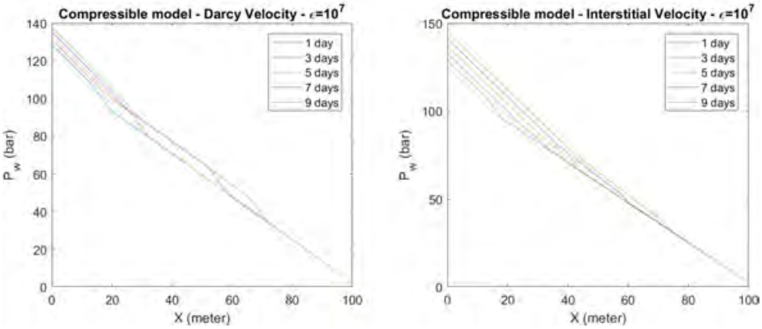

FIGURE 8. The water pressure evolution in the compressible model for the case with Darcy velocity in viscous term (left figure) and the case with interstitial velocity in viscous term (right figure). Water pressure increases with time in the water displacing part of the reservoir layer which leads to a compression effect where the magnitude of the viscous terms increase and thereby slows down the displacement of the water front.

process for gas to displace oil. This is a natural consequence of the fact that gas is much more compressible than water. The high gas pressure which results from the increased viscous effect will generate a strong compression of gas. It is also interesting to see that the fluctuation in the gas saturation profile becomes stronger as time elapses, which is not observed in the case of water injection. However, the elevated constant water level is almost the same in both cases (compare the left and the right subfigures in Fig. 9).

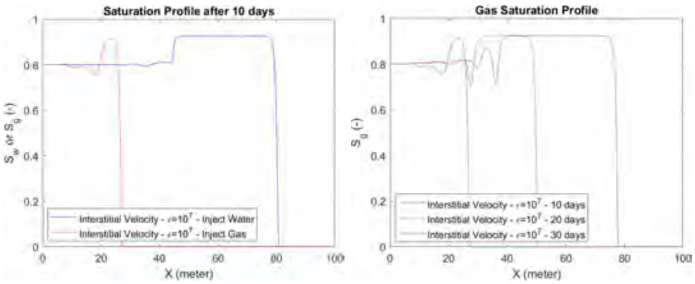

FIGURE 9. Left: Comparison of saturation profiles for water injection and gas injection, respectively, after the same time period (10 days) in the compressible model using interstitial velocity in viscous term ($\varepsilon_w = \varepsilon_o = \varepsilon = 10^7$). Right: The gas saturation profile shown at different times.

4. **Concluding remarks.** Some main observations from the investigations of the present manuscript are:

- We have found that exploiting the fact that the viscous term depends on the interstitial fluid flow velocity u_w, u_o, we can derive stability estimates (energy-type estimate and BD-estimate) that also naturally deal with the capillary pressure term $P_c(s_w)$. This approach seems strongly linked to the special structure of the viscous coefficients.
- We formulated finite difference schemes, both for the incompressible and compressible version of the model. These schemes allow us to systematically gain some insight into the effect of compressibility as well as the effect from the viscous terms that account for the frictional resistance within the fluid. We also observe that by using Darcy velocity in the viscous term, the resulting scheme tends to give more oscillatory behavior similar to that reported in [9].
- In particular, when the viscous coefficients $\varepsilon_w, \varepsilon_o$ become small enough, the numerical experiments carried out in a one-dimensional setting indicate that the approximate solution converges to the solution of the inviscid model. The stability estimates for the model based on interstitial fluid velocity, however, do depend on $\varepsilon_w, \varepsilon_o$ and cannot be used to ensure convergence to the inviscid model. Hence, this remains an interesting open problem.

Acknowledgments. We are grateful for instructive comments from the anonymous reviewers that helped improving certain parts of a first version of this manuscript.

Appendix A: Proof of Theorem 2.1. We apply a method similar to the one used in our previous work [16] to prove the local existence and uniqueness. Hence, in order to make the proof more compact we will heavily refer to that paper for details and highlight what is different.

First, we consider the solution space

$$S := S_{T_0,A_1} = \left\{ v \in C([0,T_0]; H_0^1 \cap H^2) \middle| \|v\|_{C([0,T_0];H^2)} \leq AA_1 \right\}$$

where $A=\max\{\frac{1}{\epsilon_o},\frac{1}{\epsilon_w}\}$, A_1 and T_0 satisfy (4.101) and (4.87), (4.88), and (4.117), respectively.

Step 1. Construct an iteration sequence.

We define an iteration sequence to approximate (2.14) which takes the following form

$$\begin{aligned}
(n^k)_t+(n^ku_o^{k-1})_x&=0\\
(m^k)_t+(m^ku_w^{k-1})_x&=0\\
s_o^kP_{ox}^k&=-\hat{k}_o^ku_o^k+\hat{k}^k(u_w^{k-1}-u_o^k)+\varepsilon_o(n^ku_{ox}^k)_x-n^kg\\
s_w^kP_{wx}^k&=-\hat{k}_w^ku_w^k-\hat{k}^k(u_w^k-u_o^k)+\varepsilon_w(m^ku_{wx}^k)_x-m^kg
\end{aligned}\tag{4.85}$$

with the initial-boundary value conditions:

$$(u_w^k,u_o^k)(0,t)=(u_w^k,u_o^k)(1,t)=0,\ t\geq 0,$$

and

$$(m^k,n^k)(x,0)=(m_0,n_0)(x),\ \ x\in[0,1],$$

for $k=1,2,3,\cdots$, where $(u_w^0,u_o^0)=(0,0)$, $s_w^k=s_w(m^k,n^k)$, $s_o^k=s_o(m^k,n^k)$, $P_w^k=P_w(m^k,n^k)$, $P_o^k=P_o(m^k,n^k)$, $\hat{k}_w^k=\hat{k}_w(m^k,n^k)$, $\hat{k}_o^k=\hat{k}_o(m^k,n^k)$, $\hat{k}^k=\hat{k}(m^k,n^k)$, and

$$(m^k,n^k)\in C([0,T_0];H^1)\cap C^1([0,T_0];L^2),\ \ (u_w^k,u_o^k)\in C([0,T_0];H_0^1\cap H^2).$$

Step 2. Boundedness of the sequence.

Assume that $u_w^{k-1},u_o^{k-1}\in S$. To prove $u_w^i,u_o^i\in S$ for all $i=0,1,2,3,...$, it suffices to prove $u_w^k,u_o^k\in S$.

In fact, as a consequence of that $u_w^{k-1},u_o^{k-1}\in S$, we have

$$\begin{cases}\|u_{w,x}^{k-1}(\cdot,t)\|_{L^\infty}\leq\|u_{w,x}^{k-1}(\cdot,t)\|_{W^{1,1}}\leq AA_1\\ \|u_{o,x}^{k-1}(\cdot,t)\|_{L^\infty}\leq\|u_{o,x}^{k-1}(\cdot,t)\|_{W^{1,1}}\leq AA_1\end{cases}\tag{4.86}$$

for $t\in[0,T_0]$.

By virtue of $(4.85)_1$, $(4.85)_2$, and (4.86), we can find positive constants C, k_0 and k_1 independent of T_0, A, and A_1 and where $T_0\leq T_1$ for some $T_1>0$ which reflects smallness on time, such that

$$\begin{cases}k_0\leq m^k\leq k_1,\ \text{and}\ k_0\leq n^k\leq k_1\ \text{on}\ [0,1]\times[0,T_0],\\ \|\frac{\partial P_w(m^k,n^k)}{\partial n^k}\|_{L^\infty([0,1]\times[0,T_0])}\leq C,\ \|\frac{\partial P_w(m^k,n^k)}{\partial m^k}\|_{L^\infty([0,1]\times[0,T_0])}\leq C,\\ \|\frac{\partial P_o(m^k,n^k)}{\partial n^k}\|_{L^\infty([0,1]\times[0,T_0])}\leq C,\ \|\frac{\partial P_o(m^k,n^k)}{\partial m^k}\|_{L^\infty([0,1]\times[0,T_0])}\leq C,\end{cases}\tag{4.87}$$

and

$$\begin{cases}\displaystyle\int_0^1|n_x^k(x,t)|^2dx\leq C,\\ \displaystyle\int_0^1|m_x^k(x,t)|^2dx\leq C.\end{cases}\tag{4.88}$$

In fact, $(4.87)_1$ as well as (4.88) are straightforward consequences of the fact that m^k and n^k are transported by the smooth vector fields u_w^{k-1} and u_o^{k-1}. Moreover, $(4.87)_{2,3}$ can then be deduced from the regularity of $(m,n)\mapsto\rho_s(m,n)$ and of $\rho_s\mapsto P_s(\rho_s)$ for $s=w,o$. See Step 2, Section 2.2 in [16] for more details.

Multiplying (4.85)$_3$ by u_o^k and u_{oxx}^k respectively, and integrating the results over $(0,1)$, we have

$$\begin{aligned}
\varepsilon_o \int_0^1 n^k |u_{ox}^k|^2\, dx =& - \int_0^1 s_o^k P_{ox}^k u_o^k\, dx - \int_0^1 \hat{k}_o^k |u_o^k|^2\, dx \\
&+ \int_0^1 \hat{k}^k (u_w^{k-1} - u_o^k) u_o^k\, dx - \int_0^1 n^k g u_o^k\, dx \\
\leq& -\frac{1}{2}\int_0^1 \hat{k}_o^k |u_o^k|^2\, dx + \frac{1}{2}\int_0^1 \hat{k}^k |u_w^{k-1}|^2\, dx - \frac{1}{2}\int_0^1 \hat{k}^k |u_o^k|^2\, dx + C \\
\leq& -\frac{1}{2}\int_0^1 \hat{k}_o^k |u_o^k|^2\, dx + \frac{I_{wo}k_1}{2}(AA_1)^2 - \frac{1}{2}\int_0^1 \hat{k}^k |u_o^k|^2\, dx + C,
\end{aligned} \tag{4.89}$$

and

$$\begin{aligned}
&\varepsilon_o \int_0^1 n^k |u_{oxx}^k|^2\, dx = -\varepsilon_o \int_0^1 (n^k)_x u_{ox}^k u_{oxx}^k\, dx + \int_0^1 s_o^k P_{ox}^k u_{oxx}^k\, dx \\
&+ \int_0^1 \hat{k}_o^k u_o^k u_{oxx}^k\, dx - \int_0^1 \hat{k}^k (u_w^{k-1} - u_o^k) u_{oxx}^k\, dx + \int_0^1 n^k g u_{oxx}^k\, dx \\
\leq& \frac{\varepsilon_o}{2}\int_0^1 n^k |u_{oxx}^k|^2\, dx + \frac{5\varepsilon_o}{2}\int_0^1 \frac{1}{n^k}|(n^k)_x|^2 |u_{ox}^k|^2\, dx + \frac{C}{\varepsilon_o} \\
&+ \frac{5}{2\varepsilon_o}\int_0^1 \frac{1}{n^k}|\hat{k}_o^k|^2 |u_o^k|^2\, dx + \frac{5}{2\varepsilon_o}\int_0^1 \frac{1}{n^k}|\hat{k}^k|^2 |u_w^{k-1} - u_o^k|^2\, dx \\
\leq& \frac{\varepsilon_o}{2}\int_0^1 n^k |u_{oxx}^k|^2\, dx + \frac{5\varepsilon_o}{2k_0}\int_0^1 |(n^k)_x|^2 |u_{ox}^k|^2\, dx + \frac{C}{\varepsilon_o} + \frac{5I_o}{2\varepsilon_o}\int_0^1 \hat{k}_o^k |u_o^k|^2\, dx \\
&+ \frac{5(I_{wo})^2 k_1 (AA_1)^2}{\varepsilon_o} + \frac{5I_{wo}}{\varepsilon_o}\int_0^1 \hat{k}^k |u_o^k|^2\, dx \\
\leq& \frac{\varepsilon_o}{2}\int_0^1 n^k |u_{oxx}^k|^2\, dx + \frac{5C\varepsilon_o}{2k_0}\Big\| |u_{ox}^k|^2 \Big\|_{L^\infty} + \frac{C}{\varepsilon_o} + \frac{5I_o}{2\varepsilon_o}\int_0^1 \hat{k}_o^k |u_o^k|^2\, dx \\
&+ \frac{5(I_{wo})^2 k_1 (AA_1)^2}{\varepsilon_o} + \frac{5I_{wo}}{\varepsilon_o}\int_0^1 \hat{k}^k |u_o^k|^2\, dx,
\end{aligned} \tag{4.90}$$

where we have used Cauchy inequality, (4.87), (4.88). Note that we obtain

$$\begin{aligned}
\Big\| |u_{ox}^k|^2 \Big\|_{L^\infty} \leq& \int_0^1 |u_{ox}^k|^2\, dx + 2\|u_{ox}^k\|_{L^2}\|u_{oxx}^k\|_{L^2} \\
\leq& (1+\frac{1}{\delta})\int_0^1 |u_{ox}^k|^2\, dx + \delta \int_0^1 |u_{oxx}^k|^2\, dx,
\end{aligned} \tag{4.91}$$

for any small $\delta > 0$, by using Sobolev inequality, Hölder inequality and Cauchy inequality.

By virtue of (4.87), (4.89), (4.90), and (4.91), we have

$$\begin{cases}
\displaystyle\int_0^1 |u_{ox}^k|^2\, dx \leq \frac{1}{\varepsilon_o}\Big[\frac{I_{wo}k_1}{2k_0}(AA_1)^2 + \frac{C}{k_0}\Big], \\
\displaystyle\int_0^1 \hat{k}_o^k |u_o^k|^2\, dx + \int_0^1 \hat{k}^k |u_o^k|^2\, dx \leq I_{wo}k_1(AA_1)^2 + 2C,
\end{cases} \tag{4.92}$$

and

$$\begin{aligned}\int_0^1 |u^k_{oxx}|^2\,dx \le \frac{10C}{(k_0)^2}(1+\frac{10C}{k_0})\int_0^1 |u^k_{ox}|^2\,dx + \frac{4C}{(\varepsilon_o)^2k_0}\\ + \frac{10I_o}{(\varepsilon_o)^2k_0}\int_0^1 \hat{k}^k_o|u^k_o|^2\,dx + \frac{20(I_{wo})^2k_1(AA_1)^2}{(\varepsilon_o)^2k_0} + \frac{20I_{wo}}{(\varepsilon_o)^2k_0}\int_0^1 \hat{k}^k|u^k_o|^2\,dx,\end{aligned} \tag{4.93}$$

where we take $\delta = \frac{k_0}{10C}$.

Putting (4.92) into (4.93), we have

$$\begin{aligned}\int_0^1 |u^k_{oxx}|^2\,dx \le& \frac{10C}{(k_0)^2}(1+\frac{10C}{k_0})\Big(\frac{I_{wo}k_1}{2\varepsilon_o k_0}(AA_1)^2 + \frac{C}{\varepsilon_o k_0}\Big) + \frac{4C}{(\varepsilon_o)^2k_0}\\ &+\frac{20(I_{wo})^2k_1(AA_1)^2}{(\varepsilon_o)^2k_0} + \Big[\frac{10I_o}{(\varepsilon_o)^2k_0} + \frac{20I_{wo}}{(\varepsilon_o)^2k_0}\Big](I_{wo}k_1(AA_1)^2 + 2C)\\ =&E_{\varepsilon_o,1}(AA_1)^2 + E_{\varepsilon_o,2},\end{aligned} \tag{4.94}$$

where

$$\begin{cases} E_{\varepsilon_o,1} = \frac{1}{\varepsilon_o}\Big[\frac{10C}{(k_0)^2}(1+\frac{10C}{k_0})\frac{I_{wo}k_1}{2k_0} + \frac{20(I_{wo})^2k_1}{\varepsilon_o k_0} + \frac{10I_oI_{wo}k_1}{\varepsilon_o k_0} + \frac{20(I_{wo})^2k_1}{\varepsilon_o k_0}\Big],\\ E_{\varepsilon_o,2} = \frac{1}{\varepsilon_o}\Big[\frac{10C}{(k_0)^2}(1+\frac{10C}{k_0})\frac{C}{k_0} + \frac{4C}{\varepsilon_o k_0} + \frac{20CI_o}{\varepsilon_o k_0} + \frac{40CI_{wo}}{\varepsilon_o k_0}\Big]. \end{cases}$$

In view of (4.92) and (4.94), we have

$$\|u^k_o(t)\|^2_{H^2} \le \Big[\frac{I_{wo}k_1}{k_0\varepsilon_o} + E_{\varepsilon_o,1}\Big](AA_1)^2 + \frac{2C}{\varepsilon_o k_0} + E_{\varepsilon_o,2}. \tag{4.95}$$

Similar to (4.89) and (4.90), we have

$$\varepsilon_w\int_0^1 m^k|u^k_{wx}|^2\,dx + \frac{1}{2}\int_0^1 \hat{k}^k_w|u^k_w|^2\,dx + \frac{1}{2}\int_0^1 \hat{k}^k|u^k_w|^2\,dx \le \frac{1}{2}\int_0^1 \hat{k}^k|u^k_o|^2\,dx + C,$$

and

$$\begin{aligned}\frac{\varepsilon_w}{2}\int_0^1 m^k|u^k_{wxx}|^2\,dx \le& \frac{5C\varepsilon_w}{k_0}(1+\frac{10C}{k_0})\int_0^1 |u^k_{wx}|^2\,dx + \frac{2C}{\varepsilon_w} + \frac{5I_w}{\varepsilon_w}\int_0^1 \hat{k}^k_w|u^k_w|^2\,dx\\ &+ \frac{10I_w}{\varepsilon_w}\int_0^1 \hat{k}^k|u^k_w|^2\,dx + \frac{10I_w}{\varepsilon_w}\int_0^1 \hat{k}^k|u^k_o|^2\,dx,\end{aligned}$$

which yield

$$\begin{cases} \int_0^1 |u^k_{wx}|^2\,dx \le \frac{1}{\varepsilon_w}[\frac{I_{wo}k_1}{2k_0}(AA_1)^2 + \frac{2C}{k_0}],\\ \int_0^1 \hat{k}^k_w|u^k_w|^2\,dx + \int_0^1 \hat{k}^k|u^k_w|^2\,dx \le I_{wo}k_1(AA_1)^2 + 4C, \end{cases} \tag{4.96}$$

and

$$\begin{aligned}\int_0^1 |u^k_{wxx}|^2\,dx \le& \frac{10C}{(k_0)^2}(1+\frac{10C}{k_0})\frac{1}{\varepsilon_w}[\frac{I_{wo}k_1}{2k_0}(AA_1)^2 + \frac{2C}{k_0}] + \frac{4C}{(\varepsilon_w)^2k_0}\\ &+ \Big[\frac{10I_w}{(\varepsilon_w)^2k_0} + \frac{20I_w}{(\varepsilon_w)^2k_0} + \frac{20I_w}{(\varepsilon_w)^2k_0}\Big](I_{wo}k_1(AA_1)^2 + 4C)\\ =&E_{\varepsilon_w,1}(AA_1)^2 + E_{\varepsilon_w,2}.\end{aligned} \tag{4.97}$$

where

$$\begin{cases} E_{\varepsilon_w,1} = \frac{1}{\varepsilon_w}\Big[\frac{10C}{(k_0)^2}(1+\frac{10C}{k_0})\frac{I_{wo}k_1}{2k_0} + \frac{10I_wI_{wo}k_1}{\varepsilon_w k_0} + \frac{20I_wI_{wo}k_1}{\varepsilon_w k_0} + \frac{20I_wI_{wo}k_1}{\varepsilon_w k_0}\Big], \\ E_{\varepsilon_w,2} = \frac{1}{\varepsilon_w}\Big[\frac{10C}{(k_0)^2}(1+\frac{10C}{k_0})\frac{2C}{k_0} + \frac{4C}{\varepsilon_w k_0} + \frac{40CI_w}{\varepsilon_w k_0} + \frac{80CI_w}{\varepsilon_w k_0} + \frac{80CI_w}{\varepsilon_w k_0}\Big]. \end{cases}$$

In view of (4.96) and (4.97), we have

$$\|u_w^k(t)\|_{H^2}^2 \le \Big[\frac{I_{wo}k_1}{k_0\varepsilon_w} + E_{\varepsilon_w,1}\Big](AA_1)^2 + \frac{4C}{\varepsilon_w k_0} + E_{\varepsilon_w,2}. \tag{4.98}$$

Letting

$$\max\Big\{\frac{I_{wo}k_1}{k_0\varepsilon_o} + E_{\varepsilon_o,1}, \frac{I_{wo}k_1}{k_0\varepsilon_w} + E_{\varepsilon_w,1}\Big\} \le \frac{1}{2} \tag{4.99}$$

which can be done by assuming for instance that ε_o and ε_w are large enough, we obtain from (4.95) and (4.98)

$$\|u_o^k(t)\|_{H^2} \le AA_1, \ \|u_w^k(t)\|_{H^2} \le AA_1, \tag{4.100}$$

where we choose that

$$A_1 \ge \frac{1}{A}\max\Big\{\Big(\frac{4C}{\varepsilon_o k_0} + 2E_{\varepsilon_o,2}\Big)^{\frac{1}{2}}, \Big(\frac{8C}{\varepsilon_w k_0} + 2E_{\varepsilon_w,2}\Big)^{\frac{1}{2}}\Big\} \tag{4.101}$$

Consequently, we have $u_w^k, u_o^k \in S$ for all $k = 1, 2, 3, \cdots$, if we assume that (4.99) is satisfied for A_1 given by (4.101) and for $T_0 \le T_1$.

Step 3. Compactness arguments.

By virtue of the estimates uniformly for k in Step 2, there exist a subsequence k_i $(i = 1, 2, 3, ...)$ and a (u_w, u_o, m, n), such that

$$\begin{aligned} &(u_w^{k_i}, u_o^{k_i}) \rightharpoonup (u_w, u_o) \text{ weak-* in } L^\infty([0,T_0]; H_0^1 \cap H^2), \\ &n^{k_i} \rightharpoonup n \text{ weak-* in } L^\infty([0,T_0]; H^1), \\ &m^{k_i} \rightharpoonup m \text{ weak-* in } L^\infty([0,T_0]; H^1), \\ &(n_t^{k_i}, m_t^{k_i}) \rightharpoonup (n_t, m_t) \text{ weak-* in } L^\infty([0,T_0]; L^2) \end{aligned} \tag{4.102}$$

as $k_i \to \infty$, where

$$(u_w, u_o) \in L^\infty([0,T_0]; H^2 \cap H_0^1), \text{ and } (m, n) \in L^\infty([0,T_0]; H^1),$$

and $n_t, m_t \in L^\infty([0,T_0]; L^2)$. Using the Aubin-Lions' compactness theorem, we can obtain some strong convergence. More precisely, there exists a subsequence still denoted by k_i without loss of generality $(i = 1, 2, 3, ...)$, such that

$$\begin{aligned} &n^{k_i} \to n \text{ in } C([0,1] \times [0,T_0]), \\ &m^{k_i} \to m \text{ in } C([0,1] \times [0,T_0]), \end{aligned} \tag{4.103}$$

as $k_i \to \infty$. It follows from (4.103) and (4.87) that

$$k_0 \le m \le k_1, \text{ and } k_0 \le n \le k_1 \text{ on } [0,1] \times [0,T_0].$$

Step 4. Convergence of $(u_w^{k_i-1}, u_o^{k_i-1})$.

We are going to investigate the convergence of the neighbor sequence of $(u_w^{k_i}, u_o^{k_i})$, i.e., $(u_w^{k_i-1}, u_o^{k_i-1})$, in order to make sure that their limits are the same, since they both appear in the approximate system (4.85).

To begin with, we need the estimates of the difference between m^{k+1} (n^{k+1}) and m^k (n^k), since there is a connection between velocity and mass due to the momentum equation. Denote $\bar{m}^{k+1} = m^{k+1} - m^k$ and $\bar{n}^{k+1} = n^{k+1} - n^k$. Then, from $(4.85)_{1,2}$ it follows

$$\begin{cases} \bar{m}_t^{k+1} + \bar{m}_x^{k+1} u_w^k + m_x^k (u_w^k - u_w^{k-1}) + \bar{m}^{k+1}[u_w^k]_x + m^k (u_w^k - u_w^{k-1})_x = 0, \\ \bar{m}^{k+1}(x,0) = 0 \end{cases} \tag{4.104}$$

and

$$\begin{cases} \bar{n}_t^{k+1} + \bar{n}_x^{k+1} u_o^k + n_x^k (u_o^k - u_o^{k-1}) + \bar{n}^{k+1}[u_o^k]_x + n^k (u_o^k - u_o^{k-1})_x = 0, \\ \bar{n}^{k+1}(x,0) = 0 \end{cases} \tag{4.105}$$

for $(x,t) \in [0,1] \times [0,T_0]$.

Using (4.104), we have

$$\frac{d}{dt}\int_0^1 |\bar{m}^{k+1}|^2\,dx \leq \bar{C}\|(u_w^k - u_w^{k-1})_x\|_{L^2}\|\bar{m}^{k+1}\|_{L^2} + \bar{C}A\|\bar{m}^{k+1}\|_{L^2}^2, \tag{4.106}$$

where $\bar{C}$ is a generic positive constant depending only on the initial data, the upper bound of T_0 and other known constants but independent of k , A and T_0. Here we have used the facts that m_x^k is bounded in L^2 and that $u_w^k \in S$, and the Poincaré inequality. Similarly, we have

$$\frac{d}{dt}\int_0^1 |\bar{n}^{k+1}|^2\,dx \leq \bar{C}\|(u_o^k - u_o^{k-1})_x\|_{L^2}\|\bar{n}^{k+1}\|_{L^2} + \bar{C}A\|\bar{n}^{k+1}\|_{L^2}^2. \tag{4.107}$$

Using $(4.85)_3$, we have

$$\begin{aligned} \varepsilon_o[n^k(u_o^k - u_o^{k-1})_x]_x &= -\varepsilon_o[(n^k - n^{k-1})(u_o^{k-1})_x]_x + (s_o^k - s_o^{k-1})P_{ox}^k \\ &\quad + s_o^{k-1}[P_o^k - P_o^{k-1}]_x + g(n^k - n^{k-1}) + [\hat{k}_o(m^k,n^k) - \hat{k}_o(m^{k-1},n^{k-1})]u_o^{k-1} \\ &\quad + \hat{k}_o^k(u_o^k - u_o^{k-1}) - \hat{k}^k[u_w^{k-1} - u_w^{k-2} - (u_o^k - u_o^{k-1})] \\ &\quad - [\hat{k}(m^k,n^k) - \hat{k}(m^{k-1},n^{k-1})](u_w^{k-2} - u_o^{k-1}), \end{aligned} \tag{4.108}$$

where $k = 2,3,4,\cdots$.

Denote $\bar{u_o}^{k+1} = u_o^{k+1} - u_o^k$ and $\bar{u_w}^{k+1} = u_w^{k+1} - u_w^k$. Then similar to the estimate of u_o^k (see (4.89)), the $\|(u_o^k - u_o^{k-1})_x\|_{L^2}$ can be evaluated as follows:

$$\begin{aligned} \|[\bar{u_o}^k]_x\|_{L^2}^2 &\leq \bar{C}\|\bar{n}^k(u_o^{k-1})_x\|_{L^2}^2 + \frac{\bar{C}}{(\varepsilon_o)^2}\|(s_o^k - s_o^{k-1})P_{ox}^k\|_{L^1}^2 \\ &+ \frac{\bar{C}}{(\varepsilon_o)^2}\|[s_o^{k-1}]_x(P_o^k - P_o^{k-1})\|_{L^1}^2 + \frac{\bar{C}}{(\varepsilon_o)^2}\|s_o^{k-1}(P_o^k - P_o^{k-1})\|_{L^2}^2 + \frac{\bar{C}}{(\varepsilon_o)^2}\|\bar{m}^k\|_{L^2}^2 \\ &- \frac{1}{\varepsilon_o k_0}\|\sqrt{\hat{k}_o^k}\bar{u_o}^k\|_{L^2}^2 + \frac{\bar{C}}{(\varepsilon_o)^2}\|\hat{k}_o(m^k,n^k) - \hat{k}_o(m^{k-1},n^{k-1})\|_{L^2}^2 \\ &- \frac{1}{2\varepsilon_o k_0}\|\sqrt{\hat{k}^k}\bar{u_o}^k\|_{L^2}^2 + \frac{1}{2\varepsilon_o k_0}\|\sqrt{\hat{k}^k}\bar{u_w}^{k-1}\|_{L^2}^2 \\ &+ \frac{\bar{C}}{(\varepsilon_o)^2}\|\hat{k}(m^k,n^k) - \hat{k}(m^{k-1},n^{k-1})\|_{L^2}^2, \end{aligned} \tag{4.109}$$

where $k = 2,3,4,\cdots$. Note that

$$\begin{cases} |s_o^k - s_o^{k-1}| \leq \bar{C}(|\bar{m}^k| + |\bar{n}^k|) \text{ and } |P_o^k - P_o^{k-1}| \leq \bar{C}(|\bar{m}^k| + |\bar{n}^k|), \\ |\hat{k}_o(m^k,n^k) - \hat{k}_o(m^{k-1},n^{k-1})| \leq \bar{C}(|\bar{m}^k| + |\bar{n}^k|) \\ \text{and } |\hat{k}(m^k,n^k) - \hat{k}(m^{k-1},n^{k-1})| \leq \bar{C}(|\bar{m}^k| + |\bar{n}^k|). \end{cases}$$

This, together with Hölder inequality, (4.109) and the boundedness of P_{ox}^k and $[s_o^{k-1}]_x$ in L^2, implies that

$$\begin{aligned}\|[\bar{u_o}^k]_x\|_{L^2}^2 \le& \bar{C}(1+A^2)(\|\bar{m}^k\|_{L^2}^2+\|\bar{n}^k\|_{L^2}^2)-\frac{1}{\varepsilon_o k_0}\|\sqrt{\hat{k}_o^k}\,\bar{u_o}^k\|_{L^2}^2\\ &-\frac{1}{2\varepsilon_o k_0}\|\sqrt{\hat{k}^k}\,\bar{u_o}^k\|_{L^2}^2+\frac{1}{2\varepsilon_o k_0}\|\sqrt{\hat{k}^k}\,\bar{u_w}^{k-1}\|_{L^2}^2,\end{aligned}\tag{4.110}$$

where $k=2,3,4,\cdots$.

Similarly, by virtue of $(4.85)_4$, we have

$$\begin{aligned}&\varepsilon_w[m^k(u_w^k-u_w^{k-1})_x]_x\\ &=-\varepsilon_w[(m^k-m^{k-1})(u_w^{k-1})_x]_x+(s_w^k-s_w^{k-1})P_{wx}^k+s_w^{k-1}[P_w^k-P_w^{k-1}]_x\\ &+g(m^k-m^{k-1})+\hat{k}_w^k(u_w^k-u_w^{k-1})+[\hat{k}_w(m^k,n^k)-\hat{k}_w(m^{k-1},n^{k-1})]u_w^{k-1}\\ &+\hat{k}^k[u_w^k-u_w^{k-1}-(u_o^k-u_o^{k-1})]+[\hat{k}(m^k,n^k)-\hat{k}(m^{k-1},n^{k-1})](u_w^{k-1}-u_o^{k-1}),\end{aligned}\tag{4.111}$$

and

$$\begin{aligned}\|[\bar{u_w}^k]_x\|_{L^2}^2 \le& \bar{C}(1+A^2)(\|\bar{m}^k\|_{L^2}^2+\|\bar{n}^k\|_{L^2}^2)-\frac{1}{\varepsilon_w k_0}\|\sqrt{\hat{k}_w^k}\,\bar{u_w}^k\|_{L^2}^2\\ &-\frac{1}{2\varepsilon_w k_0}\|\sqrt{\hat{k}^k}\,\bar{u_w}^k\|_{L^2}^2+\frac{1}{2\varepsilon_w k_0}\|\sqrt{\hat{k}^k}\,\bar{u_o}^k\|_{L^2}^2,\end{aligned}\tag{4.112}$$

where $k=2,3,4,\cdots$.

Putting (4.110) into (4.112), we have

$$\begin{aligned}\|[\bar{u_w}^k]_x\|_{L^2}^2 \le& \bar{C}_1(\|\bar{m}^k\|_{L^2}^2+\|\bar{n}^k\|_{L^2}^2)+\frac{1}{2\varepsilon_w k_0}\|\sqrt{\hat{k}^k}\,\bar{u_w}^{k-1}\|_{L^2}^2\\ \le& \bar{C}_1(\|\bar{m}^k\|_{L^2}^2+\|\bar{n}^k\|_{L^2}^2)+\frac{I_{wo}k_1}{2\varepsilon_w k_0}\|[\bar{u_w}^{k-1}]_x\|_{L^2}^2,\end{aligned}\tag{4.113}$$

for $k=2,3,4,\cdots$, where we have used (4.87) and Sobolev inequality.

Combining (4.106), (4.107), (4.110) and (4.113) with Cauchy inequality, we have

$$\begin{aligned}&\frac{d}{dt}\int_0^1(|\bar{m}^{k+1}|^2+|\bar{n}^{k+1}|^2)\,dx+\|(\bar{u_w}^{k+1})_x\|_{L^2}^2+\|(\bar{u_o}^{k+1})_x\|_{L^2}^2\\ &\le\bar{C}_2(\|\bar{m}^{k+1}\|_{L^2}^2+\|\bar{n}^{k+1}\|_{L^2}^2)+\Big(\frac{I_{wo}k_1}{\varepsilon_w k_0}+\frac{I_{wo}k_1}{\varepsilon_o k_0}\Big)(\|(\bar{u_w}^k)_x\|_{L^2}^2+\|(\bar{u_o}^k)_x\|_{L^2}^2),\end{aligned}$$

which yields

$$\frac{d}{dt}f^{k+1}(t)+g^{k+1}(t)\le\bar{C}_2f^{k+1}(t)+\Big(\frac{I_{wo}k_1}{\varepsilon_w k_0}+\frac{I_{wo}k_1}{\varepsilon_o k_0}\Big)g^k(t),\tag{4.114}$$

where

$$f^k=\int_0^1(|\bar{m}^k|^2+|\bar{n}^k|^2)\,dx,\ \ g^k=\|(\bar{u_w}^k)_x\|_{L^2}^2+\|(\bar{u_o}^k)_x\|_{L^2}^2.$$

Then, (4.114) together with Gronwall inequality yields

$$f^{k+1}(t)\le\Big(\frac{I_{wo}k_1}{\varepsilon_w k_0}+\frac{I_{wo}k_1}{\varepsilon_o k_0}\Big)\int_0^t e^{\bar{C}_2(t-s)}g^k(s)\,ds.\tag{4.115}$$

Integrating (4.114) over $[0,T_0]$, and using (4.115), we have

$$\int_0^{T_0}g^{k+1}(s)\,ds\le\Big(\bar{C}_2T_0e^{\bar{C}_2T_0}+1\Big)\Big(\frac{I_{wo}k_1}{\varepsilon_w k_0}+\frac{I_{wo}k_1}{\varepsilon_o k_0}\Big)\int_0^{T_0}g^k(s)\,ds.\tag{4.116}$$

Letting

$$\begin{cases} \bar{C}_2 T_0 e^{\bar{C}_2 T_0} \le 1, \\ \frac{I_{wo}k_1}{\varepsilon_w k_0} + \frac{I_{wo}k_1}{\varepsilon_o k_0} \le \frac{1}{4} \end{cases} \tag{4.117}$$

for small T_0 and large ε_o, ε_w. We note that (4.116) and (4.115) imply that

$$\begin{cases} \Sigma_{k=1}^{\infty} \displaystyle\int_0^{T_0} g^{k+1}(t)\, dt < \infty, \\ \Sigma_{k=1}^{\infty} \displaystyle\max_{t \in [0,T_0]} f^{k+1}(t) < \infty. \end{cases} \tag{4.118}$$

Thus, (4.118) combined with $(4.102)_1$ implies that

$$(u_w^{k_i-1}, u_o^{k_i-1}) \rightharpoonup (u_w, u_o) \text{ weak-* in } L^\infty([0,T_0]; H_0^1 \cap H^2) \tag{4.119}$$

as $k_i \to \infty$.

Step 5. Conclusion.

Based on (4.102), (4.103), and (4.119), it can be verified that (m, n, u_w, u_o) is a unique solution of (2.14)-(2.16). See [16] for more details. Thus the proof of Theorem 2.1 is complete.

Appendix B: Some issues related to the general model (1.1). The purpose of this section is to elaborate on some of the differences between the model (1.1) and other Brinkman-type of two-phase models like the one mentioned in Remark 1.2.

The incompressible, viscous version of the generalized two-phase model (1.1). It seems useful to impose some simplifying assumptions on the model (1.1) and derive a reduced version of it. We may impose the following assumptions:

- incompressible fluid, i.e., ρ_w and ρ_o are constant.
- porosity ϕ is constant

We may rescale the time such that the porosity disappears in the time derivative terms. The mass and momentum equations in (1.1) now take the form

$$\begin{aligned} (s_o)_t + \nabla \cdot (\phi s_o \mathbf{u}_o) &= \frac{Q_o}{\rho_o}, \qquad \mathbf{U}_o = \phi s_o \mathbf{u}_o \\ (s_w)_t + \nabla \cdot (\phi s_w \mathbf{u}_w) &= \frac{Q_w}{\rho_w}, \qquad \mathbf{U}_w = \phi s_w \mathbf{u}_w \\ s_o[\nabla P_w + \nabla P_c + \rho_o \mathbf{g}] - \varepsilon_o \rho_o \nabla \cdot (s_o \nabla \mathbf{u}_o) &= +\hat{k}\mathbf{u}_w - [\hat{k}_o + \hat{k}]\mathbf{u}_o \\ s_w[\nabla P_w + \rho_w \mathbf{g}] - \varepsilon_w \rho_w \nabla \cdot (s_w \nabla \mathbf{u}_w) &= -[\hat{k}_w + \hat{k}]\mathbf{u}_w + \hat{k}\mathbf{u}_o, \end{aligned} \tag{4.120}$$

where we have used that $P_c = P_o - P_w$. Note that in the rest of this paper we will use $\hat{k}_{ow} = \hat{k}$. We can solve for $\mathbf{u}_w$ and $\mathbf{u}_o$ from the two momentum balance equations in (4.120) and find that

$$\begin{aligned} \mathbf{u}_w = & \\ & - \frac{[s_w \hat{k}_o] + \hat{k}}{\hat{k}_o \hat{k}_w + \hat{k}[\hat{k}_o + \hat{k}_w]} \nabla P_w - \frac{s_o \hat{k}}{\hat{k}_o \hat{k}_w + \hat{k}[\hat{k}_o + \hat{k}_w]} \nabla P_c - \frac{(s_w \rho_w + s_o \rho_o)\hat{k} + s_w \rho_w \hat{k}_o}{\hat{k}_o \hat{k}_w + \hat{k}[\hat{k}_o + \hat{k}_w]} \mathbf{g} \\ & + (\varepsilon_w \rho_w) \frac{[\hat{k}_o + \hat{k}]}{\hat{k}_o \hat{k}_w + \hat{k}[\hat{k}_o + \hat{k}_w]} \nabla \cdot (s_w \nabla \mathbf{u}_w) + (\varepsilon_o \rho_o) \frac{\hat{k}}{\hat{k}_o \hat{k}_w + \hat{k}[\hat{k}_o + \hat{k}_w]} \nabla \cdot (s_o \nabla \mathbf{u}_o), \end{aligned}$$

$$
\begin{aligned}
&\mathbf{u}_o = \\
&-\frac{[s_o\hat{k}_w]+\hat{k}}{\hat{k}_o\hat{k}_w+\hat{k}[\hat{k}_o+\hat{k}_w]}\nabla P_w-\frac{s_o[\hat{k}_w+\hat{k}]}{\hat{k}_o\hat{k}_w+\hat{k}[\hat{k}_o+\hat{k}_w]}\nabla P_c-\frac{(s_w\rho_w+s_o\rho_o)\hat{k}+s_o\rho_o\hat{k}_w}{\hat{k}_o\hat{k}_w+\hat{k}[\hat{k}_o+\hat{k}_w]}\mathbf{g}\\
&+(\varepsilon_w\rho_w)\frac{\hat{k}}{\hat{k}_o\hat{k}_w+\hat{k}[\hat{k}_o+\hat{k}_w]}\nabla\cdot(s_w\nabla\mathbf{u}_w)+(\varepsilon_o\rho_o)\frac{[\hat{k}_w+\hat{k}]}{\hat{k}_o\hat{k}_w+\hat{k}[\hat{k}_o+\hat{k}_w]}\nabla\cdot(s_o\nabla\mathbf{u}_o).
\end{aligned}
\tag{4.121}
$$

That is, we find for $\mathbf{U}_i = \phi s_i \mathbf{u}_i$:

$$
\begin{aligned}
&\mathbf{U}_w = \\
&-\hat{\lambda}_w\nabla P_w-\frac{\phi s_o s_w\hat{k}}{\hat{k}_o\hat{k}_w+\hat{k}[\hat{k}_o+\hat{k}_w]}\nabla P_c-\hat{\lambda}_w\rho_w\mathbf{g}+\frac{\phi s_o s_w\hat{k}\Delta\rho}{\hat{k}_o\hat{k}_w+\hat{k}[\hat{k}_o+\hat{k}_w]}\mathbf{g}\\
&+(\varepsilon_w\phi\rho_w)\frac{s_w[\hat{k}_o+\hat{k}]}{\hat{k}_o\hat{k}_w+\hat{k}[\hat{k}_o+\hat{k}_w]}\nabla\cdot(s_w\nabla\mathbf{u}_w)\\
&+(\varepsilon_o\phi\rho_o)\frac{s_w\hat{k}}{\hat{k}_o\hat{k}_w+\hat{k}[\hat{k}_o+\hat{k}_w]}\nabla\cdot(s_o\nabla\mathbf{u}_o),\\
&\mathbf{U}_o = \\
&-\hat{\lambda}_o\nabla P_w-\hat{\lambda}_o\nabla P_c+\frac{\phi s_o s_w\hat{k}}{\hat{k}_o\hat{k}_w+\hat{k}[\hat{k}_o+\hat{k}_w]}\nabla P_c-\hat{\lambda}_o\rho_o\mathbf{g}-\frac{\phi s_o s_w\hat{k}\Delta\rho}{\hat{k}_o\hat{k}_w+\hat{k}[\hat{k}_o+\hat{k}_w]}\mathbf{g}\\
&+(\varepsilon_w\phi\rho_w)\frac{s_o\hat{k}}{\hat{k}_o\hat{k}_w+\hat{k}[\hat{k}_o+\hat{k}_w]}\nabla\cdot(s_w\nabla\mathbf{u}_w)\\
&+(\varepsilon_o\phi\rho_o)\frac{s_o[\hat{k}_w+\hat{k}]}{\hat{k}_o\hat{k}_w+\hat{k}[\hat{k}_o+\hat{k}_w]}\nabla\cdot(s_o\nabla\mathbf{u}_o),
\end{aligned}
\tag{4.122}
$$

where $\Delta\rho = \rho_w - \rho_o$ and with generalized mobility functions $\hat{\lambda}_i$ $(i = w, o, T)$ of the form

$$
\begin{aligned}
\hat{\lambda}_w &= \hat{\lambda}_w(s_w) = \frac{[s_w^2\hat{k}_o]+s_w\hat{k}}{\hat{k}_o\hat{k}_w+\hat{k}[\hat{k}_o+\hat{k}_w]}\phi,\\
\hat{\lambda}_o &= \hat{\lambda}_o(s_w) = \frac{[s_o^2\hat{k}_w]+s_o\hat{k}}{\hat{k}_o\hat{k}_w+\hat{k}[\hat{k}_o+\hat{k}_w]}\phi,\\
\hat{\lambda}_T &= \hat{\lambda}_T(s_w) = \hat{\lambda}_w(s_w)+\hat{\lambda}_o(s_w).
\end{aligned}
\tag{4.123}
$$

Note that the resistance force coefficients $\hat{k}_w(s_w), \hat{k}_o(s_w), \hat{k}(s_w)$ typically are functions of water saturation s_w. From (4.122) we find

$$
\begin{aligned}
&\mathbf{U}_T = \mathbf{U}_w + \mathbf{U}_o = -\hat{\lambda}_T\nabla P_w - \hat{\lambda}_o\nabla P_c - [\hat{\lambda}_w\rho_w + \hat{\lambda}_o\rho_o]\mathbf{g}\\
&+(\varepsilon_w\phi\rho_w)\frac{s_w\hat{k}_o+\hat{k}}{\hat{k}_o\hat{k}_w+\hat{k}[\hat{k}_o+\hat{k}_w]}\nabla\cdot(s_w\nabla\mathbf{u}_w)+(\varepsilon_o\phi\rho_o)\frac{s_o\hat{k}_w+\hat{k}}{\hat{k}_o\hat{k}_w+\hat{k}[\hat{k}_o+\hat{k}_w]}\nabla\cdot(s_o\nabla\mathbf{u}_o).
\end{aligned}
\tag{4.124}
$$

Remark 4.1. A fundamental difference between the above expression (4.124) for the total superficial velocity $\mathbf{U}_T$ for the mixture and the model described in Remark 1.2 and expressed by the mixture momentum balance equation (1.12), is the viscous terms. Taking the divergence of (4.124) combined with the sum of the two first equations of (4.120) and (1.3), we arrive at

$$\begin{aligned}\frac{Q_o}{\rho_o}+\frac{Q_w}{\rho_w} &= -\nabla\cdot(\hat{\lambda}_T\nabla P_w)-\nabla\cdot(\hat{\lambda}_o\nabla P_c)-\nabla\cdot([\hat{\lambda}_w\rho_w+\hat{\lambda}_o\rho_o]\mathbf{g})\\ &\quad+\nabla\cdot\Big((\varepsilon_w\phi\rho_w)\frac{s_w\hat{k}_o+\hat{k}}{\hat{k}_o\hat{k}_w+\hat{k}[\hat{k}_o+\hat{k}_w]}\nabla\cdot(s_w\nabla\mathbf{u}_w)\Big)\\ &\quad+\nabla\cdot\Big((\varepsilon_o\phi\rho_o)\frac{s_o\hat{k}_w+\hat{k}}{\hat{k}_o\hat{k}_w+\hat{k}[\hat{k}_o+\hat{k}_w]}\nabla\cdot(s_o\nabla\mathbf{u}_o)\Big).\end{aligned}\tag{4.125}$$

This gives an elliptic pressure equation for P_w. However, due to the appearance of complex viscous terms, it seems not easy to obtain H^1-estimate of P_w needed for compactness of the non-conservative pressure term $s_w\nabla P_w$ in the momentum balance equation.

We may conclude that it does not seem straightforward to analyse the incompressible, viscous model (4.120) by relying on an approach similar to the one used in [9]. The main reason is the use of interstitial fluid velocity $\mathbf{u}_i$ instead of Darcy velocity $\mathbf{U}_i=\phi s_i\mathbf{u}_i$.

The incompressible, inviscid case $\varepsilon_w=\varepsilon_o=0$. It is instructive to also derive the model where viscous terms are set to zero. Hence, in the following we consider the incompressible model (4.120) where we assume that viscous terms in the momentum equations are ignored by setting $\varepsilon_w=\varepsilon_o=0$. We observe that (4.124) gives

$$\nabla P_w=-\frac{\mathbf{U}_T}{\hat{\lambda}_T}-\frac{\hat{\lambda}_o}{\hat{\lambda}_T}\nabla P_c-[\hat{f}_w\rho_w+\hat{f}_o\rho_o]\mathbf{g},\tag{4.126}$$

where

$$\hat{f}_w=\frac{\hat{\lambda}_w}{\hat{\lambda}_T}=\hat{f}_w(s_w),\qquad \hat{f}_o=\frac{\hat{\lambda}_o}{\hat{\lambda}_T}=\hat{f}_o(s_w)\tag{4.127}$$

are the standard fractional flow functions which satisfy that $\hat{f}_w+\hat{f}_o=1$. Using (4.126) in (4.122) we get

$$\begin{aligned}\mathbf{U}_w &= -\hat{\lambda}_w\nabla P_w-\frac{\phi s_o s_w\hat{k}}{(\hat{k}_o\hat{k}_w+\hat{k}[\hat{k}_o+\hat{k}_w])}\nabla P_c-\rho_w\hat{\lambda}_w\mathbf{g}+\frac{\phi s_o s_w\Delta\rho\hat{k}}{(\hat{k}_o\hat{k}_w+\hat{k}[\hat{k}_o+\hat{k}_w])}\mathbf{g}\\ &= \mathbf{U}_T\frac{\hat{\lambda}_w}{\hat{\lambda}_T}+\frac{\hat{\lambda}_w[\hat{\lambda}_w\rho_w+\hat{\lambda}_o\rho_o]}{\hat{\lambda}_T}\mathbf{g}+\frac{\hat{\lambda}_w\hat{\lambda}_o}{\hat{\lambda}_T}\nabla P_c-\rho_w\hat{\lambda}_w\mathbf{g}\\ &\qquad\qquad-\frac{\phi s_o s_w\hat{k}}{(\hat{k}_o\hat{k}_w+\hat{k}[\hat{k}_o+\hat{k}_w])}\nabla P_c+\frac{\phi s_o s_w\Delta\rho\hat{k}}{(\hat{k}_o\hat{k}_w+\hat{k}[\hat{k}_o+\hat{k}_w])}\mathbf{g}\\ &= \mathbf{U}_T\hat{f}_w+\Big(-\hat{f}_w\hat{\lambda}_o+\frac{\phi s_o s_w\hat{k}}{(\hat{k}_o\hat{k}_w+\hat{k}[\hat{k}_o+\hat{k}_w])}\Big)\Delta\rho\mathbf{g}\\ &\qquad\qquad-\Big(-\hat{f}_w\hat{\lambda}_o+\frac{s_o s_w\hat{k}}{(\hat{k}_o\hat{k}_w+\hat{k}[\hat{k}_o+\hat{k}_w])}\Big)\nabla P_c\\ &= \mathbf{U}_T\hat{f}_w(s_w)-\hat{h}(s_w)\Delta\rho\mathbf{g}+\hat{h}(s_w)\nabla P_c(s_w),\end{aligned}\tag{4.128}$$

where $\Delta\rho = \rho_w - \rho_o$ and $\hat{h}(s_w)$ is defined by

$$\hat{h} \stackrel{\text{def}}{:=} \hat{f}_w \hat{\lambda}_o - \frac{\phi s_o s_w \hat{k}}{(\hat{k}_o \hat{k}_w + \hat{k}[\hat{k}_o + \hat{k}_w])} = \frac{s_w^2(1-s_w)^2}{s_w^2 \hat{k}_o + s_o^2 \hat{k}_w + \hat{k}} \phi = \hat{h}(s_w). \tag{4.129}$$

From this, it also follows that

$$\mathbf{U}_o = \mathbf{U}_T - \mathbf{U}_w = \mathbf{U}_T(1 - \hat{f}_w(s_w)) + \hat{h}(s_w)\Delta\rho\mathbf{g} - \hat{h}(s_w)\nabla P_c(s_w). \tag{4.130}$$

Consequently, the model (4.120) has been reduced to solving the following conservation law

$$\partial_t s_w + \nabla \cdot \mathbf{U}_w = \frac{Q_w}{\rho_w}, \tag{4.131}$$

where $\mathbf{U}_w = \mathbf{U}_w(s_w)$ is given by (4.128).

Remark 4.2. The model (4.131) combined with (4.128) (last line), (4.127), (4.129), and the generalized mobility functions as defined by (4.123), recovers the classical incompressible immiscible model except that we now also include for an additional water-oil drag force effect through the term $\hat{k}$. Setting this term to zero reproduces exactly the classical formulation. To obtain closed expressions for the generalized mobility functions $\hat{\lambda}_i$ as well as for $\hat{h}(s_w)$, we must specify appropriate functional correlations for (i) the water-rock resistance force $\hat{k}_w$; (ii) the oil-rock resistance force $\hat{k}_o$; (iii) the water-oil drag force effect $\hat{k}$. In the recent work [31] we used correlations of the following form:

$$\hat{k}_w = I_w \frac{\mu_w}{K} \phi s_w^{\alpha}, \qquad \hat{k}_o = I_o \frac{\mu_o}{K} \phi s_w^{\beta}, \qquad \hat{k} = I \frac{\mu_w \mu_o}{K} \phi s_w (1 - s_w), \tag{4.132}$$

where μ_i is fluid viscosity, K absolute permeability, I_w, I_o, I are parameters that characterize the strength of the resistance force (similar to the end points of relative permeability in classical formulation). The generalized mobility functions introduced above account for two different resistance forces, instead of only one, as in standard Darcy's equation-based formulation. Mobility functions that are measured experimentally are known to generally depend on the flow configuration. Two main flow regimes are present in the expression for $\mathbf{U}_w$ given by (4.128) and $\mathbf{U}_o$ given by (4.130): Co-current flow (i.e., flow of water and oil in the same direction) represented by the first component $\mathbf{U}_T \hat{f}_w$ and counter-current flow (i.e., flow in the opposite direction) represented by $-\hat{h}(s_w)\Delta\rho\mathbf{g}$ and $\hat{h}(s_w)\nabla P_c(s_w)$ (compare with (4.130)). The fact that the fluid-fluid interaction term $\hat{k}$ is explicitly accounted for and appears in $\hat{h}$ (4.129) and mobility functions (4.123) implies that a more accurate understanding of water-oil flow mechanisms can be sought [31].

Appendix C: A pressure evolution equation. From the two mass balance equations we get after multiplying the n mass balance with ρ_w and the m mass balance with ρ_o and summing the two resulting equations

$$\begin{aligned} &\frac{\rho_w s_o}{C_o} P_{ot} + \frac{\rho_o s_w}{C_w} P_{wt} + \rho_w (s_o \rho_o u_o)_x + \rho_o (s_w \rho_w u_w)_x \\ &= -\rho_w \rho_o s_o Q_p - \rho_w \rho_o s_w Q_p + \rho_w \rho_o Q_I \end{aligned} \tag{4.133}$$

or

$$\kappa P_{ot} - \frac{\rho_o s_w}{C_w} P_c' s_{wt} + \rho_w (s_o \rho_o u_o)_x + \rho_o (s_w \rho_w u_w)_x = \rho_w \rho_o (Q_I - Q_p), \tag{4.134}$$

with

$$\kappa = s_o \rho_w \frac{1}{C_o} + s_w \rho_o \frac{1}{C_w} = s_o \rho_w \frac{\partial \rho_o}{\partial P_o} + s_w \rho_o \frac{\partial \rho_w}{\partial P_w}. \tag{4.135}$$

Clearly,

$$s_{wt}=-s_{ot}=-\Big(\frac{n}{\rho_o}\Big)_t=-\frac{1}{\rho_o}n_t+\frac{n}{\rho_o^2}\rho_{ot}=-\frac{1}{\rho_o}n_t+\frac{n}{C_o\rho_o^2}P_{ot}.$$

Consequently,

$$-\frac{\rho_o s_w}{C_w}P_c' s_{wt}=\frac{\rho_o s_w}{C_w}P_c'\Big[\frac{1}{\rho_o}n_t-\frac{n}{C_o\rho_o^2}P_{ot}\Big]=\frac{s_w P_c'}{C_w}n_t-\frac{s_o s_w P_c'}{C_w C_o}P_{ot}.$$

Using this in (4.134) we get

$$\kappa P_{ot}+\frac{s_w P_c'}{C_w}n_t-\frac{s_o s_w P_c'}{C_w C_o}P_{ot}+\rho_w(s_o\rho_o u_o)_x+\rho_o(s_w\rho_w u_w)_x=\rho_w\rho_o(Q_I-Q_p), \quad (4.136)$$

that is,

$$\begin{aligned}\Big[\kappa-\frac{s_o s_w P_c'}{C_w C_o}\Big]P_{ot}+\Big[\rho_w-\frac{s_w P_c'}{C_w}\Big](s_o\rho_o u_o)_x+\rho_o(s_w\rho_w u_w)_x&\\ =\rho_w\rho_o(Q_I-Q_p)+\frac{s_w P_c'}{C_w}nQ_p.&\end{aligned} \quad (4.137)$$

Note that

$$\Big[\kappa-\frac{s_o s_w P_c'}{C_w C_o}\Big]=\frac{s_o\tilde\rho_w}{C_o}+\frac{s_w\rho_o}{C_w}:=\tilde\kappa, \qquad \tilde\rho_w=\rho_w-\frac{s_w P_c'}{C_w}$$

so that

$$\tilde\kappa P_{ot}+\tilde\rho_w(nu_o)_x+\rho_o(mu_w)_x=\rho_w\rho_o(Q_I-Q_p)+\frac{s_w P_c'}{C_w}nQ_p \quad (4.138)$$

or

$$\begin{aligned}&P_{ot}+\tilde\eta\tilde\rho_w(nu_o)_x+\tilde\eta\rho_o(mu_w)_x=\tilde\eta\rho_w\rho_o(Q_I-Q_p)+\tilde\eta\frac{s_w P_c'}{C_w}nQ_p,\\ &\tilde\eta=\frac{1}{\tilde\kappa}=\frac{C_w C_o}{s_o\tilde\rho_w C_w+s_w\rho_o C_o}.\end{aligned} \quad (4.139)$$

Similarly, we have for P_w:

$$\kappa P_{wt}+\frac{\rho_w s_o P_c'}{C_o}s_{wt}+\rho_w(s_o\rho_o u_o)_x+\rho_o(s_w\rho_w u_w)_x=\rho_w\rho_o(Q_I-Q_p). \quad (4.140)$$

Clearly,

$$s_{wt}=\Big(\frac{m}{\rho_w}\Big)_t=\frac{1}{\rho_w}m_t-\frac{m}{\rho_w^2}\rho_{wt}=\frac{1}{\rho_w}m_t-\frac{m}{C_w\rho_w^2}P_{wt}.$$

Consequently,

$$\frac{\rho_w s_o}{C_o}P_c' s_{wt}=\frac{\rho_w s_o}{C_o}P_c'\Big[\frac{1}{\rho_w}m_t-\frac{m}{C_w\rho_w^2}P_{wt}\Big]=\frac{s_o P_c'}{C_o}m_t-\frac{s_w s_o P_c'}{C_w C_o}P_{wt}.$$

Using this in (4.140) we get

$$\kappa P_{wt}+\frac{s_o P_c'}{C_o}m_t-\frac{s_o s_w P_c'}{C_w C_o}P_{wt}+\rho_w(s_o\rho_o u_o)_x+\rho_o(s_w\rho_w u_w)_x=\rho_w\rho_o(Q_I-Q_p), \quad (4.141)$$

that is,

$$\begin{aligned}\Big[\kappa-\frac{s_o s_w P_c'}{C_w C_o}\Big]P_{wt}+\rho_w(s_o\rho_o u_o)_x+\Big[\rho_o-\frac{s_o P_c'}{C_o}\Big](s_w\rho_w u_w)_x&\\ =\rho_w\rho_o(Q_I-Q_p)-\frac{s_o P_c'}{C_o}(\rho_w Q_I-mQ_p).&\end{aligned} \quad (4.142)$$

Note that

$$\Big[\kappa - \frac{s_o s_w P_c'}{C_w C_o}\Big] = \frac{s_o \rho_w}{C_o} + \frac{s_w \tilde{\rho}_o}{C_w} := \tilde{\kappa}, \qquad \tilde{\rho}_o = \rho_o - \frac{s_o P_c'}{C_o},$$

so that

$$\tilde{\kappa} P_{wt} + \rho_w (n u_o)_x + \tilde{\rho}_o (m u_w)_x = \rho_w \rho_o (Q_I - Q_p) - \frac{s_o P_c'}{C_o}(\rho_w Q_I - m Q_p), \tag{4.143}$$

or

$$\begin{aligned} P_{wt} + \tilde{\eta}\rho_w (n u_o)_x + \tilde{\eta}\tilde{\rho}_o (m u_w)_x &= \tilde{\eta}\rho_w \rho_o (Q_I - Q_p) - \tilde{\eta}\frac{s_o P_c'}{C_o}(\rho_w Q_I - m Q_p), \\ \tilde{\eta} = \frac{1}{\tilde{\kappa}} &= \frac{C_w C_o}{s_o \rho_w C_w + s_w \tilde{\rho}_o C_o}. \end{aligned} \tag{4.144}$$

Appendix D: Discrete schemes for the compressible/incompressible version of (1.1).

A semi-discrete scheme for the compressible model. We consider discrete schemes for both the compressible and incompressible version of (2.14). For that purpose we introduce a reformulation that brings the compressible model closer to the incompressible model. In particular, we solve explicitly only for the mass transport of $m = s_w \rho_w$ whereas the mass n is computed implicitly. This will be in the spirit of the incompressible approach where we solve the mass balance equation for s_w and computes $s_o = 1 - s_w$. Details are given below.

The starting point is the model (2.14) with (n, m, u_w, u_o) as the main (unknown) variables. We rewrite the model in the following equivalent form with (m, P_w, u_w, u_o) as the main variables:

$$\begin{aligned} (m)_t + (m u_w)_x &= -m Q_p + \rho_w Q_I \\ P_{wt} + \tilde{\eta}\rho_w (n u_o)_x + \tilde{\eta}\tilde{\rho}_o (m u_w)_x &= \tilde{\eta}\rho_w \rho_o (Q_I - Q_p) - \tilde{\eta}\frac{s_o P_c'}{C_o}(\rho_w Q_I - m Q_p) \\ s_o (P_w + P_c)_x &= -(\hat{k}_o + \hat{k}) u_o + \hat{k} u_w + n g + \varepsilon_o (n u_{ox})_x \\ s_w (P_w)_x &= -(\hat{k}_w + \hat{k}) u_w + \hat{k} u_o + m g + \varepsilon_w (m u_{wx})_x \end{aligned} \tag{4.145}$$

with

$$\tilde{\eta} = \frac{C_w C_o}{s_o \rho_w C_w + s_w \tilde{\rho}_o C_o}, \qquad \tilde{\rho}_o = \rho_o - \frac{s_o P_c'}{C_o}. \tag{4.146}$$

We refer to Appendix C and (4.144) which gives the pressure evolution equation $(4.145)_2$. Note that s_w, s_o, n, P_o are determined by

$$\begin{aligned} s_w &= \frac{m}{\rho_w(P_w)}, \qquad s_o = 1 - s_w \\ n &= s_o \rho_o(P_o) = \Big(1 - \frac{m}{\rho_w(P_w)}\Big)\rho_o(P_o) = n(m, P_w) \\ P_o &= P_c(s_w) + P_w = P_o(m, P_w) \end{aligned} \tag{4.147}$$

We solve (4.145) on our domain Ω with boundary conditions

$$u_w|_{\partial\Omega} = u_o|_{\partial\Omega} = 0 \tag{4.148}$$

and initial condition

$$m(x, t=0) = m_0(x), \qquad P_w(x, t=0) = P_w(m_0(x), n_0(x)). \tag{4.149}$$

System of ODEs. We consider the domain $\Omega = [0,1]$ and introduce a grid of N_x cells with nodes x_j placed at the center of the cells

$$x_1 = \frac{1}{2}\Delta x, \quad x_2 = (1+\frac{1}{2})\Delta x, \quad \dots, \quad x_j = (j-\frac{1}{2})\Delta x, \quad \dots, \quad x_{N_x} = (N_x-\frac{1}{2})\Delta x$$

and cell interfaces $x_{j+1/2}$ at the cell interfaces

$$x_{1/2} = 0, \quad x_{3/2} = \Delta x, \quad \dots, \quad x_{j+1/2} = j\Delta x, \quad \dots, \quad x_{N_x+1/2} = N_x\Delta x = 1,$$

where $\Delta x = 1/N_x$. We introduce the approximate mass and pressure $\{m_j(t)\}_{j=1}^{N_x}$ and $\{P_{w,j}(t)\}_{j=1}^{N_x}$ associated with the nodes $\{x_j\}_{j=1}^{N_x}$ whereas the approximate velocities $\{u_{w,j+1/2}\}_{j=0}^{N_x}$ and $\{u_{o,j+1/2}\}_{j=0}^{N_x}$ are associated with the cell interfaces $\{x_{j+1/2}\}_{j=0}^{N_x}$. In the following we describe a semi-discrete version of (4.145).

Step 1: Mass transport. We solve for $m_j(t)$ by considering the following ODE corresponding to $(4.145)_1$:

$$\frac{dm_j}{dt} + \frac{1}{\Delta x}([mu_w]_{j+1/2} - [mu_w]_{j-1/2}) = -m_j Q_{p,j} + \rho_{wj} Q_{I,j}, \qquad m = s_w \rho_w \tag{4.150}$$

where

$$[mu_w]_{j+1/2} = \begin{cases} m_j u_{w,j+1/2}, & \text{if } u_{w,j+1/2} \geq 0; \\ m_{j+1} u_{w,j+1/2}, & \text{if } u_{w,j+1/2} < 0. \end{cases} \tag{4.151}$$

This can also be expressed as

$$[mu_w]_{j+1/2} = \frac{m_j + m_{j+1}}{2} u_{w,j+1/2} - \frac{1}{2}(m_{j+1} - m_j)|u_{w,j+1/2}|.$$

Step 2: Computation of velocities and pressure. Next, we solve for $P_{w,j}(t)$ and $u_{w,j+1/2}(t)$ and $u_{o,j+1/2}(t)$ by considering the following ODE system corresponding to $(4.145)_{2,3,4}$:

$$\begin{aligned} \frac{dP_{wj}}{dt} &+ \tilde{\eta}_j \rho_{wj} \frac{1}{\Delta x}([nu_o]_{j+1/2} - [nu_o]_{j-1/2}) \\ &+ \tilde{\eta}_j \tilde{\rho}_{oj} \frac{1}{\Delta x}([mu_w]_{j+1/2} - [mu_w]_{j-1/2}) \\ &= [\tilde{\eta}\rho_w\rho_o]_j (Q_{I,j} - Q_{p,j}) - \Big[\tilde{\eta}\frac{s_o P_c'}{C_o}\Big]_j (\rho_{wj} Q_{I,j} - m_j Q_{p,j}), \end{aligned} \tag{4.152}$$

which is combined with the momentum balance equations

$$\begin{aligned} s_{o,j+1/2}\frac{1}{\Delta x}(P_{w,j+1} - P_{w,j}) &= -s_{o,j+1/2}\frac{1}{\Delta x}(P_{c,j+1} - P_{c,j}) \\ &\quad -\hat{k}_{o,j+1/2} u_{o,j+1/2} + \hat{k}_{j+1/2}\Big(u_{w,j+1/2} - u_{o,j+1/2}\Big) + n_{j+1/2} g \\ &\quad +\varepsilon_o \frac{1}{\Delta x^2}\Big(n_{j+1}[u_{o,j+3/2} - u_{o,j+1/2}] - n_j[u_{o,j+1/2} - u_{o,j-1/2}]\Big), \\ s_{w,j+1/2}\frac{1}{\Delta x}(P_{w,j+1} - P_{w,j}) &= \\ &\quad -\hat{k}_{w,j+1/2} u_{w,j+1/2} - \hat{k}_{j+1/2}\Big(u_{w,j+1/2} - u_{o,j+1/2}\Big) + m_{j+1/2} g \\ &\quad +\varepsilon_w \frac{1}{\Delta x^2}\Big(m_{j+1}[u_{w,j+3/2} - u_{w,j+1/2}] - m_j[u_{w,j+1/2} - u_{w,j-1/2}]\Big). \end{aligned} \tag{4.153}$$

Here we note that the average $s_{w,j+1/2}$ in (4.153) is based on upwind relatively $u_{w,j+1/2}$

$$s_{w,j+1/2} = \begin{cases} s_{w,j}, & \text{if } u_{w,j+1/2} > 0; \\ \frac{s_{w,j}+s_{w,j+1}}{2}, & \text{if } u_{w,j+1/2} = 0; \\ s_{w,j+1}, & \text{if } u_{w,j+1/2} < 0. \end{cases} \tag{4.154}$$

Similarly, for $s_{o,j+1/2}$ and for the interaction terms $\hat{k}_{w,j+1/2}$ and $\hat{k}_{o,j+1/2}$. In addition, $\hat{k}_{j+1/2}$ is based on upwind relatively $u_{w,j+1/2}$ and $u_{o,j+1/2}$ as follows:

$$\hat{k}_{j+1/2} = \begin{cases} \hat{k}_j, & \text{if } u_{w,j+1/2} > 0 \ \& \ u_{o,j+1/2} > 0 \ ; \\ \frac{\hat{k}_j+\hat{k}_{j+1}}{2}, & \text{if } u_{w,j+1/2}u_{o,j+1/2} \le 0; \\ \hat{k}_{j+1}, & \text{if } u_{w,j+1/2} < 0 \ \& \ u_{o,j+1/2} < 0. \end{cases} \tag{4.155}$$

Moreover, $[nu_o]_{j+1/2}$ and $[mu_w]_{j+1/2}$ appearing in (4.152) employ upwind as described in (4.151). Now, we are in a position where we can describe a fully discrete model.

A fully discrete scheme. We assume that we have given $(m_j^k, P_{w,j}^k, u_{w,j}^k, u_{o,j}^k)$. We then compute the approximate solution at time t^{k+1} expressed by $(m_j^{k+1}, P_{w,j}^{k+1}, u_{w,j}^{k+1}, u_{o,j}^{k+1})$ as follows:

Step 1: Mass transport.

$$\frac{m_j^{k+1} - m_j^k}{\Delta t} + \frac{1}{\Delta x}([mu_w]_{j+1/2}^k - [mu_w]_{j-1/2}^k) = -m_j^k Q_{p,j} + \rho_{wj}^k Q_{I,j}, \tag{4.156}$$

where

$$[mu_w]_{j+1/2}^k = \begin{cases} m_j^k u_{w,j+1/2}^k, & \text{if } u_{w,j+1/2}^k \ge 0; \\ m_{j+1}^k u_{w,j+1/2}^k, & \text{if } u_{w,j+1/2}^k < 0. \end{cases} \tag{4.157}$$

Having computed m_j^{k+1} we can compute an updated water saturation $s_{w,j}^{k+1/2}$ given by

$$s_{w,j}^{k+1/2} = \frac{m_j^{k+1}}{\rho_w(P_{w,j}^k)}. \tag{4.158}$$

Similarly, we compute updated mass $n_j^{k+1/2} = (1-s_{w,j}^{k+1/2})\rho_o(P_{o,j}^{k+1/2})$ and $P_{o,j}^{k+1/2} = P_{w,j}^k + P_c(s_{w,j}^{k+1/2})$, according to (4.147), which are needed to evaluate coefficients in the next step.

Step 2: Computation of velocities and pressure. Next, we solve simultaneously for $P_{w,j}^{k+1}$ and $u_{w,j+1/2}^{k+1}$ and $u_{o,j+1/2}^{k+1}$ by considering the following algebraic system

$$\begin{aligned} \frac{P_{wj}^{k+1} - P_{wj}^k}{\Delta t} &+ [\tilde{\eta}\rho_w]_j^{k+1/2} \frac{1}{\Delta x}\Big([n^{k+1/2}u_o^{k+1}]_{j+1/2} - [n^{k+1/2}u_o^{k+1}]_{j-1/2}\Big) \\ &+ [\tilde{\eta}\tilde{\rho}_o]_j^{k+1/2} \frac{1}{\Delta x}\Big([m^{k+1}u_w^{k+1}]_{j+1/2} - [m^{k+1}u_w^{k+1}]_{j-1/2}\Big) \\ &= [\tilde{\eta}\rho_w\rho_o]_j^{k+1/2}(Q_{I,j} - Q_{p,j}) - \Big[\tilde{\eta}\frac{s_o P_c'}{C_o}\Big]_j^{k+1/2}(\rho_{wj}^k Q_{I,j} - m_j^{k+1}Q_{p,j}), \end{aligned} \tag{4.159}$$

which is combined with the momentum balance equations

$$\begin{aligned} s^{k+1/2}_{o,j+1/2}\frac{1}{\Delta x}(P^{k+1}_{w,j+1}-P^{k+1}_{w,j}) &= -s^{k+1/2}_{o,j+1/2}\frac{1}{\Delta x}(P^{k+1/2}_{c,j+1}-P^{k+1/2}_{c,j}) \\ &\quad -\hat{k}^{k+1/2}_{o,j+1/2}u^{k+1}_{o,j+1/2}+\hat{k}^{k+1/2}_{j+1/2}\Big(u^{k+1}_{w,j+1/2}-u^{k+1}_{o,j+1/2}\Big)+n^{k+1/2}_{j+1/2}g \\ &\quad +\varepsilon_o\frac{1}{\Delta x^2}\Big(n^{k+1/2}_{j+1}[u^{k+1}_{o,j+3/2}-u^{k+1}_{o,j+1/2}]-n^{k+1/2}_{j}[u^{k+1}_{o,j+1/2}-u^{k+1}_{o,j-1/2}]\Big), \\ s^{k+1/2}_{w,j+1/2}\frac{1}{\Delta x}(P^{k+1}_{w,j+1}-P^{k+1}_{w,j}) &= \\ &\quad -\hat{k}^{k+1/2}_{w,j+1/2}u^{k+1}_{w,j+1/2}-\hat{k}^{k+1/2}_{j+1/2}\Big(u^{k+1}_{w,j+1/2}-u^{k+1}_{o,j+1/2}\Big)+m^{k+1}_{j+1/2}g \\ &\quad +\varepsilon_w\frac{1}{\Delta x^2}\Big(m^{k+1}_{j+1}[u^{k+1}_{w,j+3/2}-u^{k+1}_{w,j+1/2}]-m^{k+1}_{j}[u^{k+1}_{w,j+1/2}-u^{k+1}_{w,j-1/2}]\Big). \end{aligned} \tag{4.160}$$

Equipped with $(P^{k+1}_{w,j}, u^{k+1}_{w,j+1/2}, u^{k+1}_{o,j+1/2})$ we can now update the saturation $s_{w,j}$ by

$$s^{k+1}_{w,j}=\frac{m^{k+1}_j}{\rho_w(P^{k+1}_{w,j})}, \tag{4.161}$$

from which we also compute the updated oil mass n^{k+1}_j and pressure $P^{k+1}_{o,j}$ via (4.147). If necessary, we may repeat step 2 to improve the accuracy before we proceed to next time level.

Remark 4.3. The upwind discretization of $[n^{k+1/2}u^{k+1}_o]_{j+1/2}$ and $[m^{k+1}u^{k+1}_w]_{j+1/2}$ appearing in (4.159) are based on "old" velocities $u^k_{o,j+1/2}$ and $u^k_{w,j+1/2}$.

A semidiscrete scheme for the incompressible model. When fluids are incompressible the model (2.14) takes the following form with unknown variables (s_w, P_w, u_w, u_o)

$$\begin{aligned} (s_w)_t+(s_wu_w)_x &= -s_wQ_p+Q_I \\ (s_o)_t+(s_ou_o)_x &= -s_oQ_p \\ s_w(P_w)_x &= -\hat{k}_wu_w-\hat{k}(u_w-u_o)+s_w\rho_wg+\varepsilon_w\rho_w(s_wu_{wx})_x \\ s_o(P_w+P_c)_x &= -\hat{k}_ou_o+\hat{k}(u_w-u_o)+s_o\rho_og+\varepsilon_o\rho_o(s_ou_{ox})_x, \end{aligned} \tag{4.162}$$

subject to the boundary condition

$$u_w|_{\partial\Omega}=u_o|_{\partial\Omega}=0 \tag{4.163}$$

and initial condition

$$s_w(x,t=0)=s_{w0}(x). \tag{4.164}$$

Note that we can only determine P_w up to a constant and a reference pressure P^* at some point in the domain may be specified. An equivalent formulation of (4.162) is given by (after a summation of the two mass balance equation)

$$\begin{aligned} (s_w)_t+(s_wu_w)_x &= -s_wQ_p+Q_I \\ (s_wu_w+s_ou_o)_x &= -Q_p+Q_I \\ s_w(P_w)_x &= -\hat{k}_wu_w-\hat{k}(u_w-u_o)+s_w\rho_wg+\varepsilon_w\rho_w(s_wu_{wx})_x \\ s_o(P_w+P_c)_x &= -\hat{k}_ou_o+\hat{k}(u_w-u_o)+s_o\rho_og+\varepsilon_o\rho_o(s_ou_{ox})_x. \end{aligned} \tag{4.165}$$

This formulation is consistent with and follows directly from (4.145) by letting $C_w, C_o \to \infty$ (i.e., the fluids become incompressible). This is a consequence of the fact that $\tilde{\eta} \to \infty$ and $\tilde{\rho}_o \to \rho_o$, see (4.146).

Step 1: Mass transport. We solve the following ODE for $s_{w,j}(t)$ corresponding to $(4.165)_1$:

$$\frac{ds_{w,j}}{dt} + \frac{1}{\Delta x}([s_w u_w]_{j+1/2} - [s_w u_w]_{j-1/2}) = -s_{w,j} Q_{p,j} + Q_{I,j} \tag{4.166}$$

where

$$[s_w u_w]_{j+1/2} = \begin{cases} s_{w,j} u_{w,j+1/2}, & \text{if } u_{w,j+1/2} \geq 0; \\ s_{w,j+1} u_{w,j+1/2}, & \text{if } u_{w,j+1/2} < 0. \end{cases} \tag{4.167}$$

Step 2: Computation of velocities and pressure. Next, we solve for $P_{w,j}(t)$ and $u_{w,j+1/2}(t)$ and $u_{o,j+1/2}(t)$ by considering the algebraic system corresponding to $(4.165)_{2,3,4}$:

$$\frac{1}{\Delta x}([s_w u_w]_{j+1/2} - [s_w u_w]_{j-1/2}) + \frac{1}{\Delta x}([s_o u_o]_{j+1/2} - [s_o u_o]_{j-1/2}) = Q_{I,j} - Q_{p,j} \tag{4.168}$$

which is combined with the momentum balance equations

$$\begin{aligned} s_{w,j+1/2} \frac{1}{\Delta x}(P_{w,j+1} - P_{w,j}) &= \\ &-\hat{k}_{w,j+1/2} u_{w,j+1/2} - \hat{k}_{j+1/2}\Big(u_{w,j+1/2} - u_{o,j+1/2}\Big) + s_{w,j+1/2}\rho_w g \\ &+\varepsilon_w \frac{\rho_w}{\Delta x^2}\Big(s_{w,j+1}[u_{w,j+3/2} - u_{w,j+1/2}] - s_{w,j}[u_{w,j+1/2} - u_{w,j-1/2}]\Big) \\ s_{o,j+1/2}\frac{1}{\Delta x}(P_{w,j+1} - P_{w,j}) &= -s_{o,j+1/2}\frac{1}{\Delta x}(P_{c,j+1} - P_{c,j}) \\ &-\hat{k}_{o,j+1/2} u_{o,j+1/2} + \hat{k}_{j+1/2}\Big(u_{w,j+1/2} - u_{o,j+1/2}\Big) + s_{o,j+1/2}\rho_o g \\ &+\varepsilon_o \frac{\rho_o}{\Delta x^2}\Big(s_{o,j+1}[u_{o,j+3/2} - u_{o,j+1/2}] - s_{o,j}[u_{o,j+1/2} - u_{o,j-1/2}]\Big). \end{aligned} \tag{4.169}$$

Here we note that the average $s_{w,j+1/2}$ in (4.169) is based on upwind relatively $u_{w,j+1/2}$

$$s_{w,j+1/2} = \begin{cases} s_{w,j}, & \text{if } u_{w,j+1/2} > 0; \\ \frac{s_{w,j} + s_{w,j+1}}{2}, & \text{if } u_{w,j+1/2} = 0; \\ s_{w,j+1}, & \text{if } u_{w,j+1/2} < 0. \end{cases} \tag{4.170}$$

Similarly, for $s_{o,j+1/2}$ and for the interaction terms $\hat{k}_{w,j+1/2}$ and $\hat{k}_{o,j+1/2}$. In addition, $\hat{k}_{j+1/2}$ is based on upwind relatively $u_{w,j+1/2}$ and $u_{o,j+1/2}$

$$\hat{k}_{j+1/2} = \begin{cases} \hat{k}_j, & \text{if } u_{w,j+1/2} > 0 \text{ \& } u_{o,j+1/2} > 0\text{ ;} \\ \frac{\hat{k}_j + \hat{k}_{j+1}}{2}, & \text{if } u_{w,j+1/2} u_{o,j+1/2} \leq 0; \\ \hat{k}_{j+1}, & \text{if } u_{w,j+1/2} < 0 \text{ \& } u_{o,j+1/2} < 0. \end{cases} \tag{4.171}$$

Moreover, $[s_o u_o]_{j+1/2}$ and $[s_w u_w]_{j+1/2}$ appearing in (4.168) employ upwind as described in (4.170).

A fully discrete scheme for the incompressible model. We can now proceed with a description of a full discrete scheme for the incompressible case which bears clear similarity to the scheme for the compressible model.

Step 1: Mass transport.

$$\frac{s_{w,j}^{k+1}-s_{w,j}^{k}}{\Delta t}+\frac{1}{\Delta x}([s_w u_w]_{j+1/2}^{k}-[s_w u_w]_{j-1/2}^{k})=-s_{w,j}^{k}Q_{p,j}+Q_{I,j} \tag{4.172}$$

where

$$[s_w u_w]_{j+1/2}^{k}=\begin{cases} s_{w,j}^{k}u_{w,j+1/2}^{k}, & \text{if } u_{w,j+1/2}^{k}\geq 0;\\ s_{w,j+1}^{k}u_{w,j+1/2}^{k}, & \text{if } u_{w,j+1/2}^{k}<0. \end{cases} \tag{4.173}$$

Having computed $s_{w,j}^{k+1}$ we can compute pressure and velocities simultaneously at time level $k+1$.

Step 2: Computation of velocities and pressure. We solve for $P_{w,j}^{k+1}$ and $u_{w,j+1/2}^{k+1}$ and $u_{o,j+1/2}^{k+1}$ by considering the following algebraic system

$$\begin{aligned}\frac{1}{\Delta x}([s_w^{k+1}u_w^{k+1}]_{j+1/2}-[s_w^{k+1}u_w^{k+1}]_{j-1/2})+\frac{1}{\Delta x}([s_o^{k+1}u_o^{k+1}]_{j+1/2}-[s_o^{k+1}u_o^{k+1}]_{j-1/2})\\ =Q_{I,j}-Q_{p,j}\end{aligned} \tag{4.174}$$

which is combined with the momentum balance equations

$$\begin{aligned} s_{w,j+1/2}^{k+1}\frac{1}{\Delta x}(P_{w,j+1}^{k+1}-P_{w,j}^{k+1}) ={}& \\ &-\hat{k}_{w,j+1/2}^{k+1}u_{w,j+1/2}^{k+1}-\hat{k}_{j+1/2}^{k+1}\Big(u_{w,j+1/2}^{k+1}-u_{o,j+1/2}^{k+1}\Big)+s_{w,j+1/2}^{k+1}\rho_w g\\ &+\varepsilon_w\frac{\rho_w}{\Delta x^2}\Big({s_{w,j+1}}^{k+1}[u_{w,j+3/2}^{k+1}-u_{w,j+1/2}^{k+1}]-s_{w,j}^{k+1}[u_{w,j+1/2}^{k+1}-u_{w,j-1/2}^{k+1}]\Big),\\ s_{o,j+1/2}^{k+1}\frac{1}{\Delta x}(P_{w,j+1}^{k+1}-P_{w,j}^{k+1}) ={}& -s_{o,j+1/2}^{k+1}\frac{1}{\Delta x}(P_{c,j+1}^{k+1}-P_{c,j}^{k+1})\\ &-\hat{k}_{o,j+1/2}^{k+1}u_{o,j+1/2}^{k+1}+\hat{k}_{j+1/2}^{k+1}\Big(u_{w,j+1/2}^{k+1}-u_{o,j+1/2}^{k+1}\Big)+s_{o,j+1/2}^{k+1}\rho_o g\\ &+\varepsilon_o\frac{\rho_o}{\Delta x^2}\Big({s_{o,j+1}}^{k+1}[u_{o,j+3/2}^{k+1}-u_{o,j+1/2}^{k+1}]-s_{o,j}^{k+1}[u_{o,j+1/2}^{k+1}-u_{o,j-1/2}^{k+1}]\Big). \end{aligned} \tag{4.175}$$

Remark 4.4. The upwind discretization of $[s_w^{k+1}u_w^{k+1}]_{j+1/2}$ and $[s_o^{k+1}u_o^{k+1}]_{j+1/2}$ appearing in (4.174) are based on "old" velocities $u_{w,j+1/2}^{k}$ and $u_{o,j+1/2}^{k}$.

REFERENCES

[1] P.Ø. Andersen, Y. Qiao, D. C. Standnes and S. Evje, Co-current spontaneous imbibition in porous media with the dynamics of viscous coupling and capillary back pressure, *SPE J.*, **24** (2019), 158–177.

[2] T. Arbogast, The existence of weak solutions to single porosity and simple dual-porosity models of two-phase incompressible flow, *Nonlinear Anal.*, **19** (1992), 1009–1031.

[3] J. Bear and Y. Bachmat, *Introduction to Modeling of Transport Phenomena in Porous Media*, Kluwer Academic Publishers, Dordrecht, The Netherlands, 1990.

[4] D. Bresch, X. D. Huang and J. Li, Global weak solutions to one-dimensional non-conservative viscous compressible two-phase system, *Comm. Math. Phys.*, **309** (2012), 737–755.

[5] C. Cances, T. O. Gallouet and L. Monsaingeon, The gradient flow structure of immiscible incompressible two-phase flows in porous media, *C. R. Acad. Sci. Paris Ser. I Math.*, **353** (2015), 985–989.

[6] C. Cances and M. Pierre, An existence result for multidimensional immiscible two-phase flows with discontinuous capillary pressure field, *SIAM J. Math. Anal.*, **44** (2012), 966–992.

[7] X. Cao and I. S. Pop, Degenerate two-phase porous media flow model with dynamic capillarity, *J. Diff. Eqs.*, **260** (2016), 2418–2456.

[8] Z. Chen, Degenerate two-phase incompressible flow: I. Existence, uniqueness and regularity of a weak solution, *J. Diff. Eqs.*, **171** (2001), 203–232.

[9] G. M. Coclite, S. Mishra, N. H. Risebro and F. Weber, Analysis and numerical approximation of Brinkman regularization of two-phase flows in porous media, *Comput. Geosci.*, **18** (2014), 637–659.

[10] J. M. Delhaye, M. Giot and M. L. Riethmuller, *Thermohydraulics of Two-Phase Systems for Industrial Design and Nuclear Engineering*, Von Karman Institute, McGraw-Hill, New York, 1981.

[11] D. A. Drew and S. L. Passman, *Theory of Multicomponent Fluids*, Springer, 1999.

[12] C. J. van Duijn, Y. Fan, L. A. Peletier and I. S. Pop, Travelling wave solutions for degenerate pseudo-parabolic equation modelling two-phase flow in porous media, *Nonlinear Anal. Real World Applications*, **14** (2013), 1361–1383.

[13] C. J. van Duijn, L. A. Peletier and I. S. Pop, A new class of entropy solutions of the Buckley-Leverett equation, *SIAM J. Math. Anal.*, **39** (2007), 507–536.

[14] S. Evje, An integrative multiphase model for cancer cell migration under influence of physical cues from the microenvironment, *Chem. Eng. Sci.*, **165** (2017), 240–259.

[15] S. Evje and H. Y. Wen, Analysis of a compressible two-fluid Stokes system with constant viscosity, *J. Math. Fluid Mech.*, **17** (2015), 423–436.

[16] S. Evje and H. Y. Wen, Stability of a compressible two-fluid hyperbolic-elliptic system arising in fluid mechanics, *Nonlin. Anal.: Real World Applications*, **31** (2016), 610–629.

[17] S. Evje, W. Wang and H. Y. Wen, Global well-posedness and decay rates of strong solutions to a non-conservative compressible two-fluid model, *Arch. Rat. Mech. Anal.*, **221** (2016), 1285–1316.

[18] S. Evje and H. Y. Wen, A Stokes two-fluid model for cell migration that can account for physical cues in the microenvironment, *SIAM J. Math. Anal.*, **50** (2018), 86–118.

[19] C. Galusinski and M. Saad, On a degenerate parabolic system for compressible immiscible two-phase flows in porous media, *Adv. Diff. Eqs.*, **9** (2004), 1235–1278.

[20] C. Galusinski and M. Saad, A nonlinear degenerate system modeling water-gas in porous media, *Disc. Cont. Dyn. Syst.*, **9** (2008), 281–308.

[21] C. Galusinski and M. Saad, Two compressible immiscible fluids in porous media, *J. Diff. Eqs.*, **244** (2008), 1741–1783.

[22] S. M. Hassanizadeh, Derivation of basic equations of mass transport in porous media, Part 2. Generalized Darcy's and Fick's laws, *Adv. Water Resour.*, **9** (1986), 207–222.

[23] S. M. Hassanizadeh and W. G. Gray, Toward an improved description of the physics of two-phase flow, *Adv. Water Resour.*, **16** (1993), 53–67.

[24] S. M. Hassanizadeh and W. G. Gray, Thermodynamic basis of capillary pressure in porous media, *Water Resour. Res.*, **28** (1993), 3389–3405.

[25] R. Juanes, Nonequilibrium effects in models of three-phase flow in porous media, *Adv. Wat. Res.*, **31** (2008), 661–673.

[26] Z. Khalil and M. Saad, Degenerate two-phase compressible immiscible flow in porous media: The case where the density of each phase depends on its own pressure, *Math. Comput. Simulation*, **81** (2011), 2225–2233.

[27] M. Krotkiewski, I. Ligaarden, K.-A. Lie and D. W. Schmid, On the importance of the Stokes-Brikman equations for computing effective permeability in carbonate-karst reservoirs, *Comm. Comput. Phys.*, **10** (2011), 1315–1332.

[28] L. D. Landau and E. M. Lifshitz, *Fluid Mechanics*, Course of Theoretical Physics, 6, Pergamon Press, 1984.

[29] G. Lemon, J. R. King, H. M. Byrne, O. E. Jensen and K. M. Shakesheff, Mathematical modelling of engineered tissue growth using a multiphase porous flow mixture theory, *J. Math. Biol.*, **52** (2006), 571–594.

[30] M. Muskat, *Physical Principles of Oil Production*, McGraw-Hill, New York, 1949.

[31] Y. Qiao, P.Ø. Andersen, S. Evje and D. C. Standnes, A mixture theory approach to model co- and counter-current two-phase flow in porous media accounting for viscous coupling, *Advances Wat. Res.*, **112** (2018), 170–188.

[32] K. R. Rajagopal, On a hierarchy of approximate models for flows of incompressible fluids through porous solids, *Math. Mod. Met. Appl. Sci.*, **17** (2007), 215–252.

[33] B. Saad and M. Saad, Study of full implicit petroleum engineering finite volume scheme for compressible two phase flow in porous media, *SIAM J. Numer. Anal.*, **51** (2013), 716–741.

[34] M. M. Schuff, J. P. Gore and E. A. Nauman, A mixture theory model of fluid and solute transport in the microvasculature of normal and malignant tissues. I. Theory, *J. Math. Biol.*, **66** (2013), 1179–1207.

[35] D. C. Standnes, S. Evje and P.Ø. Andersen, A novel relative permeability model based on mixture theory approach accounting for solid-fluid and fluid-fluid interactions, *Tran. Por. Media*, **119** (2017), 707–738.

[36] D. C. Standnes and P.Ø. Andersen, Analysis of the impact of fluid viscosities on the rate of countercurrent spontaneous imbibition, *Energy & Fuels*, **31** (2017), 6928–6940.

[37] J. Urdal, J. O. Waldeland and S. Evje, Enhanced cancer cell invasion caused by fibroblasts when fluid flow is present, *Biomech. Model. Mechanobiol.*, preprint, (2019).

[38] F. J. Valdes-Parada, J. A. Ochoa-Tapia and J. Alvarez-Ramirez, On the effective viscosity for the Darcy–Brinkman equation, *Physica A*, **385** (2007), 69–79.

[39] J. O. Waldeland and S. Evje, A multiphase model for exploring cancer cell migration driven by autologous chemotaxis, *Chem. Eng. Sci.*, **191** (2018), 268–287.

[40] J. O. Waldeland and S. Evje, Competing tumor cell migration mechanisms caused by interstitial fluid flow, *J. Biomech.*, **81** (2018), 22–35.

[41] L. Wang, L.-P. Wang, Z. Guo and J. Mi, Volume-averaged macroscopic equation for fluid flow in moving porous media, *Int. J. Heat Mass Tran.*, **82** (2015), 357–368.

[42] Y. S. Wu, *Multiphase Fluid Flow in Porous and Fractured Reservoirs*, Elsevier, 2016.

Received June 2018; revised March 2019.

E-mail address: `yangyang.qiao@uis.no`
E-mail address: `mahywen@scut.edu.cn`
E-mail address: `steinar.evje@uis.no`

Paper IV

Viscous Two-phase Flow in Porous Media Driven by Source Terms: Analysis and Numerics

By:
Qiao, Yangyang
Wen, Huanyao
Evje, Steinar

Printed in:
SIAM Journal on Mathematical Analysis, 51 (6): 5103-5140 (2019).

SIAM J. MATH. ANAL.
Vol. 51, No. 6, pp. 5103–5140

VISCOUS TWO-PHASE FLOW IN POROUS MEDIA DRIVEN BY SOURCE TERMS: ANALYSIS AND NUMERICS*

YANGYANG QIAO†, HUANYAO WEN‡, AND STEINAR EVJE†

Abstract. In this work we consider the initial-boundary value problem for a generalized, compressible, porous media two-phase model. The formulation is motivated by principles from mixture theory and involves interstitial fluid velocity $\mathbf{u}_i$ instead of Darcy type velocity $\mathbf{U}_i = \phi s_i \mathbf{u}_i$, where ϕ is porosity and s_i is saturation (volume fraction) of phase i. The momentum balance equations account for fluid-rock resistance forces as well as fluid-fluid interaction effects, in addition to internal viscosity through a Brinkmann type viscous term. We explore a one-dimensional version of this model where we account for two-phase dynamics driven by injection and production of fluids through realistic source terms and where physically relevant capillary pressure is accounted for. Our investigations are twofold: (i) Various a priori estimates are derived that give rise to an existence result subject to a constraint on the magnitude of the viscous terms and the strength of the injection and production rate. (ii) A numerical finite difference scheme, designed for dealing effectively with the strong nonlinear coupling between the mass and momentum equations, is then used to demonstrate a variety of two-phase injection-production scenarios for a realistic reservoir setting. Different physical effects are highlighted such as the difference between compressible and incompressible flow, balance between gravity and pressure-driven flow, and effect of viscous coupling.

Key words. Darcy's equation, mixture theory, two-phase flow, interaction forces, viscous coupling, Brinkman equation, compressibility

AMS subject classifications. 76T10, 76N10, 65M12, 35L60

DOI. 10.1137/19M1252491

1. Introduction.

1.1. Introduction. Mathematical modeling of multiphase flow is essential in practical applications like enhanced oil recovery and geological CO_2 storage in depleted oil and gas reservoirs [5, 16, 19, 7, 41] as well as biological processes [10, 14, 23]. An instructive overview is given in [30] on how generalizations of the standard Darcy's law for single phase flow can be derived within the context of mixture theory [8]. Starting with more general momentum balance equations and using different sets of assumptions leads to a hierarchy of mathematical models. In particular, it can be shown that popular models due to Brinkman, Biot, and many others can be obtained via various approximations imposed on this more general formulation. Further extension of the viscous stress tensor is necessary in order to account for non-Newtonian fluid properties corresponding to shear-thickening or shear-thinning behavior [25, 30]. Javaheri and Jessen [18] studied the modeling of CO_2 migration in two-phase displacement of relevance to sequestration processes in saline aquifers and emphasized that it is necessary to consider the fluid-fluid interaction (water-gas) effect in numerical calculations whenever transitions between co-current and countercurrent flow occurs. For more validation of the relevance of including viscous coupling effects through fluid-fluid interaction terms we refer to the recent works [35, 34, 28] and references

---

[*] Received by the editors March 26, 2019; accepted for publication (in revised form) October 7, 2019; published electronically December 17, 2019.
https://doi.org/10.1137/19M1252491

[†] Department of Energy and Petroleum Engineering, University of Stavanger, Stavanger NO-4068, Norway (yangyang.qiao@uis.no, steinar.evje@uis.no).

[‡] School of Mathematics, South China University of Technology, Guangzhou 510641, China (mahywen@scut.edu.cn).

therein. More recently, similar models have been introduced in order to explore cell-fluid dynamics that account for cell-matrix interaction, fluid-matrix interaction, and cell-fluid interaction [39, 38, 36, 11] to mimic experimental observed cancer cell migration mechanisms that might play a role in dissemination of cancer cells from a primary tumor [32, 27]. Note that these applications require inclusion of different chemical agents (e.g., proteins and enzymes) in terms of advection-diffusion-reaction equations that account for advective transport in the flow direction. The general form of the model we are interested in describes creeping flow of two compressible immiscible fluids in a porous media (e.g., water (w), oil (o), or gas (g)) and was presented in the recent work [29]. In the current work we focus on the one-dimensional (1D) version of it where we use "w" and "o" as indices and where (n, m, u_w, u_o) are the main variables:

$$
\begin{aligned}
(\phi n)_t + (\phi n u_o)_x &= -nQ_p, && n = s_o\rho_o, \qquad Q_p \geq 0,\\
(\phi m)_t + (\phi m u_w)_x &= -mQ_p + \rho_w Q_I, && m = s_w\rho_w, \qquad Q_I \geq 0,\\
s_o P_{ox} &= -\hat{k}_o u_o + \hat{k}(u_w - u_o) + ng &&\\
&\quad + \varepsilon_o (n u_{ox})_x, &&\\
s_w P_{wx} &= -\hat{k}_w u_w - \hat{k}(u_w - u_o) + mg &&\\
&\quad + \varepsilon_w (m u_{wx})_x, && P_c = P_o - P_w = P_c(s_w),
\end{aligned}
\tag{1.1}
$$

subject to the boundary condition

$$
\begin{aligned}
&u_w(x=0,t) = u_o(x=0,t) = 0,\\
&u_w(x=1,t) = u_o(x=1,t) = 0, \qquad t \geq 0,
\end{aligned}
\tag{1.2}
$$

and initial condition

$$n(x,t=0) = n_0(x), \qquad m(x,t=0) = m_0(x), \qquad x \in [0,1]. \tag{1.3}$$

Herein, capillary pressure P_c is defined as the difference between the nonwetting fluid (oil) pressure P_o and the wetting fluid (water) pressure P_w,

$$P_c = P_o - P_w = P_c(s_w), \qquad P_c'(s_w) < 0. \tag{1.4}$$

Moreover, ϕ is the porosity of the medium, ρ_i represents density, and s_i represents the volume fraction where $i = w, o$. In addition, we have the fundamental relation that expresses that the water and oil occupy the pore space,

$$s_o + s_w = 1. \tag{1.5}$$

Furthermore, $\varepsilon_w, \varepsilon_o$ are assumed to be constant and characterize the magnitude of the viscous terms. We refer to [29] for further information and motivation for this model. The two phases will be treated as weakly compressible fluids. More precisely, we represent the water and the oil (gas) by linear pressure-density relations of the form

$$\rho_w - \tilde{\rho}_{w0} = \frac{P_w}{C_w}, \qquad \rho_o - \tilde{\rho}_{o0} = \frac{P_o}{C_o}, \qquad \left(\rho_g = \frac{P_g}{C_g}\right), \tag{1.6}$$

where C_w and C_o (C_g) essentially represent the inverse of the compressibility of water and oil (gas), respectively. This is often referred to as bulk modulus, which is a constant that describes how resistant a substance is to compression. Hence, a weakly compressible fluid corresponds to a large C_i $(i = w, o, g)$ value. Porosity ϕ is in the following assumed to be constant and is for simplicity only set to be $\phi = 1$.

Objective. In [29] we obtained an existence result for the case where the source terms Q_p and Q_I were set to zero. Appropriate regularity estimates were derived that ensure global existence subject to constraints on the viscous terms controlled by ε_i. We also derived semidicrete and fully discrete approximate systems based on rewriting the model (1.1) and using a pressure evolution equation to replace one of the mass balance equations. Some initial numerical investigations of these discrete formulations, for both the incompressible and the compressible case, were carried out. The purpose of the current manuscript is to continue these investigations but where the source terms are included, which is very essential for real-world applications. More precisely, we will (i) derive estimates and obtain an existence result where the role of source terms related to injection and production wells are accounted for; (ii) use the numerical scheme to explore in a more realistic setting the role of compressibility, the balance between countercurrent (gravity driven) and co-current (pressure driven) flow, as well as the effect of fluid-fluid interaction (viscous coupling) through $\pm\hat{k}(u_w - u_o)$, in addition to fluid-rock viscous interaction through $-\hat{k}_i u_i$ $(i = w, o)$. All the interesting dynamic is now generated from the injection and production wells through, respectively, Q_I and Q_p. A consequence of having the source terms as a driver for the dynamics is that the energy can no longer be controlled without taking into account higher order regularity terms (see Remark 2.5) of section 2.2. The main results are summed up in Theorems 2.1 and 2.2 in section 2.1.

Remark 1.1. More details about the choice of the interaction coefficients $\hat{k}$, $\hat{k}_w$, and $\hat{k}_o$ are given below, in the introduction of section 2. In addition, a functional form of the capillary pressure $P_c(s_w)$ must be specified. Combining (1.4), (1.5), and (1.6) it follows that $\rho_w = \rho_w(m, n) \geq 0$ and $\rho_o = \rho(m, n) \geq 0$ are well-defined as functions of m and n for $m, n \geq 0$ from which we also can compute $s_w = s_w(m, n)$ and $s_o = s_o(m, n)$; see [29] (beginning of section 2) for details.

Remark 1.2. For the numerical simulations in section 3 we use a numerical scheme which is based on a reformulation of (1.1). More precisely, we rewrite the model in the following equivalent form with (m, P_w, u_w, u_o) as the main variables:

$$
\begin{aligned}
(m)_t + (mu_w)_x &= -mQ_p + \rho_w Q_I, \\
P_{wt} + \tilde{\eta}\rho_w(nu_o)_x + \tilde{\eta}\tilde{\rho}_o(mu_w)_x &= \tilde{\eta}\rho_w\rho_o(Q_I - Q_p) - \tilde{\eta}\frac{s_o P_c'}{C_o}(\rho_w Q_I - mQ_p), \\
s_o(P_{wx} + P_{cx}) &= -(\hat{k}_o + \hat{k})u_o + \hat{k}u_w + ng + \varepsilon_o(nu_{ox})_x, \\
s_w P_{wx} &= -(\hat{k}_w + \hat{k})u_w + \hat{k}u_o + mg + \varepsilon_w(mu_{wx})_x
\end{aligned}
\tag{1.7}
$$

with

$$
\tilde{\eta} = \frac{C_w C_o}{s_o \rho_w C_w + s_w \tilde{\rho}_o C_o}, \qquad \tilde{\rho}_o = \rho_o - \frac{s_o P_c'}{C_o}. \tag{1.8}
$$

We refer to [29] for more details regarding the pressure evolution equation $(1.7)_2$ as well as a description of both semidiscrete and fully discrete versions of (1.7). Note that for this approach s_w, s_o, n, P_o are determined by

$$
\begin{aligned}
s_w &= \frac{m}{\rho_w(P_w)}, \qquad s_o = 1 - s_w, \\
n &= s_o\rho_o(P_o) = \Big(1 - \frac{m}{\rho_w(P_w)}\Big)\rho_o(P_o) = n(m, P_w), \\
P_o &= P_c(s_w) + P_w = P_o(m, P_w).
\end{aligned}
\tag{1.9}
$$

This approach is slightly different from the one explained in Remark 1.1, where the mass balance equations $(1.1)_{1,2}$ give us m and n, from which the other physical variables are derived.

We end this section with a brief review of some previous and recent studies of compressible, viscous two-fluid models that are naturally related to (1.1). In the recent review paper [40] useful information about different versions of such models and corresponding mathematical studies can be found. For a broad discussion of the existence and uniqueness of compressible multifluid in a 1D setting relying on a one-velocity approach we refer to [24]. We refer to [2] for results on a general multidimensional, viscous, and compressible two-fluid model and [3] for a 1D variant which lies closer to (1.1) but with inclusion of transient and acceleration terms in the momentum balance equations. An interesting recent study of a one-velocity two-phase model, obtained by summing the two momentum equations (Stokes equations) and assuming that one of the phases is largely dispersed in the other and therefore moves with the same velocity, is found in [4]. In particular, a density evolution equation is derived, similar to $(1.7)_2$, that plays a central role in their analysis. The above pressure evolution equation (1.7) represents a two-fluid, two-velocity version of such an evolution equation. This approach is also taken in [42, 17], where the full momentum equations are used but subject to the one-velocity assumption. We also refer to [37, 26] and references therein for recent results on global existence of weak solutions by relying on an energy estimate only combined with refined compensated compactness arguments. For more results on the 1D model similar to (1.1) we refer to [12, 13]. The model (1.1) and its multidimensional version seems to be a natural starting point for studying multiphase processes that involve coupled porous media-channel (or wellbore) flow. See [33, 9] for examples of such models mainly motivated by engineering related applications. Moreover, interesting analyses of incompressible and compressible versions of two-phase porous media models based on Darcy's law are found in [16, 15, 22, 1]. For analysis of numerical approximations of such models we refer to [31, 7] and references therein. Finally, for analysis of the incompressible version of (1.1) based on Darcy's law and a reformulation of the model such that it is expressed in terms of an elliptic pressure equation and nonlinear hyperbolic conservation law for the saturation with a possible rough total velocity field we refer to [20, 21, 6].

2. Stability analysis.

Notation. We first give some notation.

- $L^p = L^p([0,1])$ for $p \in [1,\infty]$.
- We define

$$\tilde{m}(t) = \int_0^1 m(x,t)\,dx; \quad \tilde{n}(t) = \int_0^1 n(x,t)\,dx. \tag{2.1}$$

Assumptions. The following assumptions are made:

- Capillary pressure $P_c(s_w)$. We assume that for $\Phi(s_w)$ such that $\Phi'(s_w) = P_c(s_w)$, the following property holds:

$$c_0(1-s_w) + \Phi(s_w) \le P_c(\tilde{s}_w)s_w, \qquad 0 \le s_w \le 1, \tag{2.2}$$

  where $\tilde{s}_w$ can be any water saturation in $[0,1]$ and c_0 is a positive small constant. See Remark 2.2 for a justification. Moreover, we assume that capillary pressure $P_c(s_w)$ is a decreasing function satisfying

$$|P_c(0)| < \infty, \qquad \inf_{s_w \in (0,1)} [-P_c'(s_w)] > 0, \tag{2.3}$$

$$\sup_{s_w \in (0,1)} P_c(s_w) < C_w \tilde{\rho}_{w0} - C_o \tilde{\rho}_{o0} := D. \tag{2.4}$$

Note that these constraints on the capillary pressure $P_c(s_w)$ are all mild and physical reasonable conditions.

- Source terms Q_I and Q_p in $(1.1)_{1,2}$ are assumed to have the following regularity:

$$\|Q_p, Q_I\|_\infty,\ \|(Q_p)_x\|_\infty,\ \|(\sqrt{Q_I})_x\|_\infty \le C \tag{2.5}$$

for some positive constant C. One possible expression, for example for Q_I, is given by

$$Q_I = \begin{cases} 0, & 0 \le x \le x_1 - \delta, \\ -Q\left(\dfrac{x_1 - x}{\delta}\right)^s + Q, & x_1 - \delta < x < x_1, \\ Q, & x_1 \le x \le x_2, \\ -Q\left(\dfrac{x - x_2}{\delta}\right)^s + Q, & x_2 < x < x_2 + \delta, \\ 0, & x_2 + \delta \le x \le 1, \end{cases} \tag{2.6}$$

where Q is a constant, $s \ge 2$, and (x_1, x_2) is a small region associated with the injector.

- The following constraint on the strength of the injection rate Q_I and the functional form of the capillary pressure $P_c(s_w)$ will be used:

$$\begin{aligned} \frac{16\varepsilon_w}{C_w}\|Q_I\|_\infty \|D - P_c\|_\infty &< \inf_{s_w \in (0,1)} |P_c'(s_w)| \\ &\le |P_c'(s_w)| \le D - P_c(s_w),\ 0 \le s_w \le 1, \end{aligned} \tag{2.7}$$

where D (constant) is defined in (2.4). For a given estimate of $\|D - P_c\|_\infty > 0$ we can make the lower limit in (2.7) as small as we want through Q_I. For more information about the last inequlity (upper bound) we refer to Remark 2.2 below.

- Interaction terms $\hat{k}_w$, $\hat{k}_o$, and $\hat{k}$ are set as follows:

$$\hat{k}_w = I_w \frac{m^2}{m+n}, \qquad \hat{k}_o = I_o \frac{n^2}{m+n}, \qquad \hat{k} = I_{wo}\frac{mn}{m+n}. \tag{2.8}$$

Remark 2.1. Clearly, in view of $(1.1)_{1,2}$, and the condition (1.2), it follows from (2.1) that

$$\begin{aligned} \tilde{m}(t) &= \int_0^1 m_0(x)\,dx - \int_0^t \int_0^1 mQ_p\,dx\,ds + \int_0^t \int_0^1 \rho_w Q_I\,dx\,ds, \\ \tilde{n}(t) &= \int_0^1 n_0(x)\,dx - \int_0^t \int_0^1 nQ_p\,dx\,ds. \end{aligned} \tag{2.9}$$

Remark 2.2. We explore the condition on capillary pressure $P_c(s_w)$ as given by (2.2) for a representative capillary pressure curve of the form $P_c(s_w) = -P_c^* \ln(\delta + \frac{s_w}{a})$

for some $\delta \in (0,1)$ and $a > 0$. In view of the relation $\Phi'(s_w) = P_c(s_w)$ we introduce two positive constants C_1 and C_2 to be determined such that

(2.10)
$$\begin{aligned}\Phi(s_w) &= -P_c^* \int_0^{\rho} \ln\Big(\frac{x}{a} + \delta\Big)\, dx - C_1 - C_2 \\ &= -P_c^* a \int_{\delta}^{s_w/a+\delta} \ln(u) du - C_1 - C_2 = P_c^* a(u - u\ln(u))\Big|_{\delta}^{s_w/a+\delta} - C_1 - C_2 \\ &= P_c^* s_w + P_c^* a\Big[\delta \ln(\delta) - (s_w/a + \delta)\ln(s_w/a+\delta)\Big] - C_1 - C_2.\end{aligned}$$

Since $x\ln(x)$ is an increasing function for $x \geq e^{-1}$ whereas for $x \in [0, e^{-1})$ it decreases from zero for $x = 0$ and takes a minimum $-e^{-1}$, it is clear that we can secure that

$$P_c^* a\Big[\delta\ln(\delta) - (s_w/a+\delta)\ln(s_w/a+\delta)\Big] - C_1 \leq 0, \qquad s_w \in [0,1],$$

for an appropriate choice of C_1 such that we conclude from (2.10) that

$$\Phi(s_w) \leq P_c^* s_w - C_2.$$

We only need to verify that

$$c_0(1 - s_w) + P_c^* s_w - C_2 \leq P_c(\tilde{s}_w) s_w$$

for $0 \leq s_w \leq 1$ and some small positive constant c_0. Clearly, $(P_c^* - P_c(\tilde{s}_w) - c_0)s_w \leq C_2 - c_0$ for an appropriate choice of the constant $C_2 = C_2(P_c^*, \tilde{s}_w)$ since $s_w \in [0,1]$.

Finally, we also verify the upper bound of (2.7). We only need to observe that

$$|P_c'(s_w)| \leq \frac{P_c^*}{\delta a}, \qquad P_c(s_w) \leq -P_c^* \ln(\delta), \qquad s_w \in [0,1]. \tag{2.11}$$

We assume that

$$P_c^*\Big[\frac{1}{\delta a} - \ln(\delta)\Big] \leq D, \qquad \delta \in (0,1), \ \ a > 0. \tag{2.12}$$

This represents a (mild) restriction on the shape and magnitude of the capillary pressure curve as $D >> P_c^*$. Hence, in light of (2.11) and (2.12), it follows that $|P_c'(s_w)| \leq \frac{P_c^*}{\delta a} \leq D - (-P_c^* \ln(\delta)) \leq D - P_c(s_w)$, which is the last inequlity of (2.7).

2.1. Main results. First, we present a local (in time) existence result.

THEOREM 2.1 (local existence). *Assume that* $m_0 \in H^1$, $n_0 \in H^1$, *and* $\inf_{x\in[0,1]} n_0 > 0$, $\inf_{x\in[0,1]} m_0 > 0$, *and that*

$$\begin{cases} \dfrac{I_{wo}k_1}{\varepsilon_w k_0} + \dfrac{I_{wo}k_1}{\varepsilon_o k_0} \leq \dfrac{1}{4}, \\ \max\left\{\dfrac{I_{wo}k_1}{k_0\varepsilon_o} + E_{\varepsilon_o,1}, \dfrac{I_{wo}k_1}{k_0\varepsilon_w} + E_{\varepsilon_w,1}\right\} \leq \dfrac{1}{2}, \end{cases}$$

where $k_0 = \min\{\frac{\inf n_0}{2e}, \frac{\inf m_0}{2e}\}$, *and* $k_1 = \max\{e\sup m_0 + 1, e\sup n_0 + 1\}$, *and*

$$\begin{cases} E_{\varepsilon_w,1} = \dfrac{1}{\varepsilon_w}\left[\dfrac{10C}{(k_0)^2}\left(1 + \dfrac{10C}{k_0}\right)\dfrac{I_{wo}k_1}{2k_0} + \dfrac{10I_wI_{wo}k_1}{\varepsilon_w k_0} + \dfrac{20I_wI_{wo}k_1}{\varepsilon_w k_0} + \dfrac{20I_wI_{wo}k_1}{\varepsilon_w k_0}\right], \\ E_{\varepsilon_o,1} = \dfrac{1}{\varepsilon_o}\left[\dfrac{10C}{(k_0)^2}\left(1 + \dfrac{10C}{k_0}\right)\dfrac{I_{wo}k_1}{2k_0} + \dfrac{20(I_{wo})^2k_1}{\varepsilon_o k_0} + \dfrac{10I_oI_{wo}k_1}{\varepsilon_o k_0} + \dfrac{20(I_{wo})^2k_1}{\varepsilon_o k_0}\right]. \end{cases}$$

Then there exists a positive constant T_0 *such that the system* (1.1) *with initial-boundary conditions* (1.2) *and* (1.3) *has a unique solution* (m, n, u_w, u_o) *on* $[0,1]\times[0,T_0]$ *in the sense that*

$$\left\{\begin{aligned}&\|(m,n,s_w,s_o,\rho_w,\rho_o)(t)\|_{H^1}+\|(u_w,u_o)(t)\|_{H^2}\le C,\\&\|\big(m_t,n_t,(s_w)_t,(s_o)_t,(\rho_w)_t,(\rho_o)_t\big)(t)\|_{L^2}\le C,\\&\inf_{(x,t)\in Q_{T_0}} m(x,t)>0,\ \inf_{(x,t)\in Q_{T_0}} n(x,t)>0,\end{aligned}\right.$$

for any $t\in[0,T_0)$*, where* $Q_{T_0}=[0,1]\times[0,T_0)$ *and* $C=C(T_0)$*.*

Remark 2.3. Without the source terms, Theorem 2.1 was derived in our previous work [29]. In the case with the source terms, we only need to slightly modify the conditions in Theorem 2.1, i.e., the definitions of k_0 and k_1, as well as account for the presence of the source terms in the proof. More precisely, the iteration scheme in the proof as in [29] should be replaced by

$$\begin{aligned}(n^k)_t+(n^k u_o^{k-1})_x&=-n^kQ_p,\\(m^k)_t+(m^k u_w^{k-1})_x&=-m^kQ_p+\rho_w(m^{k-1},n^k)Q_I,\\s_o^kP_{ox}^k&=-\hat{k}_o^k u_o^k+\hat{k}^k(u_w^{k-1}-u_o^k)+\varepsilon_o(n^ku_{ox}^k)_x-n^kg,\\s_w^kP_{wx}^k&=-\hat{k}_w^k u_w^k-\hat{k}^k(u_w^k-u_o^k)+\varepsilon_w(m^ku_{wx}^k)_x-m^kg\end{aligned}\tag{2.13}$$

with the initial-boundary value conditions

$$(u_w^k,u_o^k)(0,t)=(u_w^k,u_o^k)(1,t)=0,\ t\ge 0,$$

and

$$(m^k,n^k)(x,0)=(m_0,n_0)(x),\ \ x\in[0,1],$$

for $k=1,2,3,\ldots$, where $(u_w^0,u_o^0)=(0,0)$, $m^0=m_0$, $s_w^k=s_w(m^k,n^k)$, $s_o^k=s_o(m^k,n^k)$, $P_w^k=P_w(m^k,n^k)$, $P_o^k=P_o(m^k,n^k)$, $\hat{k}_w^k=\hat{k}_w(m^k,n^k)$, $\hat{k}_o^k=\hat{k}_o(m^k,n^k)$, $\hat{k}^k=\hat{k}(m^k,n^k)$. We omit the details for brevity.

The second main result is devoted to an almost global existence result. This result relies on the local existence result combined with certain a priori estimates as stated in (2.15) and obtained in section 2.2.

Theorem 2.2 (global existence of small data solutions). *In addition to the conditions of Theorem* 2.1*, for any given* $T>0$*, if*

$$K_1\le\min\left\{\frac{\varepsilon_w}{4}\tilde{m}_0e^{-\int_0^T\sup\limits_{x\in[0,1]}|Q_p|ds},\frac{\varepsilon_o}{4}\tilde{n}_0e^{-\int_0^T\sup\limits_{x\in[0,1]}|Q_p|ds}\right\},\tag{2.14}$$

then the system (1.1) *with initial-boundary conditions* (1.2) *and* (1.3) *has a unique solution* (m,n,u_w,u_o) *on* $[0,1]\times[0,T]$ *in the sense that*

$$(m,n)\in C([0,T];H^1)\cap C^1([0,T];L^2),\ \ (u_w,u_o)\in C([0,T];H^2\cap H_0^1),$$

where K_1 *is given by* (2.76)*.*

Moreover, we have the following estimates:

$$\int_0^1 \left[(s_w)_x^2 + (s_o)_x^2 + (\rho_w)_x^2 + (\rho_o)_x^2\right] dx \le C(T),$$

$$\int_0^1 \left[(s_w)_t^2 + (s_o)_t^2 + (\rho_w)_t^2 + (\rho_o)_t^2\right] dx \le C(T),$$

for any $t \in [0, T]$.

Remark 2.4. The constraint (2.14) implies smallness of initial data (and sufficiently large viscosity ε_w and ε_o) as well as small production rate Q_p, which is only used to get the positive lower bound of m and n. See Corollary 2.2 for the details. At the same time we also see that the injection rate Q_I has a restriction as expressed by the inequality (2.7).

2.2. Proof of Theorem 2.2. For any given $T > 0$, our aim in this section is to prove that the solution exists on the time interval $[0, T]$ under some assumptions depending on T (see (2.14)) as in Theorem 2.2. More specifically, let T^* denote the maximum time for the existence of solutions as in Theorem 2.1.[1] Then due to the local existence theorem, i.e., Theorem 2.1, we have $T^* > 0$. If $[0, T] \subset [0, T^*)$, the proof of Theorem 2.2 is done. Therefore we consider the other case only, i.e., $T \ge T^*$. We are going to prove that this assumption $T \ge T^*$ will lead to a contradiction with the definition of T^*, based on the following estimates uniformly for t, i.e.,

$$\begin{cases} \|(m, n, s_w, s_o, \rho_w, \rho_o)(t)\|_{H^1} + \|(u_w, u_o)(t)\|_{H^2} \le C(T^*), \\ \|\big(m_t, n_t, (s_w)_t, (s_o)_t, (\rho_w)_t, (\rho_o)_t\big)(t)\|_{L^2} \le C(T^*), \\ \inf\limits_{(x,t)\in Q_{T^*}} m(x,t) > 0, \quad \inf\limits_{(x,t)\in Q_{T^*}} n(x,t) > 0, \end{cases} \tag{2.15}$$

for any $t \in [0, T^*)$, where $Q_{T^*} = [0, 1] \times [0, T^*)$. In fact, (2.15) implies that T^* is not the maximum time for the existence which is the desired contradiction. Thus the case $T \ge T^*$ is not true, i.e., $[0, T] \subset [0, T^*)$.

To get (2.15) for the case $T \ge T^*$, we need a series of lemmas and corollaries as given in the remainder of this section. Due to the similarity to the model studied in [29] we will refer to this work whenever possible and focus on new aspects caused by the source terms. To simplify the proof, we let $C(T)$ denote a generic positive constant depending on the initial data and T. Moreover, for given $T > 0$, $C(T) < \infty$. Throughout the rest of the section, that is, in Lemma 2.1 through Corollary 2.4, we let $t \in [0, T^*)$.

(a) Energy estimate. From the two momentum equations of $(1.1)_{3,4}$ we get after a multiplication, respectively, by u_o and u_w, followed by integration over $[0, 1]$, integration by parts, and use of (1.2),

$$\begin{aligned} &\int_0^1 (\varepsilon_w m u_{wx}^2 + \varepsilon_o n u_{ox}^2)\, dx + \int_0^1 \hat{k}(u_w - u_o)^2\, dx + \int_0^1 \hat{k}_w u_w^2\, dx + \int_0^1 \hat{k}_o u_o^2\, dx \\ &\quad = \int_0^1 n g u_o\, dx + \int_0^1 m g u_w\, dx - \int_0^1 (s_o P_{ox} u_o + s_w P_{wx} u_w)\, dx := I_{1a} + I_{1b} \end{aligned} \tag{2.16}$$

---

[1] It means that the solution exists on $[0, T^*)$ but not on $[0, T^*]$.

with $I_{1a} = \int_0^1 ngu_o\,dx + \int_0^1 mgu_w\,dx$ and $I_{1b} = -\int_0^1 (s_oP_{ox}u_o + s_wP_{wx}u_w)\,dx$. As to I_{1b}, we observe that by using (1.6), $(1.1)_{1,2}$, (1.2), and (2.9) we can compute

$$
\begin{aligned}
&\int_0^1 s_ou_oP_{ox}\,dx \\
&\quad = C_o\int_0^1 s_ou_o(\rho_o)_x\,dx = C_o\int_0^1 nu_o(\ln(\rho_o))_x\,dx = -C_o\int_0^1 (nu_o)_x\ln(\rho_o)\,dx \\
&\quad = C_o\int_0^1 n_t\ln(\rho_o)\,dx + C_o\int_0^1 Q_pn\ln(\rho_o)dx \\
&\quad = C_o\frac{d}{dt}\int_0^1 n\ln(\rho_o)\,dx - C_o\int_0^1 s_o(\rho_o)_t\,dx + C_o\int_0^1 Q_pn\ln(\rho_o)dx \\
&\quad = C_o\frac{d}{dt}\int_0^1 n\ln(\rho_o)\,dx + C_o\int_0^1 (s_o)_t\rho_o\,dx - C_o\frac{d}{dt}\int_0^1 n\,dx + C_o\int_0^1 Q_pn\ln(\rho_o)dx \\
&\quad = C_o\frac{d}{dt}\int_0^1 n\ln(\rho_o)\,dx + \int_0^1 (s_o)_tP_o\,dx + C_o\tilde{\rho}_{o0}\int_0^1 (s_o)_t\,dx + C_o\int_0^1 Q_pn\ln(e\rho_o)dx,
\end{aligned}
\tag{2.17}
$$

and, by similar calculations,

$$
\begin{aligned}
\int_0^1 s_wu_wP_{wx}\,dx &= C_w\int_0^1 s_wu_w(\rho_w)_x\,dx = C_w\int_0^1 mu_w(\ln(\rho_w))_x\,dx \\
&= -C_w\int_0^1 (mu_w)_x\ln(\rho_w)\,dx \\
&= C_w\int_0^1 m_t\ln(\rho_w)\,dx + C_w\int_0^1 Q_pm\ln(\rho_w)dx - C_w\int_0^1 Q_I\rho_w\ln(\rho_w)dx \\
&= C_w\frac{d}{dt}\int_0^1 m\ln(\rho_w)\,dx + \int_0^1 (s_w)_tP_w\,dx + C_w\tilde{\rho}_{w0}\int_0^1 (s_w)_t\,dx \\
&\quad + C_w\int_0^1 (Q_pm - Q_I\rho_w)\ln(e\rho_w)dx.
\end{aligned}
\tag{2.18}
$$

Consequently, using that $P_w = P_o - P_c$ and (1.5), we find from summing (2.17) and (2.18) that

$$
\begin{aligned}
-I_{1b} &= C_o\frac{d}{dt}\int_0^1 n\ln(\rho_o)\,dx + C_w\frac{d}{dt}\int_0^1 m\ln(\rho_w)\,dx \\
&\quad - \int_0^1 s_{wt}P_c(s_w)\,dx + C_o\tilde{\rho}_{o0}\frac{d}{dt}\int_0^1 s_o\,dx \\
&\quad + C_w\tilde{\rho}_{w0}\frac{d}{dt}\int_0^1 s_w\,dx + C_o\int_0^1 Q_pn\ln(e\rho_o)dx \\
&\quad + C_w\int_0^1 (Q_pm - Q_I\rho_w)\ln(e\rho_w)dx.
\end{aligned}
$$

That is,

$$
\begin{aligned}
-I_{1b} = {} & C_o \frac{d}{dt}\int_0^1 n\ln(\rho_o)\,dx + C_w \frac{d}{dt}\int_0^1 m\ln(\rho_w)\,dx - \int_0^1 \Phi(s_w)_t\,dx \\
& + C_o\tilde{\rho}_{o0}\frac{d}{dt}\int_0^1 s_o\,dx + C_w\tilde{\rho}_{w0}\frac{d}{dt}\int_0^1 s_w\,dx \\
& + C_o\int_0^1 Q_p n\ln(e\rho_o)dx + C_w\int_0^1 Q_p m\ln(e\rho_w)dx \\
& - C_w\int_0^1 Q_I\rho_w\ln(e\rho_w)dx,
\end{aligned}
\tag{2.19}
$$

where we have used that $\Phi'(s_w) = P_c(s_w)$.

Total mass. In order to estimate the three last terms on the right-hand side (RHS) of (2.19) it will be useful to first control the total mass $\int(m+n)\,dx$. For that purpose, we integrate mass balance equations $(1.1)_{1,2}$ over space and time:

$$
\int_0^1 ndx = \int_0^1 n_0dx - \int_0^t\int_0^1 Q_pndxdt \tag{2.20}
$$

and

$$
\begin{aligned}
\int_0^1 mdx &= \int_0^1 m_0dx - \int_0^t\int_0^1 Q_pmdxdt + \int_0^t\int_0^1 Q_I\rho_wdxdt \\
&\le \int_0^1 m_0dx - \int_0^t\int_0^1 Q_pmdxdt + \int_0^t\int_0^1 Q_Imdxdt + \frac{C_o}{C_w}\int_0^t\int_0^1 Q_Indxdt \\
&\quad + C\int_0^t\int_0^1 s_odxdt,
\end{aligned}
\tag{2.21}
$$

where $C = C(C_o, C_w, \tilde{\rho}_{w0}, \tilde{\rho}_{o0}) = \|Q_I\|_\infty B < \infty$ with $B = \frac{1}{C_w}\max_{(x,t)}|D - P_c(s_w)|$. For the inequality in (2.21) we make use of the estimate

$$
\rho_w \le m + \frac{C_o}{C_w}n + s_oB, \tag{2.22}
$$

which can be derived from combining

$$
\rho_w = (s_w + s_o)\rho_w = s_o\rho_w + m \tag{2.23}
$$

and

$$
P_c(s_w) = P_o - P_w = C_o\rho_o - C_w\rho_w + D, \tag{2.24}
$$

where $D = C_w\tilde{\rho}_{w0} - C_o\tilde{\rho}_{o0}$. Similarly, we can also get

$$
\rho_o = n + \frac{C_w}{C_o}m + \frac{s_w[P_c(s_w) - D]}{C_o} \le n + \frac{C_w}{C_o}m + s_wZ, \tag{2.25}
$$

where $Z = \frac{1}{C_o}\max_{(x,t)}|P_c(s_w) - D|$.

Now we combine (2.20) and (2.21)

(2.26)

$$\begin{aligned}\int_0^1 (m+n)dx \leq & C_1 + \int_0^t \int_0^1 \left(Q_I m + \frac{C_o}{C_w} Q_I n \right) dxdt - \int_0^t \int_0^1 Q_p (m+n) dxdt \\ & + C \int_0^t \int_0^1 s_o dxdt \\ \leq & C_1 + C_2 \int_0^t \int_0^1 (m+n) dxdt + C \int_0^t \int_0^1 s_o dxdt,\end{aligned}$$

where $C_1 = \int_0^1 (m_0 + n_0) dx$ and $C_2 = \max_{(x,t)} \left| \max\{1, \frac{C_o}{C_w}\} Q_I - Q_p \right|$.

Using Gronwall's inequality in combination with (2.26), we can get

$$\int_0^1 (m+n)dx \leq (C_1 + CT) e^{C_2 T}. \tag{2.27}$$

Further work to estimate $-I_{1b}$. Now we can estimate the last term in (2.19) as follows. First, we note that $x \ln(x) \leq x^{3/2}$, which gives

$$\begin{aligned}&\int_0^1 Q_I \rho_w \ln(e\rho_w) dx \\ &\quad \leq e^{\frac{1}{2}} \|Q_I\|_{L^\infty} \int_0^1 \rho_w^{\frac{3}{2}} dx \leq e^{\frac{1}{2}} \|Q_I\|_{L^\infty} \left\| \rho_w^{\frac{1}{2}} \right\|_{L^\infty(0,1)} \int_0^1 \rho_w dx \\ &\quad \leq \max \left\{ 1, \frac{C_o^{\frac{3}{2}}}{C_w^{\frac{3}{2}}} \right\} e^{\frac{1}{2}} \|Q_I\|_{L^\infty} \|(m+n+C)^{\frac{1}{2}}\|_{L^\infty(0,1)} \int_0^1 (m+n+Cs_o) dx \\ &\quad \leq C_3 \|(m+n+C)^{\frac{1}{2}}\|_{L^\infty(0,1)} \int_0^1 (m+n+Cs_o) dx,\end{aligned} \tag{2.28}$$

where $C_3 = \max\{1, (\frac{C_o}{C_w})^{\frac{3}{2}}\} e^{\frac{1}{2}} (\|Q_I\|_{L^\infty} + 1)$ and we have used (2.22).

Using Sobolev inequality $W^{1,1}(0,1) \hookrightarrow L^\infty(0,1)$, we get

$$\begin{aligned}\|(m+n+C)^{\frac{1}{2}}\|_{L^\infty(0,1)} &\leq \|((m+n+C)^{\frac{1}{2}})_x\|_{L^1(0,1)} + \|(m+n+C)^{\frac{1}{2}}\|_{L^1(0,1)} \\ &\leq \|((m+n+C)^{\frac{1}{2}})_x\|_{L^2(0,1)} + \|(m+n+C)\|_{L^1(0,1)}^{\frac{1}{2}},\end{aligned} \tag{2.29}$$

where we use Hölder's inequality in the second line. In particular,

(2.30)

$$\begin{aligned}&\|((m+n+C)^{\frac{1}{2}})_x\|_{L^2(0,1)} \\ &\quad = \left(\int_0^1 \Big(\frac{1}{2} \frac{m_x + n_x}{\sqrt{m+n+C}} \Big)^2 dx \right)^{\frac{1}{2}} \leq \left(\int_0^1 \frac{1}{2} \Big(\frac{m_x^2}{m+n+C} + \frac{n_x^2}{m+n+C} \Big) dx \right)^{\frac{1}{2}} \\ &\quad \leq \left(\int_0^1 \frac{1}{2} \Big(\frac{m_x^2}{m} + \frac{n_x^2}{n} \Big) dx \right)^{\frac{1}{2}} \leq \frac{1}{2} \int_0^1 \frac{1}{2} \left(\frac{m_x^2}{m} + \frac{n_x^2}{n} \right) dx + \frac{1}{2} \\ &\quad = \frac{1}{4} \int_0^1 (mw^2 + nv^2) dx + \frac{1}{2} \\ &\quad \leq \frac{1}{4} \max \left\{ \frac{1}{\varepsilon_w}, \frac{1}{\varepsilon_o} \right\} \int_0^1 (\varepsilon_w m w^2 + \varepsilon_o n v^2) dx + \frac{1}{2}, \qquad w = \frac{m_x}{m}, \quad v = \frac{n_x}{n},\end{aligned}$$

where the Cauchy–Schwarz inequality has been used. Combining (2.29) and (2.30) with (2.28), where we also take advantage of (2.27), we find

$$\begin{aligned}
&\int_0^1 Q_I \rho_w \ln(e\rho_w)dx \\
&\quad \le C_3 \|(m+n+C)^{\frac{1}{2}}\|_{L^\infty(0,1)} \int_0^1 (m+n+Cs_o)dx \\
&\quad = C_4 \int_0^1 (m+n+Cs_o)dx \int_0^1 (\varepsilon_w m w^2 + \varepsilon_o n v^2)dx + C_5 \int_0^1 (m+n+Cs_o)dx,
\end{aligned} \tag{2.31}$$

where $C_4 = \frac{C_3}{4} max\{\frac{1}{\varepsilon_w}, \frac{1}{\varepsilon_o}\}$ and $C_5 = C_3[\frac{1}{2} + \big(C + (C_1 + CT)e^{C_2 T}\big)^{\frac{1}{2}}]$.

For the two remaining source-related terms involved in the RHS of (2.19) we note that

$$\begin{cases}
-\int_0^1 Q_p m \ln(e\rho_w)dx = -\int_0^1 Q_p m \ln(\rho_w)dx - \int_0^1 Q_p m dx, \\
-\int_0^1 Q_p n \ln(e\rho_o)dx = -\int_0^1 Q_p n \ln(\rho_o)dx - \int_0^1 Q_p n dx.
\end{cases} \tag{2.32}$$

Clearly, we need to control the terms $\int m \ln(\rho_w)$ and $\int n \ln(\rho_o)$ that also appear in the two first terms on the RHS of (2.19). First, we see that

$$\begin{aligned}
&\int_0^1 Q_p m \int_{\tilde{\rho}_w}^{\rho_w} \frac{s - \tilde{\rho}_w}{s^2}\, ds\, dx \\
&\quad = \int_0^1 Q_p m \Big[\ln(s) + \frac{\tilde{\rho}_w}{s}\Big]\Big|_{\tilde{\rho}_w}^{\rho_w} dx \\
&\quad = \int_0^1 Q_p m \ln(\rho_w)\, dx - \ln(\tilde{\rho}_w) \int_0^1 Q_p m\, dx + \tilde{\rho}_w \int_0^1 Q_p s_w\, dx - \int_0^1 Q_p m\, dx
\end{aligned} \tag{2.33}$$

and

$$\begin{aligned}
&\int_0^1 Q_p n \int_{\tilde{\rho}_o}^{\rho_o} \frac{s - \tilde{\rho}_o}{s^2}\, ds\, dx \\
&\quad = \int_0^1 Q_p n \Big[\ln(s) + \frac{\tilde{\rho}_o}{s}\Big]\Big|_{\tilde{\rho}_o}^{\rho_o} dx \\
&\quad = \int_0^1 Q_p n \ln(\rho_o)\, dx - \ln(\tilde{\rho}_o) \int_0^1 Q_p n\, dx + \tilde{\rho}_o \int_0^1 Q_p s_o\, dx - \int_0^1 Q_p n\, dx,
\end{aligned} \tag{2.34}$$

where we choose reference densities $\tilde{\rho}_w, \tilde{\rho}_o$ to be related to the total initial masses m_0 and n_0, which are expressed by $\tilde{m_0} = \tilde{m}(0)$ and $\tilde{n_0} = \tilde{n}(0)$ according to the notation in (2.1). That is, we set $\tilde{\rho}_w = \rho_w(\tilde{m_0}, \tilde{n_0})$ and $\tilde{\rho}_o = \rho_o(\tilde{m_0}, \tilde{n_0})$ which are positive constants. In light of (2.32), (2.33), and (2.34), we have

$$\begin{aligned}
&- C_w \int_0^1 Q_p m \ln(e\rho_w)dx - C_o \int_0^1 Q_p n \ln(e\rho_o)dx \\
&\quad = -C_w \int_0^1 Q_p m \int_{\tilde{\rho}_w}^{\rho_w} \frac{s - \tilde{\rho}_w}{s^2}\, ds\, dx - C_w \ln(\tilde{\rho}_w) \int_0^1 Q_p m\, dx + C_w \tilde{\rho}_w \int_0^1 Q_p s_w\, dx \\
&\qquad - 2C_w \int_0^1 Q_p m\, dx - C_o \int_0^1 Q_p n \int_{\tilde{\rho}_o}^{\rho_o} \frac{s - \tilde{\rho}_o}{s^2}\, ds\, dx - C_o \ln(\tilde{\rho}_o) \int_0^1 Q_p n\, dx
\end{aligned} \tag{2.35}$$

$$
\begin{aligned}
&+ C_o\tilde{\rho}_o \int_0^1 Q_p s_o \, dx - 2C_o \int_0^1 Q_p n \, dx \\
&\le \Big[C_w |\ln(\tilde{\rho}_w)| + C_o |\ln(\tilde{\rho}_o)| \Big] \|Q_p\|_{L^\infty} \int_0^1 (m+n)\, dx + \int_0^1 Q_p (C_w \tilde{\rho}_w s_w + C_o \tilde{\rho}_o s_o)\, dx,
\end{aligned}
$$

where we have used the nonnegative sign of Q_p and $\int_{\tilde{\rho}_i}^{\rho_i} \frac{s-\tilde{\rho}_i}{s^2}\, ds$ $(i = w, o)$ to throw away some troublesome terms. Moreover, (2.31) and (2.35) allow us to estimate the last three terms of the RHS of (2.19) as follows:

(2.36)

$$
\begin{aligned}
&C_w \int_0^1 Q_I \rho_w \ln(e\rho_w) dx - C_w \int_0^1 Q_p m \ln(e\rho_w) dx - C_o \int_0^1 Q_p n \ln(e\rho_o) dx \\
&\quad \le C_w C_4 \int_0^1 (m+n+Cs_o) dx \int_0^1 (\varepsilon_w m w^2 + \varepsilon_o n v^2) dx + C_6 \int_0^1 (m+n+Cs_o) dx \\
&\qquad + \int_0^1 Q_p (C_w \tilde{\rho}_w s_w + C_o \tilde{\rho}_o s_o)\, dx,
\end{aligned}
$$

where $C_6 = C_w C_5 + [C_w |\ln(\tilde{\rho}_w)| + C_o |\ln(\tilde{\rho}_o)|] \|Q_p\|_{L^\infty}$.

Now we continue with a discussion of the two first terms on the RHS of (2.19). Similar to (2.33) and (2.34), we have

(2.37)

$$
\int_0^1 m \int_{\tilde{\rho}_w}^{\rho_w} \frac{s-\tilde{\rho}_w}{s^2}\, ds\, dx = \int_0^1 m \ln(\rho_w)\, dx - \ln(\tilde{\rho}_w) \int_0^1 m\, dx + \tilde{\rho}_w \int_0^1 s_w\, dx - \int_0^1 m\, dx
$$

and

(2.38)

$$
\int_0^1 n \int_{\tilde{\rho}_o}^{\rho_o} \frac{s-\tilde{\rho}_o}{s^2}\, ds\, dx = \int_0^1 n \ln(\rho_o)\, dx - \ln(\tilde{\rho}_o) \int_0^1 n\, dx + \tilde{\rho}_o \int_0^1 s_o\, dx - \int_0^1 n\, dx.
$$

Hence we have

$$
\begin{aligned}
C_w \frac{d}{dt} \int_0^1 m \ln(\rho_w)\, dx &= C_w \frac{d}{dt} \int_0^1 m \int_{\tilde{\rho}_w}^{\rho_w} \frac{s-\tilde{\rho}_w}{s^2}\, ds\, dx - C_w \tilde{\rho}_w \frac{d}{dt} \int_0^1 s_w\, dx \\
&\quad + C_w \ln(e\tilde{\rho}_w) \frac{d}{dt} \int_0^1 m\, dx
\end{aligned}
\tag{2.39}
$$

and

$$
\begin{aligned}
C_o \frac{d}{dt} \int_0^1 n \ln(\rho_o)\, dx &= C_o \frac{d}{dt} \int_0^1 n \int_{\tilde{\rho}_o}^{\rho_o} \frac{s-\tilde{\rho}_o}{s^2}\, ds\, dx - C_o \tilde{\rho}_o \frac{d}{dt} \int_0^1 s_o\, dx \\
&\quad + C_o \ln(e\tilde{\rho}_o) \frac{d}{dt} \int_0^1 n\, dx.
\end{aligned}
\tag{2.40}
$$

Combining (2.19) with (2.39), and (2.40), we see that

(2.41)

$$
\begin{aligned}
&-I_{1b} + \frac{d}{dt} \int_0^1 \Phi(s_w)\, dx \\
&\quad = C_o \frac{d}{dt} \int_0^1 n \ln(\rho_o)\, dx + C_w \frac{d}{dt} \int_0^1 m \ln(\rho_w)\, dx + C_o \tilde{\rho}_{o0} \frac{d}{dt} \int_0^1 s_o\, dx \\
&\qquad + C_w \tilde{\rho}_{w0} \frac{d}{dt} \int_0^1 s_w\, dx + C_o \int_0^1 Q_p n \ln(e\rho_o) dx
\end{aligned}
$$

$$
\begin{aligned}
&+ C_w \int_0^1 Q_p m \ln(e\rho_w)dx - C_w \int_0^1 Q_I \rho_w \ln(e\rho_w)dx \\
&= C_w \frac{d}{dt}\int_0^1 m \int_{\tilde\rho_w}^{\rho_w} \frac{s-\tilde\rho_w}{s^2}\, ds\, dx + C_o \frac{d}{dt}\int_0^1 n \int_{\tilde\rho_o}^{\rho_o} \frac{s-\tilde\rho_o}{s^2}\, ds\, dx \\
&+ C_w \ln(e\tilde\rho_w)\frac{d}{dt}\int_0^1 m\, dx + C_o \ln(e\tilde\rho_o)\frac{d}{dt}\int_0^1 n\, dx \\
&+ C_o \int_0^1 Q_p n \ln(e\rho_o)dx + C_w \int_0^1 Q_p m \ln(e\rho_w)dx - C_w \int_0^1 Q_I \rho_w \ln(e\rho_w)dx \\
&+ C_o[\tilde\rho_{o0} - \tilde\rho_o]\frac{d}{dt}\int_0^1 s_o\, dx + C_w[\tilde\rho_{w0} - \tilde\rho_w]\frac{d}{dt}\int_0^1 s_w\, dx.
\end{aligned}
$$

Note that in view of (1.6), the last line of (2.41) gives us

$$
\begin{aligned}
&C_o[\tilde\rho_{o0} - \tilde\rho_o]\frac{d}{dt}\int_0^1 s_o\, dx + C_w[\tilde\rho_{w0} - \tilde\rho_w]\frac{d}{dt}\int_0^1 s_w\, dx \\
&\quad = -P_o(\tilde\rho_o)\frac{d}{dt}\int_0^1 s_o\, dx - P_w(\tilde\rho_w)\frac{d}{dt}\int_0^1 s_w\, dx \\
&\quad = -P_o(\tilde\rho_o)\frac{d}{dt}\int_0^1 s_o\, dx - P_o(\tilde\rho_o)\frac{d}{dt}\int_0^1 s_w\, dx + P_c(\tilde s_w)\frac{d}{dt}\int_0^1 s_w\, dx \\
&\quad = P_c(\tilde s_w)\frac{d}{dt}\int_0^1 s_w\, dx,
\end{aligned}
$$

where $\tilde\rho_o$, $\tilde\rho_w$, and $\tilde s_w$ are related to each other by common initial total masses $\tilde{m_0}, \tilde{n_0}$ as mentioned above. Consequently, we have that (i) $\tilde\rho_o = \rho_o(\tilde{m_0}, \tilde{n_0})$, $\tilde\rho_w = \rho_w(\tilde{m_0}, \tilde{n_0})$, and $\tilde s_w = s_w(\tilde{m_0}, \tilde{n_0})$; (ii) $P_o(\tilde\rho_o) = P_w(\tilde\rho_w) + P_c(\tilde s_w)$.

Hence, it follows from (2.41) that

(2.42)
$$
\begin{aligned}
I_{1b} =& - C_w \frac{d}{dt}\int_0^1 m \int_{\tilde\rho_w}^{\rho_w} \frac{s-\tilde\rho_w}{s^2}\, ds\, dx - C_o \frac{d}{dt}\int_0^1 n \int_{\tilde\rho_o}^{\rho_o} \frac{s-\tilde\rho_o}{s^2}\, ds\, dx \\
&- \frac{d}{dt}\int_0^1 [P_c(\tilde s_w)s_w - \Phi(s_w)]\, dx - C_w \ln(e\tilde\rho_w)\frac{d}{dt}\int_0^1 m\, dx - C_o \ln(e\tilde\rho_o)\frac{d}{dt}\int_0^1 n\, dx \\
&- C_o \int_0^1 Q_p n \ln(e\rho_o)dx - C_w \int_0^1 Q_p m \ln(e\rho_w)dx + C_w \int_0^1 Q_I \rho_w \ln(e\rho_w)dx.
\end{aligned}
$$

Inserting (2.42) in (2.16) we get

(2.43)
$$
\begin{aligned}
&C_w \frac{d}{dt}\int_0^1 m \int_{\tilde\rho_w}^{\rho_w} \frac{s-\tilde\rho_w}{s^2}\, ds\, dx + C_o \frac{d}{dt}\int_0^1 n \int_{\tilde\rho_o}^{\rho_o} \frac{s-\tilde\rho_o}{s^2}\, ds\, dx \\
&\quad + \frac{d}{dt}\int_0^1 [P_c(\tilde s_w)s_w - \Phi(s_w)]\, dx + C_w \ln(e\tilde\rho_w)\frac{d}{dt}\int_0^1 m\, dx \\
&\quad + C_o \ln(e\tilde\rho_o)\frac{d}{dt}\int_0^1 n\, dx + C_o \int_0^1 Q_p n \ln(e\rho_o)dx + C_w \int_0^1 Q_p m \ln(e\rho_w)dx
\end{aligned}
$$

$$
\begin{aligned}
&+\int_0^1 (\varepsilon_w m u_{wx}^2 + \varepsilon_o n u_{ox}^2)\,dx + \int_0^1 \hat{k}(u_w - u_o)^2\,dx + \int_0^1 \hat{k}_w u_w^2\,dx + \int_0^1 \hat{k}_o u_o^2\,dx \\
&= \int_0^1 n g u_o\,dx + \int_0^1 m g u_w\,dx + C_w \int_0^1 Q_I \rho_w \ln(e\rho_w) dx.
\end{aligned}
$$

Now we want to deal with the gravity related terms appearing on the RHS of (2.43). Clearly, we can integrate in space the mass equations $(1.1)_1$ and $(1.1)_2$ as

$$
\int_0^1\int_0^x (m+n)_t\,dy\,dx + \int_0^1\int_0^x (m u_w + n u_o)_x\,dy\,dx = \int_0^1\int_0^x (\rho_w Q_I - m Q_p - n Q_p) dy dx,
$$

which implies that

$$
\begin{aligned}
\int_0^1 (g m u_w + g n u_o) dx = &- \frac{d}{dt}\int_0^1\int_0^x g(m+n)\,dy\,dx \\
&+ \int_0^1\int_0^x g(\rho_w Q_I - m Q_p - n Q_p) dy dx.
\end{aligned} \tag{2.44}
$$

Therefore, we have

(2.45)

$$
\begin{aligned}
&\frac{d}{dt}\int_0^1 \Big[C_w m \int_{\tilde{\rho}_w}^{\rho_w} \frac{s-\tilde{\rho}_w}{s^2} + C_o n \int_{\tilde{\rho}_o}^{\rho_o} \frac{s-\tilde{\rho}_o}{s^2} \Big] ds\,dx \\
&\quad + \frac{d}{dt}\int_0^1 \Big[C_w \ln(e\tilde{\rho}_w) m + C_o \ln(e\tilde{\rho}_o) n + P_c(\tilde{s}_w) s_w - \Phi(s_w) \Big] dx \\
&\quad + \frac{d}{dt}\int_0^1\int_0^x g(m+n)\,dy\,dx + \int_0^1 \hat{k}(u_w - u_o)^2\,dx \\
&\quad + \int_0^1 \hat{k}_w u_w^2\,dx + \int_0^1 \hat{k}_o u_o^2\,dx + \int_0^1 (\varepsilon_w m u_{wx}^2 + \varepsilon_o n u_{ox}^2)\,dx \\
&= C_w \int_0^1 Q_I \rho_w \ln(e\rho_w) dx - C_o \int_0^1 Q_p n \ln(e\rho_o) dx - C_w \int_0^1 Q_p m \ln(e\rho_w) dx \\
&\quad + \int_0^1\int_0^x g(\rho_w Q_I - m Q_p - n Q_p) dy dx \\
&\le C_w C_4 \int_0^1 (m + n + C s_o) dx \int_0^1 (\varepsilon_w m w^2 + \varepsilon_o n v^2) dx + C_6 \int_0^1 (m + n + C s_o) dx \\
&\quad + \int_0^1 Q_p (C_w \tilde{\rho}_w s_w + C_o \tilde{\rho}_o s_o)\,dx + g\|Q_I\|_{L^\infty} \max\Big\{1, \frac{C_0}{C_w}\Big\} \int_0^1 (m + n + C s_o) dx,
\end{aligned}
$$

where we have used (2.36), the inequality (2.22), and that $g > 0$. Regarding the LHS of (2.45), there is a concern about the sign of the integral

$$
\int \Big[C_w \ln(e\tilde{\rho}_w) m + C_o \ln(e\tilde{\rho}_o) n + P_c(\tilde{s}_w) s_w - \Phi(s_w) \Big] dx.
$$

We now deal with this. First, it is clear from (2.2) that

$$
\int_0^1 [P_c(\tilde{s}_w) s_w - \Phi(s_w)]\,dx \ge c_0 \int_0^1 s_o\,dx. \tag{2.46}
$$

Consequently, we note that (2.20) and (2.21) combined with (2.46) give for some positive constant A to be chosen that

(2.47)
$$\begin{aligned}\frac{d}{dt}\int_0^1 A(m+n)dx \le \int_0^1 A\left(Q_I m+\frac{C_o}{C_w}Q_I n + Cs_o\right)dx \le C_{max}\int_0^1 \big(m+n+s_o\big)\,dx\\ \le C_{max}\int_0^1 \big[m+n+P_c(\tilde{s}_w)s_w-\Phi(s_w)\big]\,dx,\end{aligned}$$

where $C_{max}=\max\{A\|Q_I\|_{L^\infty_{x,t}},\frac{C_o}{C_w}A\|Q_I\|_{L^\infty_{x,t}},\frac{CA}{c_0}\}$ for some positive constant A satisfying

$$A>\max\{C_w|\ln(e\tilde{\rho}_w)|,C_o|\ln(e\tilde{\rho}_o)|\}, \tag{2.48}$$

whose reason for that choice will become clear below.

A preliminary energy inequality. Adding (2.47) to (2.45) and introducing the energy related quantity $E(t)$ defined in (2.50) below gives after using (2.27)

(2.49)

$$\begin{aligned}
&\frac{d}{dt}E(t)+\int_0^1\hat{k}(u_w-u_o)^2\,dx+\int_0^1\hat{k}_w u_w^2\,dx+\int_0^1\hat{k}_o u_o^2\,dx+\int_0^1(\varepsilon_w m u_{wx}^2+\varepsilon_o n u_{ox}^2)\,dx\\
&\le C_wC_4\int_0^1(m+n+Cs_o)dx\int_0^1(\varepsilon_w m w^2+\varepsilon_o n v^2)dx\\
&\quad + C_{max}\int_0^1\big[m+n+P_c(\tilde{s}_w)s_w-\Phi(s_w)\big]dx\\
&\quad + \left(C_6+g\|Q_I\|_{L^\infty}\max\left\{1,\frac{C_0}{C_w}\right\}\right)\int_0^1(m+n+Cs_o)dx\\
&\quad + \int_0^1 Q_p(C_w\tilde{\rho}_w s_w+C_o\tilde{\rho}_o s_o)\,dx\\
&= C_wC_4\int_0^1(m+n+Cs_o)dx\int_0^1(\varepsilon_w m w^2+\varepsilon_o n v^2)dx\\
&\quad + \int_0^1 Q_pC_w\tilde{\rho}_w s_w\,dx+\int_0^1 Q_pC_o\tilde{\rho}_o s_o\,dx\\
&\quad + C_{max}\int_0^1\big[P_c(\tilde{s}_w)s_w-\Phi(s_w)\big]dx+\left(C_6+g\|Q_I\|_{L^\infty}\max\left\{1,\frac{C_0}{C_w}\right\}\right)\int_0^1(Cs_o)dx\\
&\quad + \left(C_{max}+C_6+g\|Q_I\|_{L^\infty}\max\left\{1,\frac{C_0}{C_w}\right\}\right)\int_0^1\big(m+n)dx\\
&\le C_wC_4\Big[(C_1+CT)e^{C_2T}+C\Big]\int_0^1(\varepsilon_w m w^2+\varepsilon_o n v^2)dx+C_w\tilde{\rho}_w\int_0^1 Q_p\,dx\\
&\quad + \left[\frac{C_o\tilde{\rho}_o\|Q_p\|_\infty}{c_0}+C_{max}+\left(C_6+g\|Q_I\|_{L^\infty}\max\left\{1,\frac{C_0}{C_w}\right\}\right)\frac{C}{c_0}\right]\\
&\qquad\qquad \times\int_0^1\big[P_c(\tilde{s}_w)s_w-\Phi(s_w)\big]dx
\end{aligned}$$

$$
\begin{aligned}
&+\left(C_{max}+C_6+g\|Q_I\|_{L^\infty}\max\left\{1,\frac{C_0}{C_w}\right\}\right)\max\left\{\frac{1}{A+C_w\ln(e\tilde{\rho}_w)},\frac{1}{A+C_o\ln(e\tilde{\rho}_o)}\right\}\\
&\qquad\times\int_0^1\Big[\big(A+C_w\ln(e\tilde{\rho}_w)\big)m+\big(A+C_o\ln(e\tilde{\rho}_o)\big)n\Big]\,dx\\
&\le C_wC_4\Big[(C_1+CT)e^{C_2T}+C\Big]\int_0^1(\varepsilon_w m w^2+\varepsilon_o n v^2)dx+C_w\tilde{\rho}_w\int_0^1 Q_p\,dx+C_7E(t),
\end{aligned}
$$

where $w=\frac{m_x}{m}$ and $v=\frac{n_x}{n}$ and we also have used the relation (2.46) to estimate the last term in the fourth and fifth lines of (2.49),

$$
\int_0^1 Q_pC_o\tilde{\rho}_os_odx\le\frac{\|Q_p\|_\infty C_o\tilde{\rho}_o}{c_0}\int_0^1[P_c(\tilde{s}_w)s_w-\Phi(s_w)]dx
$$

and

$$
\int_0^1 Cs_odx\le\frac{C}{c_0}\int_0^1[P_c(\tilde{s}_w)s_w-\Phi(s_w)]dx.
$$

For the last term in line 6, we use that $\int(m+n)dx\le\max\{1/\varepsilon_1,1/\varepsilon_2\}\int(\varepsilon_1m+\varepsilon_2n)dx$ for appropriate choices of ε_1 and ε_2. Note that the two integrals in lines 8 through 10 are contained in the definition of $E(t)$, where we have introduced a constant C_7 as follows:

$$
\left\{
\begin{aligned}
C_7={}&\left(C_{max}+C_6+g\|Q_I\|_{L^\infty}\max\left\{1,\frac{C_0}{C_w}\right\}\right)\\
&\times\max\left\{\tfrac{1}{A+C_w\ln(e\tilde{\rho}_w)},\tfrac{1}{A+C_o\ln(e\tilde{\rho}_o)},\tfrac{C}{c_0}\right\}\\
&+C_{max}+\frac{C_o\tilde{\rho}_o\|Q_p\|_\infty}{c_0},\\
E(t)={}&\int_0^1\left[C_wm\int_{\tilde{\rho}_w}^{\rho_w}\frac{s-\tilde{\rho}_w}{s^2}+C_on\int_{\tilde{\rho}_o}^{\rho_o}\frac{s-\tilde{\rho}_o}{s^2}+P_c(\tilde{s}_w)s_w\right.\\
&\qquad\left.-\Phi(s_w)+\int_0^x g(m+n)\,dy\right]dx\\
&+\int_0^1\Big[\big(A+C_w\ln(e\tilde{\rho}_w)\big)m+\big(A+C_o\ln(e\tilde{\rho}_o)\big)n\Big]\,dx.
\end{aligned}
\right.
\tag{2.50}
$$

In view of (2.46) and the definition of A expressed by (2.48), it follows that $E(t)$ is nonnegative.

Remark 2.5. The energy inequality (2.49) reflects the additional complexity introduced by the source terms Q_I and Q_p. In particular, on the RHS of the inequlity we find both the appearance of the energy $E(t)$, source-dependent terms, as well as the higher order terms $w=\frac{m_x}{m}$ and $v=\frac{n_x}{n}$. This contrasts with the situation without source terms as reflected by Lemma 2.1 in [29], where the energy $E(t)$ is controlled by the initial energy $E(t=0)$.

(b) Higher order regularity of mass "m" and "n."

LEMMA 2.1. *The following estimates hold for any $t\in[0,T^*)$:*

$$
E(t)+\int_0^1\frac{1}{2}[\varepsilon_wmw^2+\varepsilon_onv^2]\,dx\le K_1,\qquad w=\frac{m_x}{m},\quad v=\frac{n_x}{n},
$$

and

$$\begin{aligned}&\int_0^t\int_0^1\Big(s_o[(\rho_o^{1/2})_x]^2+s_w[(\rho_w^{1/2})_x]^2+s_{wx}^2\Big)\,dxdt+\int_0^t\int_0^1(\varepsilon_w m u_{wx}^2+\varepsilon_o n u_{ox}^2)\,dx\,dt\\&\quad+\int_0^t\int_0^1\Big[\hat{k}(u_w-u_o)^2+\hat{k}_w u_w^2+\hat{k}_o u_o^2\Big]\,dx\,dt\le C(T),\end{aligned}$$

for some positive constant $C(T)$, where $E(t)$ is given by $(2.50)_2$ and K_1 by

$$K_1=e^{C_{11}T}\Big[E(0)+\int_0^1\frac{1}{2}[\varepsilon_w m_0 w_0^2+\varepsilon_o n_0 v_0^2]\,dx+C_w\tilde{\rho}_w\int_0^T\int_0^1 Q_p\,dx\,ds\Big],$$

and C_{11} is given by (2.75).

Proof. Note that from $(1.1)_2$ we get the following reformulated equation after expanding the advective term and taking a derivative in space:

$$(m_x)_t+(m_x u_w)_x+(mQ_p-\rho_w Q_I)_x=-(m u_{wx})_x. \tag{2.51}$$

Note the appearance of the viscosity term on the RHS of (2.51). We have from $(1.1)_4$

$$s_w P_{wx}=-\hat{k}_w u_w-\hat{k}(u_w-u_o)+\varepsilon_w(m u_{wx})_x+mg. \tag{2.52}$$

Combining (2.51) with (2.52) we arrive at

$$\begin{aligned}(\varepsilon_w m_x)_t+(\varepsilon_w m_x u_w)_x+\varepsilon_w(mQ_p-\rho_w Q_I)_x&=-\varepsilon_w(m u_{wx})_x\\&=-s_w P_{wx}-\hat{k}_w u_w-\hat{k}(u_w-u_o)+mg.\end{aligned}$$

This is the same as

$$[\varepsilon_w m w]_t+[\varepsilon_w m w u_w]_x+\varepsilon_w(mQ_p-\rho_w Q_I)_x=-s_w P_{wx}-\hat{k}_w u_w-\hat{k}(u_w-u_o)+mg$$

for

$$w=\frac{m_x}{m},$$

which clearly, by using $(1.1)_2$, can be rewritten as

$$\begin{aligned}&\varepsilon_w m w_t+\varepsilon_w m u_w w_x+\varepsilon_w(mQ_p-\rho_w Q_I)_x+\varepsilon_w w(\rho_w Q_I-mQ_p)\\&\quad=-s_w P_{wx}-\hat{k}_w u_w-\hat{k}(u_w-u_o)+mg.\end{aligned} \tag{2.53}$$

Now, we test (2.53) with w and combine it with $(1.1)_2$ and (1.2), which leads us to

$$\begin{aligned}&\frac{\varepsilon_w}{2}\frac{d}{dt}\int_0^1 m w^2\,dx+\frac{\varepsilon_w}{2}\int_0^1(\rho_w Q_I-mQ_p)w^2dx+\int_0^1\varepsilon_w w(mQ_p-\rho_w Q_I)_x dx\\&\quad=-\int_0^1 s_w P_{wx}w\,dx-\int_0^1\hat{k}_w u_w w\,dx-\int_0^1\hat{k}(u_w-u_o)w\,dx+\int_0^1 mgw\,dx.\end{aligned} \tag{2.54}$$

Similarly, for the oil phase we obtain

$$\begin{aligned}&\frac{\varepsilon_o}{2}\frac{d}{dt}\int_0^1 n v^2\,dx+\frac{\varepsilon_o}{2}\int_0^1(-nQ_p)v^2dx+\int_0^1\varepsilon_o v(nQ_p)_x dx\\&\quad=-\int_0^1 s_o P_{ox}v\,dx-\int_0^1\hat{k}_o u_o v\,dx+\int_0^1\hat{k}(u_w-u_o)v\,dx+\int_0^1 ngv\,dx\end{aligned} \tag{2.55}$$

with

$$v=\frac{n_x}{n}.$$

Source-related terms. Regarding one of the source-related terms in (2.54) we estimate as follows:

$$\begin{aligned}(2.56)\quad \int_0^1 \varepsilon_w w(mQ_p)_x dx &= \varepsilon_w \int_0^1 \left(mw^2 Q_p + \frac{m_x}{\sqrt{m}}\sqrt{m}Q_{px}\right) dx \\ &\le \varepsilon_w \int_0^1 mw^2 Q_p dx + \frac{1}{2}\varepsilon_w \int_0^1 mw^2 dx + \frac{1}{2}\varepsilon_w \int_0^1 mQ_{px}^2 dx.\end{aligned}$$

Similarly, for one of the source-related terms in (2.55) we have

$$\begin{aligned}(2.57)\quad \int_0^1 \varepsilon_o v(nQ_p)_x dx &= \varepsilon_o \int_0^1 \left(nv^2 Q_p + \frac{n_x}{\sqrt{n}}\sqrt{n}Q_{px}\right) dx \\ &\le \varepsilon_o \int_0^1 nv^2 Q_p dx + \frac{1}{2}\varepsilon_o \int_0^1 nv^2 dx + \frac{1}{2}\varepsilon_o \int_0^1 nQ_{px}^2 dx.\end{aligned}$$

By Cauchy inequality (with $\varepsilon = 1/4$), we can estimate another source-related term in (2.54) as follows:

(2.58)

$$\begin{aligned}\int_0^1 \varepsilon_w w(\rho_w Q_I)_x dx = &\int_0^1 \varepsilon_w w[\rho_w (Q_I)_x + (\rho_w)_x Q_I] dx \\ \le &\frac{\varepsilon_w}{2}\int_0^1 \rho_w Q_I w^2 dx + \varepsilon_w \int_0^1 \rho_w \frac{|(Q_I)_x|^2}{Q_I} dx + \varepsilon_w \int_0^1 \frac{|(\rho_w)_x|^2}{\rho_w} Q_I dx \\ \le &\frac{\varepsilon_w}{2}\int_0^1 \rho_w Q_I w^2 dx \\ &+ \varepsilon_w \max\left\{1, \frac{C_o}{C_w}\right\} \left\| \frac{|(Q_I)_x|^2}{Q_I} \right\|_{L^\infty} \int_0^1 (m + n + Cs_o) dx \\ &+ \varepsilon_w \int_0^1 \frac{|(\rho_w)_x|^2}{\rho_w} Q_I dx,\end{aligned}$$

where we have used (2.22). We now focus on how to estimate the last term in (2.58). Recalling (2.24), we have

$$\rho_w = s_w \rho_w + s_o \rho_w, \qquad \rho_w = \frac{C_o}{C_w}\rho_o + \frac{D - P_c(s_w)}{C_w},$$

where $D = C_w \tilde{\rho}_{w0} - C_o \tilde{\rho}_{o0}$. Thus we have

$$(2.59)\qquad \rho_w = m + \frac{C_o}{C_w} n + \frac{s_o[D - P_c(s_w)]}{C_w},$$

which implies that

$$\begin{aligned}(2.60)\qquad (\rho_w)_x &= m_x + \frac{C_o}{C_w} n_x + \frac{(s_o)_x [D - P_c(s_w)]}{C_w} - \frac{s_o P_c'(s_w)(s_w)_x}{C_w} \\ &= m_x + \frac{C_o}{C_w} n_x - (s_w)_x \frac{D - P_c(s_w) + s_o P_c'(s_w)}{C_w}.\end{aligned}$$

Substituting (2.60) into the last term on the RHS of (2.58), we have

$$\begin{aligned}\varepsilon_w\int_0^1\frac{|(\rho_w)_x|^2}{\rho_w}Q_I dx \le 4\varepsilon_w\int_0^1\frac{|m_x|^2}{\rho_w}Q_I dx + 4\varepsilon_w\left(\frac{C_o}{C_w}\right)^2\int_0^1\frac{|n_x|^2}{\rho_w}Q_I dx\\ + 4\varepsilon_w\int_0^1\frac{|(s_w)_x|^2}{\rho_w}Q_I\left[\frac{D-P_c(s_w)+s_oP_c'(s_w)}{C_w}\right]^2 dx.\end{aligned}$$

In view of (2.4) it is clear from (2.59) that

$$\rho_w \ge \frac{C_o}{C_w}n + m.$$

Therefore

$$\begin{aligned}\varepsilon_w\int_0^1\frac{|(\rho_w)_x|^2}{\rho_w}Q_I dx \le 4\varepsilon_w\|Q_I\|_{L^\infty}\int_0^1 mw^2 dx + 4\varepsilon_w\|Q_I\|_{L^\infty}\left(\frac{C_o}{C_w}\right)\int_0^1 nv^2 dx\\ + 4\varepsilon_w\left\|\left(\sqrt{Q_I}\frac{D-P_c(s_w)+s_oP_c'(s_w)}{C_w\sqrt{\rho_w}}\right)^2\right\|_{L^\infty}\int_0^1 (s_w)_x^2 dx.\end{aligned}\tag{2.61}$$

Consequently, from (2.58) we obtain

$$\begin{aligned}&\int_0^1\varepsilon_w w(\rho_wQ_I)_x dx\\ &\le \frac{\varepsilon_w}{2}\int_0^1\rho_wQ_Iw^2dx + \varepsilon_w\max\left\{1,\frac{C_o}{C_w}\right\}\left\|\frac{|(Q_I)_x|^2}{Q_I}\right\|_{L^\infty}\int_0^1(m+n+Cs_o)dx\\ &\quad + 4\varepsilon_w\|Q_I\|_{L^\infty}\int_0^1 mw^2dx + 4\varepsilon_w\|Q_I\|_{L^\infty}\left(\frac{C_o}{C_w}\right)\int_0^1 nv^2dx\\ &\quad + 4\varepsilon_w\left\|\left(\sqrt{Q_I}\frac{D-P_c(s_w)+s_oP_c'(s_w)}{C_w\sqrt{\rho_w}}\right)^2\right\|_{L^\infty}\int_0^1(s_w)_x^2dx.\end{aligned}\tag{2.62}$$

Next, we focus on the terms appearing on the RHS of (2.54):

$$-\int_0^1 s_wP_{wx}w\,dx = -\int_0^1 s_wP_{wx}\left(\frac{m_x}{m}\right)dx := J_{w,1}.$$

We note that

$$\begin{aligned}J_{w,1} &= -\int_0^1 s_wP_{wx}\frac{m_x}{m}\,dx = -\int_0^1 s_{wx}P_{wx}\,dx - \int_0^1 s_wP_{wx}\frac{s_w\rho_{wx}}{m}\,dx\\ &= -\int_0^1 s_{wx}P_{wx}\,dx - 4C_w\int_0^1 s_w[(\rho_w^{1/2})_x]^2\,dx.\end{aligned}\tag{2.63}$$

Similarly, for $J_{o,1}$ associated with (2.55)

$$\begin{aligned}J_{o,1} &= -\int_0^1 s_oP_{ox}\frac{n_x}{n}\,dx = -\int_0^1 s_{ox}P_{ox}\,dx - \int_0^1 s_oP_{ox}\frac{\alpha_o\rho_{ox}}{n}\,dx\\ &= -\int_0^1 s_{ox}P_{ox}\,dx - 4C_o\int_0^1 s_o[(\rho_o^{1/2})_x]^2\,dx.\end{aligned}\tag{2.64}$$

A preliminary higher order energy inequality. To conclude, we see that by summing (2.54) and (2.55), using (2.63) and (2.64), we get

$$
\begin{aligned}
&\frac{1}{2}\frac{d}{dt}\int_0^1 [\varepsilon_w m w^2 + \varepsilon_o n v^2]\,dx + 4C_o\int_0^1 s_o[(\rho_o^{1/2})_x]^2\,dx + 4C_w\int_0^1 s_w[(\rho_w^{1/2})_x]^2\,dx \\
&\quad + \frac{\varepsilon_w}{2}\int_0^1 \rho_w Q_I w^2 dx = \int_0^1 s_{wx}^2 P_c'(s_w)\,dx + \int_0^1 mgw\,dx + \int_0^1 ngv\,dx \\
&\quad - \int_0^1 \hat{k}(u_w - u_o)w\,dx + \int_0^1 \hat{k}(u_w - u_o)v\,dx - \int_0^1 \hat{k}_w u_w w\,dx - \int_0^1 \hat{k}_o u_o v\,dx \\
&\quad + \frac{\varepsilon_w}{2}\int_0^1 Q_p m w^2 dx + \frac{\varepsilon_o}{2}\int_0^1 Q_p n v^2 dx \\
&\quad - \int_0^1 \varepsilon_w w(mQ_p - \rho_w Q_I)_x dx - \int_0^1 \varepsilon_o v(nQ_p)_x dx,
\end{aligned}
\tag{2.65}
$$

where we again have used $P_c(s_w) = P_o - P_w$. Now, we focus on estimating the source-related terms appearing in the last line of (2.65). In particular, by referring to (2.56), (2.57), and (2.62), we can estimate the last five terms in (2.65) as follows:

$$
\begin{aligned}
&\frac{d}{dt}\int_0^1 \left[\frac{\varepsilon_w m w^2}{2} + \frac{\varepsilon_o n v^2}{2}\right] dx + 4C_o\int_0^1 s_o[(\rho_o^{1/2})_x]^2\,dx \\
&\quad + 4C_w\int_0^1 s_w[(\rho_w^{1/2})_x]^2\,dx - \int_0^1 s_{wx}^2 P_c'(s_w)\,dx \\
&\le -\int_0^1 \hat{k}(u_w - u_o)\left(\frac{m_x}{m}\right) dx + \int_0^1 \hat{k}(u_w - u_o)\left(\frac{n_x}{n}\right) dx \\
&\quad - \int_0^1 \hat{k}_w u_w\left(\frac{m_x}{m}\right) dx - \int_0^1 \hat{k}_o u_o\left(\frac{n_x}{n}\right) dx \\
&\quad + \int_0^1 m_x g\,dx + \int_0^1 n_x g\,dx + \left(\frac{3}{2}\|Q_p\|_{L^\infty} + \frac{1}{2}\right. \\
&\qquad\qquad\qquad \left. + 4\max\left\{1, \frac{C_o}{C_w}\right\}\|Q_I\|_{L^\infty}\right)\int_0^1 \big(\varepsilon_w m w^2 + \varepsilon_o n v^2\big)dx \\
&\quad + C_9\int_0^1 \big[m + n + P_c(\tilde{s}_w)s_w - \Phi(s_w)\big]dx \\
&\quad + 4\varepsilon_w\left\|\left(\sqrt{Q_I}\frac{D - P_c(s_w) + s_o P_c'(s_w)}{C_w\sqrt{\rho_w}}\right)^2\right\|_{L^\infty}\int_0^1 (s_w)_x^2 dx \\
&:= K_{w1} + K_{o1} + K_{w2} + K_{o2} + K_{w3} + K_{o3} \\
&\quad + C_8\int_0^1 \big(\varepsilon_w m w^2 + \varepsilon_o n v^2\big)dx + C_9\int_0^1 \big[m + n + P_c(\tilde{s}_w)s_w - \Phi(s_w)\big]dx \\
&\quad + C_{10}\int_0^1 (s_w)_x^2 dx,
\end{aligned}
\tag{2.66}
$$

where

$$
K_{w1} = -\int_0^1 \hat{k}(u_w - u_o)w\,dx, \quad K_{w2} = -\int_0^1 \hat{k}_w u_w w\,dx, \quad K_{w3} = \int_0^1 m_x g dx
$$

(similarly for K_{o1}, K_{o2}, and K_{o3}) and

$$\begin{aligned}
C_8 &= \frac{3}{2}\|Q_p\|_{L^\infty} + \frac{1}{2} + 4\max\left\{1, \frac{C_o}{C_w}\right\}\|Q_I\|_{L^\infty},\\
C_9 &= \max\left\{\frac{1}{2}\varepsilon_w\|Q_{px}^2\|_{L^\infty}, \frac{1}{2}\varepsilon_o\|Q_{px}^2\|_{L^\infty}\right\}\\
&\quad + \max\left\{\varepsilon_w\left\|\frac{|(Q_I)_x|^2}{Q_I}\right\|_{L^\infty}, \varepsilon_w\frac{C_o}{C_w}\left\|\frac{|(Q_I)_x|^2}{Q_I}\right\|_{L^\infty}, \frac{C}{c_0}\right\},\\
C_{10} &= 4\varepsilon_w\left\|\left(\sqrt{Q_I}\frac{D - P_c(s_w) + s_oP_c'(s_w)}{C_w\sqrt{\rho_w}}\right)^2\right\|_{L^\infty}.
\end{aligned}$$

Note that the first term on the RHS of (2.62), $\frac{\varepsilon_w}{2}\int_0^1 \rho_w Q_I w^2 dx$, has been adsorbed by a term of the same form appearing in the first line of (2.65). Note also that we use (2.5) to ensure that C_9 is a positive constant. Similarly, we use the fact that $C_w\rho_w \geq D - P_c(s_w) \geq D - \sup P_c(s_w) > 0$, as seen from the relation above (2.59) and (2.4), to conclude that C_{10} is a positive constant since

$$\begin{aligned}
C_{10} &= 4\varepsilon_w\frac{\|Q_I\|_\infty}{C_w}\left\|\frac{(D - P_c(s_w) + s_oP_c'(s_w))^2}{C_w\rho_w}\right\|_\infty\\
&\leq 8\varepsilon_w\frac{\|Q_I\|_\infty}{C_w}\left(\|D - P_c\|_\infty + \frac{P_c'(s_w)^2}{D - P_c(s_w)}\right) \leq 16\varepsilon_w\frac{\|Q_I\|_\infty}{C_w}\|D - P_c\|_\infty,
\end{aligned}\tag{2.67}$$

where we have used (2.7) (last inequality). Next, we estimate as follows by relying on Cauchy's inequality:

$$\begin{aligned}
K_{w3} &= \int_0^1 m_x g dx = g\int_0^1 \frac{m_x}{\sqrt{m}}\sqrt{m}dx\\
&\leq g\int_0^1 \frac{m_x^2}{m}dx + \frac{1}{4}g\int_0^1 mdx = g\int_0^1 mw^2dx + \frac{1}{4}g\int_0^1 mdx
\end{aligned}\tag{2.68}$$

and

$$\begin{aligned}
K_{o3} &= \int_0^1 n_x g dx = g\int_0^1 \frac{n_x}{\sqrt{n}}\sqrt{n}dx\\
&\leq g\int_0^1 \frac{n_x^2}{n}dx + \frac{1}{4}g\int_0^1 ndx = g\int_0^1 nv^2dx + \frac{1}{4}g\int_0^1 ndx.
\end{aligned}\tag{2.69}$$

In the following we make use of the functional form of the interaction coefficients $\hat{k}_o$, $\hat{k}_o$, and $\hat{k}$ as expressed in (2.8).

$$K_{w1} \leq \frac{1}{4}\int_0^1 \hat{k}(u_w - u_o)^2dx + I_{wo}\int_0^1 \frac{m_x^2}{m}dx = \frac{1}{4}\int_0^1 \hat{k}(u_w - u_o)^2dx + I_{wo}\int_0^1 mw^2dx,\tag{2.70}$$

$$K_{o1} \leq \frac{1}{4}\int_0^1 \hat{k}(u_w - u_o)^2dx + I_{wo}\int_0^1 \frac{n_x^2}{n}dx = \frac{1}{4}\int_0^1 \hat{k}(u_w - u_o)^2dx + I_{wo}\int_0^1 nv^2dx,\tag{2.71}$$

$$K_{w2} \leq \frac{1}{4}\int_0^1 \hat{k}_w u_w^2dx + I_w\int_0^1 \frac{m_x^2}{m}dx = \frac{1}{4}\int_0^1 \hat{k}_w u_w^2dx + I_w\int_0^1 mw^2dx,\tag{2.72}$$

and

$$K_{o2} \leq \frac{1}{4}\int_0^1 \hat{k}_o u_o^2dx + I_o\int_0^1 \frac{n_x^2}{n}dx = \frac{1}{4}\int_0^1 \hat{k}_o u_o^2dx + I_o\int_0^1 nv^2dx.\tag{2.73}$$

A combined low and high order energy inequality. Then we sum the energy estimate (2.49) and Bresch–Desjardin estimate (2.66) and combine the resulting inequality with the estimates (2.68)–(2.73) and obtain

$$
\begin{aligned}
&\frac{d}{dt}\Big[E(t)+\int_0^1 \frac{1}{2}(\varepsilon_w m w^2+\varepsilon_o n v^2)\,dx\Big]\\
&\quad+4C_o\int_0^1 s_o[(\rho_o^{1/2})_x]^2\,dx+4C_w\int_0^1 s_w[(\rho_w^{1/2})_x]^2\,dx-\int_0^1 s_{wx}^2(P_c'(s_w)+C_{10})\,dx\\
&\quad+\int_0^1(\varepsilon_w m u_{wx}^2+\varepsilon_o n u_{ox}^2)\,dx+\frac{1}{2}\int_0^1 \hat{k}(u_w-u_o)^2\,dx+\frac{3}{4}\int_0^1 \hat{k}_w u_w^2\,dx\\
&\quad+\frac{3}{4}\int_0^1 \hat{k}_o u_o^2\,dx\\
&\le\Bigg((g+I_{wo}+I_w+I_o)\max\Big\{\frac{1}{\varepsilon_w},\frac{1}{\varepsilon_o}\Big\}+C_8\\
&\qquad+C_wC_4\Big[(C_1+CT)e^{C_2T}+C\Big]\Bigg)\int_0^1(\varepsilon_w m w^2+\varepsilon_o n v^2)dx\\
&\quad+\Big(C_9+\frac{1}{4}g\Big)\int_0^1\big[m+n+P_c(\tilde{s}_w)s_w-\Phi(s_w)\big]dx+C_7E(t)+C_w\tilde{\rho}_w\int_0^1 Q_p\,dx\\
&\le C_{11}\Big[E(t)+\int_0^1\frac{1}{2}(\varepsilon_w m w^2+\varepsilon_o n v^2)\,dx\Big]+C_w\tilde{\rho}_w\int_0^1 Q_p\,dx,
\end{aligned}
\tag{2.74}
$$

where we make use of the fact that $P_c'(s_w)+C_{10}<0$ for all $s_w\in[0,1]$ which is guaranteed through (2.7) (first inequality) combined with (2.67). Moreover, we have introduced the notation

$$
\begin{aligned}
C_{11}=&\,2\Bigg((g+I_{wo}+I_w+I_o)\max\Big\{\frac{1}{\varepsilon_w},\frac{1}{\varepsilon_o}\Big\}+C_8+C_wC_4\Big[(C_1+CT)e^{C_2T}+C\Big]\Bigg)\\
&+\Big(C_9+\frac{1}{4}g\Big)\max\Big\{\frac{1}{A+C_w\ln(e\tilde{\rho}_w)},\frac{1}{A+C_o\ln(e\tilde{\rho}_o)},1\Big\}+C_7.
\end{aligned}
\tag{2.75}
$$

In other words, we have by application of Gronwall's inequality

$$
\begin{aligned}
E(t)&+\int_0^1\frac{1}{2}[\varepsilon_w m w^2+\varepsilon_o n v^2]\,dx\\
&\le e^{C_{11}T}\Big[E(0)+\int_0^1\frac{1}{2}[\varepsilon_w m_0 w_0^2+\varepsilon_o n_0 v_0^2]\,dx+C_w\tilde{\rho}_w\int_0^T\int_0^1 Q_p\,dx\,ds\Big]\\
&:=K_1
\end{aligned}
\tag{2.76}
$$

for $t\in[0,T^*)$, where

$$
\begin{aligned}
E(t)=\int_0^1&\Big[C_w m\int_{\tilde{\rho}_w}^{\rho_w}\frac{s-\tilde{\rho}_w}{s^2}+C_o n\int_{\tilde{\rho}_o}^{\rho_o}\frac{s-\tilde{\rho}_o}{s^2}+P_c(\tilde{s}_w)s_w-\Phi(s_w)\\
&+\int_0^x g(m+n)\,dy\Big]\,dx+\int_0^1\Big[\big(A+C_w\ln(e\tilde{\rho}_w)\big)m\\
&+\big(A+C_o\ln(e\tilde{\rho}_o)\big)n\Big]\,dx.
\end{aligned}
$$

Consequently, it follows from (2.74) and (2.76) that

$$\begin{aligned}&\int_0^t\int_0^1\Big(s_o[(\rho_o^{1/2})_x]^2+s_w[(\rho_w^{1/2})_x]^2+s_{wx}^2\Big)\,dxdt+\int_0^t\int_0^1(\varepsilon_w m u_{wx}^2+\varepsilon_o n u_{ox}^2)\,dxdt\\&+\int_0^t\int_0^1\Big[\hat{k}(u_w-u_o)^2+\hat{k}_w u_w^2+\hat{k}_o u_o^2\Big]\,dxdt\le C_{12}(T).\qquad\square\end{aligned}\tag{2.77}$$

In view of Lemma 2.1 and (2.27) it follows that $\sqrt{m},\sqrt{n}\in H^1(0,1)$. Combined with the Sobolev inequality $H^1(0,1)\hookrightarrow C([0,1])$, we have the following corollary.

Corollary 2.1. *It holds that*

$$\begin{cases}m(x,t)+n(x,t)\le C(T) & \textit{for any } (x,t)\in[0,1]\times[0,T^*),\\ \displaystyle\int_0^1(m_x^2+n_x^2)\,dx\le C(T) & \textit{for any } t\in[0,T^*).\end{cases}\tag{2.78}$$

(c) Upper and lower bounds of density and related quantities.

Lemma 2.2. *For any $(x,t)\in[0,1]\times[0,T^*)$, it holds that*

$$\begin{cases}n(x,t)\le\rho_o\le C(T),\\ m(x,t)\le\rho_w\le C(T).\end{cases}\tag{2.79}$$

We omit the proof and refer to [29, Lemma 2.3] for details.

Corollary 2.2. *It holds that for any $(x,t)\in[0,1]\times[0,T^*)$*

$$\begin{cases}m(x,t)\ge\dfrac{1}{2}\tilde{m}_0 e^{-\int_0^T\sup\limits_{x\in[0,1]}|Q_p|ds},\\ n(x,t)\ge\dfrac{1}{2}\tilde{n}_0 e^{-\int_0^T\sup\limits_{x\in[0,1]}|Q_p|ds},\end{cases}\tag{2.80}$$

provided that

$$K_1\le\min\Big\{\frac{\varepsilon_w}{4}\tilde{m}_0 e^{-\int_0^T\sup\limits_{x\in[0,1]}|Q_p|ds},\frac{\varepsilon_o}{4}\tilde{n}_0 e^{-\int_0^T\sup\limits_{x\in[0,1]}|Q_p|ds}\Big\}.\tag{2.81}$$

Proof.

$$\begin{aligned}|m(x,t)-\tilde{m}|&=\left|\int_0^1[m(x,t)-m(y,t)]\,dy\right|=\left|\int_0^1\int_y^x m_\xi(\xi,t)\,d\xi\,dy\right|\\&\le\int_0^1|m_x(x,t)|\,dx=\int_0^1\sqrt{m(x,t)}\left|\frac{m_x(x,t)}{\sqrt{m(x,t)}}\right|\,dx\\&\le\left(\int_0^1 m(x,t)\,dx\right)^{\frac{1}{2}}\left(\int_0^1\frac{|m_x(x,t)|^2}{m}\,dx\right)^{\frac{1}{2}}\\&\le\left(\frac{\tilde{m}K_1}{\varepsilon_w}\right)^{\frac{1}{2}},\end{aligned}$$

in light of (2.76). Therefore

$$m(x,t) \geq \int_0^1 m(x,t)dx - \left(\frac{\tilde{m}K_1}{\varepsilon_w}\right)^{\frac{1}{2}}.$$

Integrating the water mass balance equation $(1.1)_2$ gives

$$\tilde{m}(t) = \int_0^1 m(x,t)dx = \int_0^1 m_0(x)dx - \int_0^t \int_0^1 mQ_p dxdt + \int_0^t \int_0^1 \rho_w Q_I dxdt.$$

We can get

$$m(x,t) \geq \int_0^1 m_0(x)dx - \int_0^t \int_0^1 mQ_p dxdt + \int_0^t \int_0^1 \rho_w Q_I dxdt - \left(\frac{\tilde{m}K_1}{\varepsilon_w}\right)^{\frac{1}{2}}.$$

In order to get the lower limit of $\tilde{m}$, we consider the integration of water mass balance equation $(1.1)_2$ and can get the following inequality:

$$\frac{d}{dt}\int_0^1 m(x,t)dx \geq -\int_0^1 mQ_p dx \geq -\sup_{x\in[0,1]}|Q_p|\tilde{m}(t).$$

Therefore

$$\begin{aligned} \frac{d}{dt}\tilde{m}(t) + \sup_{x\in[0,1]}|Q_p|\tilde{m}(t) \geq 0,& \\ \tilde{m}(t)e^{\int_0^t \sup_{x\in[0,1]}|Q_p|ds} \geq \tilde{m}_0,& \\ \tilde{m}(t) \geq \tilde{m}_0 e^{-\int_0^T \sup_{x\in[0,1]}|Q_p|ds}.& \end{aligned}$$

Letting

$$K_1 \leq \frac{\varepsilon_w}{4}\tilde{m}_0 e^{-\int_0^T \sup_{x\in[0,1]}|Q_p|ds},$$

we have

$$\begin{aligned} m(x,t) &\geq [\tilde{m}(t)]^{\frac{1}{2}}\left[[\tilde{m}(t)]^{\frac{1}{2}} - \left(\frac{K_1}{\varepsilon_w}\right)^{\frac{1}{2}}\right] \\ &\geq \frac{1}{2}\tilde{m}_0 e^{-\int_0^T \sup_{x\in[0,1]}|Q_p|ds}. \end{aligned}$$

Similarly, letting

$$K_1 \leq \frac{\varepsilon_o}{4}\tilde{n}_0 e^{-\int_0^T \sup_{x\in[0,1]}|Q_p|ds},$$

we get the positive lower bound of n.

(d) High-order estimates of volume fraction and density.

LEMMA 2.3. *The following estimate holds:*

$$\int_0^1 \left[(s_w)_x^2 + (s_o)_x^2 + (\rho_w)_x^2 + (\rho_o)_x^2\right] dx \le C(T) \tag{2.82}$$

for any $t \in [0, T^*)$.

LEMMA 2.4. *For any* $t \in [0, T*)$, *it holds that*

$$\int_0^1 \left[(u_w)_x^2 + (u_o)_x^2\right] dx \le C(T). \tag{2.83}$$

COROLLARY 2.3. *For any* $t \in [0, T^*)$, *it holds that*

$$\int_0^1 \left[(u_w)_{xx}^2 + (u_o)_{xx}^2\right] dx \le C(T). \tag{2.84}$$

We refer to [29] for more details regarding the proofs of Lemma 2.3, Lemma 2.4, and Corollary 2.3 since these essentially are the same.

COROLLARY 2.4. *For any* $t \in [0, T^*)$, *it holds that*

$$\int_0^1 \left[m_t^2 + n_t^2 + (s_w)_t^2 + (s_o)_t^2 + (\rho_w)_t^2 + (\rho_o)_t^2\right] dx \le C(T). \tag{2.85}$$

Proof. By using the mass equation of water $(1.7)_1$, the Cauchy inequality, (2.78), (2.79), and (2.83), we have

(2.86)

$$\begin{aligned}
\int_0^1 m_t^2 \, dx &\le 2\int_0^1 \left[m^2 (u_w)_x^2 + m_x^2 u_w^2\right] dx + 4\int_0^1 m^2 Q_p^2 dx + 4\int_0^1 \rho_w^2 Q_I^2 dx \\
&\le 2\|m\|_{L^\infty}^2 \int_0^1 (u_w)_x^2 \, dx + 2\|u_w\|_{L^\infty}^2 \int_0^1 m_x^2 \, dx + 4\|m\|_{L^\infty}^2 \int_0^1 Q_p^2 dx \\
&\quad + 4\|\rho_w\|_{L^\infty}^2 \int_0^1 Q_I^2 dx \\
&\le C(T).
\end{aligned}$$

Similarly we get

$$\int_0^1 n_t^2 \, dx \le C(T). \tag{2.87}$$

We omit the details here since the rest of the proof can be found in [29]. ∎

With the above estimates, we get (2.15). Then we have completed the proof of Theorem 2.2.

3. Numerical results. In the following numerical tests a 1D reservoir layer is considered with one injection well at the center of the layer and two production wells at the left and right sides as shown in Figure 3.1. The volume rate $\overline{Q}_p$ of each production well is assumed to be half of the injection rate $\overline{Q}_I$ at the center of the layer. Two scenarios are investigated, respectively, with the water-oil system

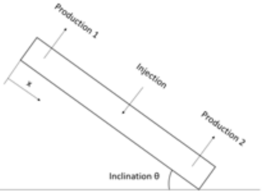

FIG. 3.1. *1D inclined reservoir. Water is pumped into the injection well to displace reservoir fluids (90% oil or gas and 10% water, initially) and its injection rate is double the production rate at two sides of the reservoir layer.*

and the water-gas system. The so-called water-oil model is as follows: pump water into the injection well and displace reservoir fluids (90% oil and 10% water, initially) to the production wells. Similarly, the water-gas model is the situation in which water is injected to displace reservoir fluids (90% gas and 10% water, initially) to the production wells. For a complete description of the discrete schemes we use for the incompressible and compressible cases we refer to [29]. They are both based on a finite difference approach.

Initial and boundary conditions. The reservoir layer is assumed to be with 10% water and 90% oil or gas, initially. For the water-oil model,

$$s_w(x, t = 0) = 0.1, \qquad s_o = 0.9, \tag{3.1}$$

and for the water-gas model,

$$s_w(x, t = 0) = 0.1, \qquad s_g = 0.9. \tag{3.2}$$

In addition, a reference pressure P_{wL} is given to the compressible model at the left boundary of the reservoir layer, initially,

$$P_{wL}(x = 0, t = 0) = 10^5 \text{ Pa}. \tag{3.3}$$

For the water-oil (-gas) model we assume a closed reservoir, i.e.,

$$u_w(x = 0, t) = u_w(x = L, t) = 0, \qquad u_i(x = 0, t) = u_i(x = L, t) = 0, \quad i = o, g. \tag{3.4}$$

Specially for the incompressible model, we give a reference pressure P_{wL} at the left boundary of the layer for the entire period of tests,

$$P_{wL}(x = 0, t) = 10^5\text{Pa}. \tag{3.5}$$

Source and interaction terms. Water is injected in the well placed in the center and reservoir fluids (water and oil/gas) are displaced to the left and the right sides of the reservoir layer. We assume that $Q_I(x)$ and $Q_p(x)$ take the form

$$Q_I(x) = \frac{\overline{Q}_I}{\sigma} \begin{cases} 1 & \text{if } |x - x_I| \le \sigma/2, \\ 0 & \text{otherwise,} \end{cases} \qquad Q_p(x) = \frac{\overline{Q}_p}{\sigma} \begin{cases} 1 & \text{if } |x - x_{pi}| \le \sigma/2, \\ 0 & \text{otherwise,} \end{cases} \tag{3.6}$$

where $(i = 1, 2)$ and $\overline{Q}_I = 0.495\text{m}^3/\text{day}$ and $\overline{Q}_p = 0.2475\text{m}^3/\text{day}$. The width of the small region associated with the injector and producer is σ. Note that the expression suggested in (2.6) represents a regularized version of (3.6). In the numerical scheme $\sigma = \Delta x$.

The model should be armed with appropriate functional correlations for fluid-rock resistance force $\hat{k}_i$ and fluid-fluid drag force $\hat{k}$. We follow [28] and use correlations of the following form:

$$\hat{k}_w = I_w \frac{\mu_w}{K}\phi s_w^{\alpha}, \qquad \hat{k}_o = I_o \frac{\mu_o}{K}\phi(1-s_w)^{\beta}, \qquad \hat{k} = I\frac{\mu_w\mu_o}{K}\phi s_w(1-s_w), \tag{3.7}$$

where μ_i is fluid viscosity, K absolute permeability, and I_w, I_o, I are parameters that characterize the strength of the interaction force.

Expressions for relative permeabilities and fractional flow function. We can relate the model described in (1.1) to more standard formulations commonly used in reservoir modeling [41], which involve flow curves such as relative permeabilities $k_{ri}(s_w)$ and water fractional flow function $f_w(s_w)$. It is sufficient to impose the simplifying assumptions that the fluids are incompressible, $\rho_w = \tilde{\rho}_{w0}$ and $\rho_o = \tilde{\rho}_{o0}$, and viscosity terms are negligible, $\varepsilon_w = \varepsilon_o = 0$. First, we then can show that (1.1) is reduced to (see [28] for details)

$$(\phi s_w)_t + (U_w)_x = -s_w Q_p + Q_I, \tag{3.8}$$

with Darcy velocity $U_w = \phi s_w u_w$ given by

$$U_w = U_T \hat{f}_w(s_w) + W(s_w)\Delta\rho g \sin\theta + W(s_w)P_c(s_w)_x, \quad (U_T)_x = (U_w + U_o)_x = Q_I - Q_p, \tag{3.9}$$

with

$$\begin{aligned} \hat{f}_w(s_w) &= \frac{\hat{\lambda}_w}{\hat{\lambda}_w + \hat{\lambda}_o} = \frac{s_w^2\hat{k}_o + s_w\hat{k}}{s_w^2\hat{k}_o + (1-s_w)^2\hat{k}_w + \hat{k}}, \\ W(s_w) &= \hat{f}_w\hat{\lambda}_o - \frac{s_o s_w\hat{k}\phi}{\hat{k}_o\hat{k}_w + \hat{k}(\hat{k}_o + \hat{k}_w)} = \frac{s_w^2(1-s_w)^2\phi}{s_w^2\hat{k}_o + (1-s_w)^2\hat{k}_w + \hat{k}}, \end{aligned} \tag{3.10}$$

where we use the following notation for generalized phase mobilities $\hat{\lambda}_w$ and $\hat{\lambda}_o$:

$$\begin{aligned} \hat{\lambda}_w(s_w) &= \frac{s_w^2\hat{k}_o + s_w\hat{k}}{\hat{k}_o\hat{k}_w + \hat{k}(\hat{k}_o + \hat{k}_w)}\phi, \\ \hat{\lambda}_o(s_w) &= \frac{s_o^2\hat{k}_w + s_o\hat{k}}{\hat{k}_o\hat{k}_w + \hat{k}(\hat{k}_o + \hat{k}_w)}\phi. \end{aligned} \tag{3.11}$$

With these assumptions, relative permeabilities (see Figure 3.2 right) in the water-oil model can be expressed as follows when (3.7) is used:

$$\begin{aligned} k_{rw} &= \frac{\mu_w}{K}\hat{\lambda}_w = \frac{I_o s_w s_o^{\beta-1} + I\mu_w s_w}{I_w I_o s_w^{\alpha-1}s_o^{\beta-1} + I(I_w s_w^{\alpha}\mu_w + I_o s_o^{\beta}\mu_o)}, \\ k_{ro} &= \frac{\mu_o}{K}\hat{\lambda}_o = \frac{I_w s_o s_w^{\alpha-1} + I\mu_o s_o}{I_w I_o s_w^{\alpha-1}s_o^{\beta-1} + I(I_w s_w^{\alpha}\mu_w + I_o s_o^{\beta}\mu_o)}. \end{aligned} \tag{3.12}$$

The expression of water fractional flow function $f_w(s_w)$ in the conventional water-oil model (assuming no capillary pressure and viscous coupling effect, i.e., $P_c = 0$ and $\hat{k} = 0$) is

$$f_w(s_w) \overset{\text{def}}{:=} \frac{U_w}{U_T} = \frac{\frac{\hat{\lambda}_w}{\hat{\lambda}_w + \hat{\lambda}_o}U_T + \frac{\hat{\lambda}_w\hat{\lambda}_o}{\hat{\lambda}_w + \hat{\lambda}_o}\Delta\rho g\sin\theta}{U_T}, \tag{3.13}$$

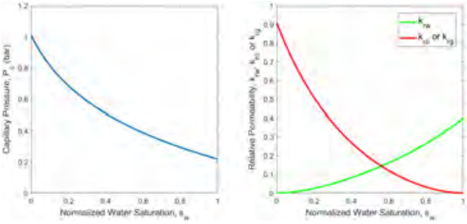

FIG. 3.2. *Left: Input capillary pressure curve $P_c(s_w)$ for water-oil or water-gas. Right: Relative permeabilities $k_{rw}(s_w), k_{rw}(s_w)$ obtained from* (3.12) *combined with data from Table* 3.1 *for the water-oil model.*

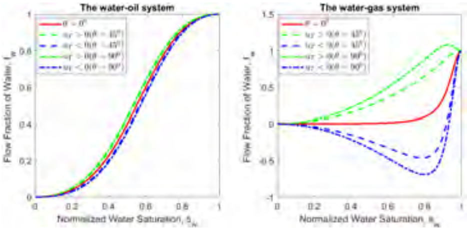

FIG. 3.3. *Water flow fractional function $f_w(s_w)$ as defined in* (3.13) *with different flow directions and layer inclinations where U_T is now a constant equal to $\pm(\overline{Q}_I/2)$. Left: Water-oil reservoir. Right: Water-gas reservoir.*

where we have used (3.9) and (3.10), where $\Delta\rho = \tilde{\rho}_{w0} - \tilde{\rho}_{o0}$ and $U_T = \int_0^x (Q_I - Q_p)dx$. In order to illustrate the water flow fraction $f(s_w)$ (see Figure 3.3) we represent U_T by a reference total velocity $\overline{U}_T \in [-\frac{\overline{Q}_I}{2}, +\frac{\overline{Q}_I}{2}]$. We refer to Table 3.1 for input data that are used. Similarly, we can also obtain the corresponding expressions for the water-gas model. For simplification, we use the same capillary relation P_c for both the water-oil and water-gas flow system. In particular, we use $P_c(s_w) = -P_c^* \ln(\delta + \frac{s_w}{a})$ (see Remark 2.2 and Figure 3.2 left), where P_c^*, a, and δ are specified in Table 3.1.

3.1. Simulation cases. For the closed system, we choose three reservoir inclinations, 0°, 45°, and 90°, and compare phase velocities (interstitial) $u_w, u_o(u_g)$, pressures $P_w, P_o(P_g)$, and normalized water saturation $s_w = \frac{1-s_{wr}}{1-s_{wr}-s_{ir}}$ $(i = o, g)$ from the incompressible model and the compressible models for both the water-oil system and water-gas system considered at two given times: $T_1 = 20$ days and $T_2 = 100$ days.

3.1.1. Comparison of compressible and incompressible water-oil models. Results for water-oil behavior in a horizontal reservoir with closed boundary are shown in Figure 3.4. The phase pressures (P_w and P_o) are higher in the compressible model than the incompressible model at both 20 days and 100 days. This is because compressible fluids in the reservoir center can adsorb the pressure energy leading to higher densities of reservoir fluids. In particular, this seems to be a natural consequence of the fact that the injected volume of water Q_I is kept fixed instead of a constraint on $\rho_w Q_I$. The phase pressure increases from 20 days to 100 days in both

TABLE 3.1

Input parameters with reservoir and fluids' properties for the simulations of the water-oil and water-gas models.

Parameter	Dimensional value	Parameter	Dimensional value
L	100 m	I_w	2.5
ϕ	1	I_o	1.1
$\tilde{\rho}_{w0}$	1 g/cm^3	I_g	1.1
$\tilde{\rho}_{o0}$	0.8 g/cm^3	I	1000 (Pa·s)$^{-1}$
$\tilde{\rho}_{g0}$	0.0018 g/cm^3	α	0.01
s_{wr}	0.3	β	0.01
s_{or}	0.2	P_c^*	$4 * 10^4$ Pa
s_{gr}	0	a	2
μ_w	1 cP	δ	0.08
μ_o	1.5 cP	C_w	10^6 m^2/s^2
μ_g	0.015 cP	C_o	$5 * 10^5$ m^2/s^2
K	1000 mD	C_g	10^5 m^2/s^2
k_{rw}^{max}	0.4	ε_w	0.1 cP
k_{ro}^{max}	0.909	ε_o	0.2 cP
k_{rg}^{max}	0.909	ε_g	0.02 cP
$\overline{Q}_I$	0.495 m^3/day	x_I	50 m
$\overline{Q}_p$	0.2475 m^3/day	x_{p1}, x_{p2}	10, 90 m
P_{wL}	10^5 Pa	A	1 m^2
N_x	101	$\triangle t$	1570 s

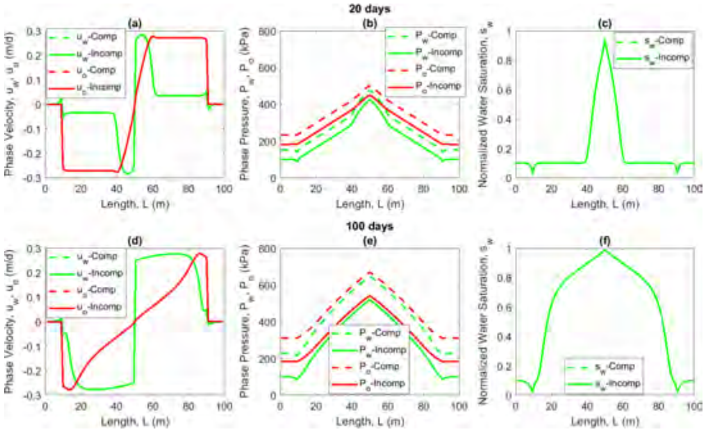

FIG. 3.4. *Comparison between the compressible and incompressible horizontal (no inclination) water-oil models at* 20 *and* 100 *days.* (a), (d) *Interstitial velocity* u_w, u_o. (b), (e) *Phase pressure* P_w, P_o. (c), (f) *Water saturation* s_w. *Obviously, all the relevant results are symmetric. A higher phase pressure is observed in the compressible model compared with incompressible model, reflecting that the compressible water and oil adsorb energy (pressure).*

models and the phase pressure difference between these two models increases over time. This can be explained by the fact that the more viscous water (which creates stronger resistance forces) fills the reservoir to a larger extent and results in a higher phase pressure P_w after 100 days. Since both water and oil are weakly compressible, there is no obvious difference seen in the phase velocities and saturations when comparing the compressible and incompressible models.

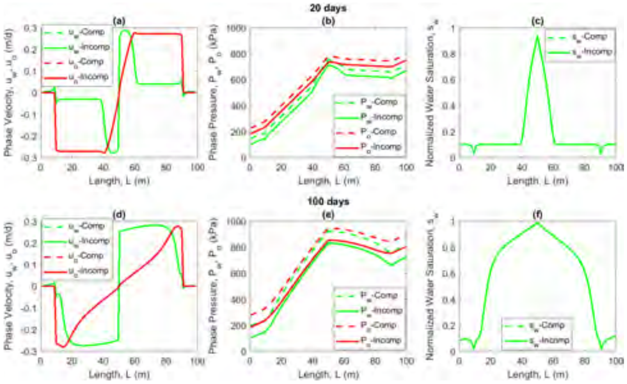

FIG. 3.5. *Comparison between the compressible and incompressible water-oil models with 45° inclination at 20 and 100 days.* (a), (d) *Interstitial velocity u_w, u_o.* (b), (e) *Phase pressure P_w, P_o.* (c), (f) *Water saturation s_w. Pressure profiles are not symmetric due to the gravity effect. Similar to Figure 3.4, a negligible difference is observed on velocity and saturation curves between the incompressible and compressible models. Phase pressure is higher in the compressible model.*

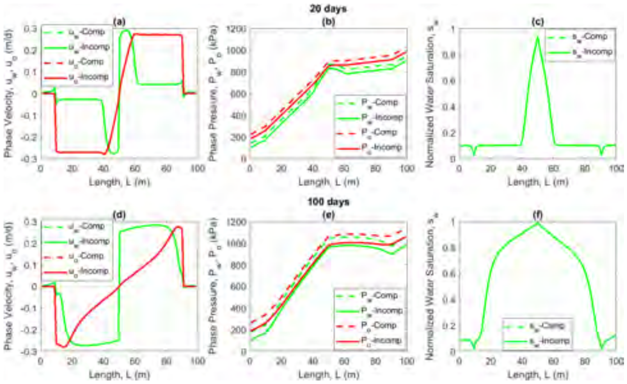

FIG. 3.6. *Comparison between the compressible and incompressible vertical water-oil models at 20 and 100 days.* (a), (d) *Interstitial velocity u_w, u_o.* (b), (e) *Phase pressure P_w, P_o.* (c), (f) *Water saturation s_w. Compared with Figures 3.4 and 3.5 we see that pressure is essentially high and flat at the lower part of the reservoir, reflecting that gravity is the driving transport mechanism in this region.*

Figures 3.5 and 3.6 show behavior for compressible and incompressible water-oil models, respectively, with 45° and 90° inclinations. Similar to the horizontal case (see Figure 3.4), the differences of phase velocities and normalized water saturation between the two models are rather negligible. Phase pressure in the compressible model is higher due to the same reason as explained for Figure 3.4. The most striking difference with the horizontal case in Figure 3.4 is that pressure in the lower part of the reservoir flattens out since gravity becomes a driving force for the displacement of

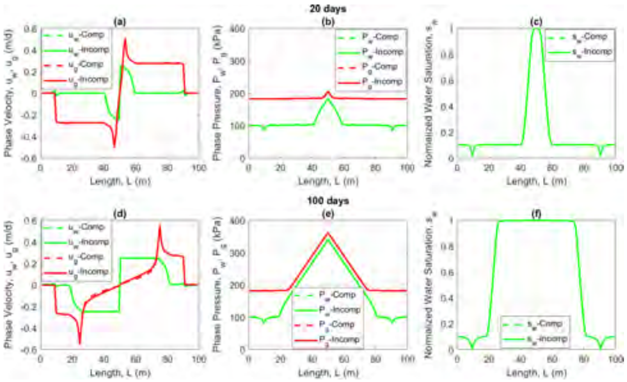

FIG. 3.7. *Comparison between the compressible and incompressible horizontal water-gas models at* 20 *and* 100 *days.* (a), (d) *Interstitial velocity* u_w, u_g. (b), (e) *Phase pressure* P_w, P_g. (c), (f) *Water saturation* s_w. *There is essentially no difference observed. Gas pressure gradients in both models are small in the undisplaced part due to the high mobility of gas (low viscosity).*

water and oil toward the producer at the bottom. In the upper part of the reservoir, however, the opposite effect is seen: a larger pressure gradient is formed since gravity must now also be overcome.

3.1.2. Comparison of compressible and incompressible water-gas models. Figure 3.7 illustrates the compressible and incompressible horizontal water-gas model with closed boundary. Water (with much higher density than gas) is injected and flows to the lower pressure region of the reservoir. Gas can easily adsorb the energy from water since gas is very compressible. For this case the phase pressure is essentially the same for the compressible and incompressible cases.

We are more interested in the cases with 45° and 90° inclinations, where we may expect to see some compressibility effects. In Figure 3.8, we study the water-gas case with 45° inclination. At 20 days there is a clear difference between the compressible and incompressible cases; a small volume fraction of gas on the left side of the injector located at around 48 m is quickly mobilized by the injected water, which tends to form a high front giving rise to narrow gas flow channels, which explains the large negative dip in gas velocity u_g. This effect is strongest for the incompressible case. In the lower part of the domain, gravity will help smear out the water front, which explains the more gentle behavior in the velocity profiles seen in this region. The remaining low water pressure P_w for the compressible case seen in the lower region of the reservoir is due to compression of gas which reduces the resistance force felt by the propagating water front.

At 100 days, it is observed that water blocks (panel (f)) the gas flowing channel located in the region 25−50 m (incompressible case) and there is no room for gas in the lower part to escape to the upper part. In the compressible model, water can to a larger extent enter the lower part of the reservoir since gas is easily compressed there with larger phase pressure. This explains the difference in the water front position in the lower region for the incompressible and compressible cases. In the upper part of the reservoir this also leads to a similar difference in the water front position.

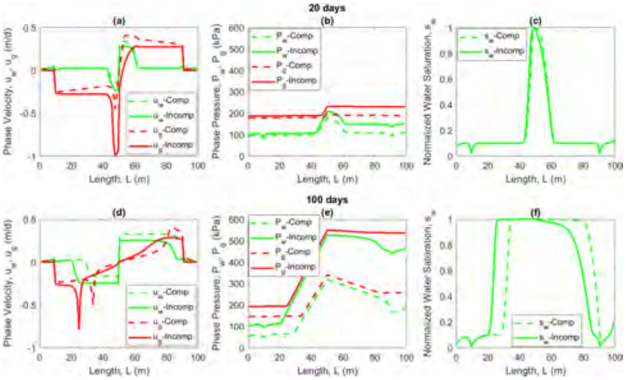

FIG. 3.8. *Comparison between the compressible and incompressible water-gas models with* 45° *inclination at* 20 *and* 100 *days.* (a), (d) *Interstitial velocity* u_w, u_g. (b), (e) *Phase pressure* P_w, P_g. (c), (f) *Water saturation* s_w. *Significant differences exist between these two models' results.*

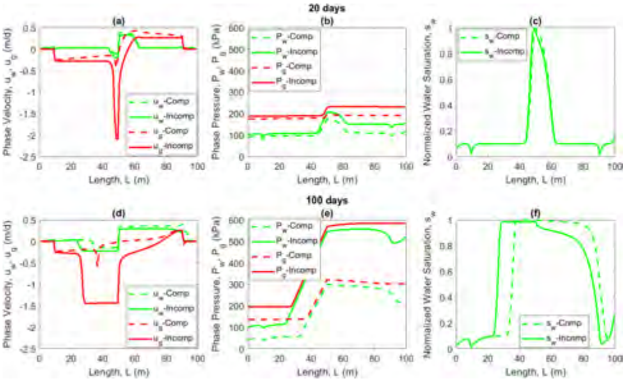

FIG. 3.9. *Comparison between the compressible and incompressible vertical water-gas models at* 20 *and* 100 *days.* (a), (d) *Interstitial velocity* u_w, u_g. (b), (e) *Phase pressure* P_w, P_g. (c), (f) *Water saturation* s_w. *The situation is similar to the one shown in Figure* 3.8 *at* 20 *days, but at a later time (*100 *days) water cannot block the gas flowing channel in the incompressible model.*

Now, we increase the 45° inclination in Figure 3.8 to 90°. The corresponding results are shown in Figure 3.9. The most striking difference between this case and the situation shown in Figure 3.8 is that in the incompressible case gas from the lower region migrates to the upper region (see negative gas velocity in the lower region). This largely amplifies the gas velocity (panels (a), (d)) as reflected by the strong negative dip right above the injector. After a time $T = 100$ days we see that there is a steady flow of gas from the lower region to the upper for the incompressible model (panel (d)). In particular, water will not block this migration (panel (f)). For the compressible model, on the other hand, water will block this upward migration of gas (compare gas velocities in panel (d)).

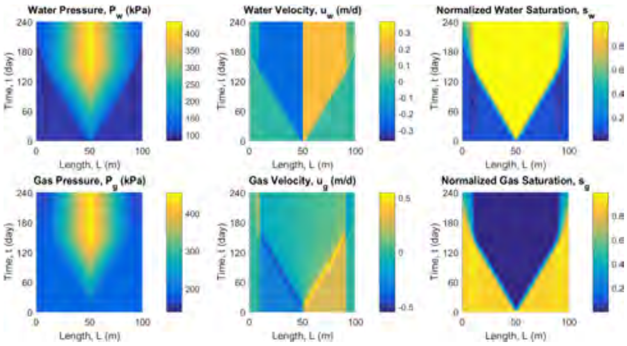

FIG. 3.10. *Space-time plot of pressures (left column), phase velocities (middle column), and normalized saturations (right column) for the compressible horizontal water-gas model. The results are symmetric and the water front reaches the production well after around* 150 *days.*

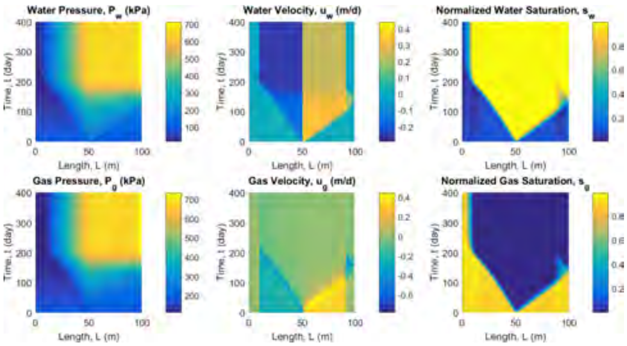

FIG. 3.11. *Space-time plot of pressures (left column), phase velocities (middle column), and normalized saturations (right column) for the compressible water-gas model with inclination* 45°*. Water displacement in the upper part is different from the lower part of the reservoir. In particular, the water front reaches the production well earlier (*100 *days) in the lower part of the reservoir, whereas it takes around* 200 *days in the upper region.*

3.1.3. More simulation results for the water-gas model. In Figures 3.10, 3.11, and 3.12 the space-time behavior of the compressible water-gas model is illustrated with inclinations 0°, 45°, and 90°, respectively. The results of the horizontal case shown in Figure 3.10 are essentially symmetric, as expected. In the case with 45° inclination (Figure 3.11), we see how the water front (right column) will reach the producer in the lower region (right side of injector) much more quickly than in the upper region (left side of injector). In Figure 3.12 we note that after the water front has reached the producer in the lower region (right column) some gas is free to start migrating toward the upper region, where it is ultimately produced in an upper-region producer (see gas velocity in middle column).

In Figure 3.13 we consider the incompressible case. A main difference between this case as compared to the compressible case shown in Figure 3.12 is that much more

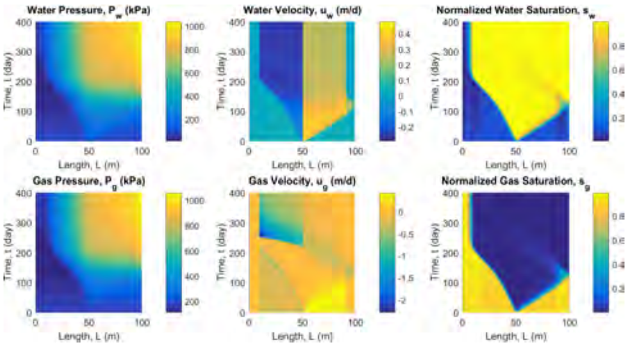

FIG. 3.12. *Space-time plot of pressures (left column), phase velocities (middle column), and normalized saturations (right column) for the compressible vertical water-gas model.*

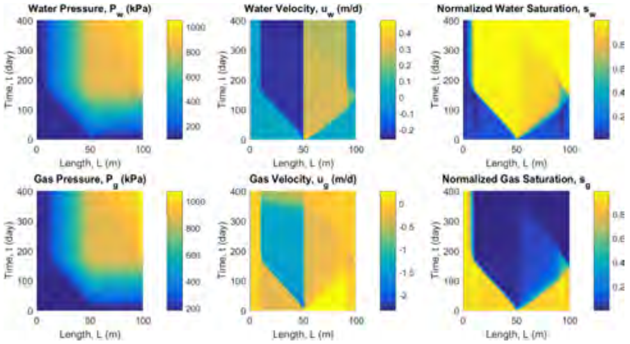

FIG. 3.13. *Space-time plot of pressures (left column), phase velocities (middle column), and normalized saturations (right column) for the incompressible vertical water-gas model.*

gas in the lower region is able to escape to the upper region in the early period when the water front is on its way to the bottom producer. Due to a stronger impact from gravity when gas is treated as an incompressible fluid, water cannot prevent trapped gas in the lower part from flowing though a narrow channel (high water saturation zone) towards to the production well in the upper part.

3.1.4. The viscous coupling effect. We want to illustrate the impact from the fluid-fluid term both in a horizontal and a vertical flow domain. More precisely, we apply an interaction coefficient $I = 3000$ in (3.7) (refer to [28] for more discussion of this aspect) and compare it to the case with $I = 0$, that is, no viscous coupling effect. In Figure 3.14 results are shown after a time $T = 100$ days. It shows that the effect of fluids' interaction can play a vital role in both horizontal and vertical cases where visible differences exist in pressure, phase velocity, and saturation compared to the results with no fluids interaction. The additional interaction force between oil and water behaves like a resistance force for water flow. Therefore it smears out the water front.

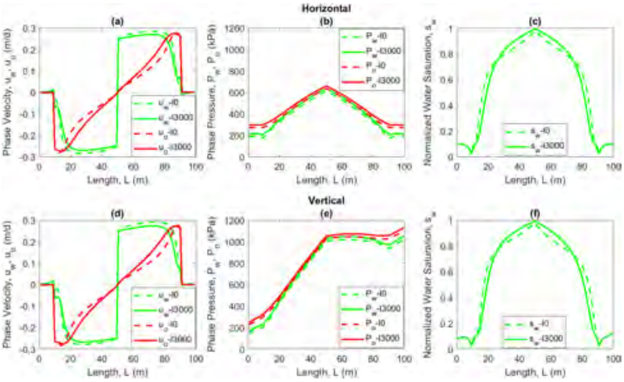

FIG. 3.14. *Comparison between two cases with* ($I > 0$) *and without* ($I = 0$) *fluid-fluid interaction effect in the horizontal and vertical compressible water-oil model at* 100 *days.* (a), (d) *Interstitial velocity* u_w, u_o. (b), (e) *Phase pressure* P_w, P_o. (c), (f) *Water saturation* s_w. *The results demonstrate how viscous coupling may affect the water-oil model where pressure, phase velocity, and saturation are all different in the water displacing part.*

REFERENCES

[1] B. Amaziane, M. Jurak, and A. Ž. Keko, *An existence result for a coupled system modeling a fully equivalent global pressure formulation for immiscible compressible two-phase flow in porous media*, J. Differential Equations, 250 (2011), pp. 1685–1718, https://doi.org/10.1016/j.jde.2010.09.008.

[2] D. Bresch, B. Desjardins, J.-M. Ghidaglia, and E. Grenier, *Global weak solutions to a generic two-fluid model*, Arch. Ration. Mech. Anal., 196 (2010), pp. 599–629, https://doi.org/10.1007/s00205-009-0261-6.

[3] D. Bresch, X. Huang, and J. Li, *Global weak solutions to one-dimensional non-conservative viscous compressible two-phase system*, Comm. Math. Phys., 309 (2012), pp. 737–755, https://doi.org/10.1007/s00220-011-1379-6.

[4] D. Bresch, P. B. Mucha, and E. Zatorska, *Finite-energy solutions for compressible two-fluid Stokes system*, Arch. Ration. Mech. Anal., 232 (2019), pp. 987–1029, https://doi.org/10.1007/s00205-018-01337-6.

[5] G. Chavent and J. Jaffré, *Mathematical Models and Finite Elements for Reservoir Simulation: Single Phase, Multiphase and Multicomponent Flows Through Porous Media*, Stud. Math. Appl. 17, Elsevier, New York, 1986.

[6] G. M. Coclite, K. H. Karlsen, S. Mishra, and N. H. Risebro, *A hyperbolic-elliptic model of two-phase flow in porous media: Existence of entropy solutions*, Int. J. Numer. Anal. Model., 9 (2012), pp. 562–583, http://global-sci.org/intro/article_detail/ijnam/647.html.

[7] G. M. Coclite, S. Mishra, N. H. Risebro, and F. Weber, *Analysis and numerical approximation of Brinkman regularization of two-phase flows in porous media*, Comput. Geosci., 18 (2014), pp. 637–659, https://doi.org/10.1007/s10596-014-9410-6.

[8] D. A. Drew and S. L. Passman, *Theory of Multicomponent Fluids*, Appl. Math. Sci. 136, Springer, New York, 1999, https://doi.org/10.1007/b97678.

[9] S. Evje, *A compressible two-phase model with pressure-dependent well-reservoir interaction*, SIAM J. Math. Anal., 45 (2013), pp. 518–546, https://doi.org/10.1137/12087195X.

[10] S. Evje, *An integrative multiphase model for cancer cell migration under influence of physical cues from the microenvironment*, Chem. Engrg. Sci., 165 (2017), pp. 240–259, https://doi.org/10.1016/j.ces.2017.02.045.

[11] S. Evje and J. O. Waldeland, *How tumor cells can make use of interstitial fluid flow in a strategy for metastasis*, Cellular Molecular Bioengineering, 12 (2019), pp. 227–254, https://doi.org/10.1007/s12195-019-00569-0.

[12] S. Evje and H. Wen, *Analysis of a compressible two-fluid Stokes system with constant viscosity*, J. Math. Fluid Mech., 17 (2015), pp. 423–436, https://doi.org/10.1007/s00021-015-0215-8.

[13] S. Evje and H. Wen, *Stability of a compressible two-fluid hyperbolic–elliptic system arising in fluid mechanics*, Nonlinear Anal. Real World Appl., 31 (2016), pp. 610–629, https://doi.org/10.1016/j.nonrwa.2016.03.011.

[14] S. Evje and H. Wen, *A Stokes two-fluid model for cell migration that can account for physical cues in the microenvironment*, SIAM J. Math. Anal., 50 (2018), pp. 86–118, https://doi.org/10.1137/16M1078185.

[15] C. Galusinski and M. Saad, *A nonlinear degenerate system modeling water-gas in reservoir flow*, Discrete Contin. Dyn. Syst. Ser. B, 9 (2008), pp. 281–308, https://doi.org/10.3934/dcdsb.2008.9.281.

[16] C. Galusinski and M. Saad, *Two compressible immiscible fluids in porous media*, J. Differential Equations, 244 (2008), pp. 1741–1783, https://doi.org/10.1016/j.jde.2008.01.013.

[17] C. Hao and H.-L. Li, *Well-posedness for a multidimensional viscous liquid-gas two-phase flow model*, SIAM J. Math. Anal., 44 (2012), pp. 1304–1332, https://doi.org/10.1137/110851602.

[18] M. Javaheri and K. Jessen, *CO_2 Mobility and transitions between cO-current and counter-current flows*, in Proceedings of the SPE Reservoir Simulation Symposium, Woodlands, TX, Society of Petroleum Engineers, 2013, https://doi.org/10.2118/163596-MS.

[19] R. Juanes, *Nonequilibrium effects in models of three-phase flow in porous media*, Adv. Water Resources, 31 (2008), pp. 661–673, https://doi.org/10.1016/j.advwatres.2007.12.005.

[20] K. H. Karlsen and N. H. Risebro, *Convergence of finite difference schemes for viscous and inviscid conservation laws with rough coefficients*, ESAIM Math. Model. Numer. Anal., 35 (2001), pp. 239–269, https://doi.org/10.1051/m2an:2001114.

[21] K. H. Karlsen, N. H. Risebro, and J. D. Towers, *L^1 Stability for Entropy Solutions of Nonlinear Degenerate Parabolic Convection-Diffusion Equations with Discontinuous Coefficients*, Matematisk Institutt, Universitetet i Oslo, 2003, http://urn.nb.no/URN:NBN:no-23721.

[22] Z. Khalil and M. Saad, *Degenerate two-phase compressible immiscible flow in porous media: The case where the density of each phase depends on its own pressure*, Math. Comput. Simul., 81 (2011), pp. 2225–2233, https://doi.org/10.1016/j.matcom.2010.12.012.

[23] G. Lemon, J. R. King, H. M. Byrne, O. E. Jensen, and K. M. Shakesheff, *Mathematical modelling of engineered tissue growth using a multiphase porous flow mixture theory*, J. Math. Biol., 52 (2006), pp. 571–594, https://doi.org/10.1007/s00285-005-0363-1.

[24] C. Michoski and A. Vasseur, *Existence and uniqueness of strong solutions for a compressible multiphase Navier–Stokes miscible fluid-flow problem in dimension $n = 1$*, Math. Models Methods Appl. Sci., 19 (2009), pp. 443–476, https://doi.org/10.1142/S0218202509003498.

[25] D. Munaf, A. Wineman, K. Rajagopal, and D. Lee, *A boundary value problem in groundwater motion analysis—comparison of predictions based on Darcy's law and the continuum theory of mixtures*, Math. Models Methods Appl. Sci., 3 (1993), pp. 231–248, https://doi.org/10.1142/S0218202593000138.

[26] A. Novotny and M. Pokorny, *Weak Solutions for Some Compressible Multicomponent Fluid Models*, https://arxiv.org/abs/1802.00798, 2018.

[27] W. J. Polacheck, J. L. Charest, and R. D. Kamm, *Interstitial flow influences direction of tumor cell migration through competing mechanisms*, Proc. Natl. Acad. Sci. USA, 108 (2011), pp. 11115–11120, https://doi.org/10.1073/pnas.1103581108.

[28] Y. Qiao, P. Ø. Andersen, S. Evje, and D. C. Standnes, *A mixture theory approach to model co- and counter-current two-phase flow in porous media accounting for viscous coupling*, Adv. Water Resources, 112 (2018), pp. 170–188, https://doi.org/10.1016/j.advwatres.2017.12.016.

[29] Y. Qiao, H. Wen, and S. Evje, *Compressible and viscous two-phase flow in porous media based on mixture theory formulation*, Netw. Heterog. Media, 14 (2019), pp. 489–536, https://doi.org/10.3934/nhm.2019020.

[30] K. Rajagopal, *On a hierarchy of approximate models for flows of incompressible fluids through porous solids*, Math. Models Methods Appl. Sci., 17 (2007), pp. 215–252, https://doi.org/10.1142/S0218202507001899.

[31] B. Saad and M. Saad, *Study of full implicit petroleum engineering finite-volume scheme for compressible two-phase flow in porous media*, SIAM J. Numer. Anal., 51 (2013), pp. 716–741, https://doi.org/10.1137/120869092.

[32] J. D. Shields, M. E. Fleury, C. Yong, A. A. Tomei, G. J. Randolph, and M. A. Swartz, *Autologous chemotaxis as a mechanism of tumor cell homing to lymphatics via interstitial*

flow and autocrine CCR7 signaling, Cancer Cell, 11 (2007), pp. 526–538, https://doi.org/10.1016/j.ccr.2007.04.020.

[33] S. Solem and S. Evje, *Relaxation limit of a compressible gas–liquid model with well–reservoir interaction*, Z. Angew. Math. Phys., 68 (2017), https://doi.org/10.1007/s00033-017-0771-2.

[34] D. C. Standnes and P. Ø. Andersen, *Analysis of the impact of fluid viscosities on the rate of countercurrent spontaneous imbibition*, Energy & Fuels, 31 (2017), pp. 6928–6940, https://doi.org/10.1021/acs.energyfuels.7b00863.

[35] D. C. Standnes, S. Evje, and P. Ø. Andersen, *A novel relative permeability model based on mixture theory approach accounting for solid–fluid and fluid–fluid interactions*, Transp. Porous Media, 119 (2017), pp. 707–738, https://doi.org/10.1007/s11242-017-0907-z.

[36] J. Urdal, J. O. Waldeland, and S. Evje, *Enhanced cancer cell invasion caused by fibroblasts when fluid flow is present*, Biomech. Model. Mechanobiol., 18 (2019), pp. 1047–1078, https://doi.org/10.1007/s10237-019-01128-2.

[37] A. Vasseur, H. Wen, and C. Yu, *Global weak solution to the viscous two-fluid model with finite energy*, J. Math. Pures Appl., 125 (2019), pp. 247–282, https://doi.org/10.1016/j.matpur.2018.06.019.

[38] J. O. Waldeland and S. Evje, *Competing tumor cell migration mechanisms caused by interstitial fluid flow*, J. Biomech., 81 (2018), pp. 22–35, https://doi.org/10.1016/j.jbiomech.2018.09.011.

[39] J. O. Waldeland and S. Evje, *A multiphase model for exploring tumor cell migration driven by autologous chemotaxis*, Chem. Engrg. Sci., 191 (2018), pp. 268–287, https://doi.org/10.1016/j.ces.2018.06.076.

[40] H. Wen, L. Yao, and C. Zhu, *Review on mathematical analysis of some two-phase flow models*, Acta Math. Sci., 38 (2018), pp. 1617–1636, https://doi.org/10.1016/S0252-9602(18)30835-X.

[41] Y.-S. Wu, *Multiphase Fluid Flow in Porous and Fractured Reservoirs*, Elsevier, New York, 2015, https://doi.org/10.1016/C2015-0-00766-3.

[42] Y. Zhang and C. Zhu, *Global existence and optimal convergence rates for the strong solutions in $H2$ to the $3D$ viscous liquid–gas two-phase flow model*, J. Differential Equations, 258 (2015), pp. 2315–2338, https://doi.org/10.1016/j.jde.2014.12.008.

V

Paper V

A Compressible Viscous Three-phase Model for Porous Media Flow Based on the Theory of Mixtures

By:
Qiao, Yangyang
Evje, Steinar

Under review in:
Advances in Water Resources.

A COMPRESSIBLE VISCOUS THREE-PHASE MODEL FOR POROUS MEDIA FLOW BASED ON THE THEORY OF MIXTURES

Y. QIAO AND S. EVJE

ABSTRACT. In this paper we focus on a general model to describe compressible and immiscible three-phase flow in porous media. The underlying idea is to replace Darcy's law by more general momentum balance equations. In particular, we want to account for viscous coupling effects by introducing fluid-fluid interaction terms. In [Qiao, et al. (2018) Adv Water Resour 112: 170-188] a water-oil model based on the theory of mixtures was explored. It was demonstrated how the inclusion of viscous coupling effects could allow the model to better capture flow regimes which involve a combination of co-current and counter-current flow. In this work we extend the model in different aspects: (i) account for three phases (water,oil,gas) instead of two; (ii) deal with both the compressible and incompressible case; (iii) include viscous terms that represent frictional forces within the fluid (Brinkman type). A main objective of this work is to explore this three-phase model, which appears to be more realistic than standard formulation, in the context of petroleum related applications. We first provide development of stable numerical schemes in a one-dimensional setting which can be used to explore the generalized water-oil-gas model, both for the compressible and incompressible case. Then, several numerical examples with waterflooding in a gas reservoir and water alternating gas (WAG) experiments in an oil reservoir are investigated. Differences and similarities between the compressible and incompressible model are highlighted, and the fluid-fluid interaction effect is illustrated by comparison of results from the generalized model and a conventional model formulation.

Keywords: multiphase flow in porous media; three-phase flow, viscous coupling; mixture theory; compressible model; water alternating gas (WAG); waterflooding

1. INTRODUCTION

Generally. The processes of multiphase flow in porous media occur in many subsurface systems and have found many applications of practical interest, such as hydrology, petroleum engineering, geothermal energy development and carbon storage [54]. The immiscible three-phase flow is always encountered in waterflooding for oil reservoirs with gas cap, in immiscible CO_2 storage in depleted oil and gas reservoirs, and steam floods and water-alternating-gas (WAG) processes [10, 25]. Darcy's law was originally developed for single-phase flow [13]. Conventional modeling of multiphase flow is normally based on Darcy's extended law [48] by incorporation of relative permeabilities [39]. However, recent experimental observations indicate that the flow mode (co-current or counter-current) can have a strong impact on the flowing phase mobilities. That is to say, the relative permeabilities are not only function of saturation but are also related to the effect of how the fluids flow relatively to each other [8, 11].

Viscous coupling. Viscous coupling (i.e., fluid-fluid interaction) was firstly mentioned by Yuster [57] by using theoretical analysis to derive that relative permeability is a function of both saturation and viscosity ratio. In addition, capillary number was also proposed to be a factor affecting relative permeabilities [17, 2]. In general, momentum transfer due to differences in interstitial velocities induces acceleration of the slower and deceleration of the faster moving fluid when the fluids are moving co-currently. Deceleration of both fluid velocities will occur if they are moving counter-currently [5, 9, 15, 33].

In order to extend the single-phase Darcy's law to multiphase flow, de la Cruz and Spanos [14] derived theoretically Darcy's empirical extended law by applying the method of volume averaging to Stokes equation. In [27, 28], Kalaydjian developed flow equations using the concepts of

---

Date: May 14, 2019.

irreversible thermodynamics [26] from a macroscopic understanding of two-phase flow in porous media. In addition, some researchers tried to gain insight into how two immiscible phases flow through a porous medium by using simple analogous models such as tubular flow [57, 6]. In [31] Langaas and Papatzacos used the Lattice Boltzmann (LB) approach to investigate effects of viscous coupling and concluded that counter-current relative permeabilities caused partly by viscous coupling are always less than the corresponding co-current curves under different levels of capillary forces. Using the same method, Li et al. [34] showed that their model was able to capture main experimental effects caused by viscous coupling. They also mentioned that the interfacial area between the fluids is a key variable for relative permeability functions for two immiscible fluids flow in porous media. A generalized model was developed in [43] for two-phase flow with viscous coupling effect. Numerical investigations showed a better agreement with the experimental tests [11] compared to the conventional modeling. The authors in [10] constructed modified transport equations for both co-current and counter-current three-phase flow through a vertical incompressible model based on partition concepts. Their equations are used to estimate the amount of model error because of a failure to account for the effect of interfacial coupling which has two types: viscous coupling and capillary coupling. Moreover, Sherafati and Jessen [51] investigated the effect of mobility changes due to flow reversals from co-current to counter-current flow on the displacement of WAG injection processes.

Complex multiphase flow in porous media and use of the theory of mixtures. The theory of mixtures offers a general framework for developing models for complex multiphase flow systems [47]. More lately, biomedical applications have been a driver for the development of various models relying on this approach. For example, the study how cancer cells are able to break loose from a primary tumor involves a solid matrix (the so-called extracellular matrix), different type of cells (cancer cells, stromal cells, immune cells), and interstitial fluid [18, 19]. Various enzymes and proteins are typically involved which are skewed in the fluid flow direction. In turn, this may impact the creeping motion of cells caused by biochemical signalling towards corresponding concentration gradients in a process denoted as chemotaxis. A recent example of this is described in [55, 53] where, respectively, a cell-fluid two-phase model and a cell-fibroblast-fluid three-phase model are developed to shed light on the experimentally observed tumor cell behavior reported in [50]. In the latter case it is explored how the tumor cell migration is strongly affected by the presence of fibroblast cells and the imposed fluid flow. The model that is derived relies on replacing Darcy's law by more general momentum balance equations which incorporate both the cell-ECM resistance force and the cell-fibroblast interaction. The latter is understood as a "viscous coupling" effect caused by a mechanical coupling that can occur between tumor cells and fibroblasts and has been reported in experimental studies [29]. Another example how generalized momentum equations can be used to capture non-standard multiphase behavior in the context of aggressive tumor cells is explored in [56]. In [42] two competing migration mechanisms were observed, one in the upstream direction and another in the downstream direction. The migration against the fluid flow reflects that the tumor cells must be understood as an active fluid (in contrast to a passive) with an ability to create forces against the substrate which is translated into motion. The use of generalized momentum equations allowed us to account for both this fluid-stress generated upstream migration and a chemotactive migration in the direction of increasing concentration of chemical concentrations [56].

In the study of tissue morphology relevant for tissue development, regeneration, and cancer it has been suggested that in analogy with the behaviour of inert fluids, some of these transitions can be interpreted as wetting transitions. It has been shown that the transition between two-dimensional epithelial monolayers and three-dimensional spheroidal aggregates can be understood as an active wetting transition whose physics differs fundamentally from that of passive wetting phenomena [40]. Hence, this represents another example where classical continuum based modeling for passive fluids must be extended to account for active fluid flow behavior.

Motivated by petroleum related applications various attempts to solve the three-phase porous media flow model have been reported during the past decade [20, 21, 22, 24]. An interesting investigation was carried out in [36] where a front-tracking algorithm was proposed for constructing very accurate solutions to one-dimensional problems (for example WAG test therein). This was explored in the context of streamline simulation which decouples the three-dimensional problem into a set of one-dimensional problems along streamlines. This work is limited to three-phase immiscible, incompressible flow and also gravity and capillarity were ignored. Different numerical methods have been implemented to simulate three-phase flow in porous media. A finite volume method was used in [37] for solving compressible, immiscible flow with gravity in heterogeneous formations by using the black oil formulation. A hybrid-upwinding scheme for phase flux was proposed in [38] for a finite difference approximation to solve the three phase transport equations in the presence of viscous and buoyancy forces. A finite element method was applied to simulate fluid injection and imbibition processes in a deformable porous media [23]. Moreover, [16] applied a semi-implicit method with discontinuous Galerkin (DG) discretization to solve the incompressible three-phase flow in two dimensions. Additional physical effects are also discussed and explored for three-phase porous media flow, such as hysteresis effects of relative permeabilities [49] and elliptic regions [24, 25, 38]. In [25] Juanes presented a nonequilibrium model of incompressible three-phase flow in porous media. The nonequilibrium effects by introducing a pair of effective water and gas saturations into the formulations have the ability to smear saturation fronts from numerical simulations.

The aim of this work. The objective of this paper is to investigate a mixture theory approach to simulate three immiscible fluids flowing in a 1D reservoir. We shall consider both the case with compressible and incompressible fluids. The model which is introduced is quite general since it can automatically capture flow that involves a combination of co-current and counter-current flow. The current work represents extension of previous work in two ways:

- Extend the incompressible two-phase model that was explored in [43, 1] to include three phases.
- Extend the compressible two-phase model studied in [45] to include three phases.

In addition, the models we study in the current work are more general than those studied in [43, 1] since we consider Stokes like momentum equations which involve viscous terms that account for internal friction due to viscosity. In particular, appropriate numerical schemes are introduced to investigate compressible and incompressible three-phase flow scenarios that are motivated by injection-production flow scenarios.

Main observations from our numerical experiments with two and three-phase flow scenarios where the flow dynamics are generated by injection of water or gas in the center of the domain and production of fluids at the left and right boundary are: (i) The simulation cases involve competition between pressure driven co-current flow and counter-current gravity driven flow; (ii) Both the incompressible and compressible discrete version of the model appear to have good stability properties. The numerical experiments indicate that the numerical schemes can be useful as a tool to deepen the insight into the relation between the incompressible and compressible version of the model. The model and its discrete approximate counterparts appear to be a good starting point for extending to more complex flow systems, as mentioned above, that involve competition between different distinct, non-standard transport mechanisms.

The rest of this paper is organized as follows. In Section 2 we briefly describe the mixture flux approach in a three-phase setting. In Section 3 we summarize the generalized three-phase porous media model, both a compressible and an incompressible version of it. Section 4 is devoted to numerical simulations to demonstrate three-phase dynamics and verify basic features of the numerical schemes. The details of the compressible and incompressible scheme are given in Appendix A - C.

2. Mixture Theory Framework

2.1. **Conventional model based on Darcy's law.**

We firstly describe the traditional formulation of incompressible multiphase flow model without source terms. Transport equations for incompressible and immiscible phases oil (o), water (w) and gas (g) in porous media are normally given by:

$$\partial_t(\phi s_i) + \nabla \cdot \mathbf{U}_i = Q_i, \tag{2.1}$$

$$\mathbf{U}_i = \phi s_i \mathbf{u}_i, \qquad (i = w, o, g), \tag{2.2}$$

where ϕ is porosity, s_i is phase saturation, Q_i is the source term, and $\mathbf{U}_i$ and $\mathbf{u}_i$ are the Darcy velocity and interstitial velocity of each phase $i = o, w, g$, respectively. The traditional macroscopic formulation of Darcy's law that relates the volumetric flux of a phase to the pressure gradient of that phase is given by:

$$\mathbf{U}_i = -\frac{Kk_{ri}}{\mu_i}(\nabla p_i - \rho_i \mathbf{g}), \qquad (i = w, o, g), \tag{2.3}$$

where K is the absolute permeability of porous media, p_i is phase pressure, $\mathbf{g}$ is the acceleration of gravity and k_{ri}, ρ_i and μ_i are phase relative permeability, density and viscosity, respectively.

2.2. **A generalized multiphase flow model based on mixture theory.**

For our investigations, the mass balance equations with source terms in the case of compressible water-oil-gas transport can be given by:

$$\begin{aligned} (\phi n_w)_t + \nabla \cdot (\phi n_w u_w) &= -n_w Q_p + \rho_w Q_{Iw}, & n_w &= s_w \rho_w \\ (\phi n_o)_t + \nabla \cdot (\phi n_o u_o) &= -n_o Q_p, & n_o &= s_o \rho_o \\ (\phi n_g)_t + \nabla \cdot (\phi n_g u_g) &= -n_g Q_p + \rho_g Q_{Ig}, & n_g &= s_g \rho_g \end{aligned} \tag{2.4}$$

where u_i, ($i = w, o, g$) represents the interstitial velocity of phase i in the porous media. In addition, Q_p is the production rate and Q_{Iw}, Q_{Ig} represent the injection rate of water and gas, respectively.

The starting point for developing our model that can account for more detailed physical mechanisms for water-oil-gas porous media flow than conventional modeling, is the theory of mixtures. This is a theory based on balance laws and conservation principles, which is well known in continuum mechanics [7, 46, 12, 4, 41], and has been widely applied to the biological tumor-growth systems which can be characterized as a mixture of interacting continua.

Neglecting inertial effects (acceleration effects), as is usual when dealing with creeping flow in porous materials, the mechanical stress balance is given by [4]:

$$0 = \nabla \cdot (s_i \sigma_i) + m_i + G_i, \qquad (i = w, o, g), \tag{2.5}$$

where σ_i refers to the Cauchy stress tensor, m_i represents the interaction forces exerted on the constituents by other constituents of the mixture, and $G_i = s_i \rho_i g$ is the external body force due to gravity. The standard expression for the stress terms σ_i, is given by

$$\sigma_i = -p_i \delta + \tau_i, \qquad (i = w, o, g), \tag{2.6}$$

where δ is the unitary tensor and

$$\tau_i = 2\mu_i e_i, \qquad e_i = \frac{1}{2}(\nabla u_i + \nabla u_i^T), \qquad (i = w, o, g). \tag{2.7}$$

The viscous part τ_i reflects that the water, oil and gas behave as a viscous fluid. According to general principles of the theory of mixtures, the interaction forces m_i between the constituents appearing in (2.5) may be described as (Preziosi et al., 2002; Ambrosi and Preziosi, 2002):

$$\begin{aligned} m_o &= p_o \nabla s_o + F_{wo} - F_{og} + M_{om}, \\ m_w &= p_w \nabla s_w - F_{wo} - F_{wg} + M_{wm}, \\ m_g &= p_g \nabla s_g + F_{wg} + F_{og} + M_{gm}, \end{aligned} \tag{2.8}$$

where F_{ij} ($i, j = o, w, g$), denotes the force (drag) that the i phase exerts on the j phase. The j phase exerts an equal and opposite force $-F_{ij}$. Similarly, M_{om}, M_{wm} and M_{gm} represent interaction forces (drag forces) between fluid and pore walls (solid matrix), respectively, for oil, water and gas. The terms $p_o \nabla s_o$, $p_w \nabla s_w$ and $p_g \nabla s_g$ are interfacial forces that arise from an averaging process. To close the system we must specify the drag force term F_{wo}, F_{wg}, and F_{og} and the stresses σ_i ($i = o, w, g$) and interaction force terms M_{im} between fluid ($i = w, o, g$) and matrix.

Drag force represents the interaction between one phase and another phase and is modelled as [47, 41, 4]:

$$\begin{aligned} F_{wo} &= \hat{k}_{wo}(u_w - u_o), \\ F_{wg} &= \hat{k}_{wg}(u_w - u_g), \\ F_{og} &= \hat{k}_{og}(u_o - u_g), \end{aligned} \tag{2.9}$$

where $\hat{k}_{ij}$ $(i, j = o, w, g)$, remains to be determined. Typically, $\hat{k}_{ij} \sim s_i s_j$ to reflect that this force term will vanish when one of the phases vanishes. Similarly, the interaction force between fluid and pore wall (matrix, which is stagnant) is naturally expressed then as [46, 47, 41, 4]:

$$M_{im} = -\hat{k}_i u_i, \qquad (i = o, w, g). \tag{2.10}$$

The coefficients $\hat{k}_{ij}$ and $\hat{k}_i$ (dimension Pa·s/m^2), that characterize the magnitude of interaction terms, can be chosen such that the model recovers the classical porous media model based on Darcy's law. At the same time the approach used here will open for development of reservoir models where more detailed physics can be taken into account.

3. A SUMMARY OF THE GENERAL THREE-FLUID MODEL FOR POROUS MEDIA FLOW

3.1. **The compressible case.** We are interested in studying a 1-D model for three compressible immiscible fluids moving in a porous media. After combining (2.4)-(2.10) the model takes the following form:

$$\begin{aligned} &(\phi n_w)_t + (\phi n_w u_w)_x = -n_w Q_p + \rho_w Q_{Iw}, \qquad n_w = s_w \rho_w, \\ &(\phi n_o)_t + (\phi n_o u_o)_x = -n_o Q_p, \qquad n_o = s_o \rho_o, \\ &(\phi n_g)_t + (\phi n_g u_g)_x = -n_g Q_p + \rho_g Q_{Ig}, \qquad n_g = s_g \rho_g \\ &s_w (P_w)_x = -\hat{k}_w u_w - \hat{k}_{wo}(u_w - u_o) - \hat{k}_{wg}(u_w - u_g) + n_w g + \varepsilon_w (n_w u_{wx})_x, \\ &s_o (P_o)_x = -\hat{k}_o u_o - \hat{k}_{wo}(u_o - u_w) - \hat{k}_{og}(u_o - u_g) + n_o g + \varepsilon_o (n_o u_{ox})_x, \\ &s_g (P_g)_x = -\hat{k}_g u_g - \hat{k}_{wg}(u_g - u_w) - \hat{k}_{og}(u_g - u_o) + n_g g + \varepsilon_g (n_g u_{gx})_x, \\ &\Delta P_{ow}(s_w) = P_o - P_w, \qquad \Delta P_{go}(s_g) = P_g - P_o \end{aligned} \tag{3.11}$$

with capillary pressure ΔP_{ow} defined as the pressure difference between the oil and water and capillary pressure ΔP_{go} defined as the pressure difference between the gas and oil. We shall apply the following correlations

$$\begin{aligned} \Delta P_{ow} &= P_o - P_w = \Delta P_{ow}(s_w) = -P_{c1}^* \ln(\delta_1 + \frac{s_w}{a_1}) \quad \text{and} \quad \delta_1, a_1 > 0, \\ \Delta P_{go} &= P_g - P_o = \Delta P_{go}(s_g) = P_{c2}^* s_g^{a_2} \quad \text{and} \quad a_2 > 0 \end{aligned} \tag{3.12}$$

with non-negative constants P_{ci}^* representing interfacial tension. In addition, we have the fundamental relation that the three phases fill the pore space

$$s_o + s_w + s_g = 1. \tag{3.13}$$

The above model must be combined with appropriate closure relations for $\rho_i = \rho_i(P_i)$. We represent the three phases by linear pressure-density relations of the form

$$\rho_w - \tilde{\rho}_{w0} = \frac{P_w}{C_w}, \qquad \rho_o - \tilde{\rho}_{o0} = \frac{P_o}{C_o}, \qquad \rho_g = \frac{P_g}{C_g} \tag{3.14}$$

where C_w, C_o and C_g represent the compressibility of water, oil and gas, respectively.

We refer to Appendix B for a semi-discrete approximation of (3.11) as well as a fully discrete scheme.

3.2. The incompressible case.

3.2.1. *Viscous flow.* We may let C_w, C_o, C_g go to infinity in (3.14). Then we obtain the incompressible version of the model (3.11). We refer to Appendix C for a semi-discrete as well as a fully discrete scheme for this incompressible case.

3.2.2. *Inviscid flow.* Moreover, in order to relate this incompressible version to the classical Darcy-based formulation we ignore the viscosity terms in the momentum equations by setting $\varepsilon_i = 0$ $(i = w, o, g)$ in $(3.11)_{4,5,6}$. Solving momentum equations with respect to interstitial phase velocities u_i, the Darcy velocities of fluid phase are expressed as follows based on (2.2):

$$\begin{aligned} U_w &= \phi s_w u_w = -\lambda_{ww}(P_{wx} - \rho_w g) - \lambda_{wo}(P_{ox} - \rho_o g) - \lambda_{wg}(P_{gx} - \rho_g g), \\ U_o &= \phi s_o u_o = -\lambda_{wo}(P_{wx} - \rho_w g) - \lambda_{oo}(P_{ox} - \rho_o g) - \lambda_{og}(P_{gx} - \rho_g g), \\ U_g &= \phi s_g u_g = -\lambda_{wg}(P_{wx} - \rho_w g) - \lambda_{og}(P_{ox} - \rho_o g) - \lambda_{gg}(P_{gx} - \rho_g g), \end{aligned} \tag{3.15}$$

and the following relations are defined:

$$\begin{aligned} \lambda_{ww} &= \frac{\phi s_w^2}{R}(R_o R_g - \hat{k}_{og}^2), & \lambda_{wo} = \lambda_{ow} &= \frac{\phi s_w s_o}{R}(\hat{k}_{wo} R_g + \hat{k}_{og}\hat{k}_{wg}), \\ \lambda_{oo} &= \frac{\phi s_o^2}{R}(R_w R_g - \hat{k}_{wg}^2), & \lambda_{wg} = \lambda_{gw} &= \frac{\phi s_w s_g}{R}(\hat{k}_{wg} R_o + \hat{k}_{og}\hat{k}_{wo}), \\ \lambda_{gg} &= \frac{\phi s_g^2}{R}(R_w R_o - \hat{k}_{wo}^2), & \lambda_{og} = \lambda_{go} &= \frac{\phi s_o s_g}{R}(\hat{k}_{og} R_w + \hat{k}_{wg}\hat{k}_{wo}), \end{aligned} \tag{3.16}$$

where

$$\begin{aligned} R_w &= \hat{k}_w + \hat{k}_{wg} + \hat{k}_{wo}, \\ R_o &= \hat{k}_o + \hat{k}_{wo} + \hat{k}_{og}, \\ R_g &= \hat{k}_g + \hat{k}_{wg} + \hat{k}_{og}, \\ R &= \hat{k}_w\hat{k}_o\hat{k}_g + (\hat{k}_w + \hat{k}_o + \hat{k}_g)(\hat{k}_{wg}\hat{k}_{wo} + \hat{k}_{og}\hat{k}_{wo} + \hat{k}_{wg}\hat{k}_{og}) \\ &\quad + \hat{k}_g\hat{k}_{wo}(\hat{k}_w + \hat{k}_o) + \hat{k}_w\hat{k}_{og}(\hat{k}_o + \hat{k}_g) + \hat{k}_o\hat{k}_{wg}(\hat{k}_w + \hat{k}_g). \end{aligned} \tag{3.17}$$

Using capillary pressure relations (3.12) it follows that (3.15) take the following equivalent form:

$$\begin{aligned} U_w &= -\hat{\lambda}_w P_{wx} - (\lambda_{wo} + \lambda_{wg})\Delta P_{owx} - \lambda_{wg}\Delta P_{gox} + (\lambda_{ww}\rho_w + \lambda_{wo}\rho_o + \lambda_{wg}\rho_g)g, \\ U_o &= -\hat{\lambda}_o P_{wx} - (\lambda_{oo} + \lambda_{og})\Delta P_{owx} - \lambda_{og}\Delta P_{gox} + (\lambda_{wo}\rho_w + \lambda_{oo}\rho_o + \lambda_{og}\rho_g)g, \\ U_g &= -\hat{\lambda}_g P_{wx} - (\lambda_{gg} + \lambda_{og})\Delta P_{owx} - \lambda_{gg}\Delta P_{gox} + (\lambda_{wg}\rho_w + \lambda_{og}\rho_o + \lambda_{gg}\rho_g)g. \end{aligned} \tag{3.18}$$

Here we define the following notation for generalized phase mobilities $\hat{\lambda}_i$:

$$\begin{aligned} \hat{\lambda}_w &= \lambda_{ww} + \lambda_{wo} + \lambda_{wg}, \\ \hat{\lambda}_o &= \lambda_{oo} + \lambda_{wo} + \lambda_{og}, \\ \hat{\lambda}_g &= \lambda_{gg} + \lambda_{wg} + \lambda_{og}. \end{aligned} \tag{3.19}$$

By summing U_w, U_o and U_g in (3.18) and using the notation introduced in (3.19), the total Darcy velocity can be expressed as follows:

$$U_T = -\hat{\lambda}_T P_{wx} - (\hat{\lambda}_o + \hat{\lambda}_g)\Delta P_{owx} - \hat{\lambda}_g \Delta P_{gox} + (\hat{\lambda}_w\rho_w + \hat{\lambda}_o\rho_o + \hat{\lambda}_g\rho_g)g \tag{3.20}$$

where we have used

$$\hat{\lambda}_T = \hat{\lambda}_w + \hat{\lambda}_o + \hat{\lambda}_g. \tag{3.21}$$

Therefore, the water pressure gradient can be derived from (3.20):

$$P_{wx} = -\frac{1}{\hat{\lambda}_T}U_T - (\hat{f}_o + \hat{f}_g)\Delta P_{owx} - \hat{f}_g\Delta P_{gox} + (\hat{f}_w\rho_w + \hat{f}_o\rho_o + \hat{f}_g\rho_g)g \tag{3.22}$$

with generalized fractional flow function:

$$\hat{f}_i = \hat{\lambda}_i/\hat{\lambda}_T, \quad (i = w, o, g). \tag{3.23}$$

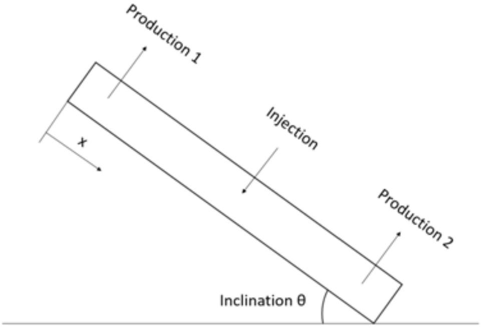

Figure 1: Reservoir model with injection and production.

Inserting (3.22) into (3.18) we get:

$$\begin{aligned} U_w &= \hat{f}_w U_T + (W_o + W_g)\Delta P_{owx} + W_g \Delta P_{gox} - (W_w\rho_w + W_o\rho_o + W_g\rho_g)g, \\ U_o &= \hat{f}_o U_T + (O_o + O_g)\Delta P_{owx} + O_g \Delta P_{gox} - (O_w\rho_w + O_o\rho_o + O_g\rho_g)g, \\ U_g &= \hat{f}_g U_T + (G_o + G_g)\Delta P_{owx} + G_g \Delta P_{gox} - (G_w\rho_w + G_o\rho_o + G_g\rho_g)g, \end{aligned} \tag{3.24}$$

where

$$\begin{aligned} W_i &= \hat{\lambda}_w \hat{f}_i - \lambda_{wi}, \\ O_i &= \hat{\lambda}_o \hat{f}_i - \lambda_{oi}, \\ G_i &= \hat{\lambda}_g \hat{f}_i - \lambda_{gi}, \quad (i = w, o, g). \end{aligned} \tag{3.25}$$

It should be noted that $W_i + O_i + G_i = 0$ $(i = w, o, g)$ in light of (3.16), (3.21), and (3.23).

4. Numerical Examples

We mainly focus on a reservoir model where there are one injection well at the center and two production wells distributed at two sides. The injection rate is equal to the total production rate and the rates of two production wells are also same (See Fig. 1). In addition, reservoir inclination θ is also accounted for in the model.

Interaction Terms.
The model $(3.11)_{4,5,6}$ should be armed with appropriate functional correlations for fluid-rock resistance force $\hat{k}_w$, $\hat{k}_o$, $\hat{k}_g$ and fluid-fluid drag force $\hat{k}_{wo}$, $\hat{k}_{wg}$, $\hat{k}_{og}$. Here we use the interaction terms suggested in the recent works [52, 43, 1]:

$$\begin{aligned} &\hat{k}_w := I_w s_w^\alpha \frac{\mu_w}{K}\phi, && \hat{k}_o := I_o s_o^\beta \frac{\mu_o}{K}\phi, && \hat{k}_g := I_g s_g^\gamma \frac{\mu_g}{K}\phi, \\ &\hat{k}_{wo} := I_{wo} s_w s_o \frac{\mu_w\mu_o}{K}\phi, && \hat{k}_{wg} := I_{wg} s_w s_g \frac{\mu_w\mu_g}{K}\phi, && \hat{k}_{og} := I_{og} s_o s_g \frac{\mu_o\mu_g}{K}\phi. \end{aligned} \tag{4.26}$$

All the interaction terms $\hat{k}_i$ and $\hat{k}_{ij}$ have dimension Pa·s/m^2. The parameters α, β and γ are dimensionless exponents whereas I_w, I_o and I_g are dimensionless friction coefficients characterizing the strength of fluid-solid interaction. Finally, I_{wo}, I_{wg} and I_{og} are coefficients characterizing the strength of the fluid-fluid drag force with dimension (Pa·s)$^{-1}$.

Parameter	Dimensional Value	Parameter	Dimensional Value
L	100 m	I_w	2.5
ϕ	0.25	I_o	1.8
$\tilde{\rho}_{w0}$	1 g/cm^3	I_g	1.1
$\tilde{\rho}_{o0}$	0.8 g/cm^3	I_{wo}	3000 (Pa·s)$^{-1}$
$\tilde{\rho}_{g0}$	0.018 g/cm^3	I_{wg}	3000 (Pa·s)$^{-1}$
s_{wr}	0.3	I_{og}	3000 (Pa·s)$^{-1}$
s_{or}	0.2	α	0.01
s_{gr}	0	β	0.01
μ_w	1 cP	γ	0.01
μ_o	1.5 cP	P_{c1}^*	$4 * 10^4$ Pa
μ_g	0.015 cP	a_1	2
K	1000 mD	δ_1	0.08
k_{rw}^{max}	0.4	P_{c2}^*	10^5 Pa
k_{ro}^{max}	0.5556	a_2	2
k_{rg}^{max}	0.9091	C_w	10^6 m^2/s^2
$\overline{Q}_{Iw}$	0.125 m^3/day	C_o	$5 * 10^5$ m^2/s^2
$\overline{Q}_{Ig}$	0.125 m^3/day	C_g	10^5 m^2/s^2
$\overline{Q}_p$	0.0625 m^3/day	ε_w	0.0 cP
N_x	101	ε_o	0.0 cP
A	1 m^2	ε_g	0.0 cP
P_{wL}	10^6 Pa	x_I	50 m
$\triangle t$	1570 s	$x_{P(1,2)}$	$10_{(1)}\&90_{(2)}$ m

Table 1: Reference input parameters in the simulations.

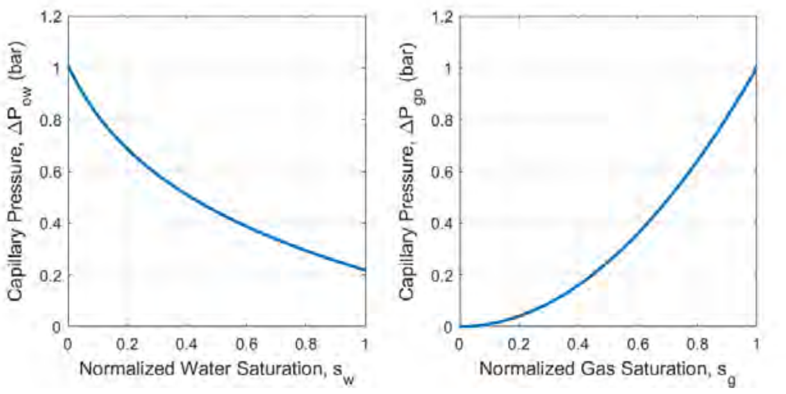

Figure 2: Left: Capillary pressure between water and oil. Right: Capillary pressure between oil and gas. We refer to (3.12) for their expressions.

Input Data.
The input parameters used in the simulations are listed in Table 1. We use 101 grid cells for a 100-meter reservoir layer. The magnitude of the interaction coefficients I_{wo}, I_{wg}, and I_{og} are chosen as in [43]. In order to avoid too many complicating effects at the same time in the subsequent discussion, we have set the viscosity terms to zero, i.e., $\varepsilon_w = \varepsilon_o = \varepsilon_g = 0$.

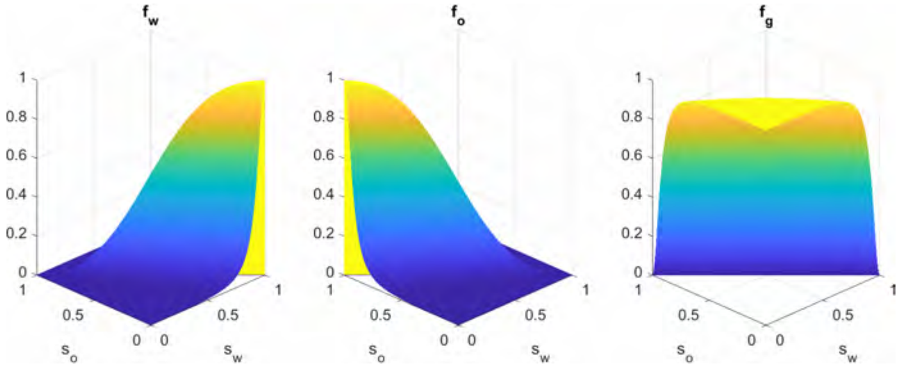

Figure 3: Phase flow fractional function (such as $f_w(s_w, s_o)$ as defined in (4.27)) for a horizontal model ($\sin\theta = 0$) where U_T is now a constant equal to $(\overline{Q}_p/2)$.

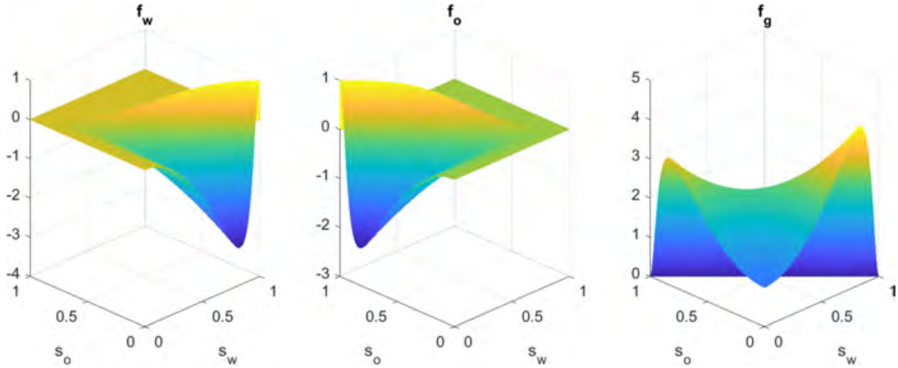

Figure 4: Phase flow fractional function (such as $f_w(s_w, s_o)$ as defined in (4.27)) for a vertical model ($\sin\theta = 1$) where U_T is now a constant equal to $-(\overline{Q}_p/2)$.

We use the similar capillary pressure relations as [44] for water and oil and [35] for oil and gas (see Fig. 2). The expression of an effective water fractional flow function $f_w(s_w, s_o)$ in the conventional water-oil-gas model (assuming no capillary pressure, i.e., $\Delta P_{ow} = \Delta P_{go} = 0$) is

$$f_w(s_w, s_o) \overset{\text{def}}{:=} \frac{U_w}{U_T} = \frac{\frac{\hat{\lambda}_w}{\hat{\lambda}_T} U_T - (W_w\rho_w + W_o\rho_o + W_g\rho_g) g \sin\theta}{U_T} \tag{4.27}$$

where we have used (3.24) and (3.25) where $U_T = \int_0^x (Q_I - Q_p)dx$. Similarly, f_o and f_g can also be expressed in the same manner. In order to illustrate the phase flow fraction f_w, f_o and f_g (see Fig. 5) we represent U_T by a reference total velocity $\overline{U}_T \in [-\frac{\overline{Q}_p}{2}, +\frac{\overline{Q}_p}{2}]$. We refer to Table 1 for other input data that are used.

Initial Conditions.
For the waterflooding case, we assume the reservoir initially is mostly filled with gas (90%) and

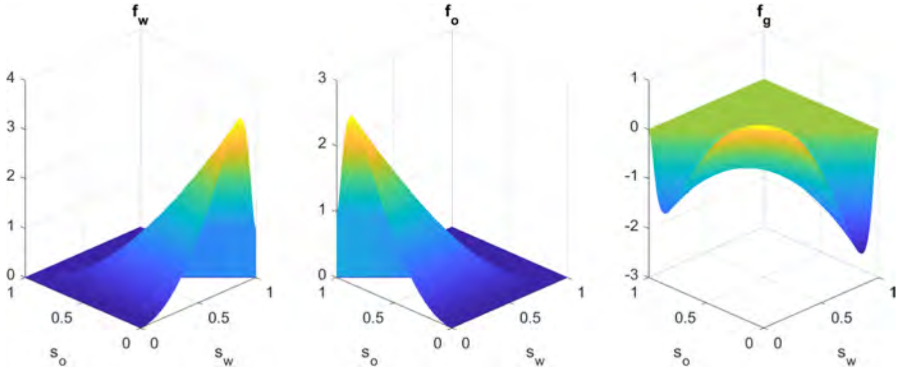

Figure 5: Phase flow fractional function (such as $f_w(s_w, s_o)$ as defined in (4.27)) for a vertical model ($\sin\theta = 1$) where U_T is now a constant equal to $(\overline{Q}_p/2)$.

some oil (10%):

$$s_g(x, t=0) = 0.9, \qquad s_o(x, t=0) = 0.1. \tag{4.28}$$

For the WAG injection case, the reservoir is assumed initially filled with oil (90%) and some extra water (10%):

$$s_o(x, t=0) = 0.9, \qquad s_w(x, t=0) = 0.1. \tag{4.29}$$

For the compressible case, a reference pressure P_{wL} at the left boundary of the layer is given at initial state,

$$P_{wL}(x=0, t=0) = 10^6\text{Pa}. \tag{4.30}$$

Boundary Conditions.

We assume a closed boundary for both compressible and incompressible models, which means that

$$u_i(x=0,t) = 0, \qquad u_i(x=L,t) = 0, \qquad i = w, o, g. \tag{4.31}$$

For the incompressible case, we give a reference pressure P_{wL} at the left boundary of the layer,

$$P_{wL}(x=0, t) = 10^6\text{Pa}. \tag{4.32}$$

Source Terms.

For WAG experiments, gas and water are injected at different time periods during the whole oil recovery process. We assume that $Q_I(x)$ and $Q_p(x)$ take the form

$$Q_{I_w,I_g}(x) = \frac{\overline{Q}_{I_w,I_g}}{\sigma}\begin{cases} 1, & \text{if } |x - x_I| \le \sigma/2; \\ 0, & \text{otherwise.}\end{cases}, \quad Q_p(x) = \frac{\overline{Q}_p}{\sigma}\begin{cases} 1, & \text{if } |x - x_{p,i}| \le \sigma/2; \\ 0, & \text{otherwise.}\end{cases} \tag{4.33}$$

where $(i = 1, 2)$ and $\overline{Q}_{I_w,I_g} = 0.125\text{m}^3/\text{day}$ and $\overline{Q}_p = 0.0625\text{m}^3/\text{day}$. The width of the small region associated with the injector and producer is σ. In the numerical scheme $\sigma = \Delta x$.

4.1. **Waterflooding in a gas reservoir.**

We first test the proposed compressible three-phase model applied to a gas reservoir development. In this example, water is injected at 50 m into a gas reservoir layer of length 100 m with a little proportion of oil (10%). Two cases, respectively, for the horizontal (Fig. 6) and vertical reservoir (Fig. 7) are shown below.

The results of the horizontal compressible three-phase model with water injection for a total period of 400 days are shown in Fig. 6 where pressures (first column), velocities (middle column) and saturations (right column) are symmetric with the injection well located at the center of reservoir layer. The gas is mostly recovered during the first 130 days, see (I), whereas oil recovery takes place over more than 300 days, see (F), due to its lower mobility than gas. It is also observed

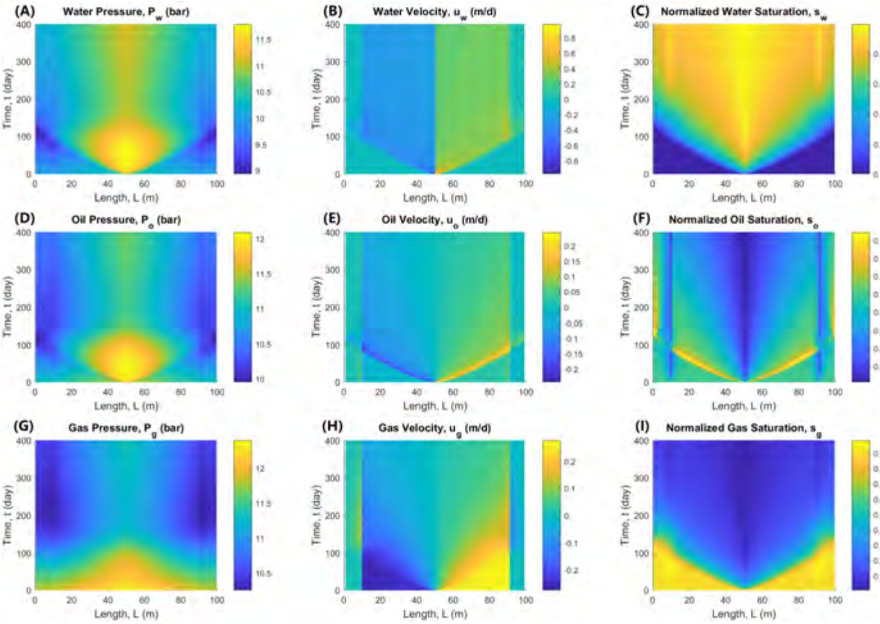

Figure 6: Results of the horizontal compressible three-phase model during a 400-day waterflooding period. (A) Water pressure plot shows a strong pressure gradient region at the early stage (before 130 days). (B) Water velocity profile. It can be seen that water front reaches the production well after around 100 days. (C) Normalized water saturation shows that the water front is fast whereas the other phases (oil and gas) are produced slowly (takes almost 300 days). (D) Oil pressure profile gives a similar result as water pressure. (E) Oil velocity behavior is similar to water velocity. (F) Normalized oil saturation plot illustrates that oil is displaced quite slowly. (G) The gas pressure gradient is very low in the gas-displaced region at the early stage due to the high mobility of gas. (H) There is no gas advancing front since gas flows easily. (I) Gas is displaced fastly and a lot of gas is recovered before 130 days.

that at early stage gas pressure along the reservoir layer has less gradient than both the water's and the oil's (see first column in Fig. 6). The injected water displaces both oil and gas in the reservoir near the injection well region where a high pressure gradient is necessary for both water and oil to flow, see panel (A) and (B), because of their low mobilities. After water has arrived the production wells at around 100 days (see C), water and oil pressures drop owing to the fact that water then can find an easy flow path to the production wells.

In Fig. 7, we show the results (phase pressures, velocities and saturations) of a compressible vertical three-phase model with a 400-day waterflooding displacement. Water is injected to displace oil and gas at both sides of the reservoir layer. It quickly fills the bottom part, then starts accumulating, see panel (C). Correspondingly, gas is displaced faster in the lower part than in the upper part because the reservoir layer is vertical. Gravity segregation is seen in the lower part where gas is squeezed upwardly, see (H) and (I). In contrast to what is shown in Fig. 6**G**, gas pressure distribution shows a similar behavior as water and oil (higher at bottom and lower at top), see first column in Fig. 7. We refer to the figure text for more details.

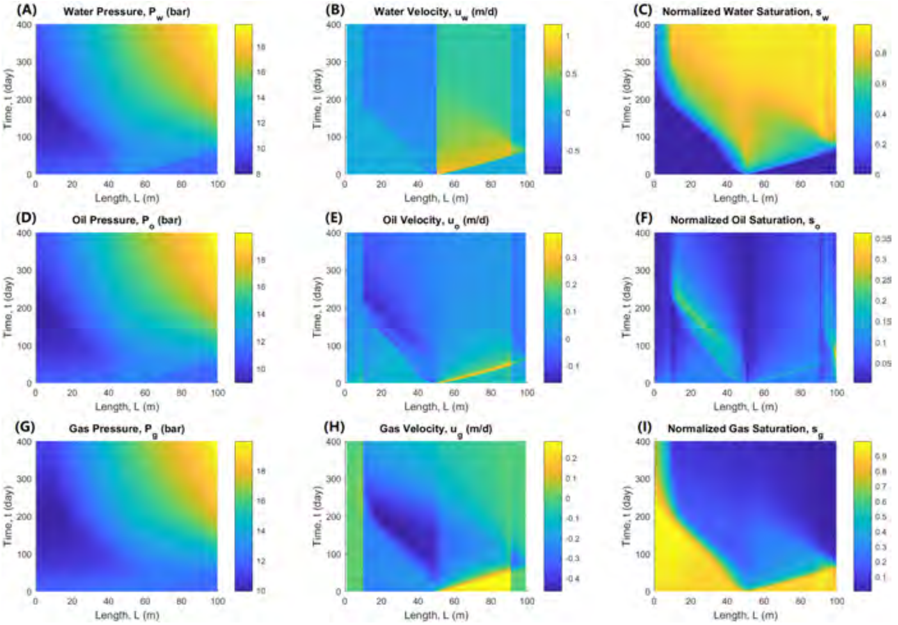

Figure 7: Results of the vertical compressible three-phase model during a 400-day waterflooding period. (A) Water pressure plot indicates that a lot of water flows toward the bottom and by that greatly increases the pressure in that region. (B) Due to the strong gravity effect water flows faster towards the bottom of layer compared the water displacement in the upper layer. (C) Normalized water saturation shows that water flows fastly to the bottom where it is accumulated before it begins to efficiently displace the upper part of the layer. (D) Oil pressure follows the similar behavior as water. (E) Water displaces the oil towards both sides from the center. However, at early time some oil in the upper part of the layer will move downwardly due to gravity. Later, the water front will displace oil upwardly. (F) The oil advancing front behaves similar as the water front. (G) Gas pressure behaves similar to the water pressure. (H) At an early stage gas is displaced towards the production well from the center. After the water front has reached the bottom production well the whole bottom part of gas (50 m to 100 m) starts moving upwards. (I) Gas is recovered slowly in the upper part whereas gas recovery in the lower part consists of two stages: initially, gas is displaced by water to the bottom production well. Then, gas in the lower zone starts flowing upwardly.

4.1.1. *Comparison of the compressible and incompressible models.*

We continue the discussion of the case shown in Fig. 7. In particular, we want to compare the behavior of the compressible and incompressible model. Constant density values $\rho_w = 1000$ kg/m^3, $\rho_o = 800$ kg/m^3 and $\rho_g = 18$ kg/m^3 are used in the incompressible model.

Fig. 8 shows a comparison between the compressible and incompressible model after 30 and 120 days. At the early time (30 days) the saturation differences are not distinct, see (C). However, after a long time (120 days) the differences are more significant, especially, in the water displacing part, see (F). This is due to the increasing phase pressure difference between compressible and incompressible model, see (B) and (E). The removal of compressed gas from the gas reservoir as (almost incompressible) water is injected clearly generates additional space for the water to fill which gives rise to a lower pressure. Moreover, there are also clear differences in the velocity, see (A) and (D).

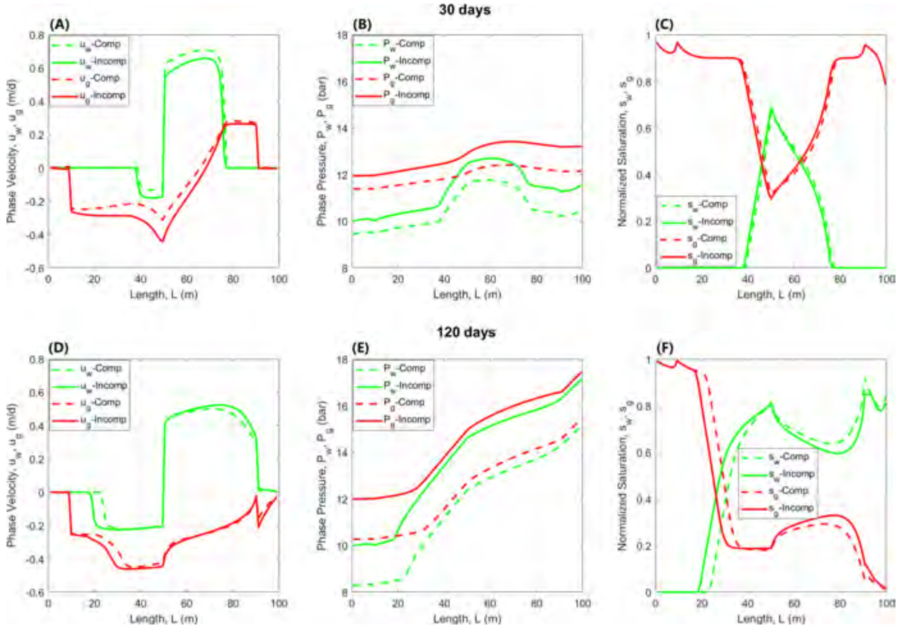

Figure 8: Comparison between the compressible and incompressible model with vertical three-phase flow. (A,D) Phase velocity u_w and u_g for water and gas, respectively. (B,E) Pressure P_w and P_g for water and gas, respectively. Almost incompressible water is injected whereas the compressible model senses that compressed gas is removed through the producers. This gives rise to a lower pressure level for the compressible model as compared to the incompressible. (C,F) Saturation s_w and s_g for water and gas, respectively.

4.2. The compressible three-phase model with a WAG experiment.

In WAG processes, the injected water will migrate towards the bottom of the formation while the injected gas will flow upwardly. Therefore, counter-current flow occurs in the vertical direction of the reservoir due to the gravity segregation of water, oil and gas. Significant differences in terms of saturation distribution and producing GOR (gas-oil-ratio) have been reported between a conventional model and models that better can account for the mix of different flow regimes (co-current and counter-current). For example, in [51] an explicit representation of flow transitions between co-current and counter-current flow was used to improve the design of WAG injection processes.

In this part, we conduct a water alternating gas (WAG) injection in a 1D reservoir (250 mD) layer which initially contains 90% oil and 10% water. The water and gas injection well is located at 50 m and two production wells are set at 10 m and 90 m. Gas is injected for the first 10 days followed by the water injection the next 10 days. Fluids can be produced in both production wells. The whole WAG experiment continues with an injection circulation of water and gas (each for 10 days).

Fig. 9 shows the result for a WAG injection process produced by the compressible three-phase vertical model where gravity segregation has a significant effect. From the simulation we see that pressure increases with time (first column in Fig. 9). Moreover, pressure values at the lower part of the layer are larger than at the upper part. Due to the density difference, water displaces oil faster in the bottom part, see (B) and (C). In addition, gas flows quickly towards the upper part

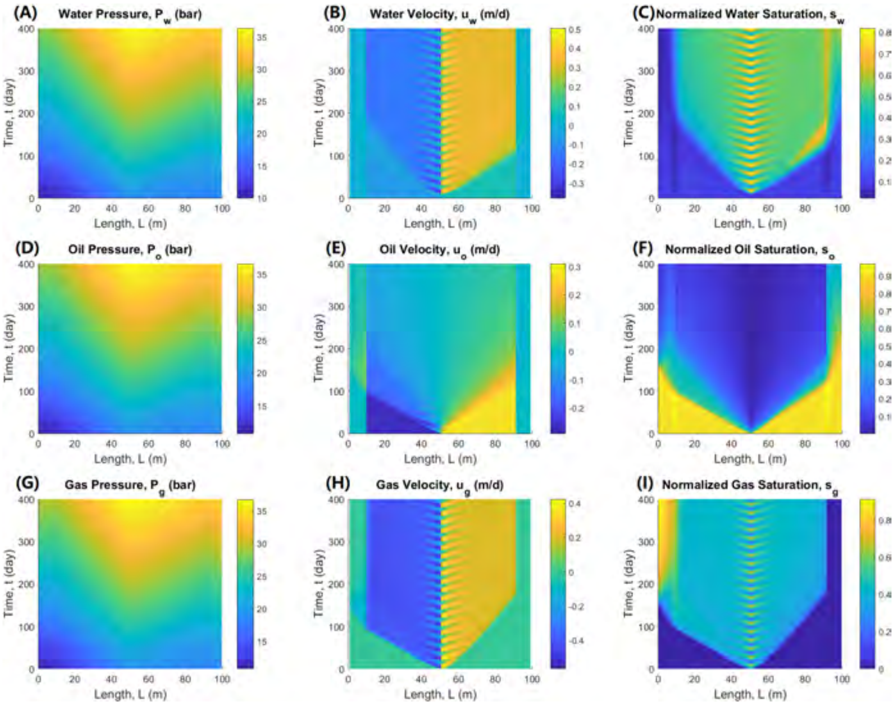

Figure 9: Results of the vertical compressible three-phase model for a 400-day WAG injection process. (A) A high pressure region in the layer center due to the water or gas injection and gravity effect. (B) Water advancing front implies that water flows faster towards the bottom of layer compared the water displacement in the upper layer due to gravity segregation. (C) Water prefers to flow towards the bottom of layer where the edge region (90 m- 100 m) is also swept by water. (D) Oil pressure follows similar behavior as water pressure. (E) The upper part of oil is recovered faster than the lower part. (F) Due to the large density difference between oil and gas, the upper part oil is recovered very quickly, even for the edge region (0 m- 10 m). (G) Gas pressure. (H) Gas advancing front is fast in the upper part of layer because of the strong gravity segregation. (I) Gas reaches the bottom production well whereas a lot of gas is accumulated in the top region.

of the reservoir layer, see the saturation plots. In the upper part oil is recovered faster than in the lower part because of the larger density difference between gas and oil than the one between water and oil, see the second column in Fig. 9. We also observe that gas reaches the bottom production well but does not move further. This can be explained by the fact that gravity segregation effect overcomes the capillarity. However, a lot of gas is accumulated in the upper edge region (0 m- 10 m) due to the buoyancy force, see (I).

4.3. **Comparison of compressible and incompressible three-phase models with WAG experiments.**

In this part, we compute solutions from incompressible three-phase models with same WAG injection process and compare the relevant results with those from the compressible three-phase model. Constant density values $\rho_w = 1000$ kg/m^3, $\rho_o = 800$ kg/m^3 and $\rho_g = 18$ kg/m^3 are used in the incompressible model

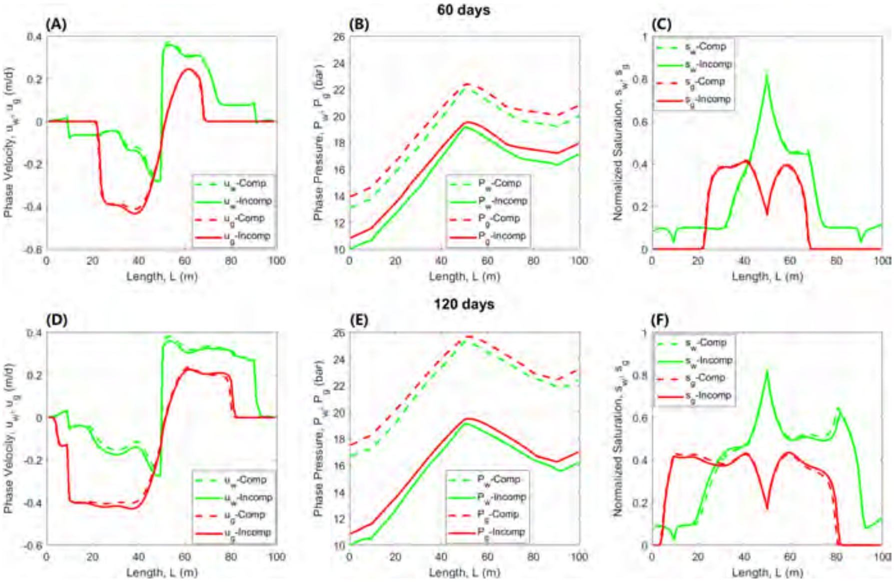

Figure 10: Comparison between the compressible and incompressible model of the vertical three-phase reservoir with a WAG process. Results are shown after 60 and 120 days. (A) Gravity segregation results in a fast advancing front of gas in the upper part of layer and a fast advancing front of water in the lower part of layer. (B) Phase pressure in the compressible model is higher since the compressed gas wants to expand when it moves to a region with lower pressure but cannot expand due to the constrained space for gas. (C) Gas prefers to move towards the upper part of layer and water prefers to flow towards the lower part. (D) At 120 days, gas reaches the upper production well and water arrives at the bottom well. (E) Phase pressure in the compressible model increases with time compared with (B). (F) The difference between the two models is enhanced with time.

Fig. 10 shows a comparison between the compressible and incompressible model of the vertical three-phase reservoir with a WAG process. Similar to what was observed in Fig. 8, differences are seen for phase velocity, pressure and saturation. With increasing time, this difference will be enhanced, especially for the pressure. This is mainly due to the gas compressibility. See (B) and (E) and the figure text for more explanation. Because of the density difference water prefers to flow towards the bottom of the layer whereas gas moves faster towards the upper part of layer, see (C) and (F).

4.3.1. *Effect of fluid-fluid interactions.*

Here we want to illustrate the impact from fluid-fluid interaction terms on the compressible model with a WAG process. Two situations are compared below: one with $I_{wo} = I_{wg} = I_{og} = 0$ and one with $I_{wo} = I_{wg} = I_{og} = 5000$.

Fig. 11 compares the results for the horizontal model for a WAG process with and without fluid-fluid interaction effect at 60 and 120 days. In (B) and (E), we observe that due to the fluid-fluid interaction, pressure is elevated compared with the case with no fluid-fluid interaction. The water velocity (A) and saturation profiles (C) show that water to a less extent displaces oil and instead flows through the original water channels when fluid-fluid interaction is included. The difference in the water saturation profiles between (C) and (F) is enhanced with time due to the additional resistance force from the fluid-fluid interaction term.

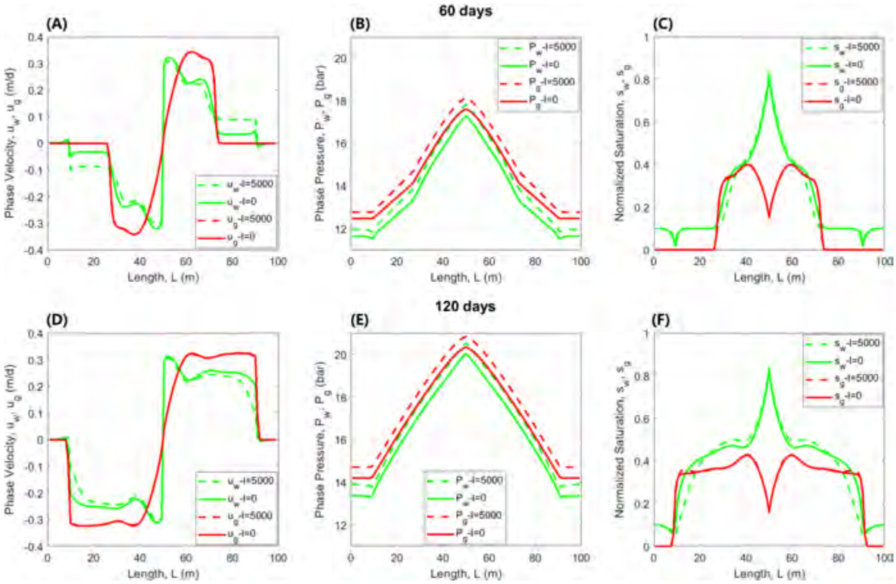

Figure 11: Comparison for the horizontal compressible model for a WAG process with and without fluid-fluid interaction effects. The situation after 60 and 120 days are plotted. (A) Phase velocity at 60 days. (B) Phase pressure at 60 days. (C) Normalized saturation at 60 days. (D) Phase velocity at 120 days. (E) Phase pressure at 120 days. (F) Normalized saturation at 120 days.

Fig. 12 compares the results for the vertical model for a WAG process with and without fluid-fluid interaction effect at 60 and 120 days. Due to the density difference a large proportion of gas flows to the upper part of layer, see (C) and (F), and more of the water flows towards the bottom part of layer. As a result, differences are seen for the water velocity (A,D) and saturation (C,F) for the case with and without fluid-fluid interaction. Similar to Fig. 11, the build-up of the water front is less efficient for the case with fluid-fluid interaction since a larger portion of water tends to move through the original water channels (A).

5. CONCLUDING REMARKS

We have presented a three-phase compressible and incompressible viscous model based on the mixture theory approach. The formulation represents an extension of the conventional Darcy-type formulations by including fluid-fluid viscous coupling effects. The three-phase flow model consists of a set of mass balance equations which are coupled to a set of momentum balance equations that involve both fluid-matrix, fluid-fluid interactions, and internal viscosity effects. Numerical schemes have been developed for both the compressible and incompressible model. Moreover, various waterflooding displacement scenarios in a gas reservoir and WAG injection in an oil reservoir have been investigated to illustrate the effects of fluid compressibility and fluid-fluid viscous coupling. Main findings are:
(i) The numerical schemes proposed in this paper appear to be robust and stable for simulation of various three-phase flow scenarios, both for the incompressible and compressible case;
(ii) Comparison of the results for the compressible and incompressible model show that the differences between these two models can be significant, especially in the vertical case where the effect

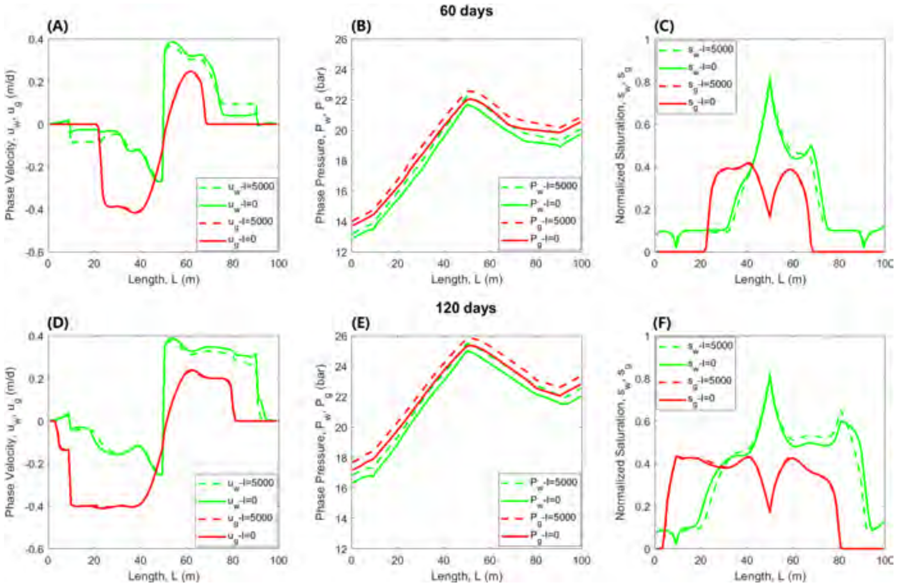

Figure 12: Comparison of the vertical compressible model for a WAG process with and without fluid-fluid interaction effect at 60 and 120 days. (A) Phase velocity at 60 days. (B) Phase pressure at 60 days. (C) Normalized saturation at 60 days. (D) Phase velocity at 120 days. (E) Phase pressure at 120 days. (F) Normalized saturation at 120 days. Water tends to flow towards the lower part of layer due to the gravity segregation, resulting in a strong fluid-fluid interaction in the lower part of layer where the water saturation profiles clearly are affected, see (D) and (F).

of gravity segregation is rather strong;
(iii) The viscous coupling (fluid-fluid interaction) can have a significant effect on the results.

References

[1] Andersen, P. Ø., Qiao, Y., Standnes, D.C and Evje, S., Co-current spontaneous imbibition in porous media with the dynamics of viscous coupling and capillary back pressure, *SPE J*, **24** (1), 158–177, 2019.

[2] Avraam, D.G. and Payatakes, A.C., Flow regimes and relative permeabilities during steady-state two-phase flow in porous media, *Journal of Fluid Mechanics*, **293**, 207–236, 1995.

[3] Avraam, D.G. and Payatakes, A.C., Generalized relative permeability coefficients during steady-state two-phase flow in porous media, and correlation with the flow mechanisms, *Transport in Porous Media*, **20** (1-2), 135–168,1995.

[4] Ambrosi, D. and Preziosi, L., On the closure of mass balance models for tumor growth, *Mathematical Models and Methods in Applied Sciences*, **12** (5), 737–754, 2002. DOI: 10.1142/S0218202502001878

[5] Ayodele, O. R., Theoretical analysis of viscous coupling in two-phase flow through porous media, *Transport in Porous Media*, **64** (2), 171–184, 2006. DOI: 10.1007/s11242-005-2809-8

[6] Bacri, J. C., Chaouche, M. and Salin, D., Modele simple de permeabilities croisees, C.R. Acad. Sci., **311**, 591–596, Series II, 1990.

[7] Bowen, R.M., Theory of Mixtures. Continuum Physics. (A. C. Eringen, ed.). New York: Academic. 1976.

[8] Bentsen, R.G. and Manai, A.A., Measurement of concurrent and countercurrent relative permeability curves using the steady-state method, *AOSTRA J. Res.*, **7**, 169-181, 1992.

[9] Bentsen, R. G. and Manai, A. A., On the use of conventional cocurrent and countercurrent effective permeabilities to estimate the four generalized permeability coefficients which arise in coupled, two-phase flow, *Transport in Porous Media,* **11**, 243–262, 1993.

[10] Bentsen, R. G. and Trivedi, J. J., Modified transport equations for the three-phase flow of immiscible, incompressible fluids through water-wet porous media, *Journal of Porous Media,* **15** (2), 2012.

[11] Bourbiaux, B.J. and Kalaydjian, F.J., Experimental study of cocurrent and countercurrent flows in natural porous media, *SPE Reservoir Engineering*, **5** (3), 361-368, 1990. DOI: 10.2118/18283-PA.

[12] Byrne, H.M. and Preziosi, L., Modelling solid tumour growth using the theory of mixtures, *Mathematical Medicine and Biology*, **20** (4), 341–366, 2003.

[13] Darcy, H., Les Fontaines Publiques de la Ville de Dijon, Dalmont, Paris, 1856.

[14] de la Cruz, V. and Spanos, T. J. T., Mobilization of oil ganglia, *AIChE Journal* **29** (5), 854–858, 1983.

[15] Dullien, F. A. L. and Dong, M., Experimental determination of the flow transport coefficients in the coupled equations of two-phase flow in porous media, *Transport in Porous Media,* **25**, 97–120, 1996.

[16] Dong, J. and Rivière, B., A semi-implicit method for incompressible three-phase flow in porous media, *Computational Geoscience,* **20**, 1169–1184, 2016.

[17] Ehrlich, R., Viscous coupling in two-phase flow in porous media and its effect on relative permeabilities, *Transport in Porous Media,* **11** (3), 201–218, 1993.

[18] Evje, S, An integrative multiphase model for cancer cell migration under influence of physical cues from the tumor microenvironment, *Chem. Eng. Sci.*, **165**, 240–259, 2017.

[19] Evje, S. and Waldeland, J.O., How tumor cells can make use of interstitial fluid flow in a strategy for metastasis, *Cel. Mol. Bioeng,* https://doi.org/10.1007/s12195-019-00569-0, 2019.

[20] Falls, A.H. and Schulte, W.M., Theory of three component, three phase displacement in porous media, *SPE Reserv. Engrg.*, **7** (3), 377–384,1992.

[21] Guzm´án, R.E. and Fayers, F.J., Mathematical properties of three-phase flow equations, *Soc. Pet. Engrg. J.*, **2** (3), 291–300, 1997.

[22] Guzm´án, R.E. and Fayers, F.J., Solution to the three-phase Buckley–Leverett problem, *Soc. Pet. Engrg. J.*, **2** (3), 301–311, 1997.

[23] Gajo, A., Cecinato, F. and Loret, B., Deformable Porous Media Saturated by Three Immiscible Fluids: Constitutive modelling and simulations of injection and imbibition tests, *Transport in Porous Media*, **116**, 19–51, 2017.

[24] Juanes, R. and Patzek, T.W., Analytical solution to the Riemann problem of three-phase flow in porous media, *Transp. Porous Media*, **55** (1), 47–70, 2004.

[25] Juanes, R., Nonequilibrium effects in models of three-phase flow in porous media, *Adv Wat Res*, **31**, 661–673, 2008.

[26] Katchalsky, A. and Curran P. A., *Nonequilibrium Thermodynamics in Biophysics*, Harvard University Press, Cambridge, 1975.

[27] Kalaydjian, F., A macroscopic description of multiphase flow in porous media involving spacetime Evolution of Fluid/Fluid Interface, *Transport in Porous Media,* **2**, 537–552, 1987.

[28] Kalaydjian, F., Origin and quantification of coupling between relative permeabilities for two-phase flows in porous media, *Transport in Porous Media,* **5** (3), 215–229, 1990.

[29] Labernadie, A. et al., A mechanically active heterotypic E-cadherin/N-cadherin adhesion enables fibroblasts to drive cancer cell invasion *Nat. Cell. Biol.*, **19**, pp. 224-236, 2017.

[30] Larsen, J.A. and Skauge, A., Simulation of the immiscible WAG process using cycle-dependent three-phase relative permeabilities, *In: Paper SPE 56475 presented at SPE Annual Technical Conference and Exhibition, Houston, TX (1999).*

[31] Langaas, K. and Papatzacos, P., Numerical investigations of the steady state relative permeability of a simplified porous medium., *Transport in Porous Media,* **45**, 241–266, 2001.

[32] Li, D., Kumar, K. and Mohanty, K.K., Compositional simulation of WAG processes for a viscous oil, *In: Paper SPE 84074 presented at SPE Annual Technical Conference and Exhibition, Denver, CO (2003).*

[33] Li, H., Pan, C. and Miller, C.T., Viscous coupling effects for two-phase flow in porous media, *Developments in Water Science,* **55**, Part 1, 247–256, 2004.

[34] Li, H., Pan, C. and Miller, C.T., Pore-scale investigation of viscous coupling effects for two-phase flow in porous media, *Physical Review E,* **72**, 2005.

[35] Lewis, R. and Pao, W., Numerical simulation of three-phase flow in fractured reservoirs, *Gas Science and Technology - Revue d'IFP Energies nouvelles*,**57**, pp. 499–514, 2002.

[36] Lie, K.A. and Juanes, R., A front-tracking method for the simulation of three-phase flow in porous media, *Computational Geosciences*,**9**, pp. 29–59, 2005.

[37] Lee, S.H., Wolfsteiner, C. and Tchelepi, H.A., Multiscale finite-volume formulation for multiphase flow in porous media: black oil formulation of compressible, three-phase flow with gravity, *Computational Geosciences*,**12**, pp. 351–366, 2008.

[38] Lee, S.H. and Efendiev, Y., C^1-Continuousrelative permeability and hybrid upwind discretization of three phase flow in porous media, *Advances in Water Resources*,**96**, pp. 209–224, 2016.

[39] Muskat, M., Wyckoff, R.D., Botset, H.G. and Meres, M.M., Flow of gas-liquid mixtures through sands, *SPE Transactions of the AIME*, **123** (1), 69–96, 1937. DOI: 10.2118/937069-G

[40] Perez-Gonzalez, C., Alert, R., Blanch-Mercader, C., Gomez-Gonzalez, M., Kolodziej, T., Bazellieres, E., Casademunt, J. and Trepat, X., Active wetting of epithelial tissues, *Nature Physics*, **15**, 79–88, 2019.

[41] Preziosi, L. and Farina, A., On Darcy's law for growing porous media, *International Journal of Non-Linear Mechanics*, **37**, 485–491, 2002.

[42] Polacheck, W.J., Charest, J.L., and Kamm, R.F., Interstitial flow influences direction of tumor cell migration through competing mechanisms, *PNAS*, **108**, pp. 11115—11120, 2011.

[43] Qiao, Y., Andersen, P.Ø., Evje, S and Standnes, D.C., A mixture theory approach to model co- and counter-current two-phase flow in porous media accounting for viscous coupling, *Adv Water Resour*, **112**, 170–188, 2018.

[44] Qiao, Y., Wen, H. and Evje, S., Viscous two-phase flow in porous media driven by source terms: analysis and numerics, submitted, 2019.

[45] Qiao, Y., Wen, H. and Evje, S., Compressible and viscous two-phase flow in porous media based on mixture theory formulation, *Netw Het Med*, **14**, 2019.

[46] Rajagopal, K.R. and Tao, L., *Mechanics of Mixtures*, Series on Advances in Mathematics for Applied Sciences-Vol. 35 (World Scientific, 1995).

[47] Rajagopal, K.R., On a hierarchy of approximate models for flows of incompressible fluids through porous solids, *Math. Mod. Met. Appl. Sci.*, **17**, 215–252, 2007.

[48] Rose, W., Myths about later-day extensions of Darcy's law, *Journal of Petroleum Science and Engineering*, **26**, 187–198, 2000.

[49] Ranaee, E., Inzoli, F., Riva, M. and Guadagnini, A., Hysteresis effects of three-phase relative permeabilities on black-oil reservoir simulation under WAG injection protocols, *Journal of Petroleum Science and Engineering*, **176**, 1161–1174, 2019.

[50] Shieh, A.C., Rozansky, H.A., Hinz, B., and Swartz, M.A., Tumor cell invasion is promoted by interstitial flow-induced matrix priming by stromal fibroblasts, *Cancer Res.*, **71**, pp. 790-800, 2011.

[51] Sherafati M. and Jessen K., Dynamic relative permeability and simulation of WAG injection processes, *Transport in Porous Media*, **117**, pp. 125–147, 2017.

[52] Standnes, D.C., Evje, S. and Andersen, P.Ø., A novel relative permeability model based on mixture theory approach accounting for solid–fluid and fluid–fluid interactions, *Transport in Porous Media*, **119**, pp. 707–738, 2017.

[53] Urdal, J., Waldeland, J.O. and Evje, S., Enhanced cancer cell invasion caused by fibroblasts when fluid flow is present, *Biomech. Model Mechanobiol.*, https://doi.org/10.1007/s10237-019-01128-2, 2019.

[54] Wu, Y.S., Multiphase fluid flow in porous and fractured reservoirs, Elsevier, 2016.

[55] Waldeland, J.O. and Evje, S., A multiphase model for exploring cancer cell migration driven by autologous chemotaxis, *Chem. Eng. Sci.*,**119**, pp. 268–287, 2018.

[56] Waldeland, J.O. and Evje, S., Competing tumor cell migration mechanisms caused by interstitial fluid flow, *J. Biomechanics*, **81**, 22–35, 2018.

[57] Yuster, S.T., Theoretical considerations of multiphase flow in idealized capillary systems, *World Petroleum Cong. Proc., Section II, The Hague*, pp. 437–445, 1951.

Appendix A

From the three mass balance equations we get after multiplying the oil mass balance with $\rho_w\rho_g$, the water mass balance with $\rho_o\rho_g$ and the c mass balance with $\rho_w\rho_o$,

$$\left\{\begin{array}{l}(s_{wt}\rho_w + s_w\rho_{wt})\rho_o\rho_g + \rho_o\rho_g(s_w\rho_w u_w)_x = -s_w\rho_w\rho_o\rho_g Q_p/\phi + \rho_w\rho_o\rho_g Q_{Iw}/\phi,\\ (s_{ot}\rho_o + s_o\rho_{ot})\rho_w\rho_g + \rho_w\rho_g(s_o\rho_o u_o)_x = -s_o\rho_w\rho_o\rho_g Q_p/\phi,\\ (s_{gt}\rho_g + s_g\rho_{gt})\rho_w\rho_o + \rho_w\rho_o(s_g\rho_g u_g)_x = -s_g\rho_w\rho_o\rho_g Q_p/\phi + \rho_w\rho_o\rho_g Q_{Ig}/\phi,\end{array}\right. \tag{5.34}$$

and summing the three resulting equations

$$f_1 + f_2 + f_3 = f_4, \tag{5.35}$$

where

$$\begin{aligned} f_1 &= s_{wt}\rho_w\rho_o\rho_g + s_{ot}\rho_w\rho_o\rho_g + s_{gt}\rho_w\rho_o\rho_g = \rho_w\rho_o\rho_g(s_{wt} + s_{ot} + s_{gt}) = 0,\\ f_2 &= s_w\rho_{wt}\rho_o\rho_g + s_o\rho_{ot}\rho_w\rho_g + s_g\rho_{gt}\rho_w\rho_o,\\ f_3 &= \rho_o\rho_g(s_w\rho_w u_w)_x + \rho_w\rho_g(s_o\rho_o u_o)_x + \rho_w\rho_o(s_g\rho_g u_g)_x,\\ f_4 &= -s_w\rho_w\rho_o\rho_g Q_p/\phi + \rho_w\rho_o\rho_g Q_{Iw}/\phi - s_o\rho_w\rho_o\rho_g Q_p/\phi - s_g\rho_w\rho_o\rho_g Q_p/\phi + \rho_w\rho_o\rho_g Q_{Ig}/\phi\\ &= \rho_w\rho_o\rho_g(Q_{Iw} + Q_{Ig} - Q_p)/\phi. \end{aligned}$$

Here we want to focus on dealing with expression f_2.

$$f_2 = s_w\rho_o\rho_g\frac{P_{wt}}{C_w} + s_o\rho_w\rho_g\frac{P_{ot}}{C_o} + s_g\rho_w\rho_o\frac{P_{gt}}{C_g}, \tag{5.36}$$

$$\begin{aligned}
&P_{ot} = (P_w + \Delta P_{ow})_t = P_{wt} + \Delta P'_{ow} s_{wt},\\
&P_{gt} = (P_w + \Delta P_{ow} + \Delta P_{go})_t = P_{wt} + \Delta P'_{ow} s_{wt} + \Delta P'_{go} s_{gt} \quad \textit{and}\\
&s_{gt} = -(s_{wt} + s_{ot}) = -(s_{wt} + \frac{n_{ot}}{\rho_o} - \frac{n_o}{C_o \rho_o^2} P_{ot}) = -(s_{wt} + \frac{n_{ot}}{\rho_o} - \frac{n_o}{C_o \rho_o^2}(P_{wt} + \Delta P'_{ow} s_{wt})).
\end{aligned} \tag{5.37}$$

Therefore we have

$$f_2 = (\kappa \rho_w + \frac{s_w \rho_o \rho_g}{C_w}) P_{wt} + \kappa \rho_w \Delta P'_{ow} s_{wt} - \frac{s_g \rho_w \rho_o}{C_g} \Delta P'_{go} s_{wt} - \frac{s_g \rho_w}{C_g} n_{ot}; \tag{5.38}$$

where

$$\kappa = \frac{s_o \rho_g}{C_o} + \frac{s_g \rho_o}{C_g} + \frac{s_g s_o}{C_o C_g}. \tag{5.39}$$

Clearly,

$$s_{wt} = \Big(\frac{n_w}{\rho_w}\Big)_t = \frac{1}{\rho_w} n_{wt} - \frac{m}{\rho_w^2} \rho_{wt} = \frac{1}{\rho_w} n_{wt} - \frac{m}{C_w \rho_w^2} P_{wt}.$$

Consequently,

$$\begin{aligned}
f_2 =& \Big[\kappa \rho_w + \frac{s_w \rho_o \rho_g}{C_w} - \frac{s_w}{C_w}(\kappa \Delta P'_{ow} - \frac{s_g \rho_o}{C_g} \Delta P'_{go})\Big] P_{wt} - (\kappa \Delta P'_{ow} - \frac{s_g \rho_o}{C_g} \Delta P'_{go})(s_w \rho_w u_w)_x\\
&+ \frac{s_g \rho_w}{C_g}(s_o \rho_o u_o)_x - \frac{s_g \rho_w}{C_g} s_o \rho_o Q_p - (\rho_w s_w Q_p - \rho_w Q_{Iw})(\kappa \Delta P'_{ow} - \frac{s_g \rho_o}{C_g} \Delta P'_{go}).
\end{aligned} \tag{5.40}$$

Since that $f_1 = 0$, (5.35) will have the following form:

$$\begin{aligned}
&\Big[\kappa \rho_w + \frac{s_w \rho_o \rho_g}{C_w} - \frac{s_w}{C_w}(\kappa \Delta P'_{ow} - \frac{s_g \rho_o}{C_g} \Delta P'_{go})\Big] P_{wt} + (\rho_o \rho_g + \frac{s_g \rho_o}{C_g} \Delta P'_{go} - \kappa \Delta P'_{ow})(s_w \rho_w u_w)_x\\
&+ (\rho_w \rho_g + \frac{s_g \rho_w}{C_g})(s_o \rho_o u_o)_x + \rho_w \rho_o (s_g \rho_g u_g)_x = \rho_w \rho_o \rho_g (Q_{Iw} + Q_{Ig} - Q_p)/\phi + \frac{s_g \rho_w}{C_g} s_o \rho_o Q_p/\phi +\\
&(\rho_w s_w Q_p/\phi - \rho_w Q_{Iw}/\phi)(\kappa \Delta P'_{ow} + \frac{s_g \rho_o}{C_g} \Delta P'_{go}).
\end{aligned} \tag{5.41}$$

The upper equation can be reformulated to be

$$P_{wt} + \tilde{\eta}_1 (n_w u_w)_x + \tilde{\eta}_2 (n_o u_o)_x + \tilde{\eta}_3 (n_g u_g)_x = \tilde{\eta}_4 Q_p/\phi + \tilde{\eta}_5 Q_{Iw}/\phi + \tilde{\eta}_6 Q_{Ig}/\phi; \tag{5.42}$$

where

$$\begin{aligned}
\eta &= \kappa \rho_w + \frac{s_w \rho_o \rho_g}{C_w} - \frac{s_w}{C_w}(\kappa \Delta P'_{ow} - \frac{s_g \rho_o}{C_g} \Delta P'_{go})\\
\tilde{\eta}_1 &= \frac{1}{\eta}(\rho_o \rho_g + \frac{s_g \rho_o}{C_g} \Delta P'_{go} - \kappa \Delta P'_{ow})\\
\tilde{\eta}_2 &= \frac{1}{\eta}(\rho_w \rho_g + \frac{s_g \rho_w}{C_g})\\
\tilde{\eta}_3 &= \frac{1}{\eta} \rho_w \rho_o\\
\tilde{\eta}_4 &= \frac{1}{\eta}\Big[\frac{s_g \rho_w}{C_g} s_o \rho_o + \rho_w s_w (\kappa \Delta P'_{ow} - \frac{s_g \rho_o}{C_g} \Delta P'_{go}) - \rho_w \rho_o \rho_g\Big]\\
\tilde{\eta}_5 &= \frac{1}{\eta}\Big[\rho_w \rho_o \rho_g - \rho_w (\kappa \Delta P'_{ow} - \frac{s_g \rho_o}{C_g} \Delta P'_{go})\Big]\\
\tilde{\eta}_6 &= \frac{1}{\eta} \rho_w \rho_o \rho_g.
\end{aligned} \tag{5.43}$$

Remark 5.1. *$\Delta P'_{ow}$ is always non-positive and $\Delta P'_{go}$ non-negative.*

Appendix B: Numerical discretization of compressible version

We develop a numerical scheme for this general three-fluid flow model in a 1D setting. The proposed numerical methods are described separately for the compressible (Appendix B) and incompressible (Appendix C) model.

5.1. **A semi-discrete scheme for the compressible model.**

We consider a slight reformulation of the model where we shall make use of the pressure evolution equation (5.42). This will be convenient to account for the highly nonlinear coupling between the mass and momentum equations through the pressure terms. It also makes the discretization of the compressible and incompressible model consistent. The original model takes the form with $(n_w, n_o, n_g, u_w, u_o, u_g)$ as the main variables:

$$\begin{aligned}
(\phi n_w)_t + (\phi n_w u_w)_x &= -n_w Q_p + \rho_w Q_{Iw}, \qquad n_w = s_w \rho_w \\
(\phi n_o)_t + (\phi n_o u_o)_x &= -n_o Q_p, \qquad\qquad\quad\; n_o = s_o \rho_o \\
(\phi n_g)_t + (\phi n_g u_g)_x &= -n_g Q_p + \rho_g Q_{Ig}, \qquad n_g = s_g \rho_g \\
s_w (P_w)_x &= -\hat{k}_w u_w - \hat{k}_{wo}(u_w - u_o) - \hat{k}_{wg}(u_w - u_g) + n_w g + \varepsilon_w (n_w u_{wx})_x, \\
s_o (P_o)_x &= -\hat{k}_o u_o - \hat{k}_{wo}(u_o - u_w) - \hat{k}_{og}(u_o - u_g) + n_o g + \varepsilon_o (n_o u_{ox})_x, \\
s_g (P_g)_x &= -\hat{k}_g u_g - \hat{k}_{wg}(u_g - u_w) - \hat{k}_{og}(u_g - u_o) + n_g g + \varepsilon_g (n_g u_{gx})_x, \\
\Delta P_{ow}(s_w) &= P_o - P_w, \qquad \Delta P_{go}(s_g) = P_g - P_o.
\end{aligned} \tag{5.44}$$

Note that we may rewrite the model in the following equivalent form with $(n_w, n_o, P_w, u_w, u_o, u_g)$ as the main variables

$$\begin{aligned}
(\phi n_w)_t + (\phi n_w u_w)_x &= -n_w Q_p + \rho_w Q_{Iw}, \\
(\phi n_o)_t + (\phi n_o u_o)_x &= -n_o Q_p, \\
P_{wt} + \tilde{\eta}_1 (n_w u_w)_x + \tilde{\eta}_2 (n_o u_o)_x + \tilde{\eta}_3 (n_g u_g)_x &= \tilde{\eta}_4 Q_p/\phi + \tilde{\eta}_5 Q_{Iw}/\phi + \tilde{\eta}_6 Q_{Ig}/\phi, \\
s_w (P_w)_x &= -\hat{k}_w u_w - \hat{k}_{wo}(u_w - u_o) - \hat{k}_{wg}(u_w - u_g) - n_w g + \varepsilon_w (n_w u_{wx})_x, \\
s_o (P_w + \Delta P_{ow})_x &= -\hat{k}_o u_o - \hat{k}_{wo}(u_o - u_w) - \hat{k}_{og}(u_o - u_g) - n_o g + \varepsilon_o (n_o u_{ox})_x, \\
s_g (P_w + \Delta P_{ow} + \Delta P_{go})_x &= -\hat{k}_g u_g - \hat{k}_{wg}(u_g - u_w) - \hat{k}_{og}(u_g - u_o) - n_g g + \varepsilon_g (n_g u_{gx})_x, \\
\Delta P_{ow}(s_w) &= P_o - P_w, \qquad \Delta P_{go}(s_g) = P_g - P_o.
\end{aligned} \tag{5.45}$$

Here n_g is determined by

$$\begin{aligned}
n_g &= s_g \rho_g (P_g) = (1 - s_w - s_o) \rho_g (P_g) \\
&= \Big(1 - \frac{n_w}{\rho_w(P_w)} - \frac{n_o}{\rho_o(P_o)}\Big) \rho_g(P_g) = n_g(n_w, n_o, P_w),
\end{aligned} \tag{5.46}$$

where $P_o = P_o(s_w, P_w) = P_o(n_w, P_w)$ and $P_g = P_g(s_w, s_o, P_w) = P_g(n_w, n_o, P_w)$. We may solve (5.45) on our domain Ω with boundary conditions

$$u_w|_{\partial\Omega} = u_o|_{\partial\Omega} = u_g|_{\partial\Omega} = 0 \tag{5.47}$$

and initial condition

$$\begin{aligned}
n_w(x, t=0) &= n_{w0}(x), \qquad n_o(x, t=0) = n_{o0}(x). \\
n_g(x, t=0) &= n_{g0}(x), \qquad P_w(x=0, t=0) = P_{wL}.
\end{aligned} \tag{5.48}$$

System of ODEs.

We consider the domain $\Omega = [0, 1]$ and introduce a grid of N_x cells with nodes x_j placed at the center of the cells

$$x_1 = \frac{1}{2}\Delta x, \quad x_2 = (1 + \frac{1}{2})\Delta x, \quad \dots, \quad x_j = (j - \frac{1}{2})\Delta x, \quad \dots, \quad x_{N_x} = (N_x - \frac{1}{2})\Delta x$$

and cell interfaces $x_{j+1/2}$ at the cell interfaces

$$x_{1/2}=0, \quad x_{3/2}=\Delta x, \quad \dots, \quad x_{j+1/2}=j\Delta x, \quad \dots, \quad x_{N_x+1/2}=N_x\Delta x=1,$$

where $\Delta x=1/N_x$. We introduce the approximate masses $\{n_{wj}(t)\}_{j=1}^{N_x}$, $\{n_{oj}(t)\}_{j=1}^{N_x}$, and $\{n_{g_j}(t)\}_{j=1}^{N_x}$ associated with the nodes $\{x_j\}_{j=1}^{N_x}$ whereas the approximate velocities $\{u_{w,j+1/2}\}_{j=0}^{N_x}$, $\{u_{o,j+1/2}\}_{j=0}^{N_x}$, and $\{u_{g,j+1/2}\}_{j=0}^{N_x}$ are associated with the cell interfaces $\{x_{j+1/2}\}_{j=0}^{N_x}$.

Step 1: Mass transport.
We solve for $n_{wj}(t)$ by considering the following ODE:
for the water phase,

$$\dot{n}_{w,j}+\frac{1}{\Delta x}([n_wu_w]_{j+1/2}-[n_wu_w]_{j-1/2})=-n_{wj}Q_{p,j}/\phi+\rho_{wj}Q_{Iw,j}/\phi, \qquad n_w=s_w\rho_w \tag{5.49}$$

where

$$[n_wu_w]_{j+1/2}=\begin{cases} n_{wj}u_{w,j+1/2}, & \text{if } u_{w,j+1/2}\geq 0;\\ n_{wj+1}u_{w,j+1/2}, & \text{if } u_{w,j+1/2}<0.\end{cases} \tag{5.50}$$

This can also be expressed as

$$[n_wu_w]_{j+1/2}=\frac{n_{wj}+n_{w,j+1}}{2}u_{w,j+1/2}-\frac{1}{2}(n_{w,j+1}-n_{wj})|u_{w,j+1/2}|$$

for the oil phase,

$$\dot{n}_{o,j}+\frac{1}{\Delta x}([n_ou_o]_{j+1/2}-[n_ou_o]_{j-1/2})=-n_{oj}Q_{p,j}/\phi, \qquad n_o=s_o\rho_o \tag{5.51}$$

where

$$[n_ou_o]_{j+1/2}=\begin{cases} n_{oj}u_{o,j+1/2}, & \text{if } u_{o,j+1/2}\geq 0;\\ n_{oj+1}u_{o,j+1/2}, & \text{if } u_{o,j+1/2}<0.\end{cases} \tag{5.52}$$

Remark 5.2. *It should be pointed out that* $Q_{p,j}=\frac{\overline{Q}_p}{\sigma}$ *and* $Q_{Iw,j}=\frac{\overline{Q}_{Iw}}{\sigma}$ *(where* j *refers to a grid cell which contains a producer/injector) due to the fact that production* Q_p *or injection* Q_{Iw} *in 5.44 is interpreted as a value at a point location. The width of the small region associated with the injector and producer is* $\sigma=\Delta x$ *consistent with* (4.33)*. This also applies for* $Q_{Ig,j}$ *in* (5.53)*, that is to say,* $Q_{Ig,j}=\frac{\overline{Q}_{Ig}}{\sigma}$.

Step 2: Computation of velocities and pressure.
Next, we solve for $P_{w,j}(t)$ and $u_{w,j+1/2}(t)$, $u_{o,j+1/2}(t)$ and $u_{g,j+1/2}(t)$ by considering the following ODE system:

$$\begin{aligned}\dot{P}_{w,j}&+\tilde{\eta}_{1,j}\frac{1}{\Delta x}([n_wu_w]_{j+1/2}-[n_wu_w]_{j-1/2})+\tilde{\eta}_{2,j}\frac{1}{\Delta x}([n_ou_o]_{j+1/2}-[n_ou_o]_{j-1/2})\\ &+\tilde{\eta}_{3,j}\frac{1}{\Delta x}([n_gu_g]_{j+1/2}-[n_gu_g]_{j-1/2})=\tilde{\eta}_{4,j}Q_{p,j}/\phi+\tilde{\eta}_{5,j}Q_{Iw,j}/\phi+\tilde{\eta}_{6,j}Q_{Ig,j}/\phi\end{aligned} \tag{5.53}$$

which is combined with the momentum balance equations

$$
\begin{aligned}
&s_{w,j+1/2}\frac{1}{\Delta x}(P_{w,j+1}-P_{w,j}) = \\
&\qquad\qquad -\hat{k}_{w,j+1/2}u_{w,j+1/2}-\hat{k}_{wo,j+1/2}\Big(u_{w,j+1/2}-u_{o,j+1/2}\Big)-\hat{k}_{wg,j+1/2}\Big(u_{w,j+1/2}-u_{g,j+1/2}\Big)\\
&\quad -gn_{w,j+1/2}+\varepsilon_w\frac{1}{\Delta x^2}\Big(n_{w,j+1}[u_{w,j+3/2}-u_{w,j+1/2}]-n_{w,j}[u_{w,j+1/2}-u_{w,j-1/2}]\Big)\\
&s_{o,j+1/2}\frac{1}{\Delta x}(P_{w,j+1}-P_{w,j}) = -s_{o,j+1/2}\frac{1}{\Delta x}(\Delta P_{ow,j+1}-\Delta P_{ow,j})\\
&\qquad\qquad -\hat{k}_{o,j+1/2}u_{o,j+1/2}-\hat{k}_{wo,j+1/2}\Big(u_{o,j+1/2}-u_{w,j+1/2}\Big)-\hat{k}_{og,j+1/2}\Big(u_{o,j+1/2}-u_{g,j+1/2}\Big)\\
&\quad -gn_{o,j+1/2}+\varepsilon_o\frac{1}{\Delta x^2}\Big(n_{o,j+1}[u_{o,j+3/2}-u_{o,j+1/2}]-n_{o,j}[u_{o,j+1/2}-u_{o,j-1/2}]\Big)\\
&s_{g,j+1/2}\frac{1}{\Delta x}(P_{w,j+1}-P_{w,j}) = -s_{g,j+1/2}\frac{1}{\Delta x}(\Delta P_{ow,j+1}-\Delta P_{ow,j}+\Delta P_{go,j+1}-\Delta P_{go,j})\\
&\qquad\qquad -\hat{k}_{g,j+1/2}u_{g,j+1/2}-\hat{k}_{wg,j+1/2}\Big(u_{g,j+1/2}-u_{w,j+1/2}\Big)-\hat{k}_{og,j+1/2}\Big(u_{g,j+1/2}-u_{o,j+1/2}\Big)\\
&\quad -gc_{g,j+1/2}+\varepsilon_g\frac{1}{\Delta x^2}\Big(c_{g,j+1}[u_{g,j+3/2}-u_{g,j+1/2}]-n_{g,j}[u_{g,j+1/2}-u_{g,j-1/2}]\Big)
\end{aligned}
\tag{5.54}
$$

Here we note that the average $s_{w,j+1/2}$ in (5.54) is based on upwind relatively $u_{w,j+1/2}$

$$
s_{w,j+1/2}=\begin{cases} s_{w,j}, & \text{if } u_{w,j+1/2}>0;\\ \frac{s_{w,j}+s_{w,j+1}}{2}, & \text{if } u_{w,j+1/2}=0;\\ s_{w,j+1}, & \text{if } u_{w,j+1/2}<0.\end{cases}
\tag{5.55}
$$

Similarly, for $s_{o,j+1/2}$, $s_{g,j+1/2}$ and for the interaction terms $\hat{k}_{w,j+1/2}$, $\hat{k}_{o,j+1/2}$ and $\hat{k}_{g,j+1/2}$. For $\hat{k}_{wo,j+1/2}$, $\hat{k}_{og,j+1/2}$ and $\hat{k}_{wg,j+1/2}$ we use the following method:

$$
\hat{k}_{wo,j+1/2}=\begin{cases} \hat{k}_{wo,j}, & \text{if } u_{w,j+1/2}>0\ \&\ u_{o,j+1/2}>0\ ;\\ \frac{\hat{k}_{wo,j}+\hat{k}_{wo,j+1}}{2}, & \text{if } u_{w,j+1/2}u_{o,j+1/2}\le 0;\\ \hat{k}_{wo,j+1}, & \text{if } u_{w,j+1/2}<0\ \&\ u_{o,j+1/2}<0.\end{cases}
\tag{5.56}
$$

$\hat{k}_{wg,j+1/2}$ and $\hat{k}_{og,j+1/2}$ are also approximated using the similar way. On the other hand, $[n_w u_w]_{j+1/2}$, $[n_o u_o]_{j+1/2}$ and $[n_g u_g]_{j+1/2}$ appearing in (5.53) employ upwind as described in (5.50).

Now, we are in a position where we can describe a fully discrete model.

5.2. **A fully discrete scheme.**
We assume that we have given $(n^k_{w,j}, n^k_{o,j}, P^k_{w,j}, u^k_{w,j}, u^k_{o,j}, u^k_{g,j})$. We then compute the approximate solution at time t^{k+1} expressed by $(n^{k+1}_{w,j}, n^{k+1}_{o,j}, P^{k+1}_{w,j}, u^{k+1}_{w,j}, u^{k+1}_{o,j}, u^{k+1}_{g,j})$ as follows:

Step 1: Mass transport.

$$
\frac{n^{k+1}_{w,j}-n^k_{w,j}}{\Delta t}+\frac{1}{\Delta x}([n_w u_w]^k_{j+1/2}-[n_w u_w]^k_{j-1/2}) = -n^k_{w,j}Q^k_{p,j}/\phi+\rho^k_{wj}Q^k_{Iw,j}/\phi
\tag{5.57}
$$

where

$$
[n_w u_w]^k_{j+1/2}=\begin{cases} n^k_{w,j}u^k_{w,j+1/2}, & \text{if } u^k_{w,j+1/2}\ge 0;\\ n^k_{w,j+1}u^k_{w,j+1/2}, & \text{if } u^k_{w,j+1/2}<0.\end{cases}
\tag{5.58}
$$

$$
\frac{n^{k+1}_{o,j}-n^k_{o,j}}{\Delta t}+\frac{1}{\Delta x}([n_o u_o]^k_{j+1/2}-[n_o u_o]^k_{j-1/2}) = -n^k_{o,j}Q^k_{p,j}/\phi
\tag{5.59}
$$

where

$$
[n_o u_o]^k_{j+1/2}=\begin{cases} n^k_{o,j}u^k_{o,j+1/2}, & \text{if } u^k_{w,j+1/2}\ge 0;\\ n^k_{o,j+1}u^k_{o,j+1/2}, & \text{if } u^k_{w,j+1/2}<0.\end{cases}
\tag{5.60}
$$

Having computed $n_{w,j}^{k+1}$ and $n_{o,j}^{k+1}$ we can compute an updated water saturation $s_{w,j}^{k+1/2}$ and $s_{o,j}^{k+1/2}$ given by

$$s_{w,j}^{k+1/2} = \frac{n_{w,j}^{k+1}}{\rho_w(P_{w,j}^k)}, \qquad s_{o,j}^{k+1/2} = \frac{n_{o,j}^{k+1}}{\rho_o(P_{o,j}^{k+1/2})} = \frac{n_{o,j}^{k+1}}{\rho_o(P_{w,j}^k + \Delta P_{ow}(s_{w,j}^{k+1/2}))}. \tag{5.61}$$

Similarly, we compute updated mass $n_{g,j}^{k+1/2}$ and $P_{g,j}^{k+1/2}$ needed to evaluate coefficients in the next step.

Step 2: Computation of velocities and pressure.
Next, we solve simultaneously for $P_{w,j}^{k+1}$ and $u_{w,j+1/2}^{k+1}$, $u_{o,j+1/2}^{k+1}$ and $u_{g,j+1/2}^{k+1}$ by considering the following algebraic system

$$\begin{aligned} \frac{P_{w,j}^{k+1} - P_{w,j}^k}{\Delta t} &+ \tilde{\eta}_{1,j}^{k+1/2} \frac{1}{\Delta x}([n_w^{k+1} u_w^{k+1}]_{j+1/2} - [n_w^{k+1} u_w^{k+1}]_{j-1/2}) + \tilde{\eta}_{2,j}^{k+1/2} \frac{1}{\Delta x}([n_o^{k+1} u_o^{k+1}]_{j+1/2} \\ &- [n_o^{k+1} u_o^{k+1}]_{j-1/2}) + \tilde{\eta}_{3,j}^{k+1/2} \frac{1}{\Delta x}([n_g^{k+1/2} u_g^{k+1}]_{j+1/2} - [n_g^{k+1/2} u_g^{k+1}]_{j-1/2}) = \\ &\tilde{\eta}_{4,j}^{k+1/2} Q_{p,j}^k/\phi + \tilde{\eta}_{5,j}^{k+1/2} Q_{Iw,j}^k/\phi + \tilde{\eta}_{6,j}^{k+1/2} Q_{Ig,j}^k/\phi \end{aligned} \tag{5.62}$$

which is combined with the momentum balance equations

$$\begin{aligned} &s_{w,j+1/2}^{k+1/2} \frac{1}{\Delta x}(P_{w,j+1}^{k+1} - P_{w,j}^{k+1}) = \\ &\qquad -\hat{k}_{w,j+1/2}^{k+1/2} u_{w,j+1/2}^{k+1} - \hat{k}_{wo,j+1/2}^{k+1/2}\Big(u_{w,j+1/2}^{k+1/2} - u_{o,j+1/2}^{k+1/2}\Big) - \hat{k}_{wg,j+1/2}^{k+1/2}\Big(u_{w,j+1/2}^{k+1/2} - u_{g,j+1/2}^{k+1/2}\Big) \\ &\quad -n_{w,j+1/2}^{k+1} g + \varepsilon_w \frac{1}{\Delta x^2}\Big(n_{w,j+1}^{k+1}[u_{w,j+3/2}^{k+1} - u_{w,j+1/2}^{k+1}] - n_{w,j}^{k+1}[u_{w,j+1/2}^{k+1} - u_{w,j-1/2}^{k+1}]\Big) \\ &s_{o,j+1/2}^{k+1/2} \frac{1}{\Delta x}(P_{w,j+1}^{k+1} - P_{w,j}^{k+1}) = -s_{o,j+1/2}^{k+1/2} \frac{1}{\Delta x}(\Delta P_{ow,j+1}^{k+1/2} - \Delta P_{ow,j}^{k+1/2}) \\ &\qquad -\hat{k}_{o,j+1/2}^{k+1/2} u_{o,j+1/2}^{k+1} - \hat{k}_{wo,j+1/2}^{k+1/2}\Big(u_{o,j+1/2}^{k+1} - u_{w,j+1/2}^{k+1}\Big) - \hat{k}_{og,j+1/2}^{k+1/2}\Big(u_{o,j+1/2}^{k+1} - u_{g,j+1/2}^{k+1}\Big) \\ &\quad -n_{o,j+1/2}^{k+1} g + \varepsilon_o \frac{1}{\Delta x^2}\Big(n_{o,j+1}^{k+1/2}[u_{o,j+3/2}^{k+1} - u_{o,j+1/2}^{k+1}] - n_{o,j}^{k+1/2}[u_{o,j+1/2}^{k+1} - u_{o,j-1/2}^{k+1}]\Big) \\ &s_{g,j+1/2}^{k+1/2} \frac{1}{\Delta x}(P_{w,j+1}^{k+1} - P_{w,j}^{k+1}) = -s_{g,j+1/2}^{k+1/2} \frac{1}{\Delta x}(\Delta P_{ow,j+1}^{k+1/2} - \Delta P_{ow,j}^{k+1/2} + \Delta P_{go,j+1}^{k+1/2} - \Delta P_{go,j}^{k+1/2}) \\ &\qquad -\hat{k}_{g,j+1/2}^{k+1/2} u_{g,j+1/2}^{k+1} - \hat{k}_{wg,j+1/2}^{k+1/2}\Big(u_{g,j+1/2}^{k+1} - u_{w,j+1/2}^{k+1}\Big) - \hat{k}_{og,j+1/2}^{k+1/2}\Big(u_{g,j+1/2}^{k+1} - u_{o,j+1/2}^{k+1}\Big) \\ &\quad -n_{g,j+1/2}^{k+1/2} g + \varepsilon_g \frac{1}{\Delta x^2}\Big(n_{g,j+1}^{k+1/2}[u_{g,j+3/2}^{k+1} - u_{g,j+1/2}^{k+1}] - n_{g,j}^{k+1/2}[u_{g,j+1/2}^{k+1} - u_{g,j-1/2}^{k+1}]\Big) \end{aligned} \tag{5.63}$$

Equipped with $(P_{w,j}^{k+1}, u_{w,j+1/2}^{k+1}, u_{o,j+1/2}^{k+1}, u_{g,j+1/2}^{k+1})$ we can now update the saturation

$$s_{w,j}^{k+1} = \frac{n_{w,j}^{k+1}}{\rho_w(P_{w,j}^{k+1})}, \qquad s_{o,j}^{k+1} = \frac{n_{o,j}^{k+1}}{\rho_o(P_{o,j}^{k+1})} = \frac{n_{o,j}^{k+1}}{\rho_o(P_{w,j}^{k+1} + \Delta P_{ow,j}^{k+1}(s_{w,j}^{k+1}))} \tag{5.64}$$

from which we also compute the updated gas mass $n_{g,j}^{k+1}$ via (5.46). If necessary, we may repeat step 2 to improve the accuracy before we proceed to next time level.

Remark 5.3. *The upwind discretization of* $[n_w^{k+1} u_w^{k+1}]_{j+1/2}$, $[n_o^{k+1/2} u_o^{k+1}]_{j+1/2}$ *and* $[n_g^{k+1/2} u_g^{k+1}]_{j+1/2}$ *appearing in* (5.62) *are based on "old" velocities* $u_{w,j+1/2}^k$, $u_{o,j+1/2}^k$ *and* $u_{g,j+1/2}^k$.

APPENDIX C: NUMERICAL DISCRETIZATION OF INCOMPRESSIBLE VERSION

We first describe a semi-discrete approximation of the incompressible version of model (3.11).

5.3. **A semidiscrete scheme for the incompressible model.**
When fluids are incompressible the model (5.45) takes the form

$$\begin{aligned}
(s_w)_t + (s_w u_w)_x &= -s_w Q_p/\phi + Q_{Iw}/\phi, \\
(s_o)_t + (s_o u_o)_x &= -s_o Q_p/\phi, \\
(s_w u_w + s_o u_o + s_g u_g)_x &= -Q_p/\phi + Q_{Iw}/\phi + Q_{Ig}/\phi, \\
s_w (P_w)_x &= -\hat{k}_w u_w - \hat{k}_{wo}(u_w - u_o) - \hat{k}_{wg}(u_w - u_g) + n_w g + \varepsilon_w \rho_w (s_w u_{wx})_x, \\
s_o (P_o)_x &= -\hat{k}_o u_o - \hat{k}_{wo}(u_o - u_w) - \hat{k}_{og}(u_o - u_g) + n_o g + \varepsilon_o \rho_o (s_o u_{ox})_x, \\
s_g (P_g)_x &= -\hat{k}_g u_g - \hat{k}_{wg}(u_g - u_w) - \hat{k}_{og}(u_g - u_o) + n_g g + \varepsilon_g \rho_g (s_g u_{gx})_x, \\
\Delta P_{ow}(s_w) &= P_o - P_w, \qquad \Delta P_{go}(s_g) = P_g - P_o.
\end{aligned} \tag{5.65}$$

Step 1: Mass transport.

$$\dot{s}_{w,j} + \frac{1}{\Delta x}([s_w u_w]_{j+1/2} - [s_w u_w]_{j-1/2}) = -s_{w,j} Q_{p,j}/\phi + Q_{Iw,j}/\phi \tag{5.66}$$

where

$$[s_w u_w]_{j+1/2} = \begin{cases} s_{w,j} u_{w,j+1/2}, & \text{if } u_{w,j+1/2} \geq 0; \\ s_{w,j+1} u_{w,j+1/2}, & \text{if } u_{w,j+1/2} < 0. \end{cases} \tag{5.67}$$

$$\dot{s}_{o,j} + \frac{1}{\Delta x}([s_o u_o]_{j+1/2} - [s_o u_o]_{j-1/2}) = -s_{o,j} Q_{p,j}/\phi \tag{5.68}$$

where

$$[s_o u_o]_{j+1/2} = \begin{cases} s_{o,j} u_{o,j+1/2}, & \text{if } u_{o,j+1/2} \geq 0; \\ s_{o,j+1} u_{o,j+1/2}, & \text{if } u_{o,j+1/2} < 0. \end{cases} \tag{5.69}$$

Step 2: Computation of velocities and pressure.
Next, we solve for $P_{w,j}(t)$ and $u_{w,j+1/2}(t)$, $u_{o,j+1/2}(t)$ and $u_{g,j+1/2}(t)$ by considering the following ODE system:

$$\begin{aligned}
&\frac{1}{\Delta x}([s_w u_w]_{j+1/2} - [s_w u_w]_{j-1/2}) + \frac{1}{\Delta x}([s_o u_o]_{j+1/2} - [s_o u_o]_{j-1/2}) + \frac{1}{\Delta x}([s_g u_g]_{j+1/2} - [s_g u_g]_{j-1/2}) \\
&= Q_{Iw,j}/\phi + Q_{Ig,j}/\phi - Q_{p,j}/\phi
\end{aligned} \tag{5.70}$$

which is combined with the momentum balance equations

$$\begin{aligned}
&s_{w,j+1/2}\frac{1}{\Delta x}(P_{w,j+1}-P_{w,j}) = \\
&\qquad -\hat{k}_{w,j+1/2}u_{w,j+1/2} - \hat{k}_{wo,j+1/2}\Big(u_{w,j+1/2}-u_{o,j+1/2}\Big) - \hat{k}_{wg,j+1/2}\Big(u_{w,j+1/2}-u_{g,j+1/2}\Big) \\
&\quad -gs_{w,j+1/2}\rho_w + \varepsilon_w\frac{\rho_w}{\Delta x^2}\Big(s_{w,j+1}[u_{w,j+3/2}-u_{w,j+1/2}] - s_{w,j}[u_{w,j+1/2}-u_{w,j-1/2}]\Big), \\
&s_{o,j+1/2}\frac{1}{\Delta x}(P_{w,j+1}-P_{w,j}) = -s_{o,j+1/2}\frac{1}{\Delta x}(\Delta P_{ow,j+1}-\Delta P_{ow,j}) \\
&\qquad -\hat{k}_{o,j+1/2}u_{o,j+1/2} - \hat{k}_{wo,j+1/2}\Big(u_{o,j+1/2}-u_{w,j+1/2}\Big) - \hat{k}_{og,j+1/2}\Big(u_{o,j+1/2}-u_{g,j+1/2}\Big) \\
&\quad -gs_{o,j+1/2}\rho_o + \varepsilon_o\frac{\rho_o}{\Delta x^2}\Big(s_{o,j+1}[u_{o,j+3/2}-u_{o,j+1/2}] - s_{o,j}[u_{o,j+1/2}-u_{o,j-1/2}]\Big), \\
&s_{g,j+1/2}\frac{1}{\Delta x}(P_{w,j+1}-P_{w,j}) = -s_{g,j+1/2}\frac{1}{\Delta x}(\Delta P_{ow,j+1}-\Delta P_{ow,j}+\Delta P_{go,j+1}-\Delta P_{go,j}) \\
&\qquad -\hat{k}_{g,j+1/2}u_{g,j+1/2} - \hat{k}_{wg,j+1/2}\Big(u_{g,j+1/2}-u_{w,j+1/2}\Big) - \hat{k}_{og,j+1/2}\Big(u_{g,j+1/2}-u_{o,j+1/2}\Big) \\
&\quad -gs_{g,j+1/2}\rho_g + \varepsilon_g\frac{\rho_g}{\Delta x^2}\Big(s_{g,j+1}[u_{g,j+3/2}-u_{g,j+1/2}] - s_{g,j}[u_{g,j+1/2}-u_{g,j-1/2}]\Big).
\end{aligned} \tag{5.71}$$

Here we note that the average $s_{w,j+1/2}$ in (5.71) is based on upwind relatively $u_{w,j+1/2}$

$$s_{w,j+1/2} = \begin{cases} s_{w,j}, & \text{if } u_{w,j+1/2} > 0; \\ \frac{s_{w,j}+s_{w,j+1}}{2}, & \text{if } u_{w,j+1/2} = 0; \\ s_{w,j+1}, & \text{if } u_{w,j+1/2} < 0. \end{cases} \tag{5.72}$$

Similarly, for $s_{o,j+1/2}$, $s_{g,j+1/2}$ and for the interaction terms $\hat{k}_{w,j+1/2}$, $\hat{k}_{o,j+1/2}$, and $\hat{k}_{g,j+1/2}$. In addition, $\hat{k}_{wo,j+1/2}$ is based on upwind relatively $u_{w,j+1/2}$ and $u_{o,j+1/2}$

$$\hat{k}_{wo,j+1/2} = \begin{cases} \hat{k}_{wo,j}, & \text{if } u_{w,j+1/2} > 0 \ \& \ u_{o,j+1/2} > 0\ ; \\ \frac{\hat{k}_{wo,j}+\hat{k}_{wo,j+1}}{2}, & \text{if } u_{w,j+1/2}u_{o,j+1/2} \le 0; \\ \hat{k}_{wo,j+1}, & \text{if } u_{w,j+1/2} < 0 \ \& \ u_{o,j+1/2} < 0. \end{cases} \tag{5.73}$$

$\hat{k}_{wg,j+1/2}$ and $\hat{k}_{og,j+1/2}$ are also approximated using the similar way. On the other hand, $[s_wu_w]_{j+1/2}$, $[s_ou_o]_{j+1/2}$ and $[s_gu_g]_{j+1/2}$ appearing in (5.70) employ upwind as described in (5.72).

5.4. **A fully discrete scheme for the incompressible model.**

Step 1: Mass transport.

$$\frac{s_{w,j}^{k+1}-s_{w,j}^k}{\Delta t} + \frac{1}{\Delta x}([s_wu_w]_{j+1/2}^k - [s_wu_w]_{j-1/2}^k) = -s_{w,j}^kQ_{p,j}^k/\phi + Q_{Iw,j}^k/\phi \tag{5.74}$$

where

$$[s_wu_w]_{j+1/2}^k = \begin{cases} s_{w,j}^k u_{w,j+1/2}^k, & \text{if } u_{w,j+1/2}^k \ge 0; \\ s_{w,j+1}^k u_{w,j+1/2}^k, & \text{if } u_{w,j+1/2}^k < 0. \end{cases} \tag{5.75}$$

$$\frac{s_{o,j}^{k+1}-s_{o,j}^k}{\Delta t} + \frac{1}{\Delta x}([s_ou_o]_{j+1/2}^k - [s_ou_o]_{j-1/2}^k) = -s_{o,j}^kQ_{p,j}^k/\phi \tag{5.76}$$

where

$$[s_ou_o]_{j+1/2}^k = \begin{cases} s_{o,j}^k u_{o,j+1/2}^k, & \text{if } u_{o,j+1/2}^k \ge 0; \\ s_{o,j+1}^k u_{o,j+1/2}^k, & \text{if } u_{o,j+1/2}^k < 0. \end{cases} \tag{5.77}$$

Having computed $s_{w,j}^{k+1}$ and $s_{o,j}^{k+1}$ we can compute pressure and velocities simultaneously at time level $k+1$.

Step 2: Computation of velocities and pressure.
We solve for $P^{k+1}_{w,j}$ and $u^{k+1}_{w,j+1/2}$, $u^{k+1}_{o,j+1/2}$ and $u^{k+1}_{g,j+1/2}$ by considering the following algebraic system

$$\begin{aligned}&\frac{1}{\Delta x}([s^{k+1}_w u^{k+1}_w]_{j+1/2} - [s^{k+1}_w u^{k+1}_w]_{j-1/2}) + \frac{1}{\Delta x}([s^{k+1}_o u^{k+1}_o]_{j+1/2} - [s^{k+1}_o u^{k+1}_o]_{j-1/2})\\ &+ \frac{1}{\Delta x}([s^{k+1}_g u^{k+1}_g]_{j+1/2} - [s^{k+1}_g u^{k+1}_g]_{j-1/2}) = Q^k_{I,j}/\phi - Q^k_{p,j}/\phi\end{aligned} \tag{5.78}$$

which is combined with the momentum balance equations

$$\begin{aligned}
&s^{k+1/2}_{w,j+1/2}\frac{1}{\Delta x}(P^{k+1}_{w,j+1} - P^{k+1}_{w,j}) =\\
&\qquad -\hat{k}^{k+1/2}_{w,j+1/2}u^{k+1}_{w,j+1/2} - \hat{k}^{k+1/2}_{wo,j+1/2}\Big(u^{k+1/2}_{w,j+1/2} - u^{k+1/2}_{o,j+1/2}\Big) - \hat{k}^{k+1/2}_{wg,j+1/2}\Big(u^{k+1/2}_{w,j+1/2} - u^{k+1/2}_{g,j+1/2}\Big)\\
&\quad -s^{k+1}_{w,j+1/2}\rho_w g + \varepsilon_w\frac{\rho_w}{\Delta x^2}\Big(s^{k+1}_{w,j+1}[u^{k+1}_{w,j+3/2} - u^{k+1}_{w,j+1/2}] - s^{k+1}_{w,j}[u^{k+1}_{w,j+1/2} - u^{k+1}_{w,j-1/2}]\Big)\\
&s^{k+1/2}_{o,j+1/2}\frac{1}{\Delta x}(P^{k+1}_{w,j+1} - P^{k+1}_{w,j}) = -s^{k+1/2}_{o,j+1/2}\frac{1}{\Delta x}(\Delta P^{k+1/2}_{ow,j+1} - \Delta P^{k+1/2}_{ow,j})\\
&\qquad -\hat{k}^{k+1/2}_{o,j+1/2}u^{k+1}_{o,j+1/2} - \hat{k}^{k+1/2}_{wo,j+1/2}\Big(u^{k+1}_{o,j+1/2} - u^{k+1}_{w,j+1/2}\Big) - \hat{k}^{k+1/2}_{og,j+1/2}\Big(u^{k+1}_{o,j+1/2} - u^{k+1}_{g,j+1/2}\Big)\\
&\quad -s^{k+1}_{o,j+1/2}\rho_o g + \varepsilon_o\frac{\rho_o}{\Delta x^2}\Big(s^{k+1/2}_{o,j+1}[u^{k+1}_{o,j+3/2} - u^{k+1}_{o,j+1/2}] - s^{k+1/2}_{o,j}[u^{k+1}_{o,j+1/2} - u^{k+1}_{o,j-1/2}]\Big)\\
&s^{k+1/2}_{g,j+1/2}\frac{1}{\Delta x}(P^{k+1}_{w,j+1} - P^{k+1}_{w,j}) = -s^{k+1/2}_{g,j+1/2}\frac{1}{\Delta x}(\Delta P^{k+1/2}_{ow,j+1} - \Delta P^{k+1/2}_{ow,j} + \Delta P^{k+1/2}_{go,j+1} - \Delta P^{k+1/2}_{go,j})\\
&\qquad -\hat{k}^{k+1/2}_{g,j+1/2}u^{k+1}_{g,j+1/2} - \hat{k}^{k+1/2}_{wg,j+1/2}\Big(u^{k+1}_{g,j+1/2} - u^{k+1}_{w,j+1/2}\Big) - \hat{k}^{k+1/2}_{og,j+1/2}\Big(u^{k+1}_{g,j+1/2} - u^{k+1}_{o,j+1/2}\Big)\\
&\quad -s^{k+1/2}_{g,j+1/2}\rho_g g + \varepsilon_g\frac{\rho_g}{\Delta x^2}\Big(s^{k+1/2}_{g,j+1}[u^{k+1}_{g,j+3/2} - u^{k+1}_{g,j+1/2}] - s^{k+1/2}_{g,j}[u^{k+1}_{g,j+1/2} - u^{k+1}_{g,j-1/2}]\Big)
\end{aligned} \tag{5.79}$$

Remark 5.4. *The upwind discretization of* $[s^{k+1}_w u^{k+1}_w]_{j+1/2}$, $[s^{k+1}_o u^{k+1}_o]_{j+1/2}$ *and* $[s^{k+1}_g u^{k+1}_g]_{j+1/2}$ *appearing in* (5.78) *are based on "old" velocities* $u^k_{w,j+1/2}$, $u^k_{o,j+1/2}$ *and* $u^k_{g,j+1/2}$.

VI

Paper VI

A General Cell-fluid Navier-Stokes Model with Inclusion of Chemotaxis

By:
Qiao, Yangyang
Evje, Steinar

Accepted in:
Mathematical Models and Methods in Applied Sciences.

A GENERAL CELL-FLUID NAVIER-STOKES MODEL WITH INCLUSION OF CHEMOTAXIS

YANGYANG QIAO[1] AND STEINAR EVJE[1,*]

Abstract. The main purpose of this work is to explore a general cell-fluid model which is based on a mixture theory formulation that accounts for the interplay between oxytactically (chemotaxis toward gradient in oxygen) moving bacteria cells in water and the bouyance forces caused by the difference in density between cells and fluid. The model involves two mass balance and two general momentum balance equations, respectively, for the cell and fluid phase, combined with a convection-diffusion-reaction equation for oxygen. In particular, the momentum balance equations include interaction terms which describe the cell-fluid drag force effect. Hence, the model is an extension of the classical Navier-Stokes equation in two different ways: (i) inclusion of two phases (cell and fluid) instead of one; (ii) inclusion of a chemotactic transport mechanism. The model can be understood as a natural generalization of the much studied chemotaxis-Stokes model explored by [Tuval, et al. (2005), PNAS 102]. Assuming that cells and water are incompressible, we explore the nonlinear dynamics inherent in the model in a 2D setting by using an appropriate finite difference scheme. First, we explore the model for parameters in a range which ensures that it lies close to the previously studied chemotaxis-Stokes model (essentially very low cell volume fraction) and where oxygen is available at the water surface. Main observations are (i) formation of sinking finger-shaped plumes and (ii) convergence to plumes that possibly can be stationary (i.e., persist over time). The general cell-fluid model provides new insight into the role played by the cell-fluid interaction term. Formation of falling plumes requires a sufficiently strong cell-fluid interaction such that the difference between cell and water velocity becomes small. A weakening of this term typically implies that the falling plumes will detach from the upper layer. Hence, this term controls the competition between gravity segregation and chemotaxis effect on the formation of cell plumes. Second, we explore the model where assumptions used to derive the chemotaxis-Stokes have been relaxed. In particular, we explore cases with large cell volume fraction (far beyond the regime captured by the chemotaxis-Stokes model), which gives rise to rich pattern-formation behavior. The general cell-fluid model opens for exploring a hierarchy of different ”submodels”. Hence, it seems to be an interesting model for further investigations of various, general cell-fluid spatio-temporal evolution dynamics, both from an experimental and mathematical point of view.

Keywords: two-phase, mixture theory, Navier-Stokes, chemotaxis-Navier Stokes, bioconvection, chemotaxis, finite difference

1. Introduction

1.1. Various cell-fluid phenomena.

Vast numbers of microorganisms are suspended in temperate aqueous environments. Oceans and rivers, puddles and droplets, the fluid interiors of animals, all host an array of splendidly varied creatures [31]. Although their presence is usually not obvious, they constitute the major part of the world's biomass. Microorganisms interact with each other and with the world, at length scales that vary upward from the size of an individual, say 10^{-4} cm, to the dimensions of the entire body of fluid in which they live. Various microorganisms respond to stimuli by swimming (in average) in particular directions. Such phenomena are called taxes. Common examples of taxes of importance are gravitaxis (or geotaxis), a response to gravity or acceleration; phototaxis, a response to light; and chemotaxis, a response to chemical gradients. Responses to shear in the ambient flow are sometimes called rheotaxis. Some bacteria

---

Date: October 29, 2019.

[1] Faculty of Science and Technology, University of Stavanger, NO-4068 Stavanger, Norway
Emails: yangyang.qiao@uis.no, steinar.evje@uis.no.
[*] Corresponding author.

contain magnetic particles (magnetosomes), which cause them to swim along magnetic field lines (magnetotaxis).

Bioconvection is the name given to the process of spontaneous pattern formation in suspensions of upswimming microorganisms. Typically, the cells are denser than the medium they swim in, nevertheless they tend to swim upwards, on average, in still water, and the patterns die away if the cells stop swimming. The cause of the upswimming orientation can be different (gravity-sensing, bottom-heaviness, chemotaxis, phototaxis), but the patterns show great similarities between different species and orientation mechanisms.

Complex bioconvection patterns form when a suspension of the bacterium Bacillus subtilis is placed in a chamber with its upper surface open to the air. These arise because the cells are heavier (approximately 10%) than water, yet, they are able to swim up an oxygen gradient and concentrate in a layer below the water surface, which will undergo Rayleigh-Taylor type instabilities for sufficiently high concentrations. The reason that the cells swim upwards is that they are aerotactic, i.e. they swim up gradients of oxygen, and they consume oxygen. When the vertical density gradient becomes large enough, an overturning instability occurs, analogous to Rayleigh-Bénard convection in a layer of fluid heated from below, which ultimately evolves into the observed patterns [25, 26].

The authors of [25] investigated numerical experiments for both shallow- (< 1 cm deep) and deep-layer (≥ 2 cm deep) chambers assuming the fluid motion is zero. It was found that, for both shallow and deep chambers, a thin boundary layer, densely packed with cells, formed near the surface. Beneath this layer the suspension becomes severely depleted of cells. Furthermore, in the deep chamber cases, a discontinuity in the cell concentration arises between this cell-depleted region and a cell-rich region further below, where no significant oxygen concentration gradients develop before the oxygen is fully consumed. The results obtained from their model are in good qualitative agreement with the experimental observations.

Bacterial chemotaxis, i.e., oriented swimming along chemical gradients, is generally viewed as locomotion in an otherwise quiescent fluid. Yet, the very flagella which propel the cell inevitably stir up the fluid through their high-speed rotation, bundling, and unbundling. Conventional arguments showing the irrelevance of advection compared to diffusion are based on the smallnes of the Peclet number Pe. However, the collective hydrodynamics of concentrated assemblies of cells greatly changes this situation, yielding $Pe > 1$. Such assemblies can arise due to the joint action of chemotaxis, a symmetry breaking source of metabolite(s), and gravity. Once concentrated, the collectively driven hydrodynamics may globally outcompete diffusion.

In [11] striking collective effects were reported in bacterial suspensions in which strong microscale mixing arises from two related aspects of cellular swimming in fluid drops: self-concentration and large-scale dynamic coherence. The first arises from chemotactically generated accumulations of cells that encounter, then slide down a slanted meniscus, resulting in even higher concentrations. Dynamic coherence develops within that nearly close packed population. It appears as jets and surges, straddled by vortices, often moving $> 100\mu$m/s, over scales $> 100\mu$m, yielding $Pe \geq 1$. These speeds and lengths exceed greatly the swimming speeds and size of the organisms.

As another example, the research reported in [7] provided experimental and theoretical insights into a state which exhibited large-scale orientational coherence, analogous to the molecular alignment of nematic liquid crystals, coupled with remarkable spatial and temporal correlations of velocity and vorticity. The appearance of turbulent dynamics in a system which is nominally in the regime of Stokes flow can be understood by accounting for the local energy input by the swimmers.

1.2. **A popular cell-fluid model for low cell density.** Several related coupled chemotaxis-fluid models have been proposed to describe the collective behaviour of a suspension of oxytactic bacteria in an incompressible fluid under the assumptions that the contribution of bacteria to the bacteria-fluid suspension is suffciently small and that more detailed cell-cell interactions (such as hydrodynamic interaction) are neglected [6]. The suspension is considered to be dilute, so that the volume fraction $vV_b \ll 1$ where v is the number density of cells (bacteria) and V_b is the average volume of the cell. Assuming fluid and bacteria are incompressible, the following model has been proposed [40]

$$\begin{aligned} & v_t + \mathbf{u} \cdot \nabla v + \chi \nabla \cdot (v r(C) \nabla C) = D_v \Delta v \\ & \rho(\mathbf{u}_t + \mathbf{u} \cdot \nabla \mathbf{u}) + \nabla p = v \nabla \mathbf{\Phi} + \eta \Delta \mathbf{u}, \qquad \nabla \cdot \mathbf{u} = 0 \\ & C_t + \mathbf{u} \cdot \nabla C = D_C \Delta C - \kappa v r(C). \end{aligned} \tag{1.1}$$

The first equation of (1.1) describes the mass balance equation for the bacteria v subject to an internal interplay between a fluid-driven advection effect through $\mathbf{u} \cdot \nabla v$, chemotaxis toward higher concentration of oxygen C via $\nabla \cdot (nr(C) \nabla C)$, and diffusive spreading of bacteria in the fluid through $D_v \Delta v$. Herein, C is the concentration of oxygen, $\mathbf{u}$ is the velocity field of a fluid which is governed by the incompressible Navier-Stokes equations with density ρ, pressure p and viscosity η, as expressed by $(1.1)_2$. Moreover, in the fluid momentum balance equation of $(1.1)_2$, the term $\nabla \mathbf{\Phi} = V_b g(\rho_b - \rho)\mathbf{e}_y$ describes the gravitational force exerted by a bacterium onto the fluid along the downwards unit vector $\mathbf{e}_y$ proportional to the volume of the bacterium V_b with density ρ_b where ρ_b is slightly higher than the fluid density ρ. This formulation relies on the the Boussinesq approximation in which the density variations caused by bacteria appear only through the buoyant forcing $\nabla \mathbf{\Phi}$. A dimensionless cut-off function $r(C)$ models an inactivity threshold of the bacteria due to low oxygen supply. Experiments suggest that the cut-off function can be modelled by a step function $r(C) = H(C - C^*)$ [40] where $H(\cdot)$ denotes the Heaviside function. The parameters χ and κ control the magnitude of chemotaxis and consumption of oxygen, respectively, whereas D_v and D_C are diffusion constants.

Simulation results.
Various numerical schemes have been proposed to solve (1.1). Tuval et al. conducted experiments with Bacillus subtilis in a drop with meniscus geometry and investigated the corresponding mathematical model (1.1) consisting of oxygen diffusion and consumption, chemotaxis, and viscous fluid dynamics by using a finite element-based method [40]. The vortex was showned to advectively enhance uptake of oxygen into the suspension, and the wedge geometry led to a singularity in the chemotactic dynamics near the contact line. Chertock et al. [6] explored a high-resolution vorticity-based hybrid finite volume/finite difference scheme. The scheme was used to demonstrate formation of sinking plumes, possible merging of neighbouring plumes, and convergence towards numerically stable stationary plumes. In [9] the authors made use of a previously developed upwind finite element method to solve the chemotaxis-diffusion-convection system. Three regimes were emphasized: First, a spatial layered structure is created. Bacteria agglomerate in the upper stack layer, thus forming a depletion layer, where the bacterial density is very low. Subsequently, bacterial convection strengthens with time and instabilities in the stack layer appear. Finally, plumes of bacterial falling in the fluid are generated. The authors of [27] studied numerically the nonlinear dynamics of the 3D version of (1.1). An operator splitting-type Navier-Stokes solver was used to avoid a too strong restriction on the time step. They presented numerical examples showing the formation of falling bacterial plumes out of random initial data and the convergence towards stationary bacterial plumes.

Mathematical analysis.
The interest for the model (1.1) has also triggered mathematicians to explore more fundamental issues related to the well-posedness and stability properties of this model. We refer to [47] for an instructive overview of different mathematical results. Here we briefly mention some examples of such work. Local-in-time weak solutions have been obtained for a boundary-value problem of (1.1) in the three-dimensional setting [28]. Global existence was shown in Duan et al. [13, 10] for small initial concentrations of the oxygen C and without the convection term in the $\mathbf{u}$-equation, that is, for the Stokes equation instead of the Navier-Stokes equation, which is a reasonable simplification for the expected low Reynolds number flow. See also [39] for existence result with porous media-type nonlinear diffusion. In addition, [48] showed that for all reasonably regular initial data, a corresponding initial-boundary value problem for the Stokes model possesses a globally defined

Variable	Description
α_c,α_w	volume fraction of cell, fluid
ρ_c,ρ_w	cell density, fluid density
n,m	cell mass, fluid mass
$\mathbf{u}_c$,$\mathbf{u}_w$	cell velocity, fluid velocity
C	oxygen concentration
P_c, P_w	cell pressure, fluid pressure
ΔP, Λ	cell-cell stress, chemotactic stress
ε_c,ε_w	effective viscosity cell, fluid
$\hat{\zeta}$	cell-fluid interaction coefficient (drag force)
K	consumption rate (oxygen)
D_C	diffusion coefficient (oxygen)

Table 1: Nomenclature description for model (1.2)

weak solution. [46] showed that for the system (1.1) suitable regularity assumptions on the initial data entail the following: If $N = 2$, then the full chemotaxis-Navier–Stokes system admits a unique global classical solution. If $N = 3$, then the simplified chemotaxis-Stokes system (Stokes) possesses at least one global weak solution. Furthermore, in [47] (see also [50]) a first stabilization type of result was obtained showing that the solution in a two-dimensional chemotaxis-Navier-Stokes system stabilizes to the spatially uniform equilibrium when time goes infinitely. The result obtained in [49] indicates that under certain boundary conditions, the possibly destabilizing action of chemotactic cross-diffusion in (1.1) does not substantially affect the regularity properties of the fluid flow, at least on large time scales. Moreover, [38] investigated an incompressible chemotaxis-Navier-Stokes system with slow p-Laplacian diffusion for (1.1).

1.3. **A general cell-fluid model.**

It is of interest to study a general cell-fluid model which naturally can represent the model (1.1) as a special case. Hence, we shall in the following describe such a model by relying on a mixture theory multiphase formulation. In the multiphase modeling framework, the cell-fluid environment is considered as a mixture of two interacting continua [2, 35, 12, 36, 33]. The cellular phase comprises cells represented by a volume fraction α_c moving with a velocity $\mathbf{u}_c$ and the fluid phase represented by the volume fraction α_w moving with a velocity $\mathbf{u}_w$. The model takes the following form (see Table 1 for the different variables):

$$\begin{aligned}
n_t + \nabla\cdot(n\mathbf{u}_c) &= 0, \qquad\qquad n = \alpha_c\rho_c\\
m_t + \nabla\cdot(m\mathbf{u}_w) &= 0, \qquad\qquad m = \alpha_w\rho_w\\
(n\mathbf{u}_c)_t + \nabla\cdot(n\mathbf{u}_c\otimes\mathbf{u}_c) + \alpha_c\nabla P_c &= \hat{\zeta}(\mathbf{u}_w-\mathbf{u}_c) + n\mathbf{g} + \varepsilon_c\nabla\cdot(n(\nabla\mathbf{u}_c+\nabla\mathbf{u}_c^T))\\
(m\mathbf{u}_w)_t + \nabla\cdot(m\mathbf{u}_w\otimes\mathbf{u}_w) + \alpha_w\nabla P_w &= \hat{\zeta}(\mathbf{u}_c-\mathbf{u}_w) + m\mathbf{g} + \varepsilon_w\nabla\cdot(m(\nabla\mathbf{u}_w+\nabla\mathbf{u}_w^T))\\
C_t + \nabla\cdot(C\mathbf{u}_w) &= \nabla\cdot(D_C\nabla C) - K\alpha_c C.
\end{aligned} \tag{1.2}$$

The two first equations describe mass balance of the cell and fluid phase, respectively. The entire volume is occupied by the two phases, i.e.,

$$\alpha_c + \alpha_w = 1. \tag{1.3}$$

The next two equations in (1.2) are the corresponding momentum balance equations. The cell momentum equation $(1.2)_3$ accounts for two migration mechanisms: (i) diffusive migration towards a lower volume fraction of cells α_c; (ii) chemotactic migration towards a region with higher concentration of oxygen C. This is achieved by letting the cell phase pressure P_c feel additional stress due to cell-cell interaction through a term $\Delta P(\alpha_c)$ as well as a chemotaxis-related stress $\Lambda(C)$ through the relation

$$P_c = P_w + \Delta P(\alpha_c) + \Lambda(C). \tag{1.4}$$

This means that the stress P_c associated with the cells differs from the fluid pressure P_w because of the cell-cell stress term $\Delta P(\alpha_c)$ and the chemotaxis stress term $\Lambda(C)$ and will trigger cells to move in order to even out this pressure difference. We shall use the increasing function

$$\Delta P(\alpha_c) = P_c^* \ln(\alpha_c) + R^* \tag{1.5}$$

for some positive constant $P_c^* > 0$ and R^* with unit Pa. Note that ΔP plays the same role as capillary pressure in a more classical fluid-mechanical setting where P_c^* is then associated with the surface tension. The ability of the cancer cells to generate motion towards a positive gradient in C (chemotaxis) is expressed through $\Lambda(C)$ here set to be the decreasing function

$$\Lambda(C) = \Lambda_0 - \Lambda_1 C, \tag{1.6}$$

where Λ_0, Λ_1 are constant parameters with units Pa. Moreover, there is also a drag force between the cell phase and the fluid. This effect is accounted for through the cell-fluid interaction term $\pm\hat{\zeta}(\mathbf{u}_w - \mathbf{u}_c)$, see $(1.2)_{3,4}$ where

$$\hat{\zeta} = I\hat{k}\alpha_w \alpha_c^{1+r_{cw}}, \quad \hat{k} > 0, \quad r_{cw} \geq 0, \tag{1.7}$$

where I ($\mathrm{Pa}\cdot\mathrm{s/m^2}$) remains to be determined as well as the dimensionless $\hat{k}$ and r_{cw}. We shall in this work set $\hat{k} = 1$ and $r_{cw} = 0$.

The viscous stress terms with constant coefficients $\varepsilon_c, \varepsilon_w$ (kinematic viscosity) represent internal viscous effects associated with the cell and fluid phase, respectively. Finally, the gravity effect is accounted for through the terms that involve $\mathbf{g} = g\mathbf{e}_y = (0, g)$ where the y-axis is directed downward and g is the gravity constant. Finally, we may use linear density-pressure relations of the following form for compressible phases

$$\rho_w - \tilde{\rho}_{w0} = \frac{P_w}{C_w}, \qquad \rho_c - \tilde{\rho}_{c0} = \frac{P_c}{C_c} \tag{1.8}$$

where $\tilde{\rho}_{w0}, C_w$ and $\tilde{\rho}_{g0}, C_g$ are known constants. Hence, C_w, C_c represent bulk modulus (inverse of compressibility) which is a constant that describes how resistant a substance is to compression. For incompressible phases C_w, C_c tend to infinity which implies that $\rho_w = \tilde{\rho}_{w0}$ and $\rho_c = \tilde{\rho}_{c0}$.

For some applications with low Reynolds number (which expresses the ratio of intertia to viscosity) it may not be so relevant to include the acceleration terms (intertia terms) in the momentum balance which gives us the Stokes like model

$$\begin{aligned}
(\alpha_c\rho_c)_t + \nabla\cdot(\alpha_c\rho_c\mathbf{u}_c) &= 0, \qquad\qquad n = \alpha_c\rho_c \\
(\alpha_w\rho_w)_t + \nabla\cdot(\alpha_w\rho_w\mathbf{u}_w) &= 0, \qquad\qquad m = \alpha_w\rho_w \\
\alpha_c\nabla P_c &= \hat{\zeta}(\mathbf{u}_w - \mathbf{u}_c) + n\mathbf{g} + \varepsilon_c\nabla\cdot(n(\nabla\mathbf{u}_c + \nabla\mathbf{u}_c^T)) \\
\alpha_w\nabla P_w &= \hat{\zeta}(\mathbf{u}_c - \mathbf{u}_w) + m\mathbf{g} + \varepsilon_w\nabla\cdot(m(\nabla\mathbf{u}_w + \nabla\mathbf{u}_w^T)) \\
C_t + \nabla\cdot(C\mathbf{u}_w) &= \nabla\cdot(D_C\nabla C) - K\alpha_c C.
\end{aligned} \tag{1.9}$$

Remark 1.1. *The motivation for the choice of the potential functions $\Delta P(\alpha_c)$ in* (1.5)*, $\Lambda(C)$ in* (1.6)*, and the cell-fluid interaction term $\hat{\zeta}$ in* (1.7)*, is to establish a link between the simplified model* (1.1) *and the general cell-fluid models* (1.2) *and* (1.9)*. More details are given in Section 2.*

Remark 1.2. *Regarding the momentum balance laws in* (1.9) *it is similar to what has been used by Wolgemuth to study collective swimming of bacterium immersed in a fluid which may lead to complex flow caused by the interaction and feedback between the bacteria and the fluid. In* [51] *a two-phase model for the collective swimming of dense colonies of bacteria was developed which also treats the fluid and bacteria as independent, interpenetrating continuum phases. By introducing an entropically driven tendency for the bacteria to align, similar to nematic liquid crystals, the model could reproduce coherent structures and density fluctuations in a bacterial bath. The model explains turbulent flows in terms of the dipole stress that the bacteria exert on the fluid, entropic elasticity due to the rod shape of each bacterium, and the torque on the bacteria due to fluid gradients.*

1.4. **Main objective of this work.** The main objective of the current work is to provide some insight into basic mechanisms of the general model (1.2), which in different ways represents a generalization of the chemotaxis-Stokes model (1.1). In particular, our investigations are along the following lines:

- We discuss a reduced version of the model (1.2), similar to (1.9), where we can recover the link to the model (1.1) and where we can explicitly express the competition between gravity and chemotaxis.
- We consider a discrete finite difference scheme for the general cell-fluid model (1.2) in 2D where the cell and fluid phase are assumed incompressible. It is demonstrated numerically that the scheme possesses good properties like ability to preserve positivity of the cell volume fraction, is able to give non-oscillatory behavior, and can naturally be extended to include compressible phases.
- We provide 2D simulation results both for (i) low cell density where simulation results can be related to those of (1.1); (ii) high cell density where the assumptions used to derive (1.1) are relaxed and new and different behavior is seen. In particular, we highlight the essential role played by the strength of the cell-fluid interaction term $\hat{\zeta}$ given by (1.7) and determined through the parameter I. This parameter controls to what extent the cell-fluid dynamics is dominated by co-current flow where cell and fluid velocity are essentially equal or the cell-fluid behavior is more decoupled which gives room for a larger discrepancy between the cell and water velocity field.

The model (1.2) is a two-phase Navier-Stokes type of model as described by $(1.2)_{1-4}$, where the cell phase has been equipped with a chemotactic mechanism such that cells will swim towards a higher concentration in C (oxygen). The oxygen is in turn distributed by an advection-diffusion-reaction equation as given by $(1.2)_5$. Hence, the model is an extension of the classical Navier-Stokes equations in two respects: (i) extension from one phase to two phases; (ii) inclusion of a chemotactic transport mechanism.

Model (1.2) **viewed in the larger context.**

Mathematical analysis of compressible two-phase models that represent (in one or another way) an extension of the mono-phase Navier-Stokes equations, has caught the interest of different researchers more recently. Such models appear naturally in the context of various engineering-focused applications that involve a (more or less) complex interplay between several fluid phases. For example, in [14] the motivation was a gas-liquid model that can be used to explore gas-kick scenarios (i.e., uncontrolled gas-liquid flow in a one-dimensional wellbore due to sudden influx of compressed gas from the surrounding reservoir) in the context of wellbore operations. The model is based on considering one momentum equation for the mixture and therefore involves a mixture velocity of the two phases. By including an algebraic relation that describes the difference between this mixture velocity and one of the phase velocities, one can study flow regimes where the two phases flow with different velocities. A related work that focused on how to control the circulation of gas and liquid is found in [16]. A natural and highly relevant extension is to include interaction between two-phase flow in the 1D wellbore and the surrounding reservoir [15, 37]. Other gas-liquid models have been studied in a 1D setting where the two fluids can move with different velocities, which is needed for more realistic scenarios. Such models have been designed to be consistent with lab experiments, typically carried out in a one-dimensional setting. For attempts to analyse such engineering-motivated models we refer to [17, 18].

On the other hand, from a more theoretical point of view, there is a desire to take techniques and methods applied in the study of the compressible, multidimensional mono-fluid compressible Navier-Stokes equations, over to the context of multiphase Navier-Stokes models [29, 52]. An interesting recent study of a one-velocity two-phase model, obtained by summing the two momentum equations (Stokes equations) and assuming that one of the phases is largely dispersed in the other and therfore moves with the same velocity, is found in [5]. This approach is also taken in [53, 24] where the full momentum equations are used but subject to the one-velocity assumption. Recent interesting results on global existence of weak solutions by relying on an energy estimate only combined with refined compensated compactness arguments can be found in [42, 30, 45].

A fundamental restriction seems to be the use of a common fluid velocity and a common momentum balance equation. The more general two-fluid model represented by $(1.2)_{1-4}$ involves non-conservative pressure terms and make the analysis challenging. For a seminal first work in this direction, see [3, 4]. Interesting readers may also consult [22] where a stability analysis was carried out and the role of capillary pressure (i.e., use of non-equal pressure) was explored.

A more recent direction is adaption and extension of two-phase Stokes-like equations similar to (1.9) for the study of aggressive cancer cell migration mechanisms where fluid flow plays a role. A general cancer cell-fluid model was explored by numerical simulations in [19]. Then, motivated by experimental findings of fluid-sensitive migration mechanisms as reviewed in [23] a cell-fluid model was formulated in [43]. In [44] the model was further developed to shed light on the striking competition between two different fluid-sensitive migration mechanisms reported in [32]. Further investigations were done to illustrate how these two competing migration mechanisms possibly could be used to enable clusters of cancer cells to break loose from the primary tumor [20]. Mathematical analysis of such models seems rare. One small step in that direction is found in [21] where a one-dimensional cell-fluid model similar to (1.9) was studied. Existence and stability was obtained subject to appropriate constraints on initial data and model parameters. The link between the reduced model (1.9) (when phases are assumed incompressible) and the chemotaxis-Stokes model (1.1) may suggest that there is room for an interesting exchange of ideas and techniques used in previous studies of (1.1) like [47, 50] but now in the context of the formulation (1.9).

The rest of this work is organized as follows: In Section 2 we explore the inviscid, incompressible version of the model (1.9) which allows us to relate the model (1.2) and (1.1). In Section 3 we explore further the 1D version of (1.9) and suggest a finite difference scheme. In Section 4 we describe a finite difference scheme for the full 2D model (1.2). Section 5 is devoted to numerical investigations to obtain insight into the nonlinear cell-fluid dynamics captured by this model and explore similarities and differences relatively the chemotaxis-Stokes model (1.1).

2. A REDUCED MODEL: INCOMPRESSIBLE, INVISCID PHASES

The purpose of this section is to obtain more insight into the competing cell migration mechanisms that are present in the general model (1.2). We also are interested in the relation between this model and the simplified and more specific model (1.1). For that purpose we start by taking a closer look at the model (1.9).

2.1. **On the reduced version** (1.9).

We assume (i) incompressible fluids, i.e., ρ_c, ρ_w are constants; (ii) viscosity terms are ignored, i.e., $\varepsilon_c = \varepsilon_w = 0$; (iii) intertial terms are ignored (low Reynolds number assumption). This allows us to derive an explicit expression for the interstitial cell velocity $\mathbf{u}_c$ which reflects the competition between different migration mechanisms. From (1.9) we directly obtain the following form

$$\begin{aligned}
&(\alpha_c)_t + \nabla\cdot(\alpha_c \mathbf{u}_c) = 0, \\
&(\alpha_w)_t + \nabla\cdot(\alpha_w \mathbf{u}_w) = 0, \\
&\alpha_c \nabla(P_w + \Delta P(\alpha_c) + \Lambda(C)) = +\hat{\zeta}(\mathbf{u}_w - \mathbf{u}_c) + n\mathbf{g}, \qquad n = \alpha_c\rho_c \\
&\alpha_w \nabla P_w = -\hat{\zeta}(\mathbf{u}_w - \mathbf{u}_c) + m\mathbf{g}, \qquad m = \alpha_w \rho_w \\
&C_t + \nabla\cdot(C\mathbf{u}_w) = \nabla\cdot(D_C\nabla C) - K\alpha_c C.
\end{aligned} \tag{2.10}$$

The model may be combined with the boundary conditions

$$\mathbf{u}_c|_{\partial\Omega} = 0, \qquad \mathbf{u}_w|_{\partial\Omega} = 0, \qquad \frac{\partial}{\partial\nu}C|_{\partial\Omega} = 0, \qquad t > 0 \tag{2.11}$$

where ν is the outward normal on $\partial\nu$. Corresponding initial data are

$$\alpha_c(\mathbf{x}, t=0) = \alpha_{c0}(\mathbf{x}), \qquad C(\mathbf{x}, t=0) = C_0(\mathbf{x}). \tag{2.12}$$

From the two momentum equations $(2.10)_{3,4}$ we can find explicit expressions for the cell and fluid velocity, respectively, $\mathbf{u}_c$ and $\mathbf{u}_w$. The following expressions are found:

$$\begin{aligned}\alpha_c\mathbf{u}_c &= [\mathbf{U}_T\alpha_c + \hat{h}(\alpha_c)\mathbf{g}\Delta\rho] - \hat{h}(\alpha_c)\nabla(\Delta P(\alpha_c) + \Lambda(C))\\ \alpha_w\mathbf{u}_w &= [\mathbf{U}_T\alpha_w - \hat{h}(\alpha_c)\mathbf{g}\Delta\rho] + \hat{h}(\alpha_c)\nabla(\Delta P(\alpha_c) + \Lambda(C))\end{aligned} \tag{2.13}$$

with

$$\hat{h}(\alpha_c) \overset{\text{def}}{:=} \frac{\alpha_c^2\alpha_w^2}{\hat{\zeta}}, \qquad \mathbf{U}_T = \alpha_c\mathbf{u}_c + \alpha_w\mathbf{u}_w \overset{\text{def}}{:=} \mathbf{U}_c + \mathbf{U}_w. \tag{2.14}$$

First, we observe from $(2.10)_4$ that

$$\frac{\alpha_w^2}{\hat{\zeta}}\nabla P_w - \frac{m\alpha_w}{\hat{\zeta}}\mathbf{g} = -\mathbf{U}_w + \alpha_w\mathbf{u}_c = \mathbf{u}_c - \mathbf{U}_T. \tag{2.15}$$

By summing $(2.10)_3$ and $(2.10)_4$ we find

$$\nabla P_w = -\alpha_c\nabla(\Delta P) - \alpha_c\nabla\Lambda + (n+m)\mathbf{g}. \tag{2.16}$$

Combining (2.15) and (2.16) and using (1.3), it follows that

$$\mathbf{u}_c = \mathbf{U}_T + \frac{\alpha_w^2}{\hat{\zeta}}\nabla P_w - \frac{m\alpha_w}{\hat{\zeta}}\mathbf{g} = \mathbf{U}_T - \frac{\alpha_w^2\alpha_c}{\hat{\zeta}}[\nabla(\Delta P) + \nabla\Lambda] + \frac{\alpha_w^2\alpha_c}{\hat{\zeta}}\mathbf{g}\Delta\rho \tag{2.17}$$

with $\Delta\rho = \rho_c - \rho_w$, from which $(2.13)_1$ follows. The expression $(2.13)_2$ follows from (2.14). The model (2.10) then can be written in the following rewritten form:

$$\begin{aligned}&(\alpha_c)_t + \nabla\cdot(\alpha_c\mathbf{u}_c) = 0\\ &\nabla\cdot(\alpha_c\mathbf{u}_c + \alpha_w\mathbf{u}_w) = 0\\ &\alpha_c\alpha_w\nabla(\Delta P(\alpha_c) + \Lambda(C)) = \hat{\zeta}(\mathbf{u}_w - \mathbf{u}_c) + \alpha_c\alpha_w\Delta\rho\mathbf{g}\\ &\nabla P_w + \alpha_c\nabla(\Delta P(\alpha_c) + \Lambda(C)) = (n+m)\mathbf{g}\\ &C_t + \nabla\cdot(C\mathbf{u}_w) = \nabla\cdot(D_C\nabla C) - K\alpha_c C\end{aligned} \tag{2.18}$$

where $\alpha_c\mathbf{u}_c$ is given by $(2.13)_1$. Note that $(2.18)_2$ follows by adding the two continuity equations in (2.10) and applying (1.3). Moreover, $(2.18)_3$ has been obtained by multiplying $(2.10)_{3,4}$, respectively, by α_w and α_c and subtracting. Finally, $(2.18)_4$ is nothing but (2.16). From the cell mass balance equation $(2.18)_1$ combined with $(2.13)_1$ we see that cell migration velocity $\mathbf{U}_c = \alpha_c\mathbf{u}_c$ is composed of three transport components:
(i) a convective term $\nabla\cdot(\mathbf{U}_T\alpha_c + \hat{h}(\alpha_c)\mathbf{g}\Delta\rho)$ which is related to bouyance and gravity segregation;
(ii) a diffusive spreading mechanism $-\nabla\cdot(\hat{h}(\alpha_c)\nabla(\Delta P(\alpha_c)))$;
(iii) a chemotaxis transport represented by $-\nabla\cdot(\hat{h}(\alpha_c)\nabla(\Lambda(C)))$.

Remark 2.1. *Models similar to* (2.10)*, however, in the context of porous media flow, have been proposed and explored more recently in the study of cancer cell migration mechanisms that are sensitive to fluid flow. This implies that there are additional interaction terms, respectively, of the form* $-\hat{\zeta}_c\mathbf{u}_c$ *included in* $(2.10)_3$ *and* $-\hat{\zeta}_w\mathbf{u}_w$ *in* $(2.10)_4$ *to account for the fluid-matrix and cell-matrix resistance force. We refer to* [19, 43, 44, 20, 41] *for examples of this activity. A main advantage of this formulation is the ability to clearly visualize the competition that takes place between different migration mechanisms which possibly makes the overall behavior complex* [23].

2.2. **On the relation between the cell-fluid model** (2.18) **and** (1.1)**.** Combining $(2.13)_1$ and $(2.18)_{1,2}$ we can write (2.18) in the following form in order to see more clearly the link to the chemotaxis-Stokes model (1.1).

$$\begin{aligned}&(\alpha_c)_t + \mathbf{U}_T\cdot\nabla\alpha_c + \mathbf{g}\Delta\rho\cdot\nabla\hat{h}(\alpha_c) = \nabla\cdot(\hat{h}(\alpha_c)\Delta P'(\alpha_c)\nabla\alpha_c) + \nabla\cdot(\hat{h}(\alpha_c)\Lambda'(C)\nabla C),\\ &\nabla P_w + \alpha_c\nabla(\Delta P(\alpha_c) + \Lambda(C)) = (n+m)\mathbf{g}, \qquad \nabla\cdot\mathbf{U}_T = 0\\ &C_t + \nabla\cdot(C\mathbf{u}_w) = \nabla\cdot(D_C\nabla C) - K\alpha_c C.\end{aligned} \tag{2.19}$$

Under the assumption $\alpha_c \ll 1$ (i.e., $\alpha_w \approx 1$) we may use
(i) $\mathbf{U}_T \approx \mathbf{u}_w$ (see (2.14));
(ii) $\Delta\rho\mathbf{g} \ll \nabla(\Delta P(\alpha_c)+\Lambda(C))$ (gravity segregation is weak relatively diffusion and chemtaxis);
(iii) $\alpha_c\nabla(\Delta P(\alpha_c)+\Lambda(C)) \ll (n+m)\mathbf{g} = \rho_w\mathbf{g}+\alpha_c\Delta\rho\mathbf{g}$ (using that $\alpha_c \approx 0$ and $\Delta\rho = \rho_c-\rho_w$).

From this, it follows that (2.19) simplifies to

$$\begin{aligned}
&(\alpha_c)_t + \mathbf{u}_w\cdot\nabla\alpha_c = \nabla\cdot(\hat{h}(\alpha_c)\Delta P'(\alpha_c)\nabla\alpha_c) + \nabla\cdot(\hat{h}(\alpha_c)\Lambda'(C)\nabla C)\\
&\nabla P_w = (n+m)\mathbf{g}, \qquad \nabla\cdot\mathbf{u}_w = 0\\
&C_t + \mathbf{u}_w\cdot\nabla C = \nabla\cdot(D_C\nabla C) - K\alpha_c C.
\end{aligned} \tag{2.20}$$

Note that the third equation of (2.18), when combined with the definition of $\hat{h}$ given by (2.14), leads to (since $\alpha_w \approx 1$)

$$\begin{aligned}
\alpha_c\mathbf{u}_c &= \alpha_c\mathbf{u}_w - \frac{\alpha_c^2\alpha_w}{\hat{\zeta}}\nabla(\Delta P+\Lambda(C)) + \frac{\alpha_c^2\alpha_w}{\hat{\zeta}}\Delta\rho\mathbf{g}\\
&= \alpha_c\mathbf{u}_w - \frac{\hat{h}}{\alpha_w}\nabla(\Delta P+\Lambda(C)) + \frac{\hat{h}}{\alpha_w}\Delta\rho\mathbf{g} \approx \alpha_c\mathbf{u}_w - \hat{h}\nabla(\Delta P+\Lambda(C)) + \hat{h}\Delta\rho\mathbf{g}.
\end{aligned}$$

Using assumption (ii), we see that this expression for the cell velocity $\alpha_c\mathbf{u}_c$, when combined with $(2.18)_1$, leads to $(2.20)_1$. Consequently, $(2.18)_3$ can be ignored since it does not contain any information not already taken care of by $(2.18)_1$. We may introduce the pressure $p = P_w - \rho_w g y$ where y is the height such that $\nabla y = (0,1)$ and $\mathbf{g} = (0,g)$. Then we see that $(2.20)_2$ can be written as

$$\nabla p = \nabla(P_w - \rho_w g y) = \nabla P_w - \rho_w\mathbf{g} = (\alpha_c\rho_c + \alpha_w\rho_w)\mathbf{g} - (\alpha_c+\alpha_w)\rho_w\mathbf{g} = \alpha_c\Delta\rho\mathbf{g},$$

with $\Delta\rho = \rho_c - \rho_w$. This is the steady state, inviscid version of the momentum balance equation

$$\rho_w(\partial_t\mathbf{u}_w + \mathbf{u}_w\cdot\nabla\mathbf{u}_w) + \nabla p = \alpha_c\Delta\rho\mathbf{g} + \eta\Delta\mathbf{u}_w, \tag{2.21}$$

where we have ignored the inertia term $\rho_w(\partial_t\mathbf{u}_w + \mathbf{u}_w\cdot\nabla\mathbf{u}_w)$ and viscosity $\eta\Delta\mathbf{u}_w$. The full momentum equation (2.21) amounts to the momentum equation in $(1.1)_2$. Hence, the model (2.20) where the momentum balance in the second line is replaced by the momentum equation (2.21), coincides with the chemotaxis-Stokes model (1.1) by an appropriate choice of the interaction coefficient $\hat{\zeta}$ involved in $\hat{h}(\alpha_c)$, as given by (2.14), and by using the correlations (1.5) and (1.6) to define $\Delta P(\alpha_c)$ and $\Lambda(C)$ with suitable constant parameters.

Remark 2.2. *The above heuristic and direct analysis brings forth some natural questions:*
(i) Can our full model (1.2) *reproduce the behavior as previously demonstrated for the chemotaxis-Stokes model* (1.1) *when $\alpha_c \ll 1$ (see for example* [6]*) and thereby justify the simplifying assumptions behind the derivation of the chemotaxis-Stokes model?*
(ii) What is the behavior predicted by the model (1.2) *when we allow α_c to increase?*

3. A 1D MODEL AND ITS DISCRETE VERSION

We now focus on the 1D version of the model (2.10). A main purpose is to gain some insight into the principles we apply when we shall develop a numerical scheme for the full model (1.2). The model takes the form

$$\begin{aligned}
(\alpha_c)_t + (\alpha_c u_c)_x &= 0, && n = \alpha_c\rho_c\\
(\alpha_w)_t + (\alpha_w u_w)_x &= 0, && m = \alpha_w\rho_w\\
\alpha_c P_{wx} + \alpha_c(\Delta P(\alpha_c)+\Lambda(C))_x &= +\hat{\zeta}(u_w - u_c) + ng\\
\alpha_w P_{wx} &= -\hat{\zeta}(u_w - u_c) + mg\\
C_t + (Cu_w)_x &= (D_C C_x)_x - K\alpha_c C, && x \in \Omega = (0,L)
\end{aligned} \tag{3.22}$$

after having ignored the viscosity terms in the momentum equations and assumed constant density ρ_w, ρ_c for both fluid and cell phase. The model is combined with the boundary conditions

$$u_c|_{x=0,L} = 0, \qquad u_w|_{x=0,L} = 0, \qquad C|_{x=0} = C^*, \qquad t > 0 \tag{3.23}$$

with a known concentration C^* and initial data are

$$\alpha_c(x, t = 0) = \alpha_{c0}(x), \qquad C(x, t = 0) = C_0(x), \qquad x \in \Omega = (0, L). \tag{3.24}$$

It is clear, in view of the previous section, that (3.22) can be rewritten as

$$\begin{aligned} &(\alpha_c)_t + (\alpha_c u_c)_x = 0 \\ &C_t + (C u_w)_x = (D_C C_x)_x - K\alpha_c C. \end{aligned} \tag{3.25}$$

More precisely, summing the two momentum equations in $(3.22)_{3,4}$, we get

$$P_{wx} = \frac{1}{\alpha_c + \alpha_w}(m+n)g - \frac{\alpha_c}{\alpha_c + \alpha_w}[\Delta P + \Lambda(C)]_x. \tag{3.26}$$

Inserting (3.26) into $(3.22)_3$ and using that $U_T = \alpha_w u_w + \alpha_c u_c$, we have

$$\frac{\alpha_c}{\alpha_c + \alpha_w}(m+n)g - \frac{\alpha_c^2}{\alpha_c + \alpha_w}[\Delta P + \Lambda]_x + \alpha_c[\Delta P + \Lambda]_x = \hat{\zeta}\big(\frac{U_T - \alpha_c u_c}{\alpha_w} - u_c\big) + ng. \tag{3.27}$$

Therefore, the explicit expression for the cell velocity u_c is

$$u_c = \frac{U_T}{\alpha_c + \alpha_w} + \hat{g}(\alpha_c, \alpha_w)\Delta\rho g - \hat{g}(\alpha_c, \alpha_w)[\Delta P(\alpha_c) + \Lambda(C)]_x \tag{3.28}$$

with

$$\hat{g}(\alpha_c, \alpha_w) = \frac{\alpha_c \alpha_w^2}{\hat{\zeta}(\alpha_c + \alpha_w)^2}. \tag{3.29}$$

Again, using $U_T = \alpha_w u_w + \alpha_c u_c$, we get the corresponding velocity of water phase

$$u_w = \frac{U_T - \alpha_c u_c}{\alpha_w} = \frac{-\alpha_c u_c}{\alpha_w}, \tag{3.30}$$

where we have used that $U_{Tx} = 0$ from summing the two first equations of (3.22), which implies that $U_T = 0$ due to the boundary condition (3.23).

Remark 3.1. *In light of* (3.28) *and the fact that* $\alpha_c + \alpha_w = 1$, *it follows that* (3.25) *can be written as*

$$\begin{aligned} &(\alpha_c)_t + f(\alpha_c)_x = P_c^*(\hat{g}(\alpha_c)\alpha_{cx})_x - \Lambda_1(\hat{h}(\alpha_c)C_x)_x \\ &C_t + (C u_w)_x = (D_C C_x)_x - K\alpha_c C. \end{aligned} \tag{3.31}$$

Herein we have used the expressions for ΔP, Λ, *and* $\hat{\zeta}$ *as given by* (1.5), (1.6), *and* (1.7), *with* $\hat{k} = 1$ *and* $r_{cw} = 0$, *where*

$$f(\alpha_c) = \hat{h}(\alpha_c)\Delta\rho g, \qquad \hat{g}(\alpha_c) = \frac{1 - \alpha_c}{I}, \qquad \hat{h}(\alpha_c) = \frac{\alpha_c^2 \alpha_w^2}{\hat{\zeta}} = \frac{\alpha_c(1 - \alpha_c)}{I} \tag{3.32}$$

and fluid velocity u_w *is given by* (3.30). *Note that* P_c^*, Λ_1, *and* I *are constant positive parameters. This model is an example of a taxis-diffusion equation (represented by* $(3.31)_1$*) which also contains a nonlinear, advective flux term through* $f(\alpha_c)_x$. *Such models are widely studied in the context of biological populations and are known to react to external stimuli and form aggregates (pattern formation). It is known that it might be challenging for numerical schemes to preserve the fundamental properties of the solutions like energy dissipation, steady states, positivity, and conservation of total mass* [1].

We now describe a discretization of this model but based on the original form (3.22) instead of the rewritten form (3.31). First, we rewrite (3.22) as

$$\begin{aligned} (\alpha_c)_t + (\alpha_c u_c)_x &= 0 \\ C_t + (C u_w)_x &= (D_C C_x)_x - K\alpha_c C \\ (\alpha_c u_c + \alpha_w u_w)_x &= 0 \\ \alpha_c P_{wx} + \alpha_c(\Delta P(\alpha_c) + \Lambda(C))_x &= +\hat{\zeta}(u_w - u_c) + ng \\ \alpha_w P_{wx} &= -\hat{\zeta}(u_w - u_c) + mg. \end{aligned} \tag{3.33}$$

We consider the domain $\Omega = [0, L]$ with $L = 1$ and introduce a grid of N_x cells with nodes x_j placed at the center of the cells

$$x_1 = \frac{1}{2}\Delta x, \quad x_2 = (1 + \frac{1}{2})\Delta x, \quad \dots, \quad x_j = (j - \frac{1}{2})\Delta x, \quad \dots, \quad x_{N_x} = (N_x - \frac{1}{2})\Delta x$$

and cell interfaces $x_{j+1/2}$ at the cell interfaces

$$x_{1/2} = 0, \quad x_{3/2} = \Delta x, \quad \dots, \quad x_{j+1/2} = j\Delta x, \quad \dots, \quad x_{N_x+1/2} = N_x \Delta x = 1,$$

where $\Delta x = 1/N_x$. We introduce the approximate cell fraction and oxygen concentration $\{\alpha_{cj}(t)\}_{j=1}^{N_x}$ and $\{C_j(t)\}_{j=1}^{N_x}$ and fluid pressure $\{P_{wj}(t)\}_{j=1}^{N_x}$ associated with the nodes $\{x_j\}_{j=1}^{N_x}$ whereas the approximate velocities $\{u_{w,j+1/2}\}_{j=0}^{N_x}$ and $\{u_{c,j+1/2}\}_{j=0}^{N_x}$ are associated with the cell interfaces $\{x_{j+1/2}\}_{j=0}^{N_x}$.

In the following we describe the fully discrete scheme of (3.33). Then we also will see how it can be interpreted as a discretization of (3.31). We assume that we know $\alpha^k_{c,j}$, C^k_j, $P^k_{w,j}$, $u^k_{c,j+1/2}$, and $u^k_{w,j+1/2}$ associated with time level t^k. We now describe how to compute these variables at the new time level t^{k+1}:

Step 1: Mass transport.

First, we solve for $\alpha^{k+1}_{c,j}$ and C^{k+1}_j by considering the following discrete schemes for $(3.33)_{1,2}$:

$$\frac{\alpha^{k+1}_{cj} - \alpha^k_{cj}}{\Delta t} + \frac{1}{\Delta x}([\alpha_c u_c]^k_{j+1/2} - [\alpha_c u_c]^k_{j-1/2}) = 0, \tag{3.34}$$

where

$$[\alpha_c u_c]^k_{j+1/2} = \begin{cases} \alpha^k_{c,j} u^k_{c,j+1/2}, & \text{if } u^k_{c,j+1/2} \geq 0; \\ \alpha^k_{c,j+1} u^k_{c,j+1/2}, & \text{if } u^k_{c,j+1/2} < 0. \end{cases} \tag{3.35}$$

and

$$\frac{C^{k+1}_j - C^k_j}{\Delta t} + \frac{1}{\Delta x}([C u_w]^k_{j+1/2} - [C u_w]^k_{j-1/2}) = \frac{D_C}{\Delta x}\Big[\frac{C^k_{j+1} - C^k_j}{\Delta x} - \frac{C^k_j - C^k_{j-1}}{\Delta x}\Big] - K\alpha^k_{c,j} C^k_j, \tag{3.36}$$

where

$$[C u_w]^k_{j+1/2} = \begin{cases} C^k_j u^k_{w,j+1/2}, & \text{if } u^k_{w,j+1/2} \geq 0; \\ C^k_{j+1} u^k_{w,j+1/2}, & \text{if } u^k_{w,j+1/2} < 0. \end{cases} \tag{3.37}$$

Step 2: Computation of velocities $u^{k+1}_{c,j+1/2}$, $u^{k+1}_{w,j+1/2}$ and fluid pressure $P^{k+1}_{w,j}$.

Next, we consider the following dicrete version of $(3.33)_{3,4,5}$ where we use that $(3.33)_3$ amounts to $U_T = 0$:

$$\begin{aligned} u^{k+1}_{w,j+1/2}\alpha^{k+1}_{w,j+1/2} + \alpha^{k+1}_{c,j+1/2} u^{k+1}_{c,j+1/2} &= U^{k+1}_{T,j+1/2} = 0 \\ \alpha^{k+1}_{c,j+1/2}\frac{1}{\Delta x}(P^{k+1}_{c,j+1} - P^{k+1}_{c,j}) &= +\hat{\zeta}^{k+1}_{j+1/2}(u^{k+1}_{w,j+1/2} - u^{k+1}_{c,j+1/2}) + n^{k+1}_{j+1/2} g, \\ \alpha^{k+1}_{w,j+1/2}\frac{1}{\Delta x}(P^{k+1}_{w,j+1} - P^{k+1}_{w,j}) &= -\hat{\zeta}^{k+1}_{j+1/2}(u^{k+1}_{w,j+1/2} - u^{k+1}_{c,j+1/2}) + m^{k+1}_{j+1/2} g. \end{aligned} \tag{3.38}$$

where

$$\alpha_{c,j+1/2}^{k+1} = \begin{cases} \alpha_{c,j}^{k+1}, & \text{if } u_{c,j+1/2}^{k} > 0; \\ \frac{\alpha_{c,j}^{k+1}+\alpha_{c,j+1}^{k+1}}{2}, & \text{if } u_{c,j+1/2}^{k} = 0; \\ \alpha_{c,j+1}^{k+1}, & \text{if } u_{c,j+1/2}^{k} < 0. \end{cases} \tag{3.39}$$

Similarly, $\alpha_{w,j+1/2}^{k+1}$ is based on upwind relatively the "old" fluid velocity $u_{w,j+1/2}^{k}$.

$$\alpha_{w,j+1/2}^{k+1} = \begin{cases} \alpha_{w,j}^{k+1}, & \text{if } u_{w,j+1/2}^{k} > 0; \\ \frac{\alpha_{w,j}^{k+1}+\alpha_{w,j+1}^{k+1}}{2}, & \text{if } u_{w,j+1/2}^{k} = 0; \\ \alpha_{w,j+1}^{k+1}, & \text{if } u_{w,j+1/2}^{k} < 0. \end{cases} \tag{3.40}$$

Note that $n_{j+1/2}^{k+1}$ and $m_{j+1/2}^{k+1}$ follow from this since densities ρ_c, ρ_w are constant. Similarly, for the interaction coefficient

$$\hat{\zeta}_{j+1/2}^{k+1} = \begin{cases} \hat{\zeta}_{j}^{k+1}, & \text{if } u_{w,j+1/2}^{k} > 0 \ \& \ u_{c,j+1/2}^{k} > 0; \\ \frac{\hat{\zeta}_{j}^{k+1}+\hat{\zeta}_{j+1}^{k+1}}{2}, & \text{if } u_{w,j+1/2}^{k} u_{c,j+1/2}^{k} \leq 0; \\ \hat{\zeta}_{j+1}^{k+1}, & \text{if } u_{w,j+1/2}^{k} < 0 \ \& \ u_{c,j+1/2}^{k} < 0. \end{cases} \tag{3.41}$$

Clearly, we have from (1.4) that $P_{c,j}^{k+1} = P_{w,j}^{k+1} + [\Delta P(\alpha_{c,j}^{k+1}) + \Lambda(C_j^{k+1})]$. Hence, from $(3.38)_{2,3}$ we get (after a summation)

$$D_+ P_{w,j}^{k+1} = \frac{[n_{j+1/2}^{k+1} + m_{j+1/2}^{k+1}]g}{[\alpha_{c,j+1/2}^{k+1} + \alpha_{w,j+1/2}^{k+1}]} - \frac{\alpha_{c,j+1/2}^{k+1}}{[\alpha_{c,j+1/2}^{k+1} + \alpha_{w,j+1/2}^{k+1}]} D_+[\Delta P(\alpha_{c,j}^{k+1}) + \Lambda(C_j^{k+1})] \tag{3.42}$$

where $D_+ a_j = \frac{1}{\Delta x}(a_{j+1} - a_j)$. Note that (3.42) is the discrete counterpart of (3.26). Obviously, we can now plug this expression for $D_+ P_{w,j}^{k+1}$ back in $(3.38)_2$ and compute an expression for $u_{c,j+1/2}^{k+1}$ (after having used $(3.38)_1$) which amounts to a discrete version of (3.28). Finally, we then obtain $u_{w,j+1/2}^{k+1}$ from $(3.38)_1$ as well as $P_{w,j}^{k+1}$ from (3.42).

Remark 3.2. *The above discretization has been explored for various two-phase and three-pase models (both incompressible and compressible versions) but without chemotaxis effect. We refer to* [34]*. The advantage is that this approach can be extended to solve the full model* (1.2)*. An interesting question for possible future investigations is whether this approach will give rise to discrete schemes that can be analyzed by methods as described in* [1] *(and references therein). In other words, does the numerical scheme preserve fundamental properties related to energy dissipation, steady states, positivity, and conservation of total mass?*

4. On the discretization of the full 2D model (1.2)

We now write the general cell-fluid model (1.2) in component form for a 2D domain with $\mathbf{x} = (x, y) \in \Omega$ where y is the downward unit vector in vertical direction and with velocity fields $\mathbf{u}_c = (u_c^x, u_c^y)$ and $\mathbf{u}_w = (u_w^x, u_w^y)$. In the following we focus on the incompressible version. The equations have been slightly reordered motivated by the discretization method that is used:

$$
\begin{aligned}
&(\alpha_c)_t + (\alpha_c u^x_c)_x + (\alpha_c u^y_c)_y = 0\\
&C_t + (C u^x_w)_x + (C u^y_w)_y = (D_C C^x_x)_x + (D_C C^y_x)_y - K\alpha_c C\\
&(\alpha_c u^x_c)_x + (\alpha_c u^y_c)_y + (\alpha_w u^x_w)_x + (\alpha_w u^y_w)_y = 0\\
&(m u^x_w)_t + (m u^x_w u^x_w)_x + (m u^x_w u^y_w)_y + \alpha_w P_{wx}\\
&\qquad\qquad = -\hat{\zeta}(u^x_w - u^x_c) + m g^x + 2\varepsilon_w (m u^x_{wx})_x + \varepsilon_w (m u^y_{wx})_y + \varepsilon_w (m u^x_{wy})_y\\
&(n u^x_c)_t + (n u^x_c u^x_c)_x + (n u^x_c u^y_c)_y + \alpha_c P_{cx}\\
&\qquad\qquad = +\hat{\zeta}(u^x_w - u^x_c) + n g^x + 2\varepsilon_c (n u^x_{cx})_x + \varepsilon_c (n u^y_{cx})_y + \varepsilon_c (n u^x_{cy})_y\\
&(m u^y_w)_t + (m u^y_w u^y_w)_y + (m u^x_w u^y_w)_x + \alpha_w P_{wy}\\
&\qquad\qquad = -\hat{\zeta}(u^y_w - u^y_c) + m g^y + 2\varepsilon_w (m u^y_{wy})_y + \varepsilon_w (m u^x_{wy})_x + \varepsilon_w (m u^y_{wx})_x\\
&(n u^y_c)_t + (n u^y_c u^y_c)_y + (n u^x_c u^y_c)_x + \alpha_c P_{cy}\\
&\qquad\qquad = +\hat{\zeta}(u^y_w - u^y_c) + n g^y + 2\varepsilon_c (n u^y_{cy})_y + \varepsilon_c (n u^x_{cy})_x + \varepsilon_c (n u^y_{cx})_x.
\end{aligned}
\tag{4.43}
$$

We refer to Appendix A for a description of the numerical scheme. It follows directly along the lines of the discretization of the 1D model presented in Section 3. In the next section focus is on how to set parameters to establish the relevant connection between (1.1) and (4.43). Then we carry out a number of simulations to explore to what extent the model (4.43) may give similar behavior as reported for the model (1.1). We also identify new type of behavior caused by terms which have been ignored in (1.1).

5. Numerical Investigations

5.1. **Scaling and input data.** In the following we follow the approach of [6] applied for the model (1.1) to determine how to set parameters in the more general model (4.43) such that we can expect to see numerical simulation results that are comparable. We denote by L_y a characteristic length (for instance, L_y to be the height of the 2D domain) and the characteristic cell density by v_r. Rescalling the dimensionless variables according to Tuval et al. [40, 6] defined by

$$
\mathbf{x}' := \frac{\mathbf{x}}{L_y}, \qquad t' := \frac{D_v}{L_y^2} t, \qquad c' := \frac{c}{c_{air}}, \qquad v' := \frac{v}{v_r}, \qquad p' := \frac{L_y^2}{\eta D_v} p, \qquad \mathbf{u}' := \frac{L_y}{D_v}\mathbf{u} \tag{5.44}
$$

leading to five relevant dimensionless parameters: α, β, γ, δ and Schmidt number Sc given by

$$
\alpha := \frac{\chi c_{air}}{D_v}, \qquad \beta := \frac{\kappa v_r L_y^2}{c_{air} D_v}, \qquad \gamma := \frac{V_b v_r g(\rho_b - \rho) L_y^3}{\eta D_v}, \qquad \delta := \frac{D_C}{D_v}, \qquad Sc := \frac{\eta}{D_v \rho}. \tag{5.45}
$$

Note that $\rho = \rho_w$ where ρ is used in (1.1) to represent water density while ρ_w is used in (1.2). Similarly, $\rho_b = \rho_c$ where ρ_b is used in (1.1) to represent the cell density whereas ρ_c is used in the formulation (1.2). These parameters characterise the system (1.1) in the following vorticity formulation [6] after dropping the prime notation in the rescaled variables:

$$
\begin{aligned}
&v_t + \nabla\cdot(\mathbf{u}v) + \alpha\nabla\cdot(v r(c)\nabla c) = \Delta v\\
&\omega_t + \nabla\cdot(\mathbf{u}\omega) = Sc\Delta\omega - \gamma Sc v_x\\
&c_t + \nabla\cdot(\mathbf{u}c) = \delta\Delta c - \beta v r(c)\\
&\Delta\psi = -\omega,
\end{aligned}
\tag{5.46}
$$

with $\mathbf{x} = (x,y)^T$, $\mathbf{u} = (u^x, u^y)^T$ and the vorticity $\omega := u^y_x - u^x_y$, the stream-function ψ where $u^x = \psi_y$ and $u^y = -\psi_x$. Below more information will be given pertaining to the quantities c_{air} and v_r.

We want to compare the reduced version of (1.9) expressed by (2.20) and (2.21) with the chemotaxis-Stokes model (1.1). We recall from (2.14) that

$$
\hat{h}(\alpha_c) = \frac{\alpha_c^2 \alpha_w^2}{\hat{\zeta}} = \frac{\alpha_c(1-\alpha_c)}{I} \approx \frac{\alpha_c}{I}
$$

for $\alpha_w \approx 1$ where we have used $\hat{k} = 1$ and $r_{cw} = 1$. Combined with $(2.20)_1$, which takes the form

$$(\alpha_c)_t + \mathbf{u}_w \cdot \nabla \alpha_c = \nabla \cdot (\hat{h}(\alpha_c) \Delta P'(\alpha_c) \nabla \alpha_c) + \nabla \cdot (\hat{h}(\alpha_c) \Lambda'(C) \nabla C),$$

we get in light of (1.5) and (1.6) that

$$(\alpha_c)_t + \mathbf{u}_w \cdot \nabla \alpha_c = \frac{P_c^*}{I} \Delta \alpha_c - \frac{\Lambda_1}{I} \nabla \cdot (\alpha_c \nabla C). \tag{5.47}$$

We may compare this directly to $(1.1)_1$. In particular, we can link the input parameters for our model to those used in [40, 6], as expressed by (5.45). In particular, the following relations are found

$$\frac{\Lambda_1}{I} = \chi, \qquad \frac{P_c^*}{I} = D_v. \tag{5.48}$$

For example, knowing η, $\rho = \rho_w$, $\rho_b = \rho_c$, L_y, V_b, and c_{air} as specified in Table 2 as input data for model (1.1), we can then deduce the different input parameters we need for (1.2) (i.e., P_c^* and Λ_1) from specified values of the dimensionless variables α, β, γ, δ, and Sc as follows:

- Given the value of Sc, from (5.45) we see that $D_v = \frac{\eta}{\rho_w Sc}$ and in light of (5.48) we can determine P_c^* from $P_c^* = D_v I$;
- Given the value of δ, we have $D_C = \delta D_v$;
- Given the value of α, we have $\chi = \frac{\alpha D_v}{c_{air}}$ and we can determine Λ_1 from $\Lambda_1 = \chi I$ according to (5.48);
- Given the value of γ, we find the reference cell density $v_r = \frac{\gamma \eta D_v}{V_b g (\rho_b - \rho) L_y^3}$;
- Given the value of β, we find the oxygen consumption rate κ from $\kappa = \frac{c_{air} D_v \beta}{v_r L_y^2}$.

See Table 3 for an example how we can derive the different parameters (right column) we need for a simulation based on the given dimensional numbers α, β, γ, δ, and Sc (left column) for model (1.2). However, we note that there is an additional degree of freedom represented through the cell-fluid drag force parameter I. If I is set to be large, the fluid-cell drag force effect largely implies that fluid and cell flow together. The additional parameter I may also indicate that there is not a unique, direct correspondance between choice of parameters set for model (1.1) and those used in (1.2) as certain effects are contained in the latter model which are ignored in the first. As I controls the cell-fluid drag force effect, essentially this term also controls the balance between gravity segregation and chemotaxis. The segregation effect between the cells and water is not accounted for in (1.1). The role played by the choice of I will be further explored in the subsequent numerical simulations.

Parameter	Dimensional Value	Parameter	Dimensional Value
T	10 min	$\varepsilon_w, \varepsilon_c$	$1 * 10^{-6}$ m^2/s
$L_x \times L_y$	6×1 mm	R^*	100 Pa
$\tilde{\rho}_{w0} = \rho = \rho_w$	1 g/cm^3	Λ_0	0 Pa
$\tilde{\rho}_{c0} = \rho_c = \rho_b$	1.1 g/cm^3	r_{cw}	0 -
$N_x \times N_y$	240×40	$\hat{k}$	1 -
c_{air}	1.5×10^{23}		
η	10^{-3} kg/(m $\cdot$ s)		
V_b	10^{-18} m^3		

Table 2: Reference input parameters in the simulations. Left column: The first 6 parameters are used in both model (1.1) and (1.2). The two last (η and V_b) are for model (1.1). Right column: Parameters used in model (1.2).

Initial and boundary data.
We use mixed boundary conditions as considered in [6]. The boundary condition at the top $\partial\Omega_{top}$ describes the fluid-air surface, where there is no cell flux. The oxygen shall be saturated with the

air oxygen concentration c_{air} and the vertical fluid and cell velocity u_w^y and u_c^y, as well as the tangential fluid and cell stress, are assumed zero [40, 26].

$$C = c_{air}, \quad u_c^y = 0 = u_w^y, \qquad \forall (x,y) \in \partial\Omega_{top}. \tag{5.49}$$

The other boundaries with no-flow condition for the system are illustrated in Fig. 1.

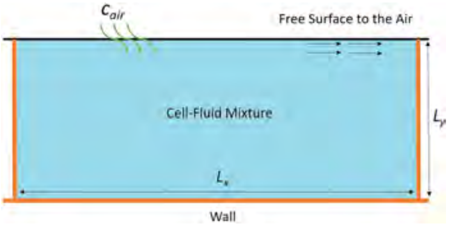

Figure 1: Boundary conditions for the system of (1.1). The air–water interface, where the oxygen concentration is equal to that of air, is not crossed by bacteria; the fluid and cell vertical velocity components equal zero and the fluid and cells are assumed to be free of tangential stress. The container walls are impermeable to bacteria and oxygen.

Input Data.
The input parameters used in the simulations are listed in Table 2. We use 240 × 40 grids for a domain corresponding to $L_x = 6$ mm and $L_y = 1$ mm. It should be also mentioned that once the oxygen concentration C is lower than $C^* = 0.3c_{air}$, chemotaxis comes to a halt and oxygen consumption rate is set to zero. This mechanism is built into the model (1.1) through the use of the step-like function $r(C)$. For the model (1.2) a step function is introduced associated with (1.6) (assuming $\Lambda_0 = 0$) in the following way:

$$\Lambda(C) = -\Lambda_1 \int_0^C r(s)ds = \begin{cases} -\Lambda_1(C - C^*), & \text{if } C \geq C^*; \\ 0, & \text{if } C < C^*. \end{cases} \tag{5.50}$$

This ensures that $\Lambda'(C) = -\Lambda_1 r(C)$ which will make our model $(2.20)_1$ consistent with the model $(1.1)_1$ since (5.47) now is replaced by

$$(\alpha_c)_t + \mathbf{u}_w \cdot \nabla\alpha_c = \frac{P_c^*}{I}\Delta\alpha_c - \frac{\Lambda_1}{I}\nabla \cdot (\alpha_c r(C)\nabla C). \tag{5.51}$$

Similarly, we also replace the consumption term $-K\alpha_c C$ in $(1.2)_5$ by $-K\alpha_c r(C)$ to mimic $(1.1)_3$.

5.2. **Results.**
We use the fact that cell volume fraction α_c used in (1.2) is related to the cell density v in (1.1) by $\alpha_c = vV_b$. Note that when we show plots of the cell volume fraction α_c it has been scaled relatively $\alpha_{c,r} = v_r V_b$ where v_r is given through the dimensionless number γ as specified in (5.45). The relation between the consumption rate κ in $(1.1)_2$ and K in $(1.2)_5$ is $K = \kappa/V_b$. The spatial domain has been scaled according to (5.44) such that the dimensionless size is $\Omega = 6 \times 1$.

Example - 1D. For the one-dimensional case, we consider the model in vertical direction with $Y = 0$ as top and $Y = 1$ as bottom and input data can be referred to Table 3. Initial condition is given by:

$$\alpha_{c0}(y) = \begin{cases} v_r V_b, & y > 0.5; \\ 0.5 v_r V_b, & \text{otherwise.} \end{cases}, \qquad C_0(y) = c_{air}. \tag{5.52}$$

The simulation result is shown in Fig. 2 and we refer to the figure text for further comments.

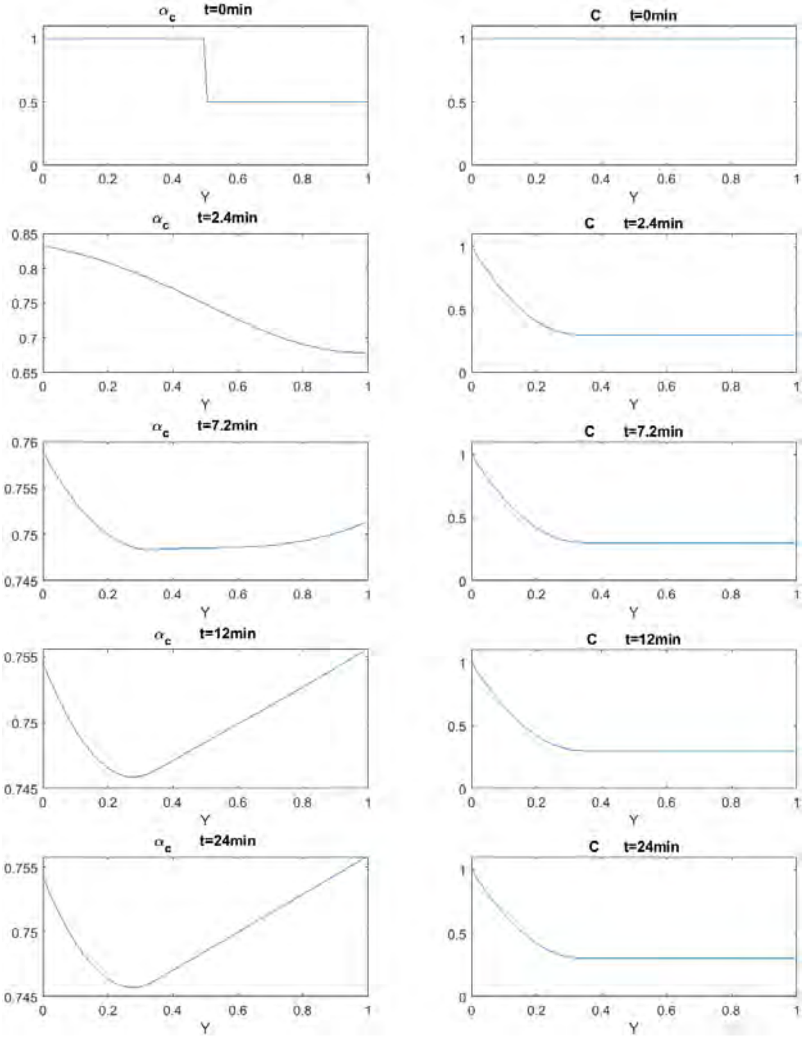

Figure 2: Cells α_c (left column) consume oxygen C (right column) such that the oxygen concentration is reduced to the limit value $C^* = 0.3$ in the lower part (right column). Since the outside air continues feeding oxygen into the system at $Y = 0$, a stable gradient of oxygen concentration is formed. Due to the gravitational and capillary effect, cells move towards the bottom as seen after a time $t = 2.4$ (left column). Gradually, a higher amount of cells will accumulate at the bottom. The cell volume fraction α_c decreases higher up before it increases again because the chemotactic swimming leads cells to the surface. See profiles after times $t = 12$ and $t = 24$ min which result from the force balance between chemotaxis and gravity.

Examples - 2D.
The final time of 2D simulations is $T = 10$ min. To highlight and color the plumes better we follow [6] and use $\min\{\frac{\alpha_c}{v_r V_b}, 1\}$ to plot α_c, which means that all large values $\frac{\alpha_c}{v_r V_b} > 1$ near the surface are drawn equally red. The initial condition is set as follows:

$$\alpha_{c0}(x,y) = \begin{cases} v_r V_b, & y > 0.499 - 0.02\sin((x-1.5)\pi); \\ 0.5 v_r V_b, & \text{otherwise.} \end{cases}, \qquad C_0(x,y) = c_{air}. \tag{5.53}$$

This is similar to examples studied in [6]. The initial perturbation of the cell volume fraction at the interface between the upper (high volume fraction) and lower region (low volume fraction) will trigger development of plumes.

Parameter	Value	Parameter	Value
Sc	1000	$D_v(=\frac{\eta}{Sc\rho_w})$	$1 * 10^{-9}$
δ	5	$P_c^*(=D_v I)$	50
α	0.025	$D_C(=\delta D_v)$	$2.5 * 10^{-9}$
γ	1000	$\Lambda_1(=\frac{\alpha D_v I}{c_{air}})$	$1.25 * 10^{-23}$
β	80	$v_r(=\frac{\gamma\eta D_v}{V_b g(\rho_b-\rho_w)L_y^3})$	$1.02 * 10^{15}$
		$\kappa(=\frac{c_{air} D_v \beta}{v_r L_y^2})$	$7.84 * 10^{6}$

Table 3: **(a) Base case**. Reference input parameters in the simulations with cell-fluid interaction coefficient $I = 5 * 10^{10}$ Pa s/m^2. Results are shown in Fig. 3 and Fig. 4.

(a) Base case: formation of falling plumes. We use input data as described in Table 3 (in terms of Sc, δ, α, γ, and β) which allow us to relate the study of the model (1.2) to (1.1). However, as noted above, in addition, we have to specify explicitly the strength of the cell-fluid drag force interaction through the parameter I, see Table 3. The motivation for the choice of I for this example is to allow formation of falling plumes but such that the plumes do not detach from the cell layer close to the surface. This requires the right balance between the effect of the gravity force, which drives the cell phase downwardly, and the upward-directed chemotactic effect controlled by Λ_1. In particular, to achieve this we found that the value of α should be small (compared to what has been used in [6]), for example, $\alpha = 0.025$. After all, the model we have derived from (1.2), which gives rise to the transport equation (5.47) used to motivate for the relations (5.48), is based on various approximations. The simulation result for this parameter set is shown in Fig. 3 (cell volume fraction α_c and oxygen concentration C) and Fig. 4 (cell velocity $\mathbf{u}_c$ and fluid velocity $\mathbf{u}_w$).

The main observation is that coherent plumes are formed similar to what has been shown in other works [6, 8]. This is a result of the fact that the cell-fluid interaction I is strong enough to ensure a dominant co-current flow where cells and water move together (see Fig. 4). The figures (see bottom figures of Fig. 4) show how the upward fluid flow between the falling plumes transports cells back to the upper layer close to the surface which can maintain a high density due to the everlasting access of oxygen that activates the upward chemotaxis effect. This mechanism continuously feeds cells into the high-concentration layer at the surface where gravity makes cells sink and by that maintains the fluid convection.

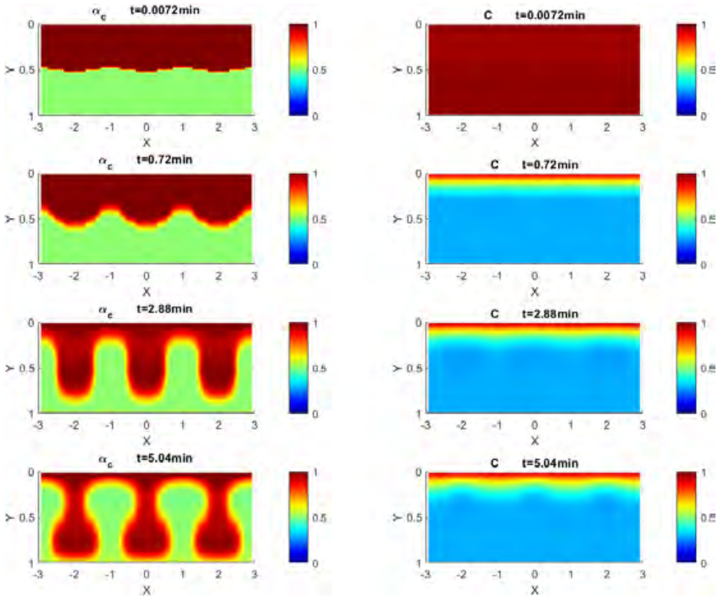

Figure 3: **(a) Base case**. Initially, a high cell volume fraction region dominates in the upper part of the domain (left column, top). We see that oxygen is consumed faster at the beginning in this region (right column, top). Since the whole system is open to the air at top side oxygen can constantly diffuse into the box whereas in the lower part oxygen is consumed by the cells such that the oxygen concentration reaches the lower limit $C = C^* = 0.3$. Beyond this limit the chemotaxis effect vanishes and gravity becomes the dominating force and the plumes will develop as cells sink towards the bottom. Clearly, cells are kept coherent in the upper region of the domain reflecting that the gravity and chemotaxis driven transport work together such that the developing plumes are maintained.

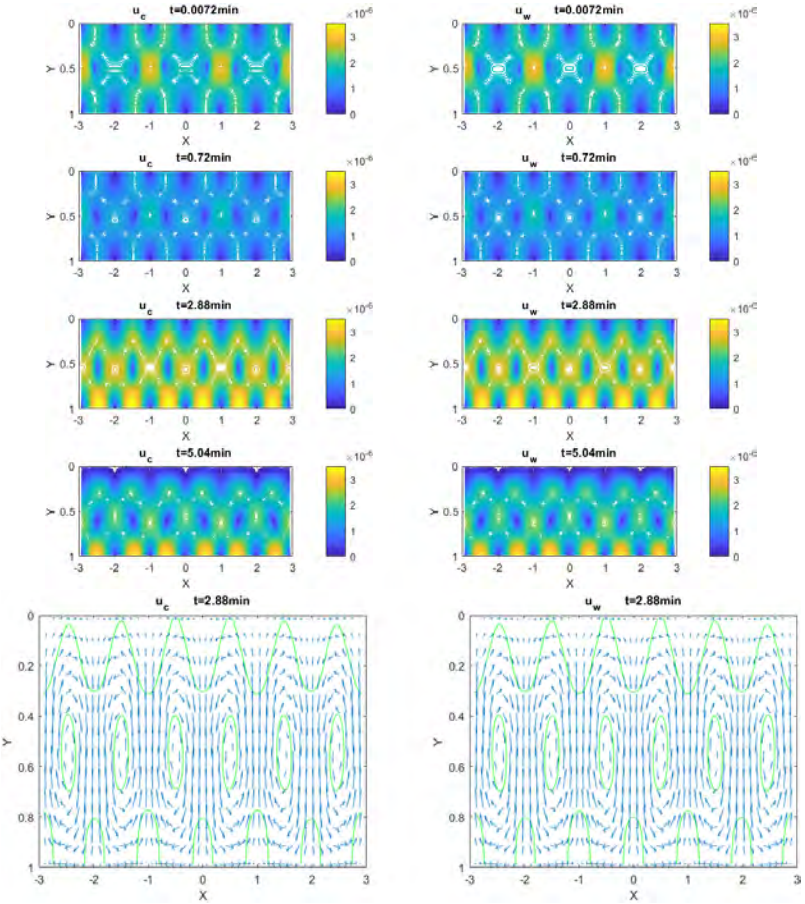

Figure 4: **(a) Base case**. The corresponding velocity field for cells $\mathbf{u}_c$ (left column) and water $\mathbf{u}_w$ (right column). Clearly, the cell-fluid interaction term I is strong enough to keep the two velocity fields close to each other generating co-current flow of cells and water. The bottom figures illustrate how the plumes are formed due to the fact that gravity dominates in the region with oxygen C close to $C^* = 0.3$ (see Fig. 3, right column and the blue region) and creates alternating subregions where cells move, respectively, downwardly and upwardly. This is an effect of gravity only. The purpose of the chemotactic swimming is to maintain the upper layer of the cells that stay close to the surface.

(b) What is the effect of reduced cell-fluid interaction I**?** We consider the same situation as for the base case. The only change is that we weaken the cell-fluid interaction I with a factor 10. See Table 4 for input data. Now, we may expect to see some clearer discrepancy between the cell velocity $\mathbf{u}_c$ and $\mathbf{u}_w$. Also, it is no longer obvious that the falling plumes can maintain the contact with the high volume fraction region close to the surface. Results are shown in Fig. 5 and Fig. 6. The main observation is that the falling plumes in fact will detach from the high cell density layer at the surface (left column) of Fig. 5. These plumes will be positioned at the bottom at final time. As gravity is the dominating force in this region we expect that the plumes will gradually even out and form a stagnant high cell volume fraction layer at the bottom.

Parameter	Value	Parameter	Value
Sc	1000	$D_v(=\frac{\eta}{Sc\rho_w})$	$1*10^{-9}$
δ	5	$P_c^*(=10D_vI)$	50
α	0.025	$D_C(=\delta D_v)$	$2.5*10^{-9}$
γ	1000	$\Lambda_1(=\frac{10\alpha D_v I}{c_{air}})$	$1.25*10^{-23}$
β	80	$v_r(=\frac{\gamma\eta D_v}{V_c g(\rho_b-\rho_w)L_y^3})$	$1.02*10^{15}$
		$\kappa(=\frac{c_{air}D_v\beta}{v_r L_y^2})$	$7.84*10^6$

Table 4: **(b) Reduced cell-fluid interaction**. Reference input parameters in the simulations with cell-fluid interaction parameter $I = 5*10^9$ Pa s/m^2 (i.e, is reduce with a factor 10 relatively the base case). Note that we have multiplied with 10 in relation for P_c^* and Λ_1 in order to keep the same values as for the base case. Results are shown in Fig. 5 and Fig. 6.

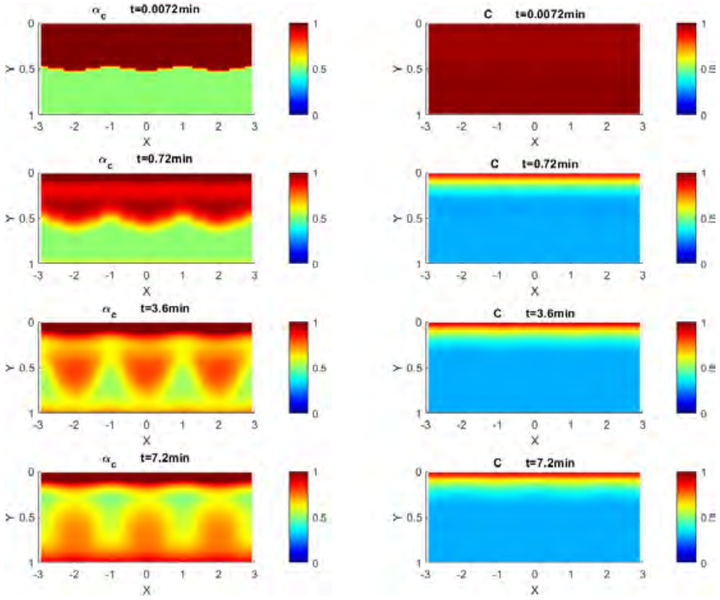

Figure 5: **(b) Reduced cell-fluid interaction**. The results in left column (cell volume fraction α_c) show that the high density region of cells (red region) is no longer continuous and separate into two parts. Referring to its velocity field results in Fig. 6, cells are free to move more independent of the water behavior due to the low fluid-cell interaction through I. The region where chemotaxis is not at work (right column, blue region) due to too low oxygen concentration is similar to the base case.

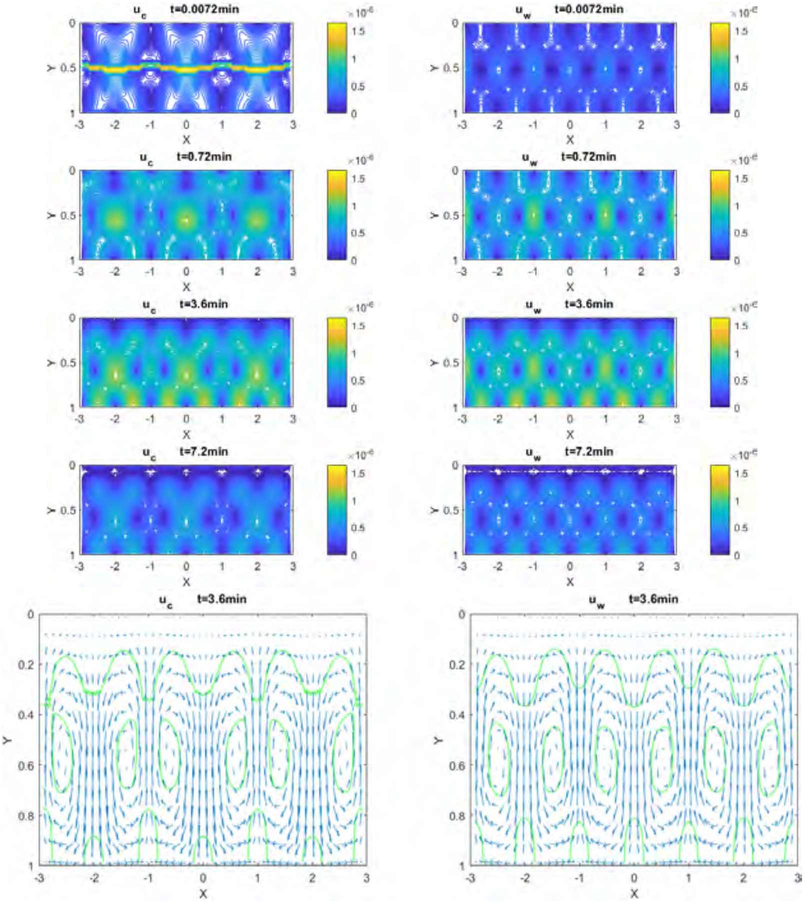

Figure 6: **(b) Reduced cell-fluid interaction**. Left column: cell velocity field $\mathbf{u}_c$. Right column: water velocity field $\mathbf{u}_w$. The bottom figures of the velocity fields $\mathbf{u}_c$ and $\mathbf{u}_w$ at time $t = 3.6$ min show that they largely possess the same general trends. However, there is a difference in the upper region close to the surface which is enough to lead to a detachment of the falling plumes.

(c) What is the effect of increased chemotaxis effect? We consider the same situation as for the base case, except that we strengthen the chemotactic swimming by increasing Λ_1 with a factor 4. See Table 5 for input data. Since chemotaxis is restricted to the high cell volume fraction region close to the surface, we may anticipate to see that the stronger chemotactic upward motion of cells can interrupt the fine-tuned balance seen for the base case where the falling plumes stay connected with the upper layer of cells. Results are shown in Fig. 7 and Fig. 8 and show that the falling plumes indeed tend to break loose from the upper layer. Note however that this detachment, as seen in Fig. 7 (left column) is quite different from the one in the previous example shown in Fig. 5 (left column). In the first case it seems to happen uniformly and globally and at an earlier time whereas in the latter case the shape of the falling plumes are maintained and the detachment is more local.

Parameter	Value	Parameter	Value
Sc	1000	$D_v(=\frac{\eta}{Sc\rho_w})$	$1*10^{-9}$
δ	5	$P_c^*(=D_vI)$	50
α	0.1	$D_C(=\delta D_v)$	$2.5*10^{-9}$
γ	1000	$\Lambda_1(=\frac{\alpha D_v I}{c_{air}})$	$5*10^{-23}$
β	80	$v_r(=\frac{\gamma\eta D_v}{V_c g(\rho_b-\rho_w)L_y^3})$	$1.02*10^{15}$
		$\kappa(=\frac{c_{air}D_v\beta}{v_r L_y^2})$	$7.84*10^{6}$

Table 5: **(c) Increased chemotactic effect**. Reference input parameters in the simulations with cell-fluid interaction parameter $I = 5*10^{10}$ Pa s/m^2 (base case) but where Λ_1 (which controls the strength of the chemotactic swimming towards higher concentration in C) is increased with a factor 4 through the higher value of α. Results are shown in Fig. 7 and Fig. 8.

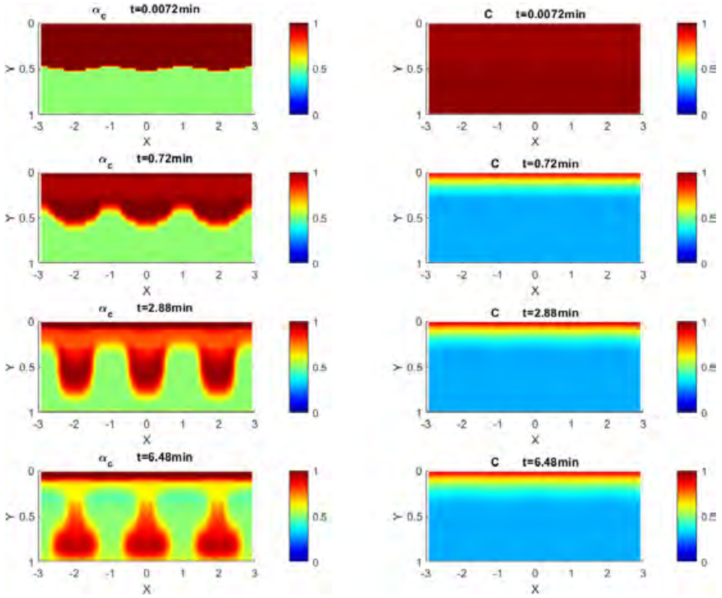

Figure 7: **(c) Increased chemotactic effect**. In this case we use a higher chemotaxis strength compared to the base case (4 times). It is seen that cells still tend to fall as three plumes, however, there is not enough cells to maintain this flow pattern closer to the surface. Here cells are under influence of a strong upward chemotactic swimming. Moreover, we observe that in this case the falling plumes have a high volume fraction in the plume heads (low part of the system) but a relatively low cell volume fraction in the middle part.

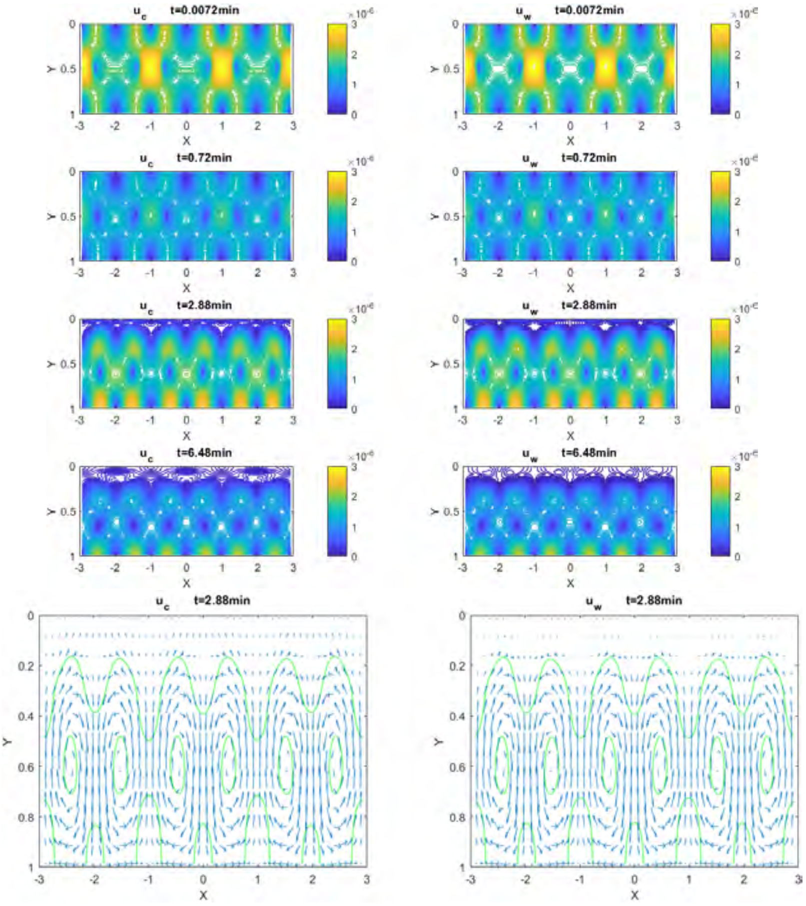

Figure 8: **(c) Increased chemotactic effect**. Left column: cell velocity field $\mathbf{u}_c$. Right column: water velocity field $\mathbf{u}_w$. This figure shows that in the middle of the process ($t = 2.88$ min) cells are still strongly attracted to the top side (compared with the base case) even though cells and water follow the same flow pattern.

(d) What is the effect of reduced chemotaxis effect? Next, we wonder what will happen if we reduce the chemotaxis effect. The input data is given in Table 6. The resulting behavior for the cell volume fraction and oxygen C is shown in Fig. 9. The most striking effect on the development of the falling plumes, as compared to the base case in Fig. 3, is that the shape of the plumes changes and they fill a larger area in the lower part of the domain and the layer at the surface becomes thinner.

Parameter	Value	Parameter	Value
Sc	1000	$D_v(=\frac{\eta}{Sc\rho_w})$	$1*10^{-9}$
δ	5	$P_c^*(=D_vI)$	50
α	$6.25\cdot10^{-3}$	$D_C(=\delta D_v)$	$2.5*10^{-9}$
γ	1000	$\Lambda_1(=\frac{\alpha D_vI}{c_{air}})$	$3.125*10^{-24}$
β	80	$v_r(=\frac{\gamma\eta D_v}{V_cg(\rho_b-\rho_w)L_y^3})$	$1.02*10^{15}$
		$\kappa(=\frac{c_{air}D_v\beta}{v_rL_y^2})$	$7.84*10^{6}$

Table 6: **(d) Reduced chemotactic effect**. Reference input parameters in the simulations with cell-fluid interaction $I=5*10^{10}$ Pa s/m^2 (base case). We reduce the chemotaxis effect by reducing Λ_1 with a factor 4 through a lower value of α.

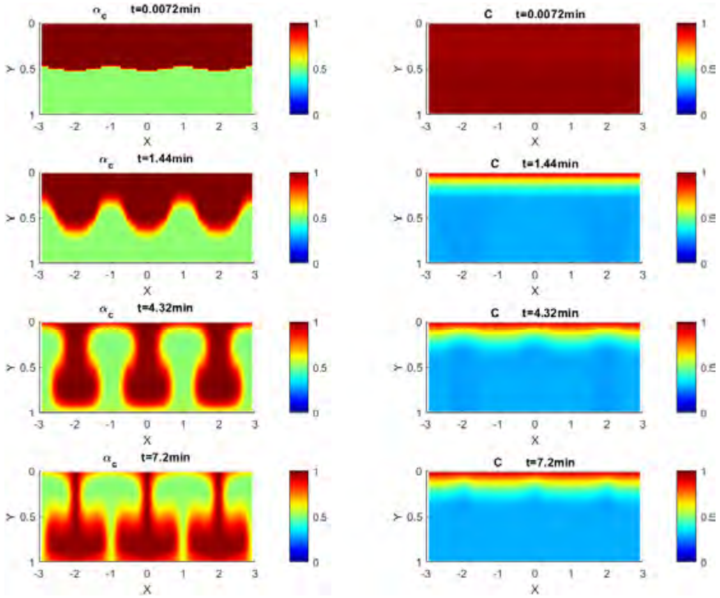

Figure 9: **(d) Reduced chemotactic effect**. Compared to the results of the base case in Fig. 3, a larger portion of the cells become part of the falling plumes instead of being captured by the high cell volume fraction layer close to the surface due. This is a natural consequence of weakening the chemotaxis effect which is responsible for maintaining the upper high density cell layer.

(e) What is the effect of increased cell volume fraction? The input data is given in Table 7 and shows that the initial cell volume fraction is increased with a factor 50 through the increase in γ with a factor 50. Results are shown in Fig. 10 and Fig. 11. The main observation is that in the very beginning (see first row of Fig. 10) falling plumes are quickly formed. However, the higher volume fraction of cells leads to a large consumption of oxygen which strongly reduces the chemotactic swimming. Gravity dominates everywhere except close to the surface and a chaotic behavior is seen through a shorter period of time. A large portion of cells sink to the bottom centrally while cells also are transported upwardly closer to the side ends, see Fig. 11, caused by upward water flow.

Parameter	Value	Parameter	Value
Sc	1000	$D_v(=\frac{\eta}{Sc\rho_w})$	$1*10^{-9}$
δ	5	$P_c^*(=D_vI)$	50
α	0.025	$D_C(=\delta D_n)$	$2.5*10^{-9}$
γ	50000	$\Lambda_1(=\frac{\alpha D_v I}{c_{air}})$	$1.25*10^{-23}$
β	80	$v_r(=\frac{\gamma\eta D_v}{V_c g(\rho_b-\rho_w)L_y^3})$	$5.1*10^{16}$
		$\kappa(=\frac{50c_{air}D_v\beta}{v_rL_y^2})$	$7.84*10^6$

Table 7: **(e) Increased cell volume fraction**. Reference input parameters with $I = 5*10^{10}$ Pa s/m^2 (base case) where we have increased γ with a factor 50. I.e., the initial cell volume fraction α_{c0} increases with a factor 50 via its dependence on v_r. Note that we keep the consumption rate κ at the same level as before by introducing a factor 50 in the expression for κ.

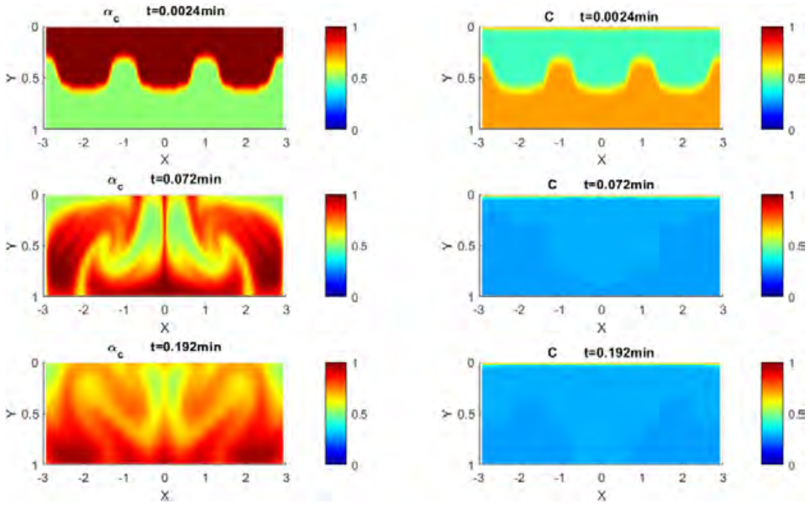

Figure 10: **(e) Increased initial cell volume fraction**. Compared with the base case, the reference cell fraction n_r increases with 50 times. The results illustrate totally different flow behavior, a fast and strong vortex-dominating redistribution of cells in a short period. Large proportions of cells fall downward due to a dominant gravitational effect.

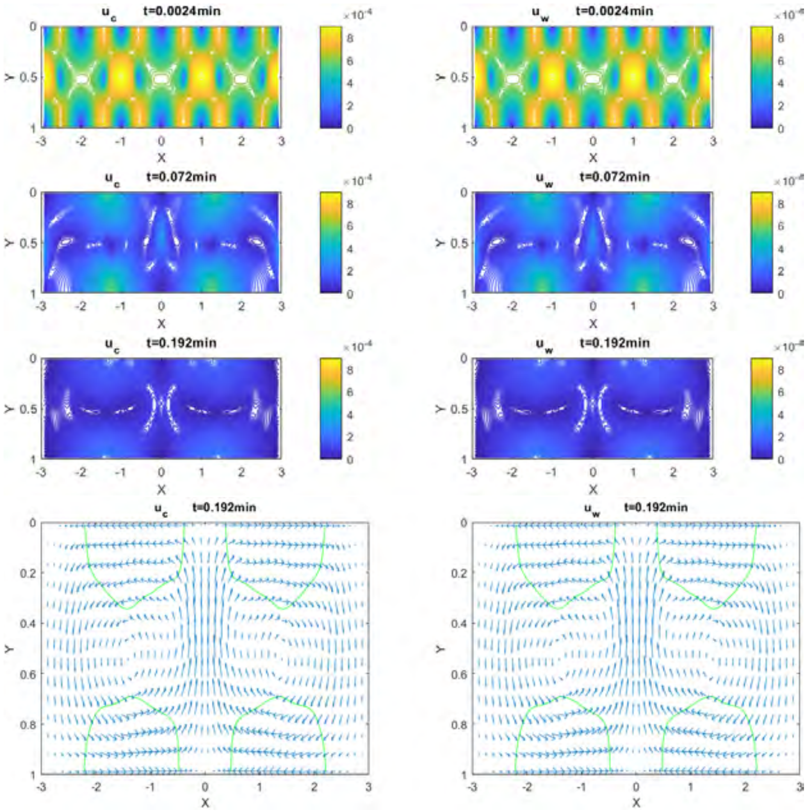

Figure 11: **(e) Increased initial cell volume fraction**. Left column: cell velocity field $\mathbf{u}_c$. Right column: water velocity field $\mathbf{u}_w$. As before, the strong fluid-cell interaction through I results in velocity fields $\mathbf{u}_c$ and $\mathbf{u}_w$ that essentially are equal.

(f) Base case with small initial perturbation of cells. In this example we want to test what happens when we consider input data as for the base case, Table 3, but we change the initial cell volume fraction such that the perturbations on the interface between the high and low cell density region are smaller. The initial condition now takes the form:

$$\alpha_{c0}(x,y) = \begin{cases} v_r V_b, & y > 0.499 - 0.0135\sin((1.2x - 1.5)\pi); \\ 0.5 v_r V_b, & \text{otherwise.} \end{cases} \tag{5.54}$$

The result is shown in Fig. 12. Clearly, the shape of the developing falling plumes is affected by the initial cell volume fraction. Otherwise, the dynamics is to a large extent similar to base case.

(g) What is the role of the fluid and cell acceleration terms? We want to explore the role played by the acceleration terms in the momentum balance equations, i.e., the two first terms in $(1.2)_{3,4}$. For the base case in (a) we find that the model produces virtually the same behavior. Next, we consider the case (e) with a higher initial cell volume fraction. This gives higher cell and water velocities and as a result we can now also see that the acceleration terms play a role. We refer to Fig. 13 and Fig. 14 which should be compared with Fig. 10 and Fig. 11.

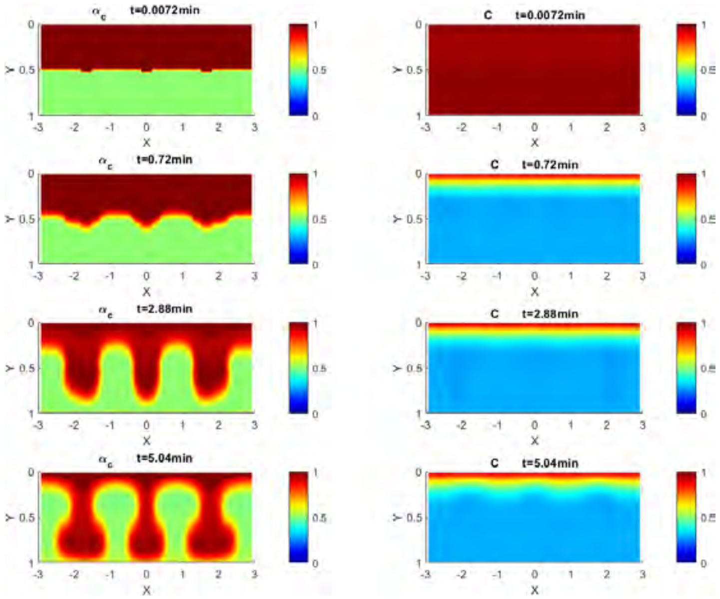

Figure 12: **(f) Base case with modified initial perturbation**. We implement the same input parameters as the base case but use different initial cell distribution with smaller perturbation as prescribed by (5.54). It is interesting to see that the shape of the falling plumes is different and the only reason is smaller perturbations on the initial interface of the cell distribution.

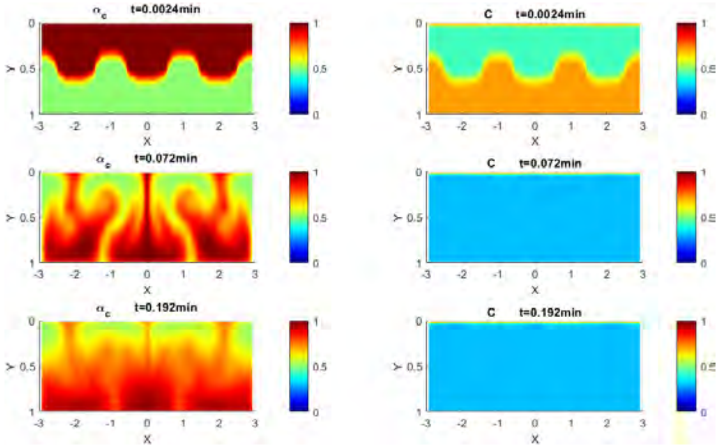

Figure 13: **(g) Increased initial cell volume fraction and acceleration effect is ignored**. Compared with Fig.10, the acceleration effect is ignored in the momentum equations and the results show the degree of vortex is smaller so that the main part of high-concentration cells flows downward with relatively stable behavior.

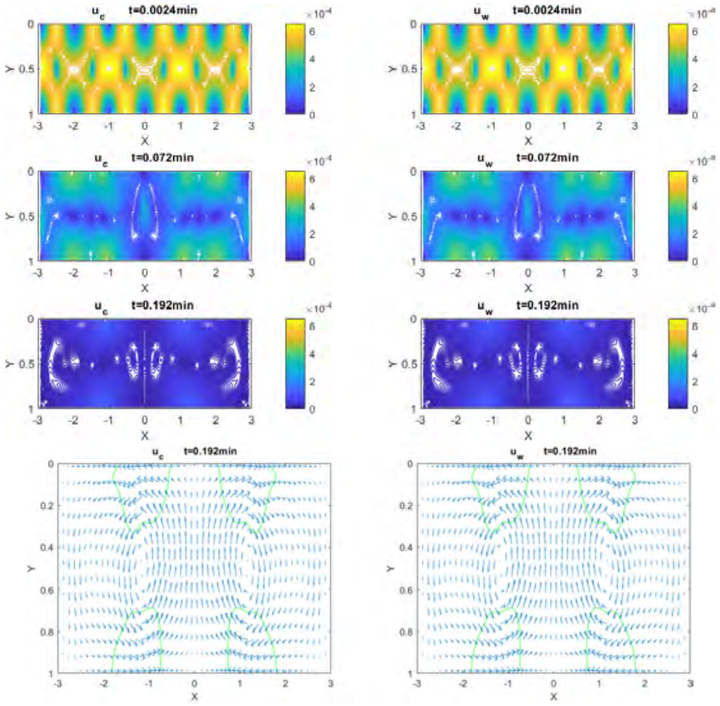

Figure 14: **(g) Increased initial cell volume fraction and acceleration effect is ignored**. Left column: cell velocity field $\mathbf{u}_c$. Right column: water velocity field $\mathbf{u}_w$. As before, the strong fluid-cell interaction through I results in velocity fields $\mathbf{u}_c$ and $\mathbf{u}_w$ that essentially are equal.

(h) Closed top surface and a high cell density cluster in the middle of the domain. In this example we shift focus and consider an example where the assumption about very low cell density, used to link (1.2) to (1.1), is relaxed. We also assume that the the domain is closed with no continuous feeding of oxygen at the top. We use input data as in Table 3 (the values in the right column except v_r). The initial cell distribution is high in the center of the domain and given by

$$\alpha_{c0}(x,y) = 0.7\exp(-(25((x/10)^2 + (y-0.5)^2)^{0.5} - 0.5)^2). \tag{5.55}$$

The results are shown in Fig. 15 and Fig. 16. Main observations are:

(i) Time $t = 0.0144$. Quickly the initial coherent cell cluster splits into two parts. One which flows upwardly, another that move to the bottom, see Fig. 15 (second row), both driven by chemotaxis. The initial cell cluster quickly consumes oxygen and creates gradients in C which the cells move towards. The strong coupling between cell and fluid phase creates vortex-dominated motion where the water that surrounds the moving cell clusters enters to fill the left behind void.

(ii) Times $t = 0.0432$, $t = 0.144$, and $t = 0.288$. Both in the upper and lower cell cluster there is a vortex-like behavior that continues developing. The lower cluster spreads quicker in the horizontal direction, most likely because of additional momentum from the gravity force. Both cell clusters experience strong deacceleration as they hit the boundary and are forced to go horizontally.

(iii) Times $t = 1.44$, $t = 4.32$, and $t = 14.4$. The vortices start collapsing as oxygen is consumed and chemotaxis effect comes to a halt. Gravity segregation becomes the dominating mechanism and slowly leading to accumulation of more and more cells in the lower region.

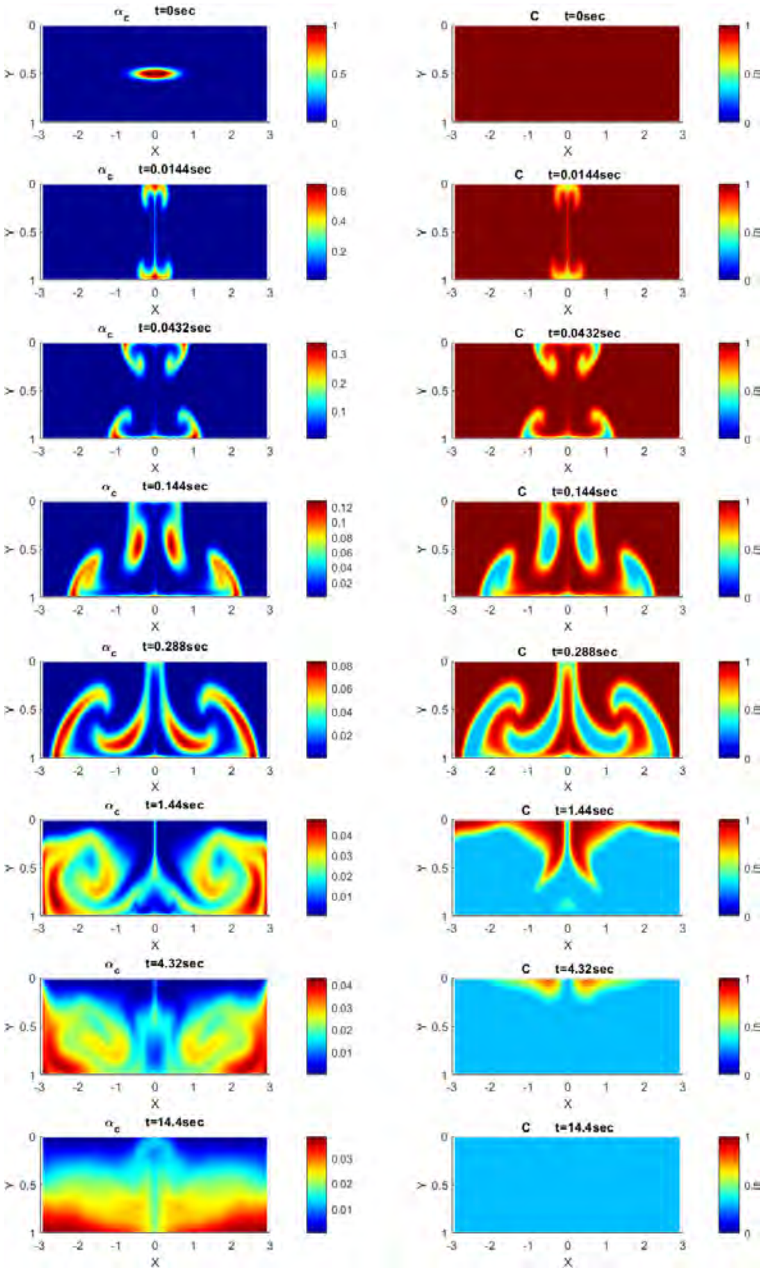

Figure 15: **(h) Surface is closed and high initial density of cells located in the center**. Left column: Cell volume fraction α_c. Right column: Oxygen concentration C.

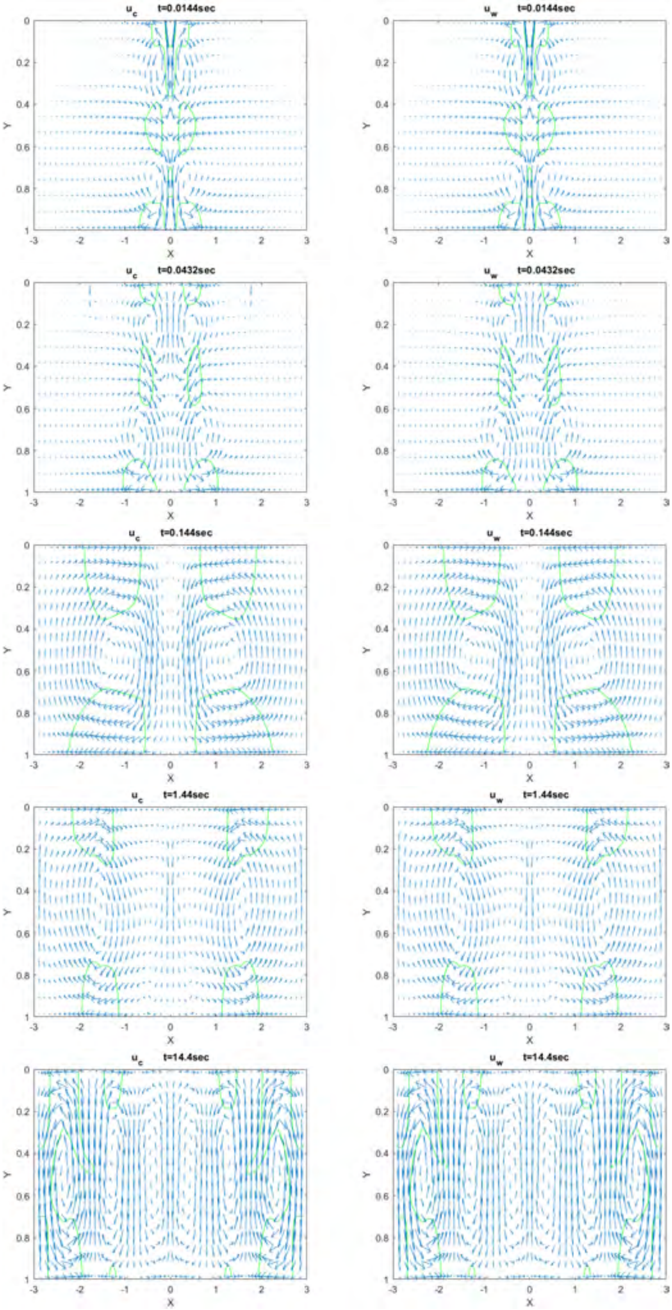

Figure 16: **(h) Surface is closed and high initial density of cells located in the center**. Left column: cell velocity field $\mathbf{u}_c$. Right column: water velocity field $\mathbf{u}_w$.

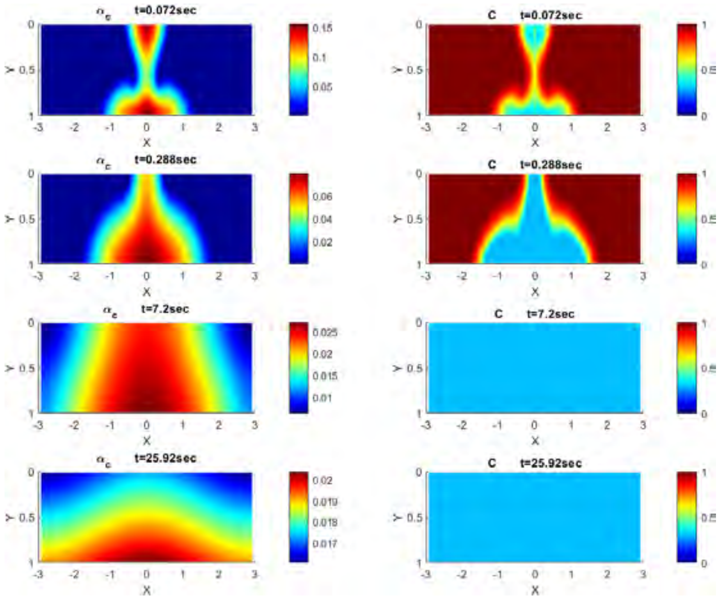

α_c t=0.072sec

C t=0.072sec

α_c t=0.288sec

C t=0.288sec

α_c t=7.2sec

C t=7.2sec

α_c t=25.92sec

C t=25.92sec

Figure 17: **Revisit of example (h) with 1000 times weaker cell-fluid interaction** I. The cells are more free to move independent from the fluid. Gravity segregation will lead to a sedimentation of cells towards the bottom.

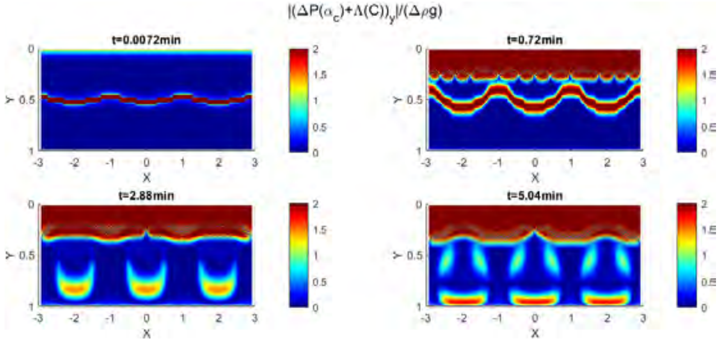

$|(\Delta P(\alpha_c)+\Lambda(C))_y|/(\Delta\rho g)$

t=0.0072min

t=0.72min

t=2.88min

t=5.04min

Figure 18: **Diffusive and chemotactic spreading versus gravity segregation**. We revisit the base case and visualize the magnitude of the diffusive and chemotactic term appearing on the right hand side of assumption (ii) in Section 2.2 given by $(\Delta P(\alpha_c) + \Lambda(C))_y$ and compare it with the gravity segregation term $\Delta\rho\mathbf{g}$ appearing on the left hand side. Note that the red part of the colorbar covers values up till around 10. We see that gravity segregration cannot be ignored, neither at the head of the plumes nor higher up towards the central part which plays a role in shaping the plumes, and by that shows a difference between model (1.2) and (1.1).

5.3. **Some final remarks.**

- The base case (a) shows formation of falling plumes. As time elapses it seems that the magnitude of the velocity field decreases and it may not be likely that this pattern can persist for eternal time. To our understanding this does not rule out the possibility that there might be a choice of parameters that can ensure a "perfect" balance between chemotaxis and gravity such that a stationary plume pattern can be achieved. However, this may require unlimited access to oxygen to maintain the chemotactic effect.
- Example (b) illustrates the role played by the cell-fluid drag force term as a controller of the internal competition between gravity and chemotaxis. A weaker I will interrupt the fine tuned balance (seen in the base case) between gravity and chemotaxis that maintains the connection between the falling plumes and the upper layer. On the other hand, if we increase I, say with a factor of 100, simulations show that (not included in the paper) that the stronger cell-fluid coupling leads to a thicker cell-layer close to the surface and also increases the head of the falling plumes. This illustrates how I controls the gravity segregation effect which is included in the model (1.2) we use but is ignored in (1.1). In Fig. 17 we revisit case (h) where we have reduced the cell-fluid interaction I by a factor 1000. The effect is dramatic. Now gravity segregation becomes much more dominating and the interplay between the cell and fluid phase will instead create a slow separation-dominated process quite different from the behavior seen in Fig. 15.
- We can illustrate the difference between the two models (1.2) and (1.1) for the base case example by estimating the strength of gravity segregation through $\Delta\rho\mathbf{g}$ versus the sum of the diffusion and chemotaxis through $(\Delta P(\alpha_c) + \Lambda(C))_y$ in vertical direction. The result is shown in Fig. 18 and explains why we may expect to see some difference in the behavior of the two models.
- The case studied in (h) with a closed domain illustrates how complicated and colorful behavior is produced as a result of the interplay between chemotaxis and gravity during a transient period of time. In the early stage chemotaxis completely dominates and gives birth to strong vortices that later will collapse. At the later stage gravity dominates as oxygen is consumed. After sufficiently long time chemotaxis vanishes and gravity segregation and diffusion will dictate the long-time behavior of the cell and fluid mass. We expect the velocity fields to slowly decrease to zero. This behavior seems consistent with the precise mathematical stabilization results obtained, e.g. in [47, 50] for a model similar to (1.1). The main reason why a stationary flow pattern cannot be produced, from our understanding, is the lack of oxygen which implies that chemotaxis will come to a halt after a finite time.

References

[1] L. Almeida, F. Bubba, B. Perthame and C. Pouchol, Energy and implicit discretization of the Fokker-Planck and Keller-Segel type equations, *Netw. Het. Med.* **14** (2019) 23–41.

[2] R. M. Bowen, Theory of mixtures, *Continuum Physics* (1976).

[3] D. Bresch, B. Desjardins, J.-M. Ghidaglia and E. Grenier, Global weak solutions to a generic two-fluid model, *Arch. Rational Mech. Anal.* **196** (2010) 599–629.

[4] D. Bresch, X. D. Huang and J. Li, Global weak solutions to one-dimensional non-conservative viscous compressible two-phase system, *Comm. Math. Phys.* **309** (2012) 737-755.

[5] D. Bresch, P. B. Mucha and E. Zatorska, Finite-energy solutions for compressible two-fluid Stokes system, *Arch. Rational Mech. Anal.* **232** (2019) 987-1029.

[6] A. Chertock, K. Fellner, A. Kurganov, A. Lorz and P. A. Markowich, Sinking, merging and stationary plumes in a coupled chemotaxis-fluid model: a high-resolution numerical approach, *J. Fluid Mech.* **694** (2012) 155–190.

[7] L. H. Cisneros, R. Cortez, C. Dombrowski, R. E. Goldstein and J. O. Kessler, Fluid dynamics of self-propelled microorganisms, from individuals to concentrated populations, *Exp. Fluids* **43** (2007) 737–753.

[8] A. Decoene, S. Martin and B. Maury, Microscopic modelling of active bacterial suspensions, *Math. Model. Nat. Phenom.* **6** (2011) 98–129.

[9] Y. Deleuze, C.-Y. Chiang, M. Thiriet and T. W. H. Sheu, Numerical study of plume patterns in a chemotaxis–diffusion–convection coupling system, *Comput. Fluids* **126** (2016) 58–70.

[10] M. Di Francesco, A. Lorz and P. Markowich, Chemotaxis-fluid coupled model for swimming bacteria with nonlinear diffusion: global existence and asymptotic behavior, *Discrete Contin. Dyn. Syst. Ser. A* **28** (2010) 1437–1453.

[11] C. Dombrowski, L. Cisneros, S. Chatkaew, R. Goldstein and J. Kessler, Self-concentration and large-scale coherence in bacterial dynamics, *Phys. Rev. Lett.* **93** (2004) 098103-1–098103-4.

[12] D. A. Drew and S. L. Passman, Theory of multicomponent fluids (Springer, 1999).

[13] R. Duan, A. Lorz and P. Markowich, Global solutions to the coupled chemotaxis-fluid equations, *Commun. Part. Diff. Eq.* **35** (2010) 1635–1673.

[14] S. Evje, Weak solutions for a gas-liquid model relevant for describing gas-kick in oil wells, *SIAM J. Math. Anal.* **43** (2011) 1887–1922.

[15] S. Evje, A compressible two-phase model with pressure-dependent well-reservoir iteraction, *SIAM J. Math. Anal.* **45** (2013) 518–546.

[16] S. Evje, Genuine two-phase flow dynamics with a free interface separating gas-liquid mixture from gas, *SIAM J. Math. Anal.* **45** (2013) 2894–2923.

[17] S. Evje and H. Wen, Global solutions of a viscous gas-liquid model with unequal fluid velocities in a closed conduit, *SIAM J. Math. Anal.* **47** (2015) 381–406.

[18] S. Evje and H. Wen, Weak solutions of a two-phase Navier-Stokes model with a general slip law, *J. Funct. Anal.* **268** (2015) 93–139.

[19] S. Evje, An integrative multiphase model for cancer cell migration under influence of physical cues from the microenvironment, *Chem. Eng. Science* **165** (2017) 240–259.

[20] S. Evje and J. O. Waldeland, How tumor cells can make use of interstitial fluid flow in a strategy for metastasis, *Cell. Mol. Bioeng.* **12** (2019) 227–254.

[21] S. Evje and H. Wen, A Stokes two-fluid model for cell migration that can account for physical cues in the microenvironment, *SIAM J. Math. Anal.* **50** (2018) 86—118.

[22] S. Evje, W. Wang and H. Wen, Global well-posedness and decay rates of strong solutions to a non-conservative compressible two-fluid model *Arch. Rational Mech. Anal.* **221** (2016) 1285–1316.

[23] U. Haessler, J. C. M. Teo, D. Foretay, P. Renaud and M. A. Swartz, Migration dynamics of breast cancer cells in a tunable 3D interstitial flow chamber, *Integrative Biol.* **4** (2012) 401–409.

[24] C. Hao and H. Li, Well-posedness for a multidimensional viscous liquid-gas two-phase flow model, *SIAM J. Math Anal.* **44** (2012) 1304–1332.

[25] A. Hillesdon, T. J. Pedley and J. O. Kessler, The development of concentration gradients in a suspension of chemotactic bacteria, *Bull. Math. Biol.* **57** (1995) 299–344.

[26] A. Hillesdon and T. J. Pedley, Bioconvection in suspensions of oxytactic bacteria: linear theory, *J. Fluid Mech.* **324** (1996) 223–259.

[27] H. G. Lee and J. Kim, Numerical investigation of falling bacterial plumes caused by bioconvection in a three-dimensional chamber, *Eur. J. Mech. B. Fluids* **52** (2015) 120–130.

[28] A. Lorz, Coupled chemotaxis fluid model, *Math. Models Methods Appl. Sci.* **20** (2010) 987–1004.

[29] C. Michoski and A. Vasseur, Existence and uniqueness of strong solutions for a compressible multiphase Navier-Stokes miscible fluid-flow problem in dimension n = 1, *Math. Models Methods Appl. Sci.* **19** (2009) 443—476.

[30] A. Novotny and M. Pokorny, Weak solutions for some compressible multicomponent fluid models, *Arch. Rational. Mech. Anal.* (2019), https://doi.org/10.1007/s00205-019-01424-2.

[31] T. J. Pedley and J. O. Kessler, Hydrodynamic phenomena in suspensions of swimming micro-organisms, *Ann. Rev. Fluid Mech.* **24** (1992) 313–358.

[32] W. J. Polacheck, J. L. Charest and R. D. Kamm, Interstitial flow influences direction of tumor cell migration through competing mechanisms, *Proc. Natl. Acad. Sci. USA* **108** (2011) 11115—11120.

[33] Y. Qiao, P. Ø. Andersen, S. Evje and D. C. Standnes, A mixture theory approach to model co- and counter-current two-phase flow in porous media accounting for viscous coupling, *Adv. Water Res.* **112** (2018) 170–188.

[34] Y. Qiao, H. Wen and S. Evje, Compressible and viscous two-phase flow in porous media based on mixture theory formulation, *Netw. Het. Med.* **14** (2019) 489–536.

[35] K. R. Rajagopal and L. Tao, *Mechanics of Mixtures*, Series on Advances in Mathematics for Applied Sciences, Vol. 35 (World Scientific, 1995).

[36] K. R. Rajagopal, On a hierarchy of approximate models for flows of incompressible fluids through porous solids, *Math. Models Methods Appl. Sci.* **17** (2007) 215-252.

[37] S. Solem and S. Evje, Relaxation limit of a compressible gas-liquid model with well-reservoir interaction, *Zeitschrift für angewandte Mathematik und Physik* **68** (2017) 23.

[38] W. Tao and Y. Li, Global weak solutions for the three-dimensional chemotaxis-Navier–Stokes system with slow -Laplacian diffusion, *Nonlinear Anal. Real World Appl.* **45** (2019) 26–52.

[39] Y. Tao and M. Winkler, Global existence and boundedness in a Keller-Segel-Stokes model with arbitrary porous medium diffusion, *Discrete Contin. Dyn. Syst. A* **32** (2012) 1901–1914.

[40] I. Tuval, L. Cisneros, C. Dombrowski, C. W. Wolgemuth, J. O. Kessler, and R. E. Goldstein, Bacterial swimming and oxygen transport near contact lines, *Proc. Natl. Acad. Sci. USA* **102** (2005) 2277–2282.

[41] J. Urdal, J. O. Waldeland and S. Evje, Enhanced cancer cell invasion caused by fibroblasts when fluid flow is present, *Biomech. Model Mechanobiol.* **18** (2019) 1047–1078.

[42] A. Vasseur, H. Wen and C. Yu, Global weak solution to the viscous two-phase model with finite energy, *J. Math. Pures Appl.* **125** (2019) 247–282.

[43] J. O. Waldeland and S. Evje, A multiphase model for exploring cancer cell migration driven by autologous chemotaxis, *Chem. Eng. Sci.* **191** (2018) 268–287.

[44] J. O. Waldeland and S. Evje, Competing tumor cell migration mechanisms caused by interstitial fluid flow, *J. Biomech.* **81** (2018) 22–35.

[45] H. Wen, Global existence of weak solution to compressible two-fluid model without any domination condition in three dimensions, *arXiv preprint arXiv:1902.05190* (2019).

[46] M. Winkler, Global large-data solutions in a chemotaxis-(Navier–)Stokes system modeling cellular swimming in fluid drops, *Commun. Part. Diff. Eq.* **37** (2012) 319–351.

[47] M. Winkler, Stabilization in a two-dimensional chemotaxis-Navier–Stokes system, *Arch. Ration. Mech. Anal.* **211** (2014) 455–487.

[48] M. Winkler, Boundedness and large time behavior in a three-dimensional chemotaxis-Stokes system with nonlinear diffusion and general sensitivity, *Calc. Var. Partial Dif.* **54** (2015) 3789–3828.

[49] M. Winkler, How far do chemotaxis-driven forces influence regularity in the Navier-Stokes system?, *Trans. Am. Math. Soc.* **369** (2017) 3067–3125.

[50] M. Winkler, Global existence and stabilization in a degenerate chemotaxis-Stokes system with mildly strong diffusion enhancement, *J. Diff. Eqs.* **264** (2018) 6109–6151.

[51] C. W. Wolgemuth, Collective swimming and the dynamics of bacterial turbulence, *Biophys. J.* **95** (2008) 1564–1574.

[52] H. Wen, L. Yao and C. Zhu, Review on mathematical analysis of some two-phase flow models, *Acta Math. Sci.* **38B** (2018) 1617–1636.

[53] Y. Zhang and C. Zhu, Global existence and optimal convergence rates for the strong solutions in H^2 to the 3D viscous liquid-gas two-phase flow model, *J. Diff. Eq.* **258** (2015) 2315–2338.

APPENDIX A: NUMERICAL SCHEME FOR THE 2D MODEL (4.43) WITH INCOMPRESSIBLE PHASES

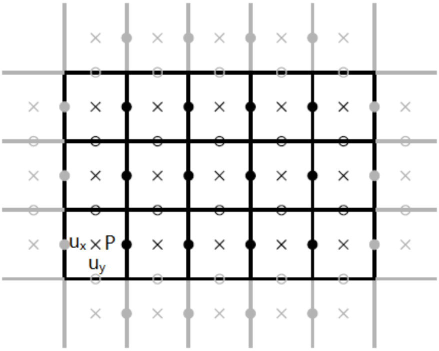

Figure 19: Staggered grid with boundary cells.

We consider the domain $\Omega = [0,1] \times [0,1]$ in the x-direction and y-direction. For the x-direction

$$x_1 = \frac{1}{2}\Delta x, \quad x_2 = (1+\frac{1}{2})\Delta x, \quad \dots, \quad x_j = (j-\frac{1}{2})\Delta x, \quad \dots, \quad x_{N_x} = (N_x - \frac{1}{2})\Delta x$$

with cell interfaces $x_{j+1/2}$ at the cell interfaces

$$x_{1/2} = 0, \quad x_{3/2} = \Delta x, \quad \dots, \quad x_{j+1/2} = j\Delta x, \quad \dots, \quad x_{N_x+1/2} = N_x \Delta x = 1,$$

where $\Delta x = 1/N_x$. Similar for the y-direction

$$y_1 = \frac{1}{2}\Delta y, \quad y_2 = (1+\frac{1}{2})\Delta y, \quad \dots, \quad y_i = (i-\frac{1}{2})\Delta y, \quad \dots, \quad y_{N_y} = (N_y - \frac{1}{2})\Delta y$$

with cell interfaces $y_{i+1/2}$ at the cell interfaces

$$y_{1/2} = 0, \quad y_{3/2} = \Delta y, \quad \dots, \quad y_{i+1/2} = i\Delta y, \quad \dots, \quad y_{N_y+1/2} = N_y \Delta y = 1,$$

where $\Delta y = 1/N_y$. We consider the following finite difference scheme for (4.43).

Step 1: Mass transport.
The following discrete version of $(4.43)_1$ is used

$$\frac{\alpha^{k+1}_{c,ij}-\alpha^{k}_{c,ij}}{\Delta t}+\frac{1}{\Delta x}([\alpha_c u^x_c]^k_{i+1/2,j}-[\alpha_c u^x_c]^k_{i-1/2,j})+\frac{1}{\Delta y}([\alpha_c u^y_c]^k_{i,j+1/2}-[\alpha_c u^y_c]^k_{i,j-1/2})=0. \tag{5.56}$$

where

$$[\alpha_c u^x_c]^k_{i+1/2,j}=\begin{cases}\alpha^k_{c,i,j}u^{x,k}_{c,i+1/2,j}, & \text{if } u^{x,k}_{c,i+1/2,j}\geq 0;\\ \alpha^k_{c,i+1,j}u^{x,k}_{c,i+1/2,j}, & \text{if } u^{x,k}_{c,i+1/2,j}<0.\end{cases} \tag{5.57}$$

and

$$[\alpha_c u^y_c]^k_{i,j+1/2}=\begin{cases}\alpha^k_{c,i,j}u^{y,k}_{c,i,j+1/2}, & \text{if } u^{y,k}_{c,i,j+1/2}\geq 0;\\ \alpha^k_{c,i,j+1}u^{y,k}_{c,i,j+1/2}, & \text{if } u^{y,k}_{c,i,j+1/2}<0.\end{cases} \tag{5.58}$$

Similarly, the following discrete version of $(4.43)_2$ is used

$$\begin{aligned}&\frac{C^{k+1}_{ij}-C^{k}_{ij}}{\Delta t}+\frac{1}{\Delta x}([Cu^x_w]^k_{i+1/2,j}-[Cu^x_w]^k_{i-1/2,j})+\frac{1}{\Delta y}([Cu^y_w]^k_{i,j+1/2}-[Cu^y_w]^k_{i,j-1/2})=\\ &\frac{D_C}{\Delta x}\Big[\frac{C^k_{i+1,j}-C^k_{i,j}}{\Delta x}-\frac{C^k_{i,j}-C^k_{i-1,j}}{\Delta x}\Big]+\frac{D_C}{\Delta y}\Big[\frac{C^k_{i,j+1}-C^k_{i,j}}{\Delta y}-\frac{C^k_{i,j}-C^k_{i,j-1}}{\Delta y}\Big]-K\alpha^k_{c,ij}C^k_{ij},\end{aligned} \tag{5.59}$$

where

$$[Cu^x_w]^k_{i+1/2,j}=\begin{cases}C^k_{i,j}u^{x,k}_{w,i+1/2,j}, & \text{if } u^{x,k}_{w,i+1/2,j}\geq 0;\\ C^k_{i+1,j}u^{x,k}_{w,i+1/2,j}, & \text{if } u^{x,k}_{w,i+1/2,j}<0.\end{cases} \tag{5.60}$$

and

$$[Cu^y_w]^k_{i,j+1/2}=\begin{cases}C^k_{i,j}u^{y,k}_{w,i,j+1/2}, & \text{if } u^{y,k}_{w,i,j+1/2}\geq 0;\\ C^k_{i,j+1}u^{y,k}_{w,i,j+1/2}, & \text{if } u^{y,k}_{w,i,j+1/2}<0.\end{cases} \tag{5.61}$$

Step 2: Computation of velocities and pressure.
The purpose is to solve for $P^{k+1}_{c,ij}$ and $u^{x,k+1}_{w,i+1/2,j}$, $u^{x,k+1}_{c,i+1/2,j}$, $u^{y,k+1}_{w,i,j+1/2}$ and $u^{y,k+1}_{c,i,j+1/2}$ by considering the algebraic system corresponding to $(4.43)_{3,4,5,6,7}$. A discrete version of $(4.43)_3$ takes the form

$$\begin{aligned}&\frac{1}{\Delta x}([\alpha^{k+1}_w u^{x,k+1}_w]_{i+1/2,j}-[\alpha^{k+1}_w u^{x,k+1}_w]_{i-1/2,j})\\ &\qquad+\frac{1}{\Delta x}([\alpha^{k+1}_c u^{x,k+1}_c]_{i+1/2,j}-[\alpha^{k+1}_c u^{x,k+1}_c]_{i-1/2,j})\\ &+\frac{1}{\Delta y}([\alpha^{k+1}_w u^{y,k+1}_w]_{i,j+1/2}-[\alpha^{k+1}_w u^{y,k+1}_w]_{i,j-1/2})\\ &\qquad+\frac{1}{\Delta y}([\alpha^{k+1}_c u^{y,k+1}_c]_{i,j+1/2}-[\alpha^{k+1}_c u^{y,k+1}_c]_{i,j-1/2})=0.\end{aligned} \tag{5.62}$$

Remark 5.1. *The upwind discretization of* $[\alpha^{k+1}_w u^{x,k+1}_w]_{i+1/2,j}$ *and* $[\alpha^{k+1}_w u^{y,k+1}_w]_{i,j+1/2}$ *appearing in* (5.62) *are based on "old" velocities* $u^{x,k}_{w,i+1/2,j}$ *and* $u^{y,k}_{w,i,j+1/2}$. *That is,*

$$\begin{aligned}[]
[\alpha^{k+1}_w u^{x,k+1}_w]_{i+1/2,j}&=\alpha^{k+1}_{w,i+1/2,j}u^{x,k+1}_{w,i+1/2,j}\\ [\alpha^{k+1}_w u^{y,k+1}_w]_{i,j+1/2}&=\alpha^{k+1}_{w,i,j+1/2}u^{y,k+1}_{w,i,j+1/2}\end{aligned} \tag{5.63}$$

with

$$\begin{aligned}\alpha^{k+1}_{w,i+1/2,j}&=\frac{\alpha^{k+1}_{w,i,j}+\alpha^{k+1}_{w,i+1,j}}{2}-\frac{1}{2}(\alpha^{k+1}_{w,i+1,j}-\alpha^{k+1}_{w,i,j})sgn(u^{x,k}_{w,i+1/2,j})\\ \alpha^{k+1}_{w,i,j+1/2}&=\frac{\alpha^{k+1}_{w,i,j}+\alpha^{k+1}_{w,i,j+1}}{2}-\frac{1}{2}(\alpha^{k+1}_{w,i,j+1}-\alpha^{k+1}_{w,i,j})sgn(u^{y,k}_{w,i,j+1/2})\end{aligned} \tag{5.64}$$

Similarly, for $[\alpha_c^{k+1}u_c^{x,k+1}]_{i+1/2,j}$ *and* $[\alpha_c^{k+1}u_c^{y,k+1}]_{i,j+1/2}$.

The total mass balance equation (5.62) is combined with the momentum balance equation $(4.43)_{4,5,6,7}$ to solve for $u_{w,i+1/2,j}^{x,k+1}$, $u_{w,i,j+1/2}^{y,k+1}$, $u_{c,i+1/2,j}^{x,k+1}$, $u_{c,i,j+1/2}^{y,k+1}$, and $P_{c,i,j}^{k+1}$. First, from $(4.43)_4$ we have

$$
\begin{aligned}
&\frac{m_{i+1/2,j}^{k+1}u_{w,i+1/2,j}^{x,k+1} - m_{i+1/2,j}^{k}u_{w,i+1/2,j}^{x,k}}{\Delta t} \\
&+ \frac{[mu_w^x]_{i+1,j}^{k+1/2}\frac{u_{w,i+1/2,j}^{x,k+1}+u_{w,i+3/2,j}^{x,k+1}}{2}}{\Delta x} - \frac{[mu_w^x]_{i,j}^{k+1/2}\frac{u_{w,i-1/2,j}^{x,k+1}+u_{w,i+1/2,j}^{x,k+1}}{2}}{\Delta x} \\
&+ \frac{[mu_w^y]_{i+1/2,j+1/2}^{k+1/2}\frac{u_{w,i+1/2,j}^{x,k+1}+u_{w,i+1/2,j+1}^{x,k+1}}{2}}{\Delta y} - \frac{[mu_w^y]_{i+1/2,j-1/2}^{k+1/2}\frac{u_{w,i+1/2,j-1}^{x,k+1}+u_{w,i+1/2,j}^{x,k+1}}{2}}{\Delta y} \\
&+ \alpha_{w,i+1/2,j}^{k+1}\frac{1}{\Delta x}(P_{c,i+1,j}^{k+1} - P_{c,i,j}^{k+1}) = \alpha_{w,i+1/2,j}^{k+1}\frac{1}{\Delta x}(\Delta P_{i+1,j}^{k+1} - \Delta P_{i,j}^{k+1} + \Lambda_{i+1,j}^{k+1} - \Lambda_{i,j}^{k+1}) \\
&+ \hat{\zeta}_{i+1/2,j}^{k+1}\Big(u_{c,i+1/2,j}^{x,k+1} - u_{w,i+1/2,j}^{x,k+1}\Big) + m_{i+1/2,j}^{k+1}g \\
&+ \frac{2\varepsilon_w}{\Delta x^2}\Big(m_{i+1,j}^{k+1}[u_{w,i+3/2,j}^{x,k+1} - u_{w,i+1/2,j}^{x,k+1}] - m_{i,j}^{k+1}[u_{w,i+1/2,j}^{x,k+1} - u_{w,i-1/2,j}^{x,k+1}]\Big) \\
&+ \varepsilon_w\frac{[m]_{i+1/2,j+1/2}^{k+1}\frac{u_{w,i+1,j+1/2}^{y,k+1}-u_{w,i,j+1/2}^{y,k+1}}{\Delta x} - [m]_{i+1/2,j-1/2}^{k+1}\frac{u_{w,i+1,j-1/2}^{y,k+1}-u_{w,i,j-1/2}^{y,k+1}}{\Delta x}}{\Delta y} \\
&+ \varepsilon_w\frac{[m]_{i+1/2,j+1/2}^{k+1}\frac{u_{w,i+1/2,j+1}^{x,k+1}-u_{w,i+1/2,j}^{x,k+1}}{\Delta y} - [m]_{i+1/2,j-1/2}^{k+1}\frac{u_{w,i+1/2,j}^{x,k+1}-u_{w,i+1/2,j-1}^{x,k+1}}{\Delta y}}{\Delta y}
\end{aligned}
\tag{5.65}
$$

with

$$
\begin{aligned}
[mu_w^x]_{i+1,j}^{k+1/2} &= \Big[m_{i+1,j}^{k+1}\frac{u_{w,i+1/2,j}^{x,k} + u_{w,i+3/2,j}^{x,k}}{2}\Big] \\
[mu_w^y]_{i+1/2,j+1/2}^{k+1/2} &= \Big[\frac{m_{i+1/2,j}^{k+1} + m_{i+1/2,j+1}^{k+1}}{2}\,\frac{u_{w,i,j+1/2}^{y,k} + u_{w,i+1,j+1/2}^{y,k}}{2}\Big] \\
[m]_{i+1/2,j+1/2}^{k+1} &= \Big[\frac{m_{i+1/2,j}^{k+1} + m_{i+1/2,j+1}^{k+1}}{2}\Big]
\end{aligned}
\tag{5.66}
$$

where $\alpha_{w,i+1/2,j}^{k+1}$ and $m_{i+1/2,j}^{k+1}$ are discretized as $(5.64)_1$ (recalling that ρ_w is constant). Similarly, for $(4.43)_5$ we have

$$
\begin{aligned}
&\frac{n_{i+1/2,j}^{k+1} u_{c,i+1/2,j}^{x,k+1} - n_{i+1/2,j}^{k} u_{c,i+1/2,j}^{x,k}}{\Delta t} \\
&+ \frac{[nu_c^x]_{i+1,j}^{k+1/2} \frac{u_{c,i+1/2,j}^{x,k+1} + u_{c,i+3/2,j}^{x,k+1}}{2}}{\Delta x} - \frac{5 \frac{u_{c,i-1/2,j}^{x,k+1} + u_{c,i+1/2,j}^{x,k+1}}{2}}{\Delta x} \\
&+ \frac{[nu_c^y]_{i+1/2,j+1/2}^{k+1/2} \frac{u_{c,i+1/2,j}^{x,k+1} + u_{c,i+1/2,j+1}^{x,k+1}}{2}}{\Delta y} - \frac{[nu_c^y]_{i+1/2,j-1/2}^{k+1/2} \frac{u_{c,i+1/2,j-1}^{x,k+1} + u_{c,i+1/2,j}^{x,k+1}}{2}}{\Delta y} \\
&+ \alpha_{c,i+1/2,j}^{k+1} \frac{1}{\Delta x} (P_{c,i+1,j}^{k+1} - P_{c,i,j}^{k+1}) = -\hat{\zeta}_{i+1/2,j}^{k+1} \Big(u_{c,i+1/2,j}^{x,k+1} - u_{w,i+1/2,j}^{x,k+1} \Big) + n_{i+1/2,j}^{k+1} g \\
&+ \frac{2\varepsilon_c}{\Delta x^2} \Big(n_{i+1,j}^{k+1} [u_{c,i+3/2,j}^{x,k+1} - u_{c,i+1/2,j}^{x,k+1}] - n_{i,j}^{k+1} [u_{c,i+1/2,j}^{x,k+1} - u_{c,i-1/2,j}^{x,k+1}] \Big) \\
&+ \varepsilon_c \frac{[n]_{i+1/2,j+1/2}^{k+1} \frac{u_{c,i+1,j+1/2}^{y,k+1} - u_{c,i,j+1/2}^{y,k+1}}{\Delta x} - [n]_{i+1/2,j-1/2}^{k+1} \frac{u_{c,i+1,j-1/2}^{y,k+1} - u_{c,i,j-1/2}^{y,k+1}}{\Delta x}}{\Delta y} \\
&+ \varepsilon_c \frac{[n]_{i+1/2,j+1/2}^{k+1} \frac{u_{c,i+1/2,j+1}^{x,k+1} - u_{c,i+1/2,j}^{x,k+1}}{\Delta y} - [n]_{i+1/2,j-1/2}^{k+1} \frac{u_{c,i+1/2,j}^{x,k+1} - u_{c,i+1/2,j-1}^{x,k+1}}{\Delta y}}{\Delta y}
\end{aligned}
\tag{5.67}
$$

with

$$
\begin{aligned}
[nu_c^x]_{i+1,j}^{k+1/2} &= \Big[n_{i+1,j}^{k+1} \frac{u_{c,i+1/2,j}^{x,k} + u_{c,i+3/2,j}^{x,k}}{2} \Big] \\
[nu_c^y]_{i+1/2,j+1/2}^{k+1/2} &= \Big[\frac{n_{i+1/2,j}^{k+1} + n_{i+1/2,j+1}^{k+1}}{2} \frac{u_{c,i,j+1/2}^{y,k} + u_{c,i+1,j+1/2}^{y,k}}{2} \Big] \\
[n]_{i+1/2,j+1/2}^{k+1} &= \Big[\frac{n_{i+1/2,j}^{k+1} + n_{i+1/2,j+1}^{k+1}}{2} \Big]
\end{aligned}
\tag{5.68}
$$

where $n_{i+1/2,j}^{k+1}$ is discretized similar to $(5.64)_1$.

Furthermore, for $(4.43)_6$ we have

$$
\begin{aligned}
&\frac{m_{i,j+1/2}^{k+1} u_{w,i,j+1/2}^{y,k+1} - m_{i,j+1/2}^{k} u_{w,i,j+1/2}^{y,k}}{\Delta t} \\
&+ \frac{[mu_w^y]_{i,j+1}^{k+1/2} \frac{u_{w,i,j+1/2}^{y,k+1} + u_{w,i,j+3/2}^{y,k+1}}{2}}{\Delta y} - \frac{[mu_w^y]_{i,j}^{k+1/2} \frac{u_{w,i,j-1/2}^{y,k+1} + u_{w,i,j+1/2}^{y,k+1}}{2}}{\Delta y} \\
&+ \frac{[mu_w^x]_{i+1/2,j+1/2}^{k+1/2} \frac{u_{w,i,j+1/2}^{y,k+1} + u_{w,i+1,j+1/2}^{y,k+1}}{2}}{\Delta x} - \frac{[mu_w^x]_{i-1/2,j+1/2}^{k+1/2} \frac{u_{w,i-1,j+1/2}^{y,k+1} + u_{w,i,j+1/2}^{y,k+1}}{2}}{\Delta x} \\
&+ \alpha_{w,i,j+1/2}^{k+1} \frac{1}{\Delta x} (P_{c,i,j+1}^{k+1} - P_{c,i,j}^{k+1}) = \alpha_{w,i,j+1/2}^{k+1} \frac{1}{\Delta x} (\Delta P_{i,j+1}^{k+1} - \Delta P_{i,j}^{k+1} + \Lambda_{i,j+1}^{k+1} - \Lambda_{i,j}^{k+1}) \\
&+ \hat{\zeta}_{i,j+1/2}^{k+1} \Big(u_{c,i,j+1/2}^{y,k+1} - u_{w,i,j+1/2}^{y,k+1} \Big) + m_{i,j+1/2}^{k+1} g \\
&+ \frac{2\varepsilon_w}{\Delta y^2} \Big(m_{i,j+1}^{k+1} [u_{w,i,j+3/2}^{y,k+1} - u_{w,i,j+1/2}^{y,k+1}] - m_{i,j}^{k+1} [u_{w,i,j+1/2}^{y,k+1} - u_{w,i,j-1/2}^{y,k+1}] \Big) \\
&+ \varepsilon_w \frac{[m]_{i+1/2,j+1/2}^{k+1} \frac{u_{w,i+1/2,j+1}^{x,k+1} - u_{w,i+1/2,j}^{x,k+1}}{\Delta y} - [m]_{i-1/2,j+1/2}^{k+1} \frac{u_{w,i-1/2,j+1}^{x,k+1} - u_{w,i-1/2,j}^{x,k+1}}{\Delta y}}{\Delta x} \\
&+ \varepsilon_w \frac{[m]_{i+1/2,j+1/2}^{k+1} \frac{u_{w,i+1,j+1/2}^{y,k+1} - u_{w,i,j+1/2}^{y,k+1}}{\Delta x} - [m]_{i-1/2,j+1/2}^{k+1} \frac{u_{w,i,j+1/2}^{y,k+1} - u_{w,i-1,j+1/2}^{y,k+1}}{\Delta x}}{\Delta x}
\end{aligned}
\tag{5.69}
$$

with

$$\begin{aligned}
[mu_w^y]_{i,j+1}^{k+1/2} &= \Big[m_{i,j+1}^{k+1}\frac{u_{w,i,j+1/2}^{y,k}+u_{w,i,j+3/2}^{y,k}}{2}\Big] \\
[mu_w^x]_{i+1/2,j+1/2}^{k+1/2} &= \Big[\frac{m_{i,j+1/2}^{k+1}+m_{i+1,j+1/2}^{k+1}}{2}\,\frac{u_{w,i+1/2,j}^{x,k}+u_{w,i+1/2,j+1}^{x,k}}{2}\Big] \\
[m]_{i+1/2,j+1/2}^{k+1} &= \Big[\frac{m_{i,j+1/2}^{k+1}+m_{i+1,j+1/2}^{k+1}}{2}\Big]
\end{aligned} \tag{5.70}$$

where $m_{i,j+1/2}^{k+1}$ is discretized by $(5.64)_2$. Finally, for $(4.43)_7$ we have

$$\begin{aligned}
&\frac{n_{i,j+1/2}^{k+1}u_{c,i,j+1/2}^{y,k+1}-n_{i,j+1/2}^{k}u_{c,i,j+1/2}^{y,k}}{\Delta t} \\
&+\frac{[nu_c^y]_{i,j+1}^{k+1/2}\frac{u_{c,i,j+1/2}^{y,k+1}+u_{c,i,j+3/2}^{y,k+1}}{2}}{\Delta y}-\frac{[nu_c^y]_{i,j}^{k+1/2}\frac{u_{c,i,j-1/2}^{y,k+1}+u_{c,i,j+1/2}^{y,k+1}}{2}}{\Delta y} \\
&+\frac{[nu_c^x]_{i+1/2,j+1/2}^{k+1/2}\frac{u_{c,i,j+1/2}^{y,k+1}+u_{c,i+1,j+1/2}^{y,k+1}}{2}}{\Delta x}-\frac{[nu_c^x]_{i-1/2,j+1/2}^{k+1/2}\frac{u_{c,i-1,j+1/2}^{y,k+1}+u_{c,i,j+1/2}^{y,k+1}}{2}}{\Delta x} \\
&+\alpha_{c,i,j+1/2}^{k+1}\frac{1}{\Delta x}(P_{c,i,j+1}^{k+1}-P_{c,i,j}^{k+1})=-\hat{\zeta}_{i,j+1/2}^{k+1}\Big(u_{c,i,j+1/2}^{y,k+1}-u_{w,i,j+1/2}^{y,k+1}\Big)+n_{i,j+1/2}^{k+1}g \\
&+\frac{2\varepsilon_c}{\Delta y^2}\Big(n_{i,j+1}^{k+1}[u_{c,i,j+3/2}^{y,k+1}-u_{c,i,j+1/2}^{y,k+1}]-n_{i,j}^{k+1}[u_{c,i,j+1/2}^{y,k+1}-u_{c,i,j-1/2}^{y,k+1}]\Big) \\
&+\varepsilon_c\frac{[n]_{i+1/2,j+1/2}^{k+1}\frac{u_{c,i+1/2,j+1}^{x,k+1}-u_{c,i+1/2,j}^{x,k+1}}{\Delta y}-[n]_{i-1/2,j+1/2}^{k+1}\frac{u_{c,i-1/2,j+1}^{x,k+1}-u_{c,i-1/2,j}^{x,k+1}}{\Delta y}}{\Delta x} \\
&+\varepsilon_c\frac{[n]_{i+1/2,j+1/2}^{k+1}\frac{u_{c,i+1,j+1/2}^{y,k+1}-u_{c,i,j+1/2}^{y,k+1}}{\Delta x}-[n]_{i-1/2,j+1/2}^{k+1}\frac{u_{c,i,j+1/2}^{y,k+1}-u_{c,i-1,j+1/2}^{y,k+1}}{\Delta x}}{\Delta x}
\end{aligned} \tag{5.71}$$

with

$$\begin{aligned}
[nu_c^y]_{i,j+1}^{k+1/2} &= \Big[n_{i,j+1}^{k+1}\frac{u_{c,i,j+1/2}^{y,k}+u_{c,i,j+3/2}^{y,k}}{2}\Big] \\
[nu_c^x]_{i+1/2,j+1/2}^{k+1/2} &= \Big[\frac{n_{i,j+1/2}^{k+1}+n_{i+1,j+1/2}^{k+1}}{2}\,\frac{u_{c,i+1/2,j}^{x,k}+u_{c,i+1/2,j+1}^{x,k}}{2}\Big] \\
[n]_{i+1/2,j+1/2}^{k+1} &= \Big[\frac{n_{i,j+1/2}^{k+1}+n_{i+1,j+1/2}^{k+1}}{2}\Big]
\end{aligned} \tag{5.72}$$

where $n_{i,j+1/2}^{k+1}$ is discretized similar to $(5.64)_2$.